ASPHERIC GEODESIC LENSES FOR AN INTEGRATED OPTICAL SPECTRUM ANALYSER

A Thesis

Submitted to the Faculty of Engineering

of the University of Glasgow

for the degree of

Doctor of Philosophy

by

Gordon Frank Doughty, B.A.

November 1983

This work is dedicated to the author's wife, Patricia.

PROLOGUE

"..... every one who has succeeded in this line has done so, not by following written or communicated instructions, but by striking out a new line for himself; and I think I am correct in saying that there is hardly to be found any case of a person attaining notable success in the art of figuring optical surfaces by rigidly following directions or instructions given or bequeathed by others."

Sir Howard Grubb, 1886.

TABLE OF CONTENTS

ACKNOWLEDGEMENTS & DECLARATION viii

SUMMARY xiii

KEY TO ABBREVIATIONS AND SYMBOLS xv

CHAPTER 1 INTRODUCTION

1.1 Integrated Optical Signal-Processing 1

1.2 The integrated-optical spectrum analyser 2

1.2.1 Spectrum analysis by acousto-optic Bragg-deflection 2

1.2.2 The integrated-optical spectrum analyser (IOSA) 7

1.2.3 User requirements 10

1.3 Choice of materials and components for an IOSA 10

1.4 Titanium-diffused waveguides in lithium niobate 13

1.5 Focusing in integrated optics 15

1.5.1 Gratings and zone plates 15

1.5.2 Mode-index lenses 19

1.5.3 Configurational elements 19

1.6 Choice of geodesic lenses for the lithium niobate IOSA 21

1.7 Main findings of this work 24

CHAPTER 2 THEORY AND DESIGN OF GEODESIC LENSES 26

2.1 Specification of lenses for an IOSA 26

2.1.1 Choice of practical IOSA and lens dimensions 26

2.1.2 Propagation of truncated Gaussian-beam 28

2.1.3 Field curvature 29

2.1.4 Lens dimensions and image size 32

2.2 Geometrical optics of geodesic lenses 33

2.2.1 Introduction 33

2.2.2 Fermat's principle 33

2.2.3 Geodesics on surfaces of revolution 35

2.2.4 Ray-tracing expressions 40

2.3 Methods of designing geodesic lenses 43

2.3.1 Spherical lenses and their limitations 43

2.3.2 Edge-rounding of spherical lenses 48
2.3.3 Numerical optimisation: aspheric lens-profiles 49
2.3.4 Transformation of Luneberg-lens designs 50
2.3.5 Exact solution for lenses with perfect ray-traces 51
2.4 Modifications to the exact-solution profile of Sottini, Russo and Righini 57
2.4.1 Problems with small radii of curvature 57
2.4.2 Bridging over locally highly-curved regions 58
2.4.3 Profile tolerances related to spectrum analyser performance 64
2.5 Conclusions 67

CHAPTER 3 REVIEW OF LITHIUM NIOBATE COMPONENT FORMATION-PROCESSES AND METHODS USED FOR PLANE-SUBSTRATE PRODUCTION
3.1 Introduction 68
3.2 Aspherical surfaces 68
3.3 Cutting lithium niobate crystals 69
3.4 Machines for generating and polishing components 70
3.5 Grinding and lapping 77
3.6 Polishing 81
3.6.1 Surface finish 81
3.6.2 Laps and surface flatness 85
3.6.3 Rate of material removal in polishing 86
3.7 Preparation of plane parallel substrates for the present work 89
3.8 Conclusions 91

CHAPTER 4 ULTRASONIC GENERATION OF GEODESIC LENSES
4.1 Introduction 92
4.2 Modification of an ultrasonic drill 94
4.3 Methods of preparing ultrasonic tools 96
4.4 Tool wear 102
4.5 Lens generation 103
4.6 Conclusions 108

CHAPTER 5 GENERATION OF GEODESIC LENSES BY COMPUTER-CONTROLLED MACHINES

5.1 Review of computer-controlled aspheric generators 110
5.2 Lens generation on a jig grinder 112
5.2.1 Introduction 112
5.2.2 Plane grinding and polishing 117
5.2.3 Lens generating and polishing 121
5.3 Single-point diamond-turning of plane lithium niobate surfaces 125
5.4 Diamond-turning of geodesic lenses 133
5.4.1 Diamond-turning on a contact-lens lathe 133
5.4.2 Diamond-turning on a high-precision machine 135
5.4.3 Additions and setting adjustments to aspheriser 138
5.4.4 Turning of geodesic lenses 146
5.5 Conclusions 154

CHAPTER 6 POLISHING OF GENERATED LENSES

6.1 Large-area flexible-polisher 155
6.2 Small-area microcomputer-controlled polishing machine (MCPM) 159
6.3 Development of small-area polishing head 160
6.4 Construction of MCPM - hardware 165
6.4.1 Accuracy and design of mechanical components 165
6.4.2 Lens mounting and rotation spindle 166
6.4.3 Polishing-head positioning-unit 168
6.4.4 Positioning-unit electronics 170
6.4.5 Auxiliary equipment 172
6.5 Construction of MCPM - software 173
6.6 Use and evaluation of MCPM 180
6.7 Conclusions 183

CHAPTER 7 EVALUATION OF GEODESIC LENSES

7.1 Measurement of lens profile 184
7.1.1 Interferometric methods 184
7.1.2 Scanning depth-probe methods 188
7.1.3 Sira surface-form gauge 191
7.1.4 Development of geodesic-lens measuring-machine 196
7.2 Formation of waveguides and coupling 200
7.2.1 Formation of titanium-diffused waveguides on plane and concave surfaces 200
7.2.2 Methods of coupling light into waveguides 201
7.3 Assessment of surface roughness 206
7.3.1 Roughness of plane lithium niobate surfaces before and after waveguide formation 206
7.3.2 Measurements of roughness of lens surfaces 209
7.4 Assessment of lens imaging-performance 211
7.4.1 Measurement of lens focal-length 211
7.4.2 Measurement of image profile and width 212
7.5 Comparison of measured imaging-performance with that calculated from profile measurements 222
7.6 Conclusions 225

CHAPTER 8 ECONOMIC ASPECTS OF GEODESIC LENS FABRICATION

8.1 Introduction 228
8.2 Cost of machines and labour 228
8.2.1 Introduction 229
8.2.2 Capital equipment 229
8.2.3 Labour requirement 231
8.2.4 Number of machines required 232
8.3 Fabrication cost per lens 233
8.3.1 Introduction 233
8.3.2 Small number of lenses 234
8.3.3 Number of lenses which justifies MCPM purchase 235
8.3.4 Large number of lenses 235
8.4 Conclusions 238

CHAPTER 9 CONCLUSIONS

9.1 Introduction 239

9.2 Overall IOSA design: substrate and lenses 239

9.3 Geodesic lens design 240

9.4 Lens generation by ultrasonic impact-grinding 243

9.5 Lens generation by CNC grinding 244

9.6 lens generation by diamond-turning 245

9.7 Lens polishing 246

9.8 Lens evaluation 247

9.9 Choice of a geodesic-lens fabrication method 248

9.10 Summary of original work in this thesis. 249

9.11 Publications 249

REFERENCES 250

APPENDIX I Derivation of expressions for the slope of exact ray-tracing lens (Sottini, Russo and Righini), and for the second derivatives. I-1

APPENDIX II Derivation of approximations used for small arcs, tool setting and profile assessment errors. II-1

LIST OF TABLES AND ILLUSTRATIONS

TABLES

1. Aberration of a spherical geodesic-lens. 47
2. Circular arcs fitted to a Sottini, Russo and Righini lens profile without bridging over highly-curved regions. 63
3. Circular arcs fitted to a Sottini, Russo and Righini lens profile bridging over highly-curved regions. 63
4. Sottini,Russo and Righini rule-of-thumb approximation for tolerable lens-depth errors. 65
5. Measurements of ultrasonic tool and lens profiles. 98
6. Format and details of data required to control a Moore G18 jig grinder with GE 1050 computer for producing a 21-arc lens. 116
7. Variation of polishing feed-rate with radial-zone position. 120
8. Machines which could possibly diamond-turn geodesic lenses. 126
9. Diamond turning of plane lithium-niobate substrates on Bryant Symons facing-lathe. 129
10. Linear-interpolation points used for diamond-turning on a Moore aspherising machine. 140
11. Typical series of cuts and tests during diamond-turning of a geodesic lens. 149
12. Sequence of energising stepper-motor coils. 170
13. 8 bit coding of polishing-machine steps. 176
14. All possible step-values. 177
15. Memory map of loaded system. 179
16. Sign rules for the four loops through the polishing data-file. 179
17. Measured attenuation of narrow light-beams through lens. 215
18. Five combinations of lens-fabrication techniques. 229
19. Labour time per lens required by each combination of fabrication methods. 232

FIGURES

1.1 Spectrum analysis by acousto-optic Bragg deflection 3

1.2 Geodesic-lens integrated-optical microwave-spectrum analyser. 8

1.3 Focusing elements for surface waveguides. 16

2.1 Fitting one or two IOSA onto a 61mm diameter boule section. 27

2.2 Effect of field curvature on defocusing at detector array. 30

2.3 Ratio of worst-case defocused spot-width to detector-element size as a function of lens focal-length. 31

2.4 Layout and dimensions of IOSA with two identical lenses. 34

2.5 Relationship between infinitesimals on a geodesic surface. 36

2.6 Plane projection of ray paths on and beyond an axisymmetrical geodesic lens. 36

2.7 Geodesic path on a spherical surface. 44

2.8 Geometrical trace of rays from infinity through a spherical-section geodesic lens, illustrating spherical aberration. 46

2.9 Definition of terms used in SRR derivation of perfectly-focusing geodesic-lens profile. 53

2.10 A family of lens profiles with F/12.7 relative aperture. 55

2.11 A geodesic lens profile derived by the SRR method, with diameter 10mm, and edge-rounding beyond 3.7mm, for conjugates infinity and 18.5mm. 56

2.12 Local radius of curvature of an SRR-designed geodesic lens. 59

2.13 Method of fitting circular arcs to an SRR-lens profile. 61

2.14 Ray-traced spot-size around the position of the designed focus of a circular-arc-approximated geodesic-lens profile, compared with the perfect SRR-profile and the diffraction limit. 66

3.1 Methods of generating and polishing flat, spherical and aspherical surfaces. 72

3.2 Methods of fabricating aspheric depressions in $LiNbO_3$. 76
3.3 Graph of removal rate against time for alkaline silica-sol on a polyurethane-foam pad. 88
4.1 Ultrasonic drill as modified to grind geodesic lenses. 95
4.2 Drawing of tool for ultrasonically-grinding lens depressions. 97
4.3 Two ultrasonic tools which were turned by a tungsten-carbide profile-tool, which was in turn cut on a numerically-controlled spark-eroder. 97
4.4 Profile of tungsten-carbide tool, and coordinates of wire spark-eroder path. 101
4.5 Ultrasonic generation of a geodesic lens in progress. 104
4.6 Effect of temperature on rate of ultrasonic generation. 104
4.7 Measured profiles of ultrasonic tool and a generated lens,and amount of tool wear in generating the lens. 106
5.1 Moore jig grinder. 113
5.2 Surface roughness due to turning-tool radius (R) and feedrate (F). 118
5.3 Wear of resin-bonded diamond grinding-tool when forming a lens depression in $LiNbO_3$. 123
5.4 Single-point diamond-turning tool: definition of parameters. 130
5.5 Photograph of plane, diamond-turned $LiNbO_3$ Y-face. 131
5.6 Photomicrographs of plane, diamond-turned $LiNbO_3$. 131
5.7 Diamond-turning lathe for opthalmic contact lenses 134
5.8 Phase-contrast photomicrograph (35x) of central part of a spherical lens which was diamond-turned on a contact-lens lathe. 134
5.9 Moore aspheric-generating machine 136
5.10 Vacuum chuck for holding an IOSA substrate. 136
5.11 Envelope of diamond-turning tool-path at a junction between linear-interpolation sections. 141

5.12 Qualitative effect of positioning errors of turning tool or measuring probe. 145
5.13 Photographs of geodesic lenses after diamond-turning. 147
5.14 Lens-profile errors indicated by LVDT-probe measurement. 151
5.15 LVDT-probe measurement around an annulus of radius 3.7mm, showing apparent anisotropy of diamond-turned depth. 151
5.16 Nomarski phase-constrast micrograph of central part of a diamond-turned $LiNbO_3$ lens, showing anisotropy of surface roughness and annular ridges related to imperfections of machine-slide motion. 153
5.17 Talystep trace of profile over central 0.1mm diameter of a diamond-turned lens. 153
6.1 Flexible polishing-heads for geodesic-lens depressions. 156
6.2 Polishing arrangement using a small pad on a Kavo K9 dental-drill mounted on the reciprocating arm of a Logitech PM2A machine. 161
6.3 Small flexible polishing-head used in the arrangement of Figure 6.2 161
6.4 Polishing head containing a flexible polyurethane-foam insert, mounted on a motor and gearbox assembly. 164
6.5 Hydraulic-ram polishing-head for use with polyurethane inserts, and (below) a worn and a fresh felt polishing-cone. 164
6.6 Microcomputer-controlled polishing machine. 167
6.7 Three-axis drive-assembly for MCPM. 167
6.8 LVDT measuring-probe mounted on MCPM for axis alignment. 174
6.9 Felt-cone polishing-pad and pool of colloidal silica in a diamond-turned geodesic-lens depression mounted on the MCPM. 174
7.1 Interferograms of spherical part of a geodesic lens. 187

7.2 Profile of central 0.9mm diameter of a polished lens. 190
7.3 Sira aspheric-profile measuring-machine. 192
7.4 Output from Sira machine for a diamond-turned Sottini, Russo and Righini lens. 192
7.5 Errors measured in an aspheric geodesic-lens by the Sira surface-form gauge. 195
7.6 Deviation of distance-transducer from linear calibration of 183.2 μm/volt 198
7.7 Polishing edges of IOSA. 202
7.8 Sketch of lens-testing rig. 204
7.9 Photograph of lens-testing rig. 204
7.10 Testing performance of one lens. 205
7.11 Testing performance of lens pair. 205
7.12 Angular dependence of in-plane scattered light: Ti-$LiNbO_3$ guide. 208
7.13 Talystep traces of central part of aspheric geodesic-lens: after diamond-turning and after polishing. 210
7.14 Comparison of measured and calculated variation of focal length with aperture for an edge-rounded spherical lens. 213
7.15 Plot of intensity of the image of an edge-rounded spherical lens for a 3.65mm input beamwidth. 214
7.16 Variation of focused-spot diameter with input beamwidth for an edge-rounded spherical lens. 216
7.17 Projected image from IOSA lens. 218
7.18 Plot of intensity contours of a geodesic-lens image as relayed to a video camera. 220
7.19 Graph of intensity versus distance across a geodesic-lens image. 221
7.20 Measurements of spotwidth between closest minima. 222
8.1 Graph of cost per lens versus quantity required over three years for five combinations of fabrication technique. 236

ACKNOWLEDGEMENTS & DECLARATION

The author would like to record great appreciation of his supervisors Professor J.Lamb and Dr R.M. DeLaRue, for providing the opportunity, encouragement and guidance for carrying out this work. Financial support was provided by The Procurement Executive (MOD) and monitored by Dr B. Wheeler and Mr P. Williams of the Admiralty Surface Weapons Establishment, whose valuable assistance is duly recorded.

Some of the work reported in this thesis was carried out with or by colleagues, whose contributions are most gratefully acknowledged. Dr R.B.Wilson was responsible for adaptation of the ultrasonic-grinding machine, Mr J.Singh for waveguide fabrication, Mr J.F.Smith for diamond-turning with the contact-lens machine, for most of the mechanical design and construction of the microprocessor-controlled polishing-machine, and also much of its use in lens polishing, and Mr N. Finlayson for providing ray-tracing of the author's lens designs. The latter three colleagues also assisted with final lens evaluation.

Many valuable discussions were held with other members of the Electronics and Electrical Engineering Department of the University of Glasgow particularly Mr G.Boyle, Dr H.Davie, Mr R.Hutchins, Dr M.MacCauley, Dr D. Winning, and Dr S. Wright. Much advice and practical assistance was provided by Mr H. Anderson (and his staff), Mr J.Clarke, Mrs L. Hobbs, Mr K. Piechowiak, and Mr D. Thomson.

The author would like to acknowledge the contributions to this work by a large number of other individuals and organisations.

Help was given on lens design by Dr G.C. Righini of I.O.R.E., Florence, Professor M.Berry of the University of Bristol, and Professor P. Lagasse and Dr J. Van der Donk of the University of Gent.

Advice and practical assistance on the supply and optical working of lithium niobate was provided by many of the author's former colleagues at Barr and Stroud Ltd (particularly Dr B. Duchart, Mr C. Forsyth, Mr M. Fraser, Mr D. Gibson, Mr J. Millar, Mr T. Moran, Mr J. Morrison, Mr I. Murray, Mr G. Robertson and Dr A. Worrall), and by Dr R. Wilson of Logitech Ltd.

Assistance with lens grinding was obtained from Dr N. Christie of the University of Strathclyde (for ultrasonic grinding tools) and from Mr J. Flowers and Mr L. Barratt of R.L.Smith Ltd (for CNC jig grinding).

Help with diamond-turning was given by Mr P. Hannah and Mr S. Murcko of The Moore Special Tool Co, Mr M. Styles, Mr D. Whitchurch, and Mr R. Bruce of Bryant Symons Ltd, Mr K. Geere and Mr B. Walker of Dominion Contact Lens Ltd and Ealing Beck Ltd.

Help and advice on metrology was given by Dr K. Birch of the National Physical Laboratory, Mr W. Woodward and Mr G. Bannerman of the National Engineering Laboratory, Mr H. Ross, Mr B. Monaghan, Dr W. Johnston and Mr C. MacDonald of Barr and Stroud Ltd and Mr T. Williams of Sira Ltd. Mr S. Gratze of Marconi Research Centre permitted results to be quoted of measurements of the imaging performance of a geodesic lens.

Some of the work reported in this thesis has been previously published by the author and colleagues. Aspects of Chapters 1, 2 and 3 appear in Reference 114. Some of the material of Chapters 3, 4 and 5 is discussed in References 115 and 116, and again in reference 117 together with mention of some of the preliminary results which are presented in Chapters 6 and 7.

SUMMARY

The work discussed in this thesis was carried out to establish design and fabrication techniques for geodesic lenses on a lithium niobate substrate for an integrated-optical microwave-spectrum analyser (IOSA) which uses titanium-diffused waveguides.

Fourier transformation by acousto-optic Bragg deflection is discussed in Chapter 1, particulary in an integrated-optics format. This leads on to considering the signal-processing performance required of a typical IOSA, and methods of focusing of waveguided light.

The design of a particular substrate and pair of geodesic lenses is discussed in Chapter 2. The geometrical theory of geodesic-lens ray-tracing is presented, and methods of designing lenses are compared. An exact solution for perfect geometrical-imaging was found to give practical difficulties: a satisfactory technique for modifying the exact solution is described.

IOSA geodesic lenses require extremely smooth surfaces and unusual aspheric-profiles. Techniques for producing polished surfaces on lithium niobate and for forming aspheric profiles are reviewed in Chapter 3. Potentially suitable methods for IOSA-lens fabrication are selected.

Geodesic-lens profiles were generated by three methods. Ultrasonic impact-grinding is discussed in Chapter 4. Generation with computer-controlled machines (a jig grinder and a diamond-turning machine) is described in Chapter 5.

Lens polishing is described in Chapter 6, particularly with a low-cost microprocessor-controlled polishing machine which was developed especially during this work.

Several geodesic lenses were made, both singly and as pairs on IOSA substrates. Chapter 7 describes how waveguides were formed on these lenses and how their profile accuracy and focusing performance were assessed.

Economic aspects of the alternative geodesic-lens fabrication-methods are compared in Chapter 8. The main results of this work are discussed in Chapter 9, and suggestions for further work are proposed.

KEY TO ABBREVIATIONS USED THROUGHOUT THESIS

IOSA	integrated-optical microwave-spectrum analyser
SAW	surface acoustic wave
LVDT	linear variable distance transducer, or linear variable differential transformer
CNC	computer numerically-controlled
MCPM	microprocessor-controlled polishing-machine
Ra	roughness average

KEY TO FREQUENTLY USED SYMBOLS

X_s	length of substrate
Z_s	width of substrate
X_d	distance between geodesic lens edges - interaction space.
n_o	ordinary refractive-index of substrate
n_e	extraordinary refractive-index of substrate
Δn	refractive-index difference between waveguide and substrate.
λ_o, λ	wavelength of laser light in vacuum, in waveguide
N	number of detector elements
S_d	distance between detector element centres
Λ	SAW wavelength
V	SAW propagation velocity
f_o	centre frequency of the SAW
Δf	IOSA frequency resolution
B_s	IOSA frequency bandwidth
β	Bragg diffraction angle
R, ϕ, Z	general cylindrical coordinates of axisymmetric lens
Z(R)	depth of lens as function of radial position
S	distance measured along surface of generating curve
a	distance of object from lens centre
b	distance of image from lens centre
c	radius of entire geodesic lens
d	radial distance to inner edge-rounding boundary
W	greatest width of light beam within lens

F — focal length of lens

K — nearest-approach distance of a ray to lens centre

C — local radius of curvature of the lens profile

R_{MC}, Z_{MC} — coordinates of the centre of an arc which approximately fits the lens profile.

L — radius of curvature of the approximating arc

g — factor in diffraction expressions applying to image-width between nulls

D — width of image between first nulls

X_i, Y_i, Z_i, A_i, C_i — positions on the axes of various CNC machines

M, N, G, X, Y, A, C, I, J, K, F — programme codes to initiate various CNC machine tool functions

F_r — feedrate - radial velocity of tool/polisher over lens

T — radius of curvature of tool or measuring-probe tip

V_l — rotational velocity of lens or substrate

V_p — rotational velocity of polishing tool

P_r — pressure of polishing pad on lens at radius R

dh(r)/dt — polishing removal-rate at position R

ds(r)/dt — relative polishing-speed at position R

k — Preston's-law constant

p_v — peak-to-valley surface roughness

ΔL — error of tool- or probe-tip position

ΔE — error of lens profile (measured normal to surface)

CHAPTER 1: INTRODUCTION

1.1 INTEGRATED OPTICAL SIGNAL PROCESSING

The concept of an Integrated Optical device [1] is one in which optical and electrical components are formed monolithically on the surface of a small solid substrate, using the planar fabrication technology which has been established so successfully for integrated circuits. The fundamental principle of operation is the control and processing of light signals which propagate in waveguides on the surface of the substrate. The components which may be integrated onto the substrate surface include: light sources, light detectors, beamsplitters, lenses and a variety of electrode structures which transduce electrical signals from sources outside the system into electrical fields or acoustic waves on the surface of the substrate. The operation of many of the devices which have been proposed depends upon interactions involving the electro-optic effect or the acousto-optic effect.

Integrated Optical devices are expected to perform signal processing or switching very efficiently. Their major potential applications include: logic devices, analogue to digital converters, beam deflectors, modulators, tunable optical filters, second harmonic generators, convolution and correlation filters, and spectrum analysers.

The ideal Integrated Optical device would offer many potential advantages over non-optical systems and over bulk optical systems (i.e. systems where the interactions take place within the bulk of a material rather than on the surface, and where the system is made of several discrete devices which must be assembled together). These advantages include sensitivity (because interactions are confined within thin planar waveguides), high-speed operation, parallel processing capability, small dimensions (with component widths comparable to wavelengths of light), light weight and ruggedness.

In practice, of course, it will not be possible to attain the ideal. Because of materials limitations it will be inefficient, difficult or impossible to fabricate all of the required components monolithically. Practical systems may therefore have to be made by a hybrid combination of monolithic devices and discrete components. Hybridisation need not be a damaging limitation. One device which has been seen as having particular promise in a hybrid form is the Integrated Optical Spectrum Analyser (IOSA) [2 - 10].

The most crucial component which must be developed further before an IOSA may be satisfactorily produced is the element which focuses waveguided light, and this must be integral with the surface of the device. The subject of this thesis is the development of one such focusing element - the geodesic lens.

1.2 INTEGRATED OPTICAL SPECTRUM ANALYSER

1.2.1 Spectrum Analysis by Acousto-optic Bragg deflection

Microwave spectrum analysis may be performed by a Fourier transformation system in which the electromagnetic microwaves are transduced using the piezoelectric effect coupled to a suitable transparent elastic solid to produce a moving acoustic-wave, which in turn forms a refractive index phase-grating (Figure 1.1).

A collimated light beam is guided into the region of the moving phase-grating, and the resulting acousto-optic interaction diffracts the light beam. The general nature of the diffracted light intensity pattern depends on the values of the wavelength of the light in the medium, (i.e. λ_o/n where λ_o is the vacuum wavelength and n the refractive index of propagation), the wavelength of the acoustic wave, Λ, and the width of the acoustic beam, L. When L is very long compared with Λ, or more

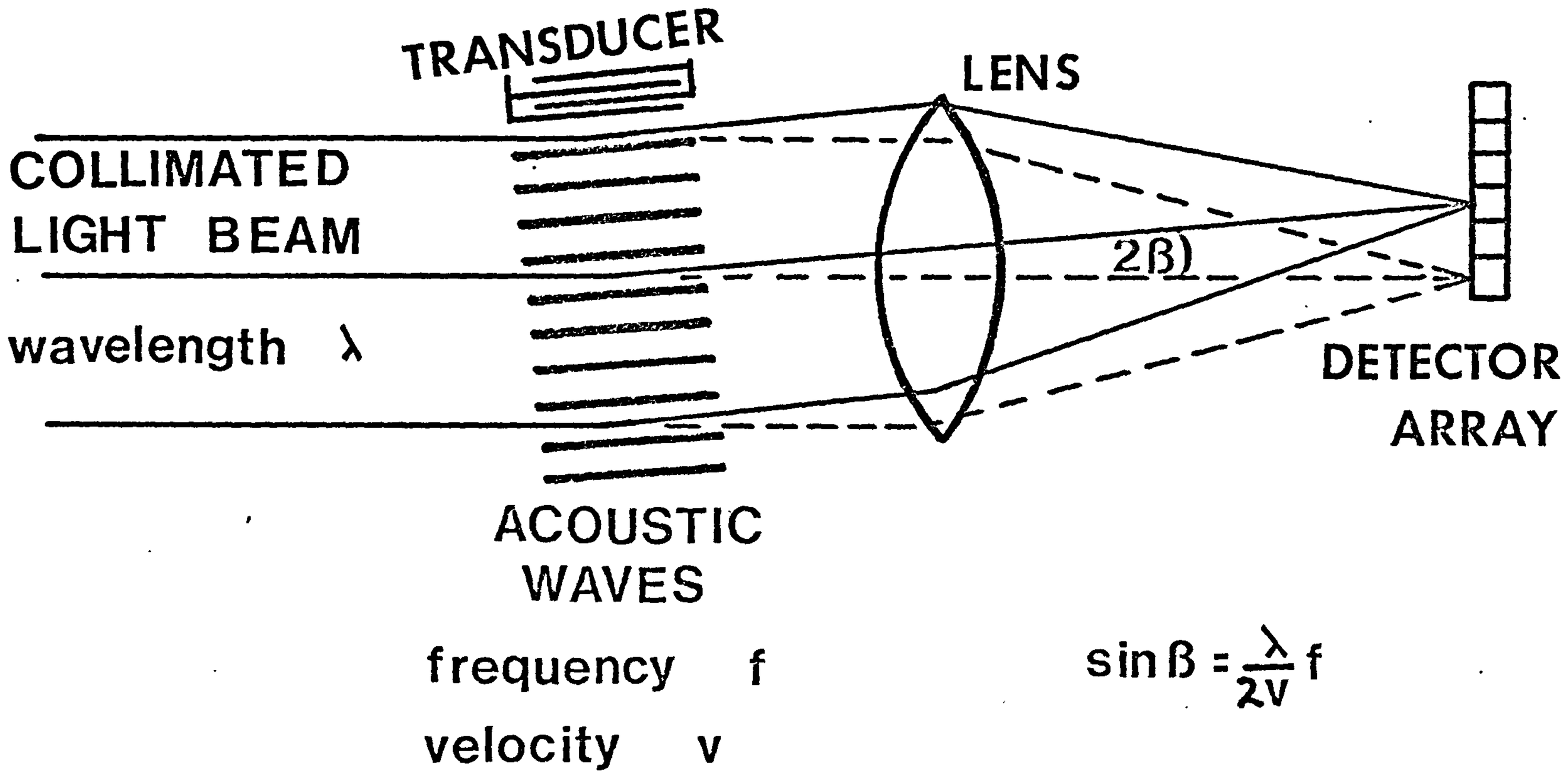

FIG.1.1 Spectrum analysis by acousto-optic Bragg deflection.

precisely when

$$\frac{2\pi\lambda L}{\Lambda^2} \gg 1 \qquad \text{.....1.1}$$

then the Bragg regime is in force, so that multiple reflections from many grating periods combine to diffract light into very few orders.

The proportion of light diffracted into each order depends on the angle at which the light beam meets the acoustic wavefront. Light may be directed into only the zeroth and first orders by satisfying the Bragg condition[1] : the acoustic beam is tilted at angle β to the optical beam direction, and the deflection of the optical beam into the first order is given by the angle 2β, where

$$\beta = \sin^{-1}(\lambda/2\Lambda) \qquad \text{.....1.2}$$

For small angles the deflection of the beam may be simplified to

$$2\beta = \frac{\lambda}{\Lambda} = \frac{\lambda f}{V} \qquad \text{.....1.3}$$

where f is the frequency and V is the velocity of the acoustic wave. The diffraction angle is related, therefore, almost linearly to the frequency of the acoustic wave. For an example, consider light of wavelength, λ, .38μm, and acoustic wave of velocity, V, 3500 m s^{-1}, used to deflect acoustic waves over a frequency range of one octave from 1GHz to 2GHz. Over this range the simplification is in error by 3.4MHz: if the desired resolution is finer than these errors then linearity cannot be assumed.

The far-field intensity, I_1, of the first diffraction order of the optical wave is given approximately by [3,11]

$$I_1 = I_o . \sin^2\left[\frac{\pi}{\lambda} . F . L\left(\frac{M_2 . P_s}{2}\right)^{1/2}\right] \qquad \text{.....1.4}$$

where I_o is the intensity of the optical wave before the interaction, λ is the optical wavelength in the medium , F

is a non-dimensional factor with value between 0 and 1 (which depends on the overlap integral between the light and the acoustic energy distributions), L is the acoustic beamwidth, P_s is the power density of the acoustic wave, and M_2 is a figure of merit which is characteristic of the medium and which is given by

$$M_2 = \frac{n^6 p^2}{\rho v^3} \qquad \text{.....1.5}$$

where p is the photo-elastic constant, ρ is the density and V the velocity of acoustic waves in the medium. and n is the refractive index of the medium.

For spectrum analysis it is desirable to diffract a high proportion of the energy into the first diffraction order and also to have a linear relationship between diffracted energy and input energy. However, these requirements conflict, since, in Equation 1.4, I_1 is only large when the argument of the $\sin^2$ term is large, whereas I_1 is only approximately linear with power density P_s when the argument is small, so that

$$I_1 \simeq \frac{\pi^2}{2\lambda^2} L^2 . M_2 . P_s \qquad \text{.....1.6}$$

The compromise which must be made may result in insufficient light being deflected into the first-order (so that at the bottom end of the dynamic range, detection is limited by stray light and electrical noise at the light detector), or in so much light being deflected that third-order intermodulation signals may appear if (as is likely in military systems) more than one acoustic signal is present in the spectrum.

A system which satisfies the above conditions, with the acousto-optic interaction taking place within a suitable crystal, will be referred to in this thesis as a "bulk spectrum analyser". The bulk elastic material may be lithium niobate, as also may be the acoustic transducer which takes the form of a thin plate bonded to the deflector crystal, with a metallic layer in between. This assembly is called a "Bragg cell". Appropriate lenses and

photodetector arrays are used to collimate light into the Bragg cell and to focus the deflected optical beam. Thus the outputs from a linear photodetector array represent the relative strengths of signals derived from an microwave spectrum, with the detector element position indicating the frequency of each signal. Such systems have been described, using commercial acousto-optic deflectors[12] (e.g. the Itek L1000 Bragg cell) to operate at central frequencies up to about 1.9 GHz over bandwidths up to about 1 GHz with resolution of up to 1000 frequency channels.

The prime advantage of this analyser is that the outputs from all frequency channels are available simultaneously in parallel, and can then be processed further serially or in blocks or in a coded frequency-hopping manner. This should be contrasted with any of the alternative methods of spectrum analysis, where a frequency band is generally analysed by a process equivalent to sweeping a narrowband filter across it [13,14,15].

Using equation 1.3, the range of angles, $A\beta$, subtended by deflected beams over the frequency bandwidth of operation, B_s, is given by

$$A\beta = \frac{\lambda B_s}{V} \qquad \text{.....1.7}$$

The position, Z_s, of a deflected spot in the focal plane of the focusing lens (of focal length F) is given by

$$Z_s = \frac{\lambda.f.F}{V} \qquad \text{.....1.8}$$

The range of positions, ΔZ_s, corresponding to the frequency bandwidth of the analyser is given by

$$\Delta Z_s = \frac{\lambda.B_s.F}{V} \qquad \text{.....1.9}$$

This distance represents the length required for the detector element array.

The detector element separation, S_d, is related to the frequency resolution of the analyser, Δf, by

$$S_d = \frac{F.\lambda.\Delta f}{V} \qquad \text{.....1.10}$$

The width of the focused spot may be assumed at present to be the width to which a Gaussian beam of $1/e^2$ width W, propagating through the acoustic wave, is focused by a perfect, large aperture lens. This spot size is given by

$$D = \frac{4\lambda F}{\pi W} \simeq \frac{\lambda F}{W} \qquad \text{.....1.11}$$

The number of resolvable spots, N, that is the number of different frequencies which may be detected, is given simply by (if S_d is made equal to D)

$$N = \frac{B_s}{\Delta f} = \frac{\Delta Zs}{D} = \frac{B_s.W}{V} \qquad \text{.....1.12}$$

This may be restated in terms of the transit time of the acoustic wave, τ , through the light beam (τ = W/V) so that $N = B_s.\tau$. 1.13

The potential resolution of the spectrum analyser can therefore be expressed in terms of the product of a transit time and the frequency bandwidth. These factors may be used as a convenient basis for comparison with other systems for spectrum analysis. The actual resolution would depend on further factors such as whether the detector array elements are smaller than the diffracted spots, as well as all the fabrication and material imperfections.

1.2.2 Integrated Optical Spectrum Analyser (IOSA)

In the integrated optical form of the spectrum analyser (the IOSA), the microwave elecromagnetic spectrum is transduced into surface acoustic waves (SAW) and the light beam is constrained within a surface waveguide. The Bragg cell becomes effectively a two-dimensional surface rather than a three-dimensional block. Figure 1.2 illustrates the general form of such a system [4 -8].

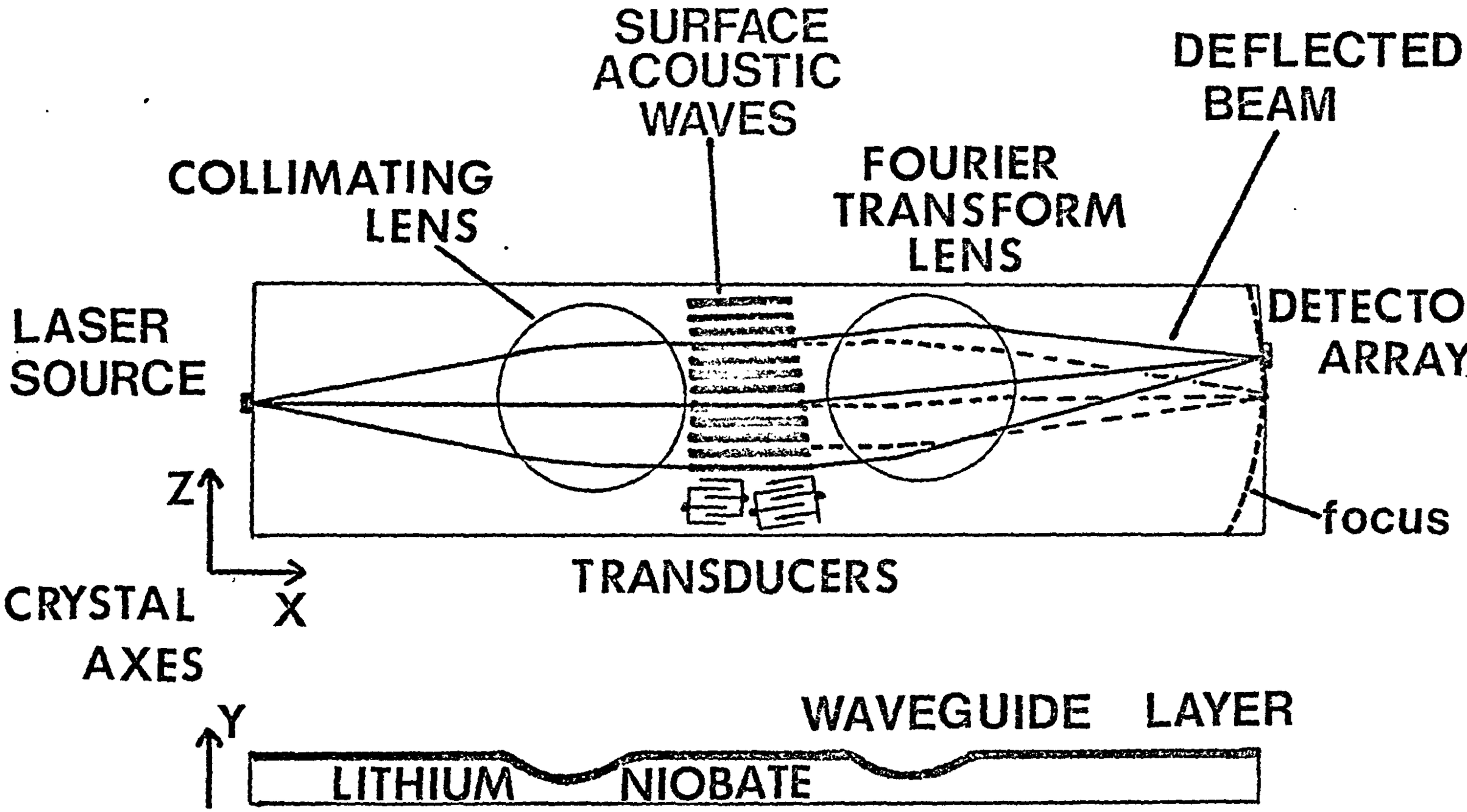

FIG 1.2 Geodesic lens integrated-optical microwave-spectrum analyser.

Light is generated by a laser source with a very small emitting area, which is either an integral structure on the substrate or a separate source closely coupled to the substrate surface. The light propagates in a waveguide which is formed over the entire surface of the substrate (an absorbing layer may be applied to the regions where no light is desired so that stray light is reduced). Initially the light from the very small emitting area diverges strongly. The diverging beam is collimated by a lens element on the surface. The collimated beam crosses a region where a surface acoustic wave (SAW) has been generated by piezoelectric transducers, which are themselves driven by signals derived from the microwave radiation which is to be analysed. An array of transducers is generally required in order to provide a wide bandwidth, The transducer array provides beam-steering so that the Bragg condition is maintained for all microwave frequencies. The acousto-optic interaction takes place within the surface waveguide. Each frequency component of the SAW diffracts light from the beam, with the diffraction angle proportional to the frequency of that component. A second lens focuses the diffracted beams onto an array of photodetectors. The photodetector array may be integral with the substrate surface, or a hybrid component coupled alongside.

Apart from the potential advantage of size over the bulk spectrum analyser, the IOSA may achieve higher diffraction efficiency for low electrical input power because both the SAW and the optical wave are confined within a small thickness of the substrate surface. This efficiency advantage is enhanced by the feature that for the same power input, strains and refractive index changes are higher for surface waves than for bulk waves. Disadvantages of the integrated version are related to the less well-developed fabrication technology: currently, integration of all the components is of potentially low yield, and suffers from defects such as high light scatter in waveguides, and photorefractive damage.

1.2.3 User requirements

The simultaneous, parallel processing capability of the Fourier transform Bragg-deflection spectrum analyser has attracted the attention of potential users in fields such as radio astronomy [16] and military electronics [13,14,15].

The operating bandwidth and frequency resolution which can be achieved in practical Bragg-deflection systems are particularly suitable for identifying radar signals. Without parallel processing there is a high chance of missing the pulsed, low duty-cycle, frequency-agile signals which are often used in modern radar systems. In Electronic Warfare (EW) systems there is a need to keep watch on a very large radio spectrum, perhaps up to frequencies of more than 20GHz [13,15].

Such an EW system could need more than twenty spectrum analyser Bragg cells because each cell may be limited to operation over only one octave (to avoid second order interaction signals). Because of the large volume and weight of this number of cells if in the bulk optical form, attention has been drawn towards the integrated optical form - the IOSA [2].

Although some prospective EW spectrum analyser systems may require frequency resolution better than about 1 MHz, resolution of about 4MHz would be adequate for other systems, and would also be sufficient in the first instance to demonstrate the effectiveness of an IOSA.

1.3 CHOICE OF MATERIALS AND COMPONENTS FOR AN IOSA

The ideal IOSA, from an integrated optics protagonist's point of view, would be totally integrated, with all components formed on the same substrate. Early work considered the use of semiconductor substrates to achieve this ideal [2,17]. Silicon planar technology with deposited layers can provide light detectors, light waveguiding and

focusing. However a light source is not available, waveguides (which must be deposited layers to obtain a higher refractive index than that of silicon) tend to scatter too much light, and the deposited piezoelectric layers (such as sputtered zinc oxide) required for SAW transduction cannot provide adequately wide bandwidths [4,10].

In principle, all of the components required for an IOSA may be formed on the surface of compound semiconductors such as gallium arsenide [2]. However the materials are only weakly piezoelectric and acoustic attenuation (3.8 db/μs measured at 1GHz) is rather high. Measurements of the optical attenuation of waveguides formed in gallium arsenide (1.4 dB/cm at wavelength 1.3μm[18] and 1.9 dB/cm at wavelength 1.15μm [19]) imply that attenuation is probably high at the 0.85μm wavelength which is likely to be used for an IOSA.

Attention has been directed to developing Bragg cells using materials with good piezoelectric and optical properties, such as lithium niobate. It may be eventually possible with these materials to develop an integrated light source (many materials are potentially capable of laser operation to some extent) and detector array (e.g. pyroelectric [20]). At present, for these materials, it is necessary to be reconciled to a hybrid IOSA, using externally-coupled light sources and detectors.

SAW are usually generated by an interdigital transducer (IDT) deposited on the substrate surface, and using the piezoelectric properties of the substrate itself [21,22]. The bandwidth of the SAW depends linearly upon the electromechanical coupling constant, k^2, of the substrate material. Lithium niobate possesses one of the highest available values of this constant, and can have a SAW bandwidth for a single IDT of 24% at low insertion loss. IDT suitable for operation up to 3 GHz or more can be made using electron-beam lithography [23]. Lithium niobate has particularly low SAW attenuation. The practical upper

frequency limit is about 2GHz: at 1.9GHz the attenuation of SAW propagating in the Z-direction on a Y-face is about 7.8 dB/cm [24], i.e. 2.7dB/μs at the SAW velocity of 3.5km/s. Attenuation varies with the square of frequency[23] so that, at 1GHz SAW attenuation would be about Ø.9dB/μs. A frequency band of one octave could therefore be operated using two or three IDT, formed by high-resolution photolithography on a lithium niobate substrate.

Lithium niobate is very transparent over the visible wavelength range from about Ø.5μm up to the infrared wavelength of about 5μm [25]. Low-loss optical waveguides may be formed by diffusion (next section).

Two major problems which may be anticipated in the use of lithium niobate for the IOSA are the inherent refractive index anisotropy of the uniaxial crystalline material, and photorefractive damage [26] where high light intensity exposure (such as at a focus) causes electron transport to produce inhomogeneity of refractive index through the electro-optic effect. The former effect is likely to limit the available apertures of focusing elements by restricting the range of angles over which rays may traverse the surface (although the variation of modal refractive index over the lens design which was fabricated in the present work has been estimated as only Ø.14% [27]) and the latter is likely to cause local absorption and scattering of light beams.

The choice of operating light wavelength, laser source, and type of detector array follows from the choice of substrate material. The most useful optical source which is available at present is the single transverse-mode heterostructure semiconductor laser, operating at a wavelength of about Ø.85μm [4,7,8,28] (e.g. the Hitachi HLP-14ØØ) which is well within the high transmission band of lithium niobate [25]. This type of laser has a particulary small effective area of radiation (about 1μm), which will lead to a potentially small image at the photodetector.

IOSA have been designed or fabricated using charge coupled device (CCD) - addressed silicon photodetector arrays [4,5,7,8,10,29]. Both the light source and the detector array were coupled to the waveguide by suitably close alignment to the extremely well-polished edge of the substrate [30,31,32].

The choice of lens element type for the IOSA is the subject of the latter part of this chapter.

1.4 TITANIUM DIFFUSED WAVEGUIDES IN LITHIUM NIOBATE

The technology of producing optical waveguides on lithium niobate crystal surfaces by diffusion is widely-used and has been extensively studied. Earlier workers used out-diffusion of lithium [33,34], but the majority have employed the in-diffusion of titanium [35,36,37,38]. In-diffusion provides a much shallower waveguide (only a few micrometres deep) which closely matches the SAW propagation depth, and therefore enables more efficient interaction. In-diffusion also produces about twice the difference in refractive index between guide and substrate than does out-diffusion, and therefore the probability of better containment of light within the guide when traversing curved surfaces such as are involved on geodesic lenses. More recently, waveguide formation by proton-exchange (PE) and by a hybrid titanium diffusion proton-exchange (TIPE) method [39] has been investigated. Of all the diffusion techniques, PE and TIPE provide the largest difference between waveguide and substrate refractive index. As will be discussed in section 1.6, the size of the refractive index difference is an important factor in the choice of focusing element type.

In the titanium diffusion technique, which was used for

almost all of the work reported in this thesis, titanium metal is deposited by high-vacuum electron-beam evaporation onto the highly-polished surface of a lithium niobate substrate (with a thickness of, for example, 3Ønm). Diffusion occurs when the substrate is then heated to about 1ØØØ^{o}C for about ten hours in an atmosphere of air or oxygen.

Waveguides formed in this manner have low propagation losses at visible wavelengths - less than 1dB/cm at about Ø.6µm wavelength can be achieved. The principle cause of loss is scattering within the waveguide. The diminished dynamic-range caused by scattered light reaching the photodetector array is more important than the actual loss within the guide. Under favorable experimental conditions waveguide scattering has been held down to a reasonable limit e.g. in-plane scattering levels of -4ØdB to -55dB relative to the peak light level at 1^{o} within the substrate from the centre [3,5,4Ø,41,42,43]. However on a more-complete IOSA device (i.e. with lenses) the scattering appears to be much higher (Chapter 7). This is probably due to reasons associated with the roughness over the lens surface, to the difficulty of producing a uniform waveguide layer on the lens and to the variations of propagation depth and crystal axis direction in the waveguide around the lens. There is some evidence that performing polishing after diffusion has been carried out can decrease the levels of scattering [42,43]. The work reported in Chapter 6 provided a machine capable of post-diffusion polishing to remove, evenly, sub-micron thicknesses from waveguides, particularly within geodesic lenses.

The problem of non-uniform titanium layer deposition around the lens depression may be tackled in several ways. Vacuum evaporation through masks, with the substrate rotating above the evaporation source, would provide a better thickness distribution than the direct evaporation, with no rotation, which was used in most of the present

work. The formation of titanium or titanium oxide layers via Langmuir-Blodgett layers [44] may provide less defects and better uniformity.

The diffusion profile varies with initial titanium layer thickness, diffusion time and wavelength [37]. Although the effective depth at which light propagates below the surface of the substrate may not be important with purely planar devices (apart from considerations of scattering due to surface roughness), a different situation arises with geodesic lenses. Because light propagates a few micrometres below the surface of the substrate, the effective lens profile is not the same as the surface profile. However the difference in effective lens profile and actual surface profile for waveguides of effective depth of only a few micrometres is less than the currently available profile fabrication and measurement accuracy (see Chapter 7).

1.5 FOCUSING IN INTEGRATED OPTICS

1.5.1 Gratings and zone plates

The use of planar fabrication technology for most of the structures in integrated optical devices leads naturally to interest in focusing components which may be made photolithographically. Grating structures are potentially suitable, and are already incorporated into integrated optical devices for applications other than focusing (e.g. for coupling light into waveguide layers, as mirrors and beamsplitters, and to control the output wavelengths of compound semiconductor lasers) [1].

Grating lenses have been investigated by several workers. These fall into two categories [45] (Figure 1.3): Bragg-deflection types, where the grating is relatively thick and Fresnel zone-plate types, where the grating is

MODE INDEX	Overlay lens 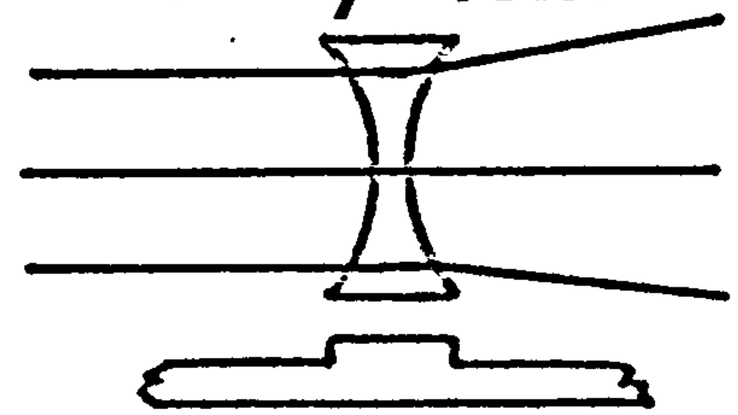 Luneberg lens 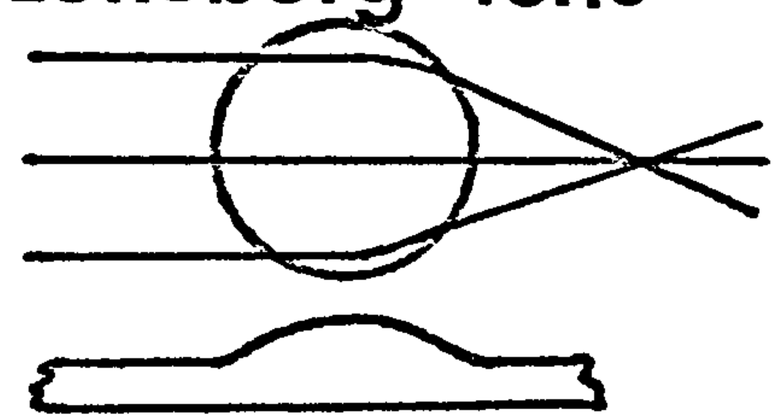
GRATINGS & ZONE - PLATES	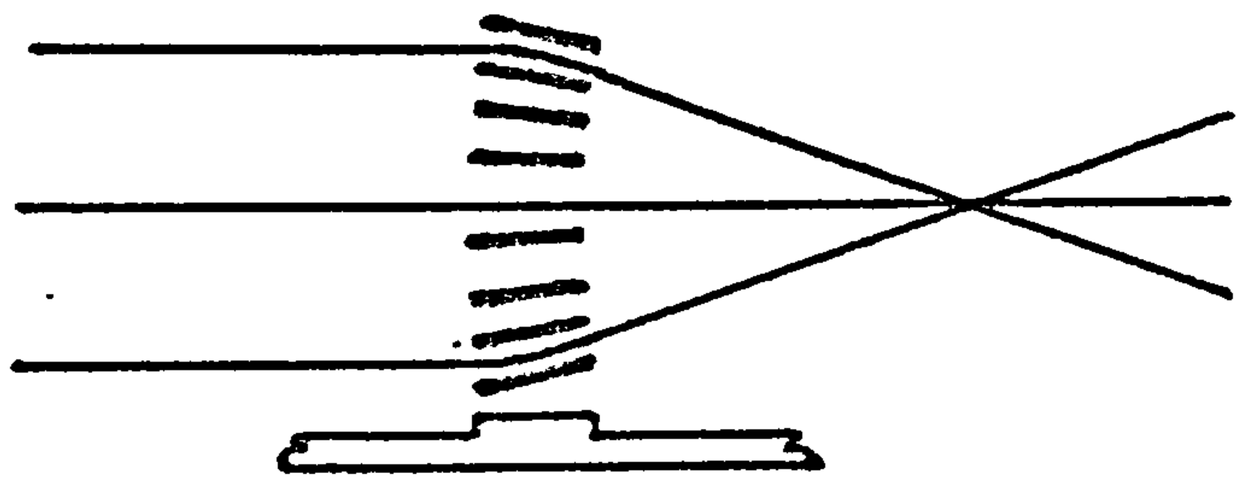
CONFIGURATIONAL	EDGE MIRRORS 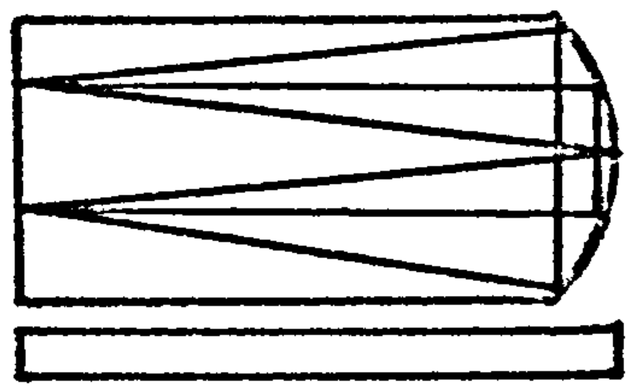 Geodesic lens 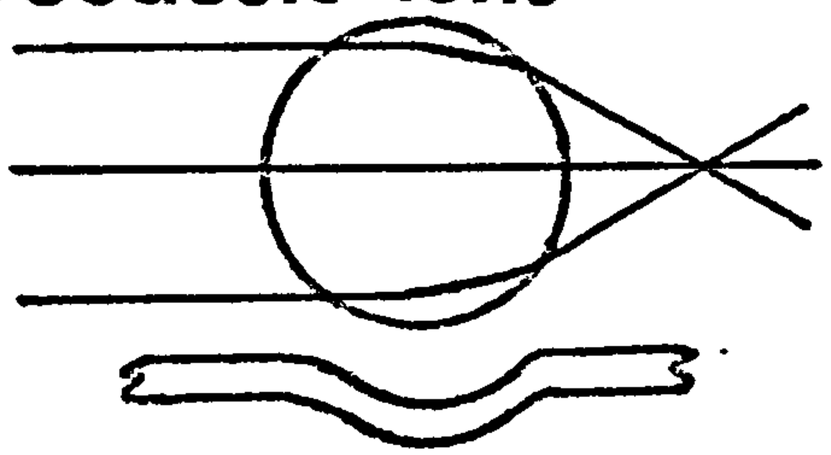

FIG 1.3 Focusing elements for surface waveguides

relatively thin. The diffraction efficiency of the former types should be greater since the Bragg condition can be satisfied to eliminate all but the zeroth and first order of diffraction. However this efficiency is only gained at the expense of sensitivity to variation of incident angle.

Tanaka [46] and also Yao and Thompson [47] made a Bragg-type lens photolithographically, where the grating lines varied their spacing and also varied their inclination to satisfy locally the Bragg condition. Tanaka's grating lens was of aperture 6mm, and consisted of lines which were 3mm long (in the general direction of the light propagation) which were spaced 100μm apart at the centre and 2μm apart at the edge of the grating. The focal length was 20mm when using a 488nm wavelength argon laser coupled into a glass waveguide.

Shubert and Harris [48] proposed a Fresnel zone grating in which the spacing of each line varies so that the deflection at each part of the grating also varies (a "chirped" grating), giving a focusing or beam-diverging effect. Such a lens was fabricated by Ashley and Chang [49] using electron-beam lithography to define a pattern in PMMA photoresist on a single-mode waveguide composed of a 1μm thick layer of barium oxide on a glass substrate. The phase grating was then made using 0.1μm of cerium oxide formed by deposition and liftoff. 105 zones, each 50μm long, were distributed over a lens aperture of 0.8mm to give a focal length of 4mm for laser light of vacuum wavelength 633nm. The image spot size was 50% greater than the calculated diffraction limit (3μm full-width at half peak). The diffraction efficiency was 25% : it has been calculated [50] that the efficiency could reach as high as 41%.

Neuman, Pitt and Walpita [51] made Fresnel zone lenses on ion-exchanged glass waveguides. The zones were either defined holographically or by electron-beam lithography, and were made using metal layers to form either absorbing or, effectively, (because the small width of the lens

structure absorbed little light) phase-shift zones. The electron-beam written zone pads were more clearly defined than those produced holographically, and gave image widths closer to the diffraction limit expected (2.4μm) and signal to first side-lobe ratios less than the predicted 14dB. The authors concluded that given some sacrifice of the latter ratio, lenses could be designed to work at 32% diffraction efficiency. Another such lens was made on a thermally oxidised silicon substrate [52,53] and an IOSA was fabricated using this lens design, a $SiO_2/Si_3N_4/SiO_2$ waveguide and a ZnO piezoelectric layer [10]. A large field angle (more than 6^o) is claimed with diffraction-limited focal spots for relative apertures up to F/3.

Another grating-type lens was made by holographic techniques [51,55] which was effectively a non-chirped Bragg-diffraction lens. This lens was intended for use as the beam expansion lens in a spectrum analyser, and could be very efficient since the angle of incidence is fixed. 16% efficiency was achieved for a lens on an ion-exchanged glass waveguide, with reasonably uniform output intensity over more than 6mm aperture.

To indicate the suitability of Bragg lenses for the lithium niobate IOSA, Bragg-grating lenses were made by reactive-ion-etching of 0.1μm grooves in titanium-diffused lithium niobate waveguides corresponding to a contact-printed grating [56]. The lens aperture was 1mm and the focal length 20mm. 87% efficiency was recorded for zones of length 0.18mm. The $1/e^2$ width of the image was about 18μm, as expected. Chang [57] produced lenses by etching Ti-diffused $LiNbO_3$ waveguides, and achieved 45% throughput diffraction efficiency, although only over an angular deviation range of about 2^o.

Although not integrated surface components, chirped-grating (graded-index or graded-thickness) reflection lenses have been fabricated by electron-beam lithography on silicon and cemented to the polished edges of lithium

niobate substrates [58,59] to demonstrate a folded beam hybrid IOSA.

1.5.2 Mode index lenses

A mode-index lens may be produced by forming a region of different refractive index to the surrounding plane waveguide (Figure 1.3). The lens area may be of constant refractive index as in the overlay lens. The lens is similar in form to a traditional bulk optical lens (including Fresnel types) seen in profile [61-65]. Generally a layer must be formed over the plane waveguide, with a large difference of mode-index, and must not have worse attenuation and scattering properties. This is difficult to achieve on lithium niobate, where it is only just possible to form a waveguide layer of higher refractive index than the substrate material. Vahey [64,65] used an aluminium overlay, but this did not attenuate too much since the lens was only a weak, correcting lens for an adjacent geodesic lens.

In the Luneberg lens [66-71] (Figure 1.3), the mode index varies symmetrically as a function of radius. Luneberg's original lens focused at its edge, but generalised designs have been devised which provide focusing between any conjugates (see section 2.3.4). As with the overlay lens, the lack of suitable materials of high refractive index, etc, has tended to discourage work on Luneberg lenses for use with the lithium niobate IOSA. Recent work with deposited chalcogenide glass layers [72] may, however, have contributed to renewed interest in this type of lens.

1.5.3 Configurational elements

The term "configurational" is used to describe elements for which focusing properties are determined by geometrical shape rather than by fine structure (as with gratings) or by graded refractive index (as with generalised Luneberg lenses) (Figure 1.3).

Mirrors for waveguided light have been proposed, reflecting the light at an edge of the substrate [2,69]. In some situations, plane mirrors may be formed at cleaved crystal edges, but for focusing it would be necessary to polish the edge of the substrate in some curved form. The author has not been able to find any reference to work on this type of focusing element. Perhaps such sytems appear unattractive because of the practical difficulties generally encountered in polishing plane edges without chips of comparable size to that of the waveguide depth [30], and because the use of mirrors tends to imply that beams must be separated along directions at large angles, which would incur problems with crystal anisotropy.

The term "geodesic lens" has been coined to describe the class of configurational elements where radiation such as electromagnetic or acoustic waves is constrained to travel around a curved surface in a manner which results in some desired form of beam shaping such as focusing.

The earliest mention of these lenses (not using the term "geodesic") was by Rinehart [73] in a paper on the geodesic equivalent of the Luneberg lens for focusing microwave radiation. The mathematical theory was further developed by Kunz [74], Toraldo di Francia [75] and Ronchi [76]. Van Duzer [67] suggested the use of such lenses for acoustic surface waves. Mason [77] discussed the anisotropy effects which are important in acoustic wave focusing, and by analogy (but less strongly) for optical waves.

Righini, Russo and Sottini (working with Toraldo di Francia) introduced the use of configurational elements into integrated optics and fabricated some components to demonstrate the principles [78-87]. In one system the IOSA is fabricated on a spherical surface, on which light originating at one point on the surface is imaged perfectly on the opposite side [87]. Most of their work, however, has concerned geodesic lenses in the form of depressions in an otherwise plane surface around which light is constrained in a surface waveguide. A hill would

operate equally successfully, although fabrication could be more difficult because material would have to be removed from a substrate in both the lens area and the surrounding plane area, rather than just removing material from a small part of an already smoothly-polished plane substrate. The most important result of the work of Righini, Russo and Sottini is that axisymmetric geodesic lenses in an isotropic medium can be designed to focus perfectly light rays between object and image conjugates which lie on circles concentric with the axis of rotation of the lens. In particular, one of these conjugates may be at infinite radius, allowing collimation and refocusing of a parallel beam.

Several other workers have reported on the theory and fabrication of geodesic lenses [5-8,64,65,68,88-117], and their work will be discussed in later chapters.

1.6 CHOICE OF GEODESIC LENSES FOR THE LITHIUM NIOBATE INTEGRATED OPTICAL SPECTRUM ANALYSER

Geodesic lenses possess several properties which indicate that they may be of significant practical advantage over other types of imaging elements for use in IOSA systems on lithium niobate.

For a perfectly smooth lens, the focusing performance depends only slightly on the difference between the waveguide effective refractive index and that of the substrate. This difference of index may in any case be very small. In contrast, many of the elements noted in subsections 1.5.1 and 1.5.2 cannot focus very strongly unless a large refractive index difference is available. In geodesic lenses the effective index does show some change as the waveguide changes its curvature, because the energy of the guided light has a maximum at different depths below the surface (and in practise the waveguide may vary in thickness around the lens surface because of

the difficulty in uniformly depositing the initial titanium layer). A more important effect is that the local curvature of the surface may exceed the value at which a significant part of the light leaks away from the waveguide. The amount of curvature which may be tolerated depends on the structure of the particular waveguide. These effects may be minimised by designing lenses with the least possible curvature or steepness.

Another unique and useful property of configurational elements, including, in particular, geodesic lenses, is that, provided the waveguide is isotropic, the ray-optics imaging performance is independent of the radiation wavelength and refractive index of the medium. Apart from diffraction (which depends on wavelength and on the effective refractive index of the waveguide) the location of a focus and the image aberrations depend only on the shape of the lens.

A geodesic lens does not split energy into directions other than required: there are no effects such as partial or low reflection (as would be experienced with edge mirrors) or multiple orders of diffraction (as occur with grating-type lenses). Apart from sensitivity to anisotropy (which is common to every type of focusing element), the focusing ability of geodesic lenses is independent of the angle of incidence of any light beam. In the author's opinion, geodesic lenses are therefore potentially more suitable than grating elements for manipulating wide collimated light beams and for focusing beams which have been Bragg deflected into a wide range of directions.

Several types of focusing element depend on photolithography or electron-beam lithography for their formation. Although these techniques are capable of high resolution (about 1μm and 10nm respectively) [118,119] their fields of view are limited (for these resolutions, about 20mm and 0.2mm respectively). Limited field of view could

restrict the size of focusing component which may be fabricated, although it is possible to stitch together many adjacent fields onto a mask within about 1μm accuracy. The restricted size and number of lines may significantly limit the performance of grating and zone-plate lenses. In principle the size of a geodesic lens is only limited by the size of substrate available. A geodesic lens may therefore be made sufficiently large that the size of the diffraction-limited focused spot is insignificant.

There are some disadvantages in the use of geodesic lenses. Because the lenses are several millimetres deep the substrate must be thicker (and therefore use more of an expensive material) than would be required for a plane element. The cost of manufacturing may be greater than that of e.g. photolithographically produced elements. Anisotropy of refractive index in lithium niobate must restrict the range of angles over which a geodesic lens may be used, and this may restrict the width of the collimated light beam and therefore increase the amount of diffraction spreading. It might be possible to compensate for anisotropy to some extent by designing lens profiles which are not symmetrical about the axis normal to the surrounding plane: this would, however, considerably increase the difficulty of fabrication. Because collimated light beams which have been Bragg deflected at different angles focus through a single lens onto a circle (unless the lens is not axisymmetrical as described above), the detector array must be curved to fit the focal circle for a high-resolution IOSA. At present it would be difficult and expensive to produce a curved detector array which could be efficiently coupled to a waveguide.

As will be discussed in Chapter 2, geodesic lenses cannot be designed with any simply curved profile, such as a conic section, without their performance being severely limited. The most obvious reason for requiring a

complicated lens profile is the need to prevent leakage of guided light as it enters and exits from the lens region on the substrate. Leakage suppression can only be achieved by providing a smooth transition from the plane region which surrounds the lens. Such a transition is not possible with the abrupt edge formed by, for example, a conic section. The complicated profiles (including smooth transitional regions) which are required are clearly more difficult to fabricate than the types of aspherical lenses used in bulk optics.

Because integrated optics uses light guided in the thin layer near the surface (e.g. in a region which is only about 2μm thick), this surface must be very smooth and free of damage (and the waveguide which is subsequently formed must be very homogeneous) to avoid scattering which would degrade the dynamic range and resolution capability of an IOSA by entering the wrong detector elements and would decrease the useful signal level. The bulk of this thesis discusses the evaluation of potential techniques for the formation of smooth, low-damage aspherical surfaces.

1.7 MAIN FINDINGS OF THIS WORK

An IOSA and its lens dimensions were designed, within the constraint given by the largest readily-available size of good quality Y-cut lithium niobate single crystal section. Although this IOSA would not be capable of the ultimate performance which is required, the performance ought to be sufficient to establish the potential of integrated optical spectrum analysers.

Lenses were designed using the method of Sottini, Russo and Righini [83] (Chapter 2). Regions of the lens profile were found to have very small local radius of curvature. The profile was modified to one which could be both fabricated and measured without unreasonable difficulty

(and it was hoped would not suffer excessive light leakage due to extreme curvature of the waveguide), but whose aberrations would be negligible.

Lens profiles were generated by ultrasonic impact grinding (Chapter 4), CNC grinding and single point diamond-turning (Chapter 5). The last method was found to be the most straightforward, and provided lenses which were within the required profile accuracy for an IOSA and which also required the least amount of polishing. The first two methods were potentially satisfactory, but require further development of equipment and techniques before being able to generate lenses of adequate profile accuracy.

Lenses were polished by flexible large area polishers, and by small-area CNC polishers (Chapter 6). The former were found to be inadequate. For the latter technique a microprocessor-controlled polishing machine (MCPM) was constructed using low-cost components which were much less precise than those of the diamond-turning machine. The MCPM was used to polish diamond-turned lenses to produce very smooth surfaces with very little (and very uniform) removal of material.

Lenses were evaluated by several techniques - surface roughness and profile measurements by optical and by mechanical methods, and focusing performance by forming waveguides and inspecting the images of a collimated laser beam coupled into the waveguide and the lens (Chapter 7). These evaluations indicated that, given sufficient further development work, geodesic lenses designed and fabricated by methods described in Chapter 6 should be satisfactory for an IOSA.

A tentative basis has been established to enable a potential manufacturer to make an economic choice of plant and processes for fabricating geodesic lenses (Chapter 8).

Suggestions for further work are summarised in Chapter 9.

CHAPTER 2:THEORY AND DESIGN OF GEODESIC LENSES

2.1 SPECIFICATION OF LENSES FOR AN IOSA

2.1.1 Choice of practical IOSA and lens dimensions

In order to test the potential of geodesic lenses it was necessary to design and fabricate them to dimensions which were close to those which would provide adequate performance in an IOSA. There were two opposing constraints on lens dimensions: to obtain good microwave frequency resolution, lenses must be of long focal length, but the size of available lithium niobate crystals tends to restrict severely the distance available for focusing.

Parameters were chosen which would provide potentially useful IOSA performance on substrates of dimensions which could be obtained without extreme difficulty:

system frequency resolution: $\Delta f = 4$ MHz
system frequency bandwidth: $B_s = 1$ GHz
number of detector elements: $N = 250$
detector element spacing: $S_d = 8$ µm
laser vacuum wavelength: $\lambda_o = 850$ nm

For Y-cut lithium niobate, with light propagating along the X-axis and surface acoustic waves propagating along the Z-axis, the effective refractive index of the waveguide optical mode is close to the extraordinary index, i.e. n_e is approximately 2.2 (the precise value depending on the waveguide formation technique and parameters), and the SAW velocity is 3500 ms^{-1}. The laser light wavelength in the waveguide,λ,is therefore approximately λ_o/n_e = 380 nm.

From Equation 1.10 the focal length required for the Fourier transform lens to achieve the above performance is

$$F = S_d.V / \Delta f.\lambda = 18.5\text{mm}.$$

The IOSA substrates which were used for this work were cut from high-quality electro-optic grade lithium niobate

boules which were grown along the Y-axis. The largest diameter boules which could be obtained were of about 65mm diameter. After grinding the edges to remove any reverse domain material as well as chips and other irregularities, the largest diameter of Y-face available was about 61mm. It would have been possible to prepare longer substrates by obtaining crystals which were grown along the Z-axis to a greater length than 61mm, and cutting slices parallel to the Z-axis axis. However this approach would have been very much more expensive.

The IOSA with the largest possible lens diameters which may be formed on a substrate of such size can be calculated: see Figure 2.1. The two lenses have been designed with identical dimensions for simplicity. The length of the substrate was $x_s = 2F + 2c + x_d$, where F is the focal length, c the lens radius, and x_d (the distance between the two lens depressions) was chosen as 8mm to accommodate easily the maximum likely width of SAW beam. The width of the substrate was $z_s = 2.c + 4$ mm, where the 4mm distance was added to allow sufficient space for an acoustic wave transducer and bonding pads. The diagonal of this rectangle must not exceed the diameter of the available Y-face, i.e.

$$(2.F + 2.c + 8)^2 + (2.c + 4)^2 < 61^2$$

Solving for c leads to a maximum possible overall lens

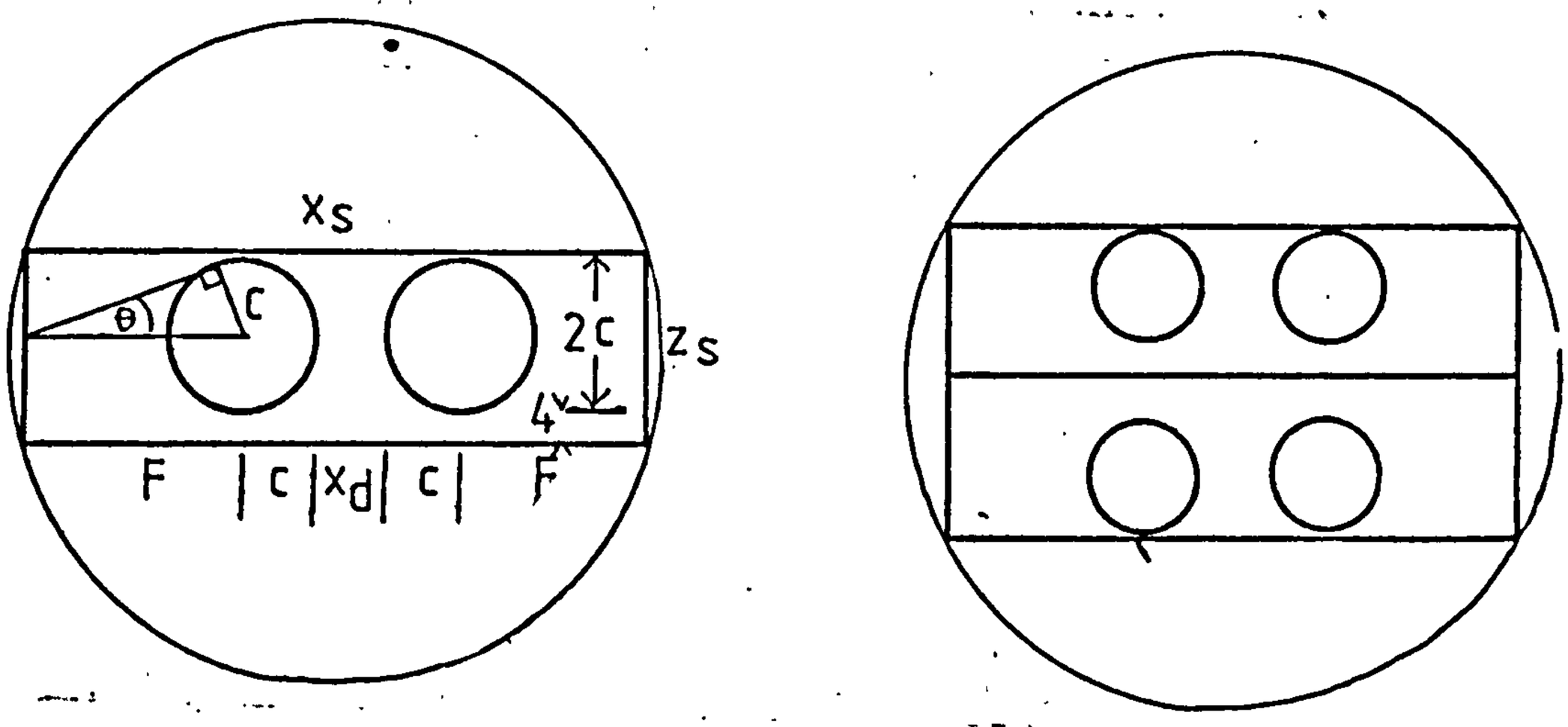

Figure 2.1 Fitting one or two IOSA onto a 61mm diameter boule section.

diameter of 13.5mm, with the IOSA dimensions 58.5mm by 17.5mm. If most of the lens aperture is used for focusing this 13.5mm lens diameter is too large, since it would involve rays meeting the edge of the substrate at angles which are very close to total internal reflection (in Figure 2.1 for TIR $1/n = \sin\theta = c/F$, i.e. $c = F/n = 18.5/2.2 = 8$mm). At such high angles there would be a great deal of Fresnel reflection loss, which could only be reduced satisfactorily by applying to the edge of the substrate a rather complex antireflection coating.

The lenses would be of smaller diameter if two IOSA substrates were cut from the same boule section. This is illustrated in Figure 2.1, where the boule diameter must be greater than the distance across two substrate widths. Solving for the lens diameter leads to the value 10mm, with each substrate 55mm long by 14mm wide. This size was used for subsequent IOSA and lens design work.

2.1.2 Propagation of a truncated Gaussian beam

The light intensity profile of the beam which enters the focusing region of the lens is determined by the Gaussian intensity profile of the laser beam and its truncation by the rectangular lens aperture W. An approximation to the image intensity profile may be obtained by convoluting the Gaussian function with the rectangular aperture diffraction function [120]. The full width of the image intensity profile is given by

$$D = g.F.\lambda/W \qquad \text{.....2.1}$$

where g is a factor which depends on the degree of truncation of the Gaussian beam and the intensity level at which the width is defined. For the extreme case in which there is no truncation of the Gaussian beam there are no minima, and it is appropriate to use $1/e^2$ intensity for both input beamwidth, W, and image size; then $g = 4/\pi$. In the IOSA the Gaussian laser beam profile is likely to be truncated at about its $1/e^2$ width [120], for which distinct intensity minima occur at a width corresponding to g =

2.5. If the Gaussian beam were truncated even closer within its $1/e^2$ width the intensity profile would approach that of a rectangular aperture, for which the width between nulls may be calculated using g = 2.

Using the performance specification and lens focal length which have been introduced in section 2.1.1, and the value of g = 2.5, Equation 2.1 shows that the image spot-width is of the same size as the detector element, 8μm, for an aperture of 2.2mm. Equation 2.1 implies that the use of a larger aperture would produce a smaller spot-width, and therefore better IOSA performance, but other effects limit the aperture which can be used. One of these effect is discussed in the next section.

2.1.3 Field curvature

Rotationally symmetric geodesic lenses in isotropic media focus from a point on one circle to a point on another, where the centres of the circles are on the axis of symmetry and the two points are collinear with the axis. Fig 2.2 illustrates how light beams entering a lens from different directions cannot, therefore, be focused precisely onto all points of a straight detector array. The length of a detector array of N elements with centre-to-centre separation S_d is $N.S_d$. If the linear detector array is placed so that the maximum departure from the correct focus is ΔF, then the following approximation may be made for the maximum width of the defocused spot. Since the angle A is likely to be very small, $\Delta F \simeq H/2$. Since H is much less than the focal length F, $\Delta F = H/2 \simeq (N.S_d)^2/16F$ (Appendix II). The maximum width of the defocused beam D depends on the lens aparture W, and the relative error in focal length: $D = W.\Delta F/F$. Thus

$$D = W\ (N.S_d/4F)^2 \qquad \text{.....2.2}$$

Figure 2.3 illustrates how the ratio of worst-case defocused spot width to detector element size (D/S_d) varies with focal length, for two particular S_d values, an aperture of 6mm and 250 elements in the detector array.

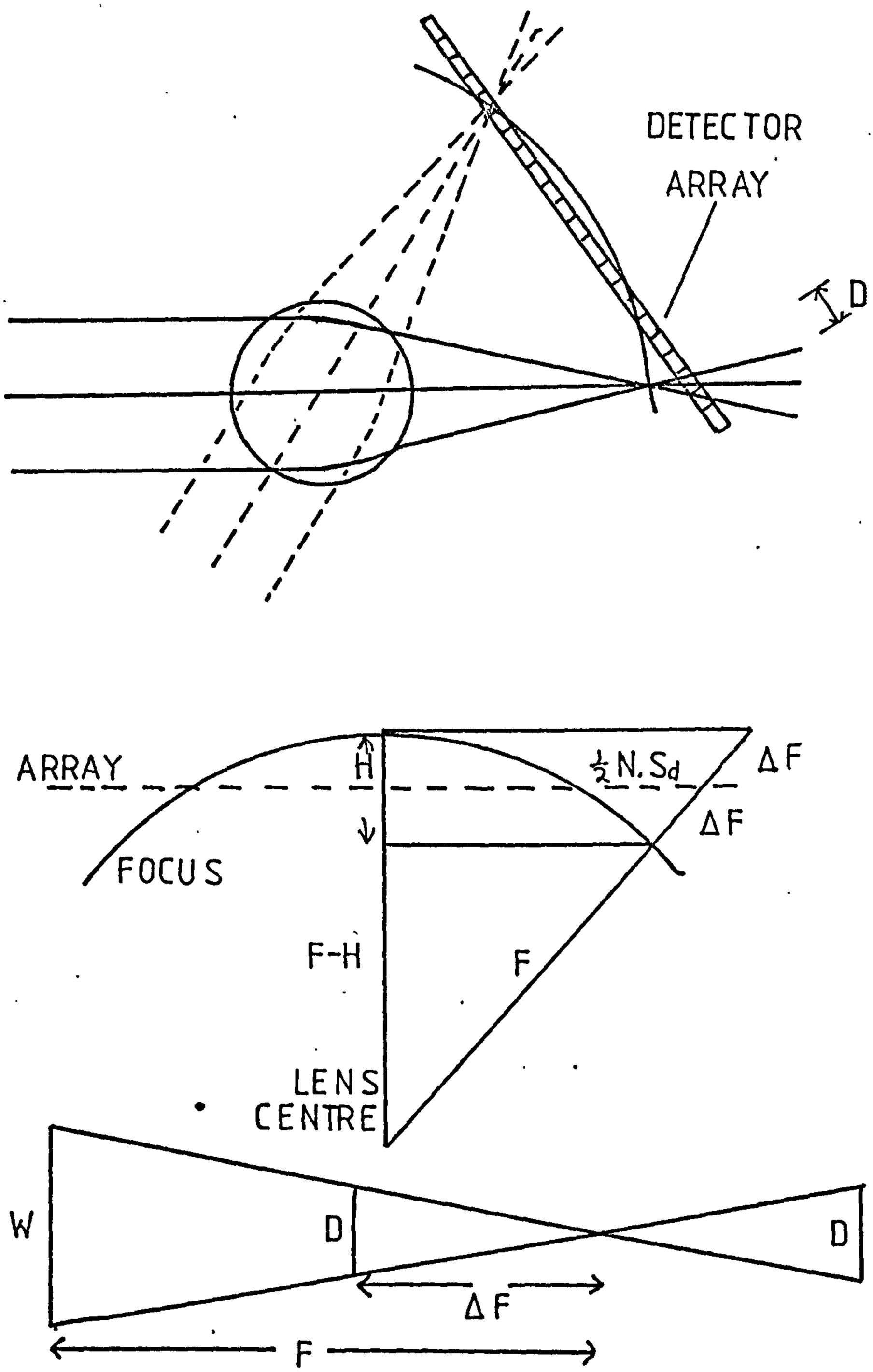

FIG. 2.2 Effect of field curvature on defocusing at detector array

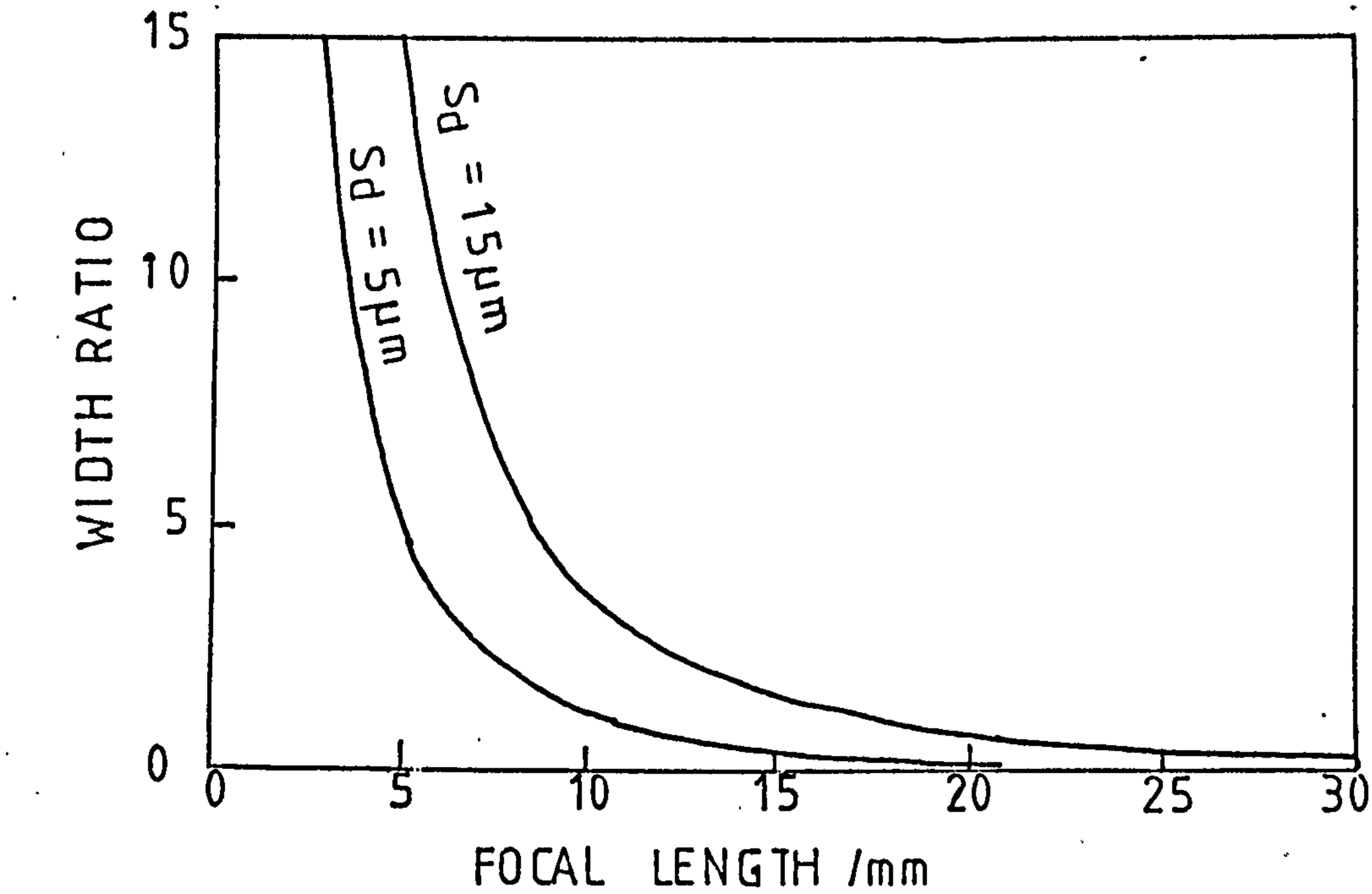

Figure 2.3 Ratio of worst-case defocused spot-width to detector element size as a function of lens focal length.

Clearly, for good resolution, the defocused spot width D must be much less than the detector separation S_d. Inserting this condition into equation 2.2 and substituting $N = B_s/\Delta f$ (equation 1.12) and $S_d = F\lambda\Delta f/V$ (the Bragg deflection equation 1.10) gives the condition that the IOSA bandwidth must satisfy

$$B_s << (16\Delta f.F.V/W\lambda)^{0.5} \qquad \text{.....2.3}$$

If this criterion does not hold then the detector array must be curved to match the focus more closely. For the example when the resolution Δf = 4 MHz, focal length F = 18.5mm, SAW velocity V = 3500 ms^{-1}, beam width W = 10mm, and light wavelength in the waveguide, λ = 380nm, the IOSA bandwidth must not be more than 1 GHz if only a straight detector array is available. However, wider bandwidth and/or smaller frequency resolution could be achieved without any need for a curved detector array if the focal length could be made longer or the lens aperture decreased.

Sottini et al have shown [86] that the total length of a two-lens IOSA may be shortened by introducing a magnifying

lens after the Fourier transform lens. However this results in an even greater need for a curved detector array because the focal circle is primarily determined by the focal length of the magnifying lens, which is necessarily shorter than that of the single Fourier transform lens which is being replaced.

2.1.4 Lens dimensions and image size

The spot-broadening effects of the previous two sections place opposing constraints on the size of the lens aperture. In Equation 2.2 spot-width is proportional to beamwidth W, but in Equation 2.1 the proportionality is inverted. A compromise may be obtained by letting the spot-width due to diffraction of a truncated Gaussian beam equal the widest spot-width due to focal curvature. Using Equations 2.1, 2.3, 1.10 and 1.12 leads to

$$W = \frac{4\ V}{B_s} \left(\frac{g.F}{\lambda}\right)^{\frac{1}{2}} \qquad \text{.....2.4}$$

For example, using the previous data (for a bandwidth of 1 GHz) the compromise lens aperture, W, is 4.9mm. This aperture is of a size which is expected to be practically attainable. For the IOSA parameters of section 2.1.1, the value of the compromise aperture is not critical because the sum of the spot-width due to diffraction (Equation 2.1) and the spot-width due to field-curvature (Equation 2.2) is smaller than the 8μm detector element size for all apertures between about 3mm and 8mm.

There may be a limit to lens aperture above which aberrations due to crystal anisotropy outweigh the smaller diffraction-limited spot, but this limit was not estimated. The lenses which were later fabricated during the work discussed in this thesis were designed to have a large aperture, 7.2mm, and it was intended to determine the best aperture for imaging performance experimentally. For a focal length of 18.5mm the Gaussian intensity-profile of the input laser beam at the edges of the 7.2mm

aperture is at about the half-intensity level, for the particular lasers which are suitable for the IOSA [28].

The lens aperture through which the beam of light passes must be less than the overall lens diameter (Section 2.3.1). This may be achieved by, for example, stopping down the beam with an absorbing waveguide overlayer.

Figure 2.4 shows the layout and dimensions of the IOSA which uses two identical lenses of the above size.

2.2 GEOMETRICAL OPTICS OF GEODESIC LENSES

2.2.1 Introduction

The following subsections show the derivation of geodesic ray tracing expressions according to a similar method to those of references 74, 94 and 102.

2.2.2 Fermat's principle

The basis of geometric optics is Fermat's principle [121] of 1657 known as the "principle of least time" or the "principle of shortest optical path". Fermat's principle asserts that the optical length

$\int_{P_2}^{P_1} n.dL$ of the ray path between any two points P_1 and P_2 (if there is no focus between them) is shorter than the optical length of any other curve which joins these points and which lies in a certain regular neighborhood of it. The principle may be reformulated for more general cases of P_1 and P_2, e.g. where a focus may occur between them. It then states that the ray path is distinguished from other curves by a stationary value of the integral, i.e. $\int_{P_2}^{P_1} n.dL = 0$. Paths in any space which follow this general principle have been called geodesics [73-117].

The work carried out for this thesis assumes that all ray paths, both on the lens surface and beyond, propagate

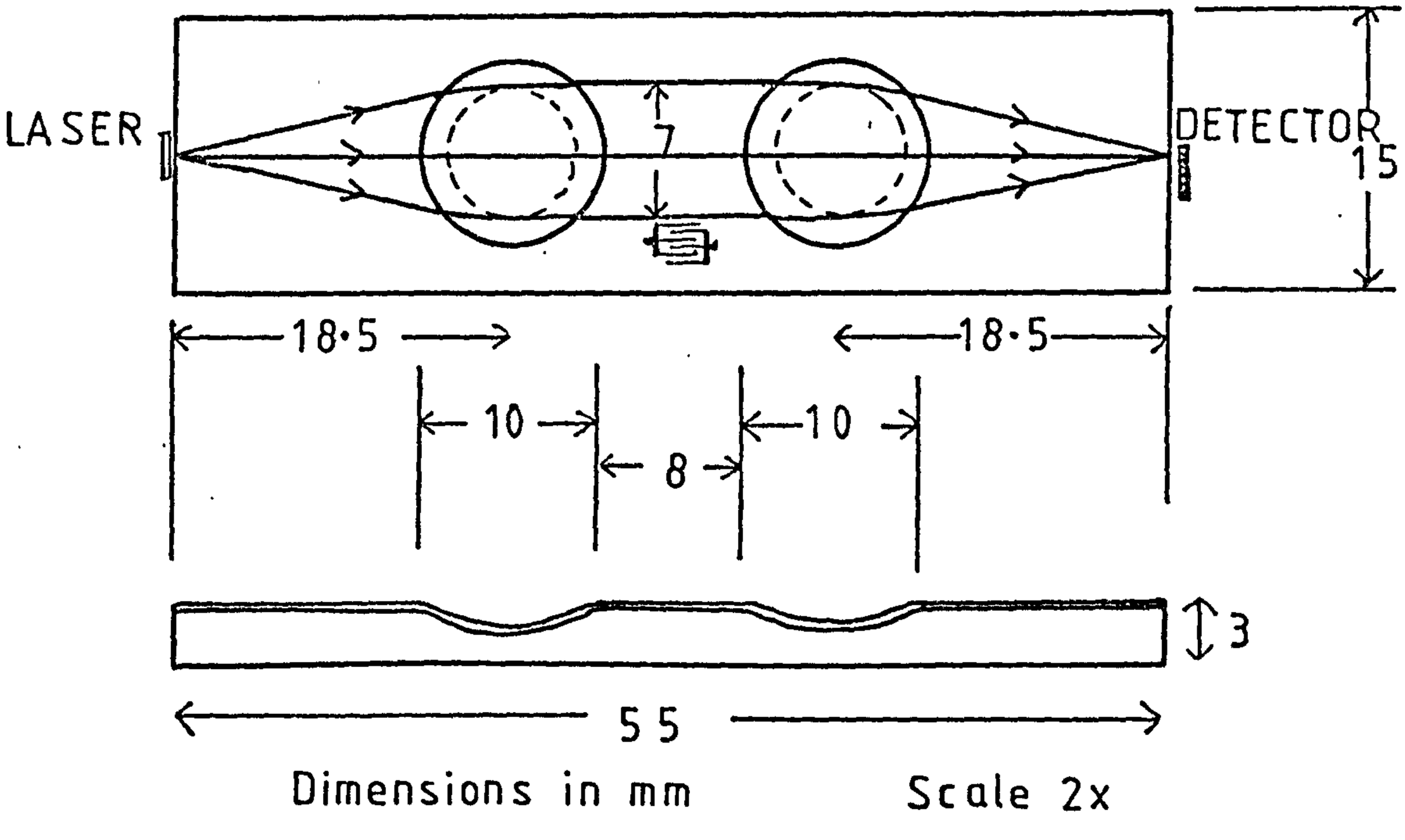

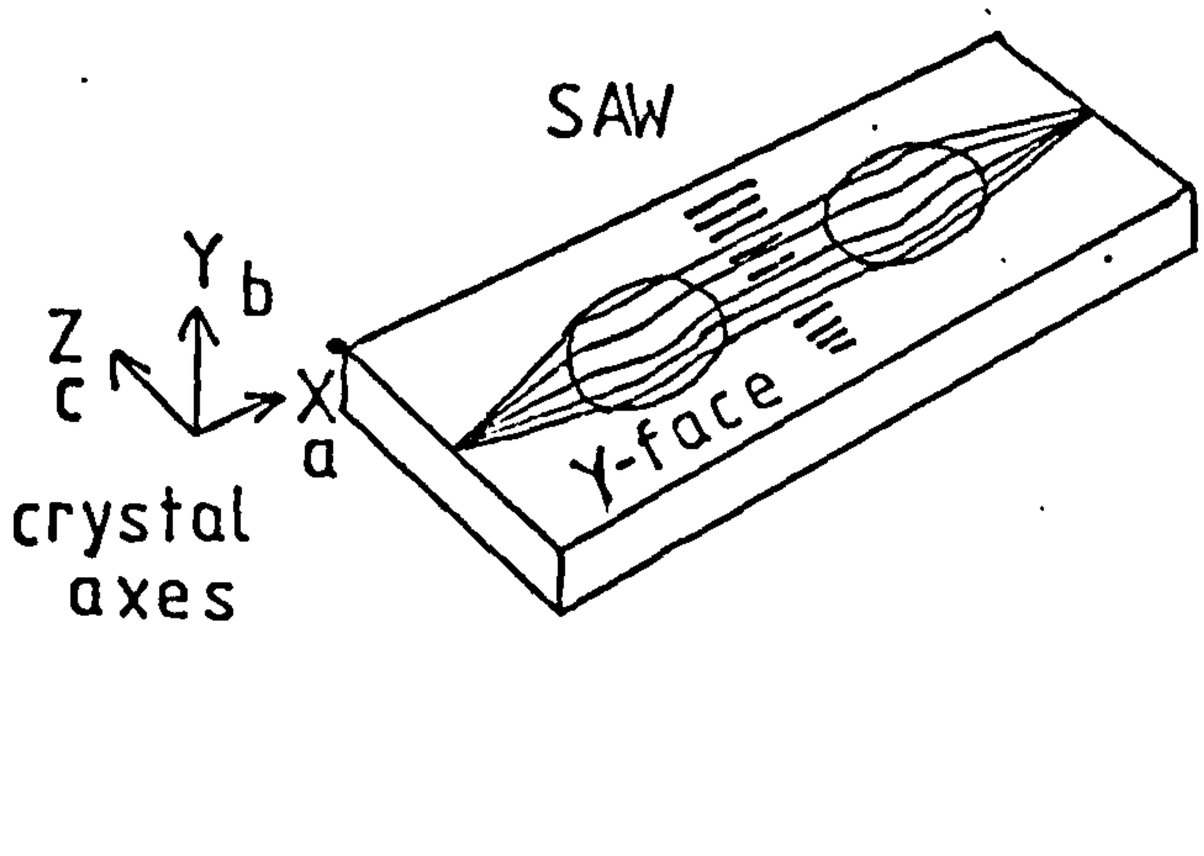

Figure 2.4 Layout and dimensions of IDSA with two identical lenses.

within a waveguide of uniform optical-mode refractive index. (This model is rather optimistic for lenses on lithium niobate: the substrate, and therefore the waveguides, are certainly anisotropic in refractive index, and curvature of the ray paths around the lenses also modifies the modal refractive indices.) When applying Fermat's Principle to a medium of uniform refractive index, real distances may be used instead of optical path lengths and the refractive index cancels out of all geometrical optics expressions. (Refractive index, is of course, relevant to the wave-optical aspects of geodesic lenses.) Fermat's expression for these geodesic lenses may therefore be stated simply as

$\delta \int_{P_2}^{P_1} dL = 0$, where δ signifies a variational displacement on the lens surface.

2.2.3 Geodesics on surfaces of revolution

Only lenses which are symmetrical about an axis perpendicular to the surface of the plane substrate are considered in this thesis. Lenses will be discussed using cylindrical coordinates: radial position (or latitude) R, azimuthal angle (or longitude) ϕ, and height Z, where R and ϕ are measured in the Y-plane of the substrate and the Z-axis is perpendicular to the Y-plane. The lens surface is defined by rotating about the Z-axis a generating curve having a profile in which the height Z is a function Z(R) of radius R (Figure 2.5).

It is useful to have an alternative description of the generating curve in terms of the length of an arc on the generating curve, S, which is a function, S(R), of the radius. The metric of the lens surface can then be expressed as

$$dL^2 = dS^2 + R^2.d\phi^2 \qquad \text{.....2.5}$$

where dL is the distance between two closely spaced points on the surface and dS and $d\phi$ are the corresponding small increments along the generating curve and around the azimuth. Equation 2.5 may be rewritten in terms of radius

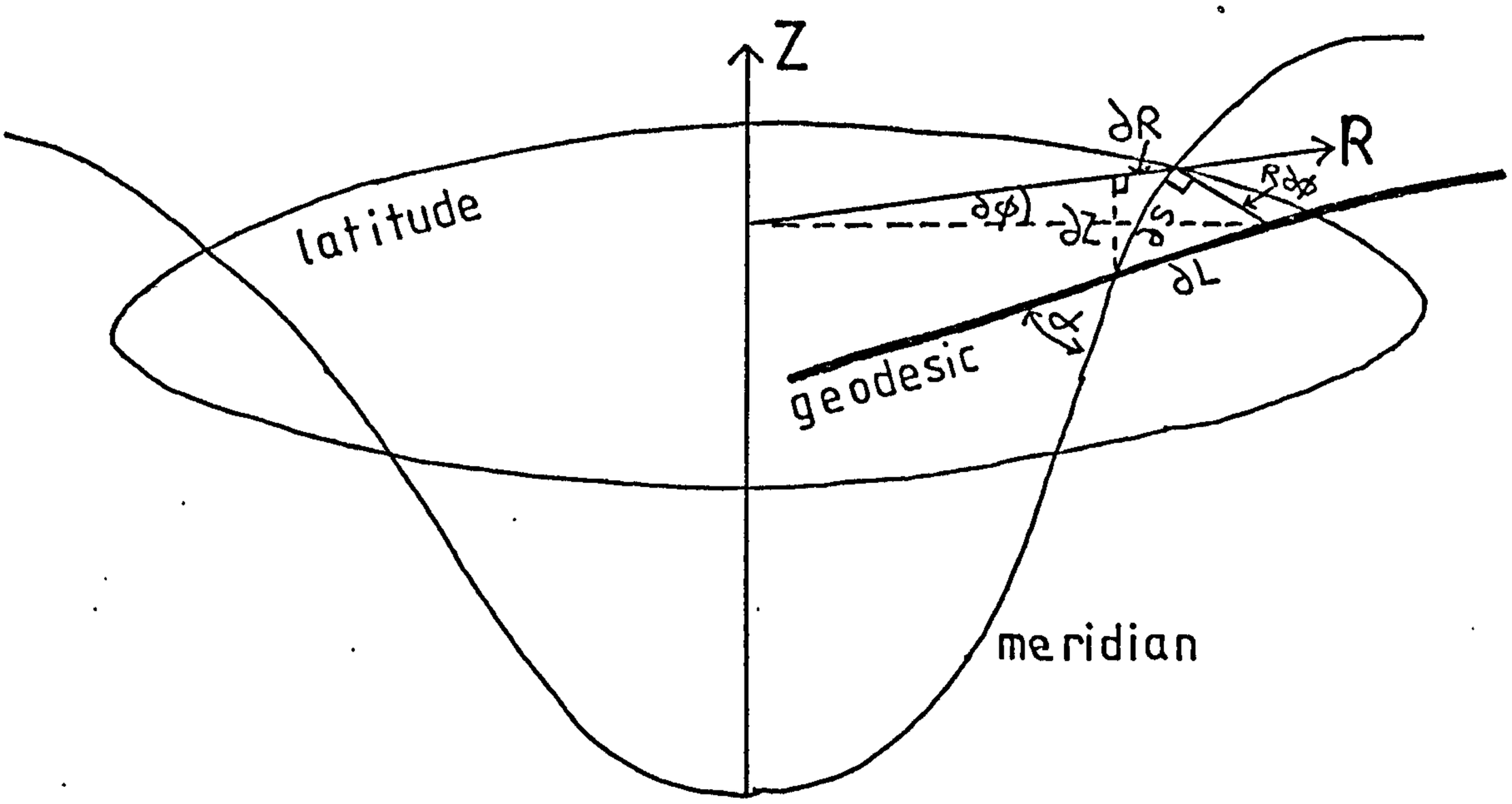

Figure 2.5 Relationship between infinitesimals on a geodesic surface.

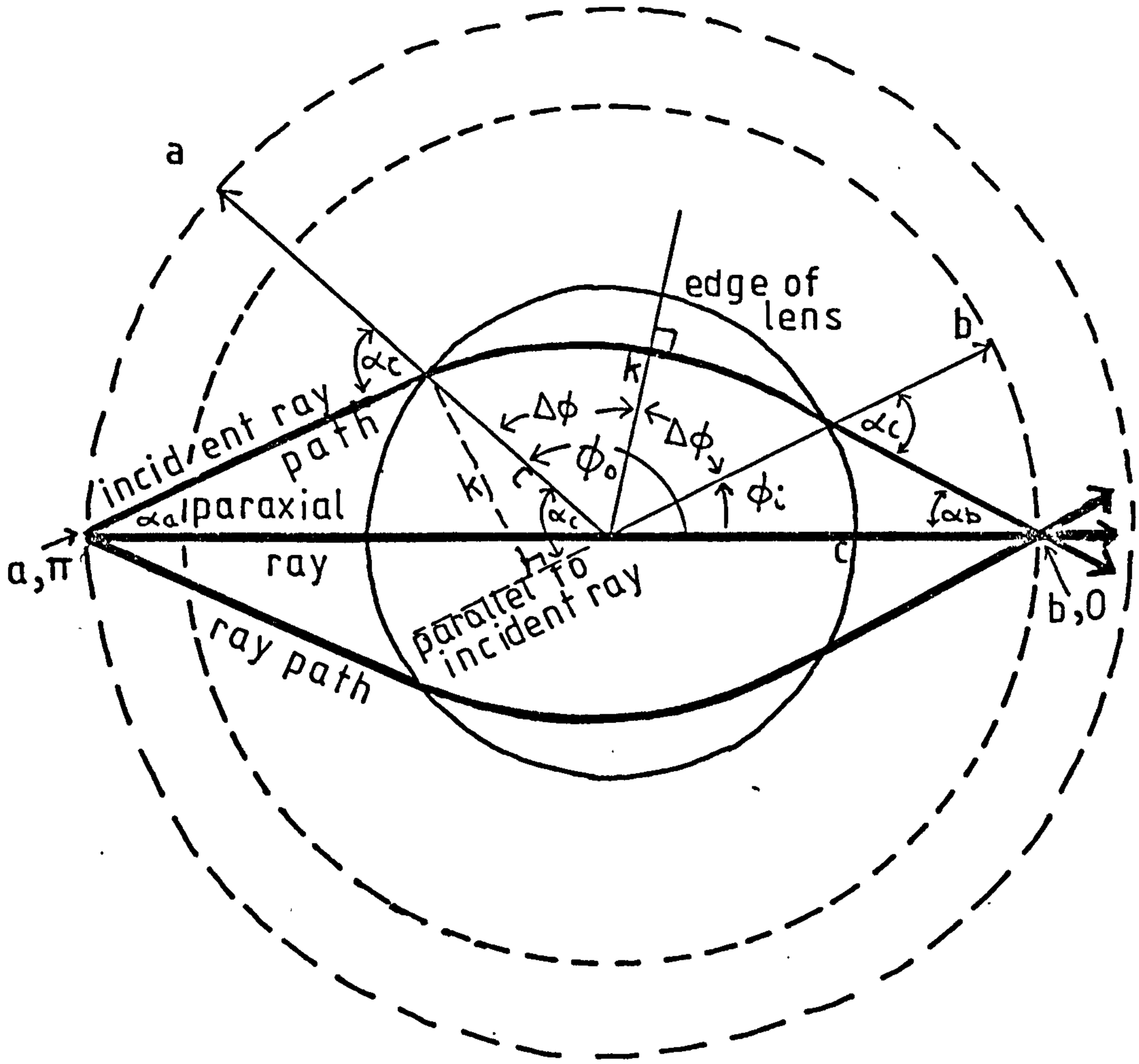

Figure 2.6 Plane projection of ray paths on and beyond an axisymmetrical geodesic lens.

R as

$$dL^2 = (S'^2.dR^2 + R^2.\phi'^2).dR^2 \qquad \text{.....2.6}$$

where dR is a small increment of radius, and all of these increments are sufficiently small to allow relationships to be represented using differentials. Primes indicate derivatives with respect to R. This expression may be substituted into the variational Fermat expression for a geodesic curve so that

$$\delta\int(S'^2.dR^2 + R^2.\phi'^2)^{0.5}.dR = 0 \qquad \text{.....2.7}$$

Since S(R), and therefore also S'(R), is some known function of R, ϕ is a dependent variable. The solution of 2.7 is given by using the calculus of variations to derive an Euler equation (see e.g. reference 121, Appendix I).

The variation of the path length between points P_1 and P_2 may be defined using equation 2.7 as

$$I(\epsilon) - I(0) = \epsilon\left(\frac{dI}{d\epsilon}\right) = \int_{R_2}^{R_1} F(S',\phi',S,\phi,R).dR$$

where $F(S',\phi',S,\phi,R)$ is a more generalised function than in 2.7, and points P_1 and P_2 are situated at the coordinates $(S_1=S(R_1),\ \phi_1=\phi(R_1),\ R_1)$ and $(S_2=S(R_2),\ \phi_2=\phi(R_2),\ R_2)$. The non-geodesic path between the points is defined using an arbitrary function t(R), with the boundary condition that $t(R_1) = t(R_2) = 0$, and an infinitessimal factor ϵ which has the value zero on the geodesic curve. For the non-geodesic curve the surface S-coordinate is replaced by $S + \epsilon t(R)$ and the longitudinal ϕ-coordinate by $\phi + \epsilon t(R)$.

To find the equation of the geodesic we need to determine for which function F the variational of the path length becomes zero. This is equivalent to finding the function F for which $dI/d\epsilon$ tends towards zero for $\epsilon = 0$. We may start by considering a neighbouring curve which departs from the geodesic curve only in ϕ-coordinates. Then the path-length integral is given by

$$I(\epsilon) = \int_{R_2}^{R_1} F(S', \phi'+\epsilon t'(R), S, \phi+\epsilon t(R), R).dR$$

Using a Taylor series the function F may be expanded with powers of ϵ:

$$I(\epsilon) \int_{R_2}^{R_1} \left[F(S', \phi', S, \phi, R) + \epsilon t(R) \frac{\partial F}{\partial \phi} + \epsilon t'(R) \frac{\partial F}{\partial \phi'} + \epsilon^2, \epsilon^3 \text{ terms} \right] dR$$

Differentiating with respect to ϵ within the integral, and allowing the terms in ϵ^2, ϵ^3 etc to vanish (since we are interested in the geodesic path, where $\epsilon = 0$):

$$\frac{dI}{d\epsilon} = \int_{R_2}^{R_1} \left(t(R) \frac{\partial F}{\partial \phi} + t'(R) \frac{\partial F}{\partial \phi'} \right) dR$$

The second term in the integral may be expanded by integrating by parts:

$$\int_{R_2}^{R_1} t'(R) \frac{\partial F}{\partial \phi'} dR = \left[t(R) \frac{\partial F}{\partial \phi'} \right]_{R_2}^{R_1} - \int_{R_2}^{R_1} t(R) \frac{d}{dR} \frac{\partial F}{\partial \phi'} dR$$

The first part of the expansion vanishes since $t(R) = 0$ at the limits. Therefore

$$0 = \left(\frac{dI}{d\epsilon} \right)_{\epsilon=0} = \int_{R2}^{R_1} t(R) \left(\frac{\partial F}{\partial \phi} - \frac{d}{dR} \frac{\partial F}{\partial \phi'} \right) dR$$

Since $t(R)$ has arbitrary but non-zero values the expression within the brackets must itself be zero. This gives the Euler equation:

$$\frac{\partial F}{\partial \phi} - \frac{d}{dR} \frac{\partial F}{\partial \phi'} = 0 \qquad \text{.....2.8}$$

Now the geodesic path length depends on the generating curve of the lens, but since the lens is symmetrical around the longitude coordinate ϕ, F is not dependent on ϕ. The first term of this expression therefore vanishes.

The differential equation of the geodesic is now

$$\frac{d}{dR} \frac{\partial F}{\partial \phi'} = 0$$

distances and the incidence angles as the ray enters and

and therefore $\frac{\partial F}{\partial \phi'}$ = a constant.

Differentiating the last expression (taking the definition of the function F from equation 2.7 and substituting from equation 2.6) gives

$$R^2.d\phi/dL = K \qquad \text{.....2.9}$$

Referring to Figure 2.5 and treating differentials as small increments it can be seen that

$$R.d\phi/dL = \sin\alpha \qquad \text{.....2.10}$$

where α is the angle between the geodesic ray path and the meridian which it crosses (α varies with incident ray position and direction).

Substituting into 2.9 produces $K = R \sin\alpha$ .....2.11 which is the fundamental equation for a geodesic on a surface of revolution. It has been called Clairaut's theorem [83], and is analogous to Snell's law of refractive optics. As a ray travels around a lens, its radial distance R from the centre and the angle α both vary continuously, the former from the lens outer radius to a minimum and back, and the latter from α_c to $\pi/2$ and back to α_c.

The value of the constant K (the "impact parameter") for any given ray on a particular geodesic lens may be determined from the angle α_c where the ray meets the lens. For example, in Figure 2.6, α_c can be calculated readily from the position of the object on a circle of radial distance R=a, azimuth ϕ=0 from the lens centre and the coordinates (c,ϕ) of the ray where it meets the edge of the lens. In this case the value of the impact parameter is given by $K = c \sin\alpha_c$. It can be seen in the figure that K is also the distance between the ray path outside the lens and a parallel drawn through the centre of the lens.

For any ray there is a turning point at which the ray is closest to the centre. This occurs on a meridian where $\alpha = \pi/2$ and $\sin\alpha$ is a maximum, i.e. unity. The distance of closest approach is therefore K. Since the radial distances and the incidence angles as the ray enters and

exits from the lens are equal, the ray paths are symmetrical about the position of closest approach.

Substituting from equation 2.6 into equation 2.10 and squaring gives

$$d\phi^2 = \frac{K^2}{R^4}\left[\left(\frac{dS}{dR}\right)^2 + R^2\left(\frac{d\phi}{dR}\right)^2\right] dR^2 \quad \ldots\ldots\ldots\ldots 2.12$$

Rearranging this leads to the change of azimuthal angle for a small distance travelled along the generating arc dS as

$$d\phi = \frac{K\ dS}{R\ (R^2 - K^2)^{0.5}} \quad \ldots\ldots\ldots\ldots 2.13$$

Referring again to Figure 2.5 it can be seen that small distances along the arc, dS, are related to small changes of height coordinate, dZ, and radial position, dR, by $dS^2 = dZ^2 + dR^2$, and therefore

$$dS = \left[\left(\frac{dZ}{dR}\right)^2 + 1\right]^{0.5} dR$$

Substituting into 2.12 leads to

$$d\phi = \pm \frac{K}{R}\left(\frac{1 + (dZ/dR)^2}{R^2 - K^2}\right)^{0.5} dR \quad \ldots\ldots\ldots\ldots 2.14$$

This expression for the change in azimuthal angle of a ray in terms of radial position, profile slope and the impact parameter could be regarded as the fundamental equation for ray paths on a geodesic lens. This equation will be used in the next section.

2.2.4 Ray-tracing expressions

Integrating equation 2.14 leads to a determinion of the path taken by a ray around a geodesic lens surface. Referring to Figure 2.6, the total change of azimuth for a ray originating at an "object" position (a,π) (situated on the "optical axis", a line which passes through the lens centre) and following a clockwise rotating path to an "image" position (b,0) also on the lens axis is -π, and

is given by

$$-\Pi = \int_{R=a}^{R=K} K.G(R)\ dR + \int_{R=K}^{R=b} -K.G(R)\ dR \qquad \text{.....2.15}$$

where the first term on the right-hand side of the equation refers to the ray entering the lens and reaching the turning point of radial distance (at which R=K), and the second term refers to the remainder of the ray path. The function G(R) represents a factor in equation 2.14, given by:

$$G(R) = \frac{1}{R}\left(\frac{1 + (dZ/dR)^2}{R^2 - K^2}\right)^{0.5}$$

Outside the lens, where R > c, the waveguide is on a plane surface and therefore $Z_r = 0$, and $Z'_r = 0$. Within the lens the azimuthal angles from the edge to the closest approach point are equal: therefore the two terms in equation 2.15 correspond to azimuthal changes of $-(\pi - \phi_o + \Delta\phi)$ and $-(\Delta\phi + \phi_i)$, respectively. These terms may therefore be divided further, into the three (negative) angles $-(\pi - \phi_o)$, $-2\,\Delta\phi$ and $-\phi_i$. Therefore

$$-\Pi = \int_a^c \frac{K\ dR}{R\ (R^2 - K^2)^{0.5}} + 2K\int_c^K G(R).dR + \int_b^c \frac{K\ dR}{R\ (R^2 - K^2)^{0.5}}$$

.....2.16

Integration of this equation will lead to determination of the ray path coordinates, and in particular the relationship between the object and image positions and the lens profile.

The terms for $(\pi - \phi_o)$ and ϕ_i are standard integrals which become:

$$-(\pi-\phi_o) = [-\sin^{-1} K/R]_a^c = -\sin^{-1} K/c + \sin^{-1} K/a$$

and $$-\phi_i = [-\sin^{-1} K/R]_b^c = -\sin^{-1} K/c + \sin^{-1} K/b.$$

These angles could have been determined from the geometry of Figure 2.6 since they are simply $\pi - \phi_o = \alpha_c - \alpha_a$ and $\phi_i = \alpha_c - \alpha_b$. The image distance b can be taken from the latter angle: $b = K / \sin(\alpha_c - \phi_i)$.

From Figure 2.6 $\phi_i = \phi_o - 2\Delta\phi$, and $\phi_o = \pi + \alpha_a - \alpha_c$ and, using $\sin(A - \pi) = -\sin(A)$:

$$b = -K / \sin(2\Delta\phi + 2\alpha_c - \alpha_a) \quad \text{.....2.17}$$

The values of α_c and α_a are determined solely by the position of the object and the diameter of the lens. However the term for $2\Delta\phi$ depends also on the lens profile. This term has a singularity at R = K which may be removed by substituting $R^2 - K^2 = (R - K)(R + K)$ and integrating by parts. Taking

$$U(R) = \frac{1}{R}\left(\frac{1 + (dZ/dR)^2}{R + K}\right)^{0.5} \quad \text{.....2.18}$$

and $V(R) = 2.(R - K)^{0.5}$

then $dV/dR = (R - K)^{-0.5}$

and $$2\Delta\phi = 2K\left(\left[U.V\right]_k^c - \int_k^c V.dU/dR.dR\right)$$

$$= 2K\left\{\left[U.2(C - K)^{0.5}\right]_K^c - \int_K^c 2.(R - K)^{0.5}\,\frac{dU}{dR}.dR\right\}$$

.....2.19

therefore $2\Delta\phi =$

$$4K\left[\left(\frac{(1 + Z'(c)^2)}{c^2}\,\frac{(c-K)}{(c+K)}\right)0.5 + \int_K^c (R - K)^{0.5}\,\frac{dU}{dR}\,.dR\right]$$

.....2.20

The first term depends only on the diameter of the lens, the position of the object and the initial slope of the lens profile z'(c). For a low-loss transition of

waveguided light from the plane region into the geodesic lens, this initial slope should be zero.

The second term depends on the shape of the lens. Differentiating U(R),

$$\frac{dU}{dR} = G(R)\ (R - K)\left(\frac{Z'(R).Z''(R)}{1 + Z'(R)^2} - \frac{1}{R} - \frac{1}{2R + K}\right)$$

To trace rays within the lens, the azimuthal angle ϕ may be found for a succession of radial distances R by evaluating the central integral of equation 2.16 from the lens edge at R=c to the radius R, where c >R > K.

2.3 METHODS OF DESIGNING GEODESIC LENSES

2.3.1 Spherical lenses and their limitations

Equation 2.20 may be evaluated analytically for the case of a spherical lens depression. Essentially the same spherical geometry problem occurs when finding the shortest navigational path between terrestial locations. Referring to Figure 2.7, $2\Delta\phi$ is the apex angle of the sphere, and α_c is the angle of incidence onto the sphere. The exit angle is the same, as are the angles on the surface inside the edge of the lens. From one of Napier's rules for the spherical triangle $\cot\Delta\phi = \cos\gamma.\tan\alpha_c$.

But $\cos\gamma = (1 - \sin^2\gamma)^{0.5} = (C_1^2 - c^2)^{0.5}/C_1$

and $\tan\alpha_c = \sin\alpha_c/(1 - \sin^2\alpha_c)^{0.5} = K/(c^2 - K^2)^{0.5}$

(using the definition of the impact parameter K from equation 2.9)

therefore $\cot\Delta\phi = K(C_1^2 - c^2)^{0.5} / C_1(c^2 - K^2)^{0.5}$.

Substituting into 2.17 gives the radius b of the image circle for this ray (Figure 2.6) where b is given by

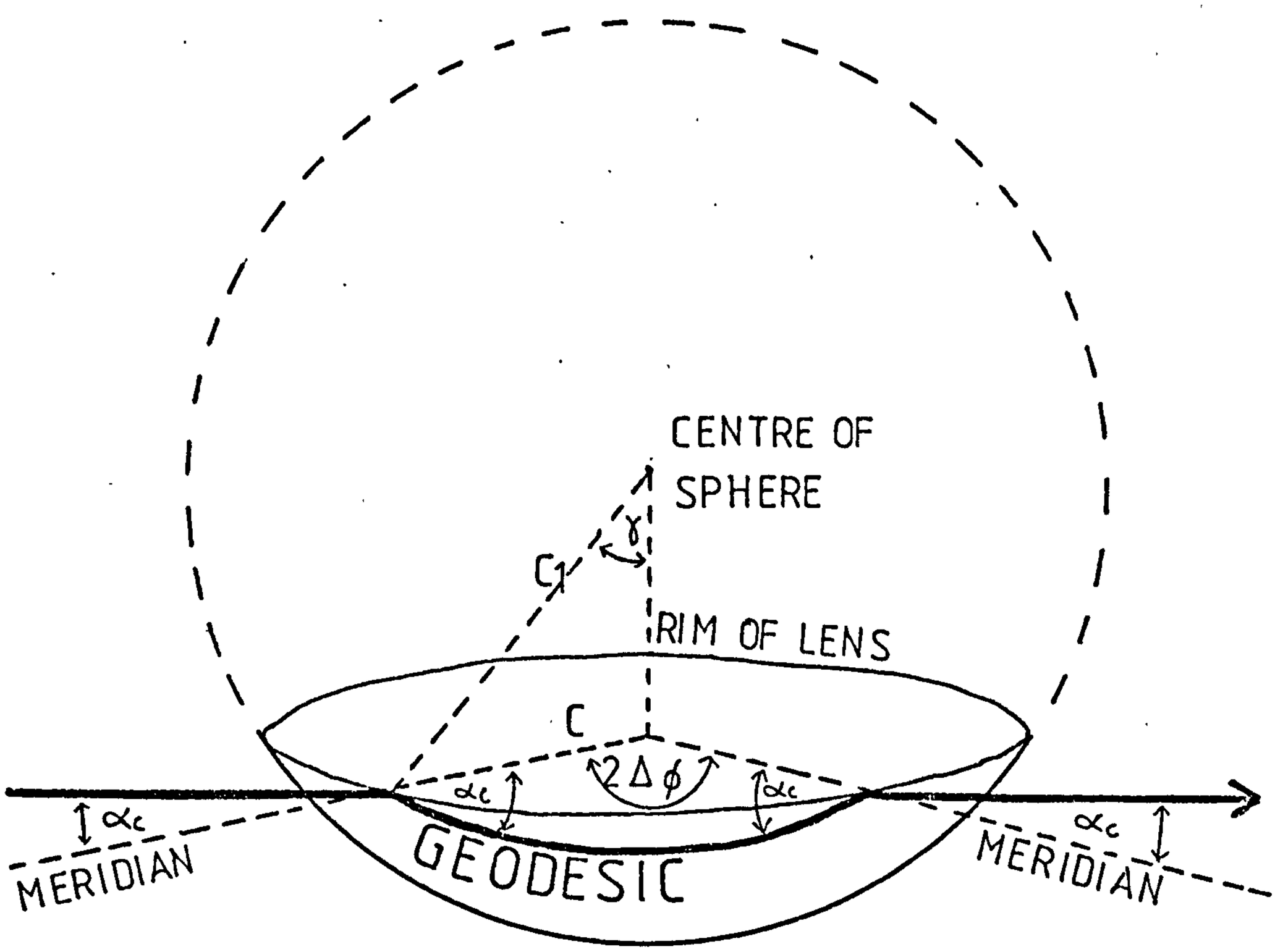

Figure 2.7 Geodesic path on a spherical surface.

$$b = \frac{-K}{\sin\left[2.\tan^{-1}\frac{C_1}{K}\left(\frac{c^2 - K^2}{C_1{}^2 - c^2}\right)^{0.5} + 2\sin^{-1}\frac{K}{c} - \sin^{-1}\frac{K}{a}\right]} \qquad \text{.....2.17}$$

This equation may be simplified for paraxial rays. For these rays the impact parameters K, incident angles α_c and divergence angles α_a are all small. Recalling that if $\tan A = X$, then $\tan 2A = 2X/(1 + X^2)$ and $2\tan^{-1} X = \tan^{-1}(2X/(1 + X^2))$, and substituting $2\Delta\phi$ (the first term in the sine of equation 2.17) for X, gives

$$2\Delta\phi = \tan^{-1}\left(\frac{2\cos\gamma.\tan\alpha_c}{\cos^2\gamma.\tan^2\alpha_c - 1}\right)$$

For very small K, $\tan\alpha_c$ tends to $\sin\alpha_c = K/c$, and $\cos^2\gamma.\tan^2\alpha_c \ll 1$, therefore

$$2\Delta\phi = -(2.K.\cos\gamma)/c.$$

Since this and all other angles in equation 2.17 are very small, sines and tangents may be replaced by the values of the angles. This simplifies 2.17 to the familiar thin-lens formula:

$1/a - 1/b = 1/F$ where F is the focal length (i.e. the modulus of distance b for infinite a) which is given by

$$F = c/2(1 - \cos\gamma) \qquad \text{.....2.18}$$

and the sign convention indicates that the image is on the opposite side of the lens centre to the object.

The last equation may be used to design the dimensions of a geodesic lens. For example, if the lens radius c = 5mm and the focal length F = 18.5mm, the radius of curvature c_1 = 9.96mm.

Aberrations of spherical lenses may be determined using the full equation 2.17. These may be described as longitudinal (i.e. the variation of focusing distance b) or transverse (i.e. the variation of the ray intercept heights). Theoretical ray-tracing of a large number of spherical geodesic lenses (where rays were focused outside

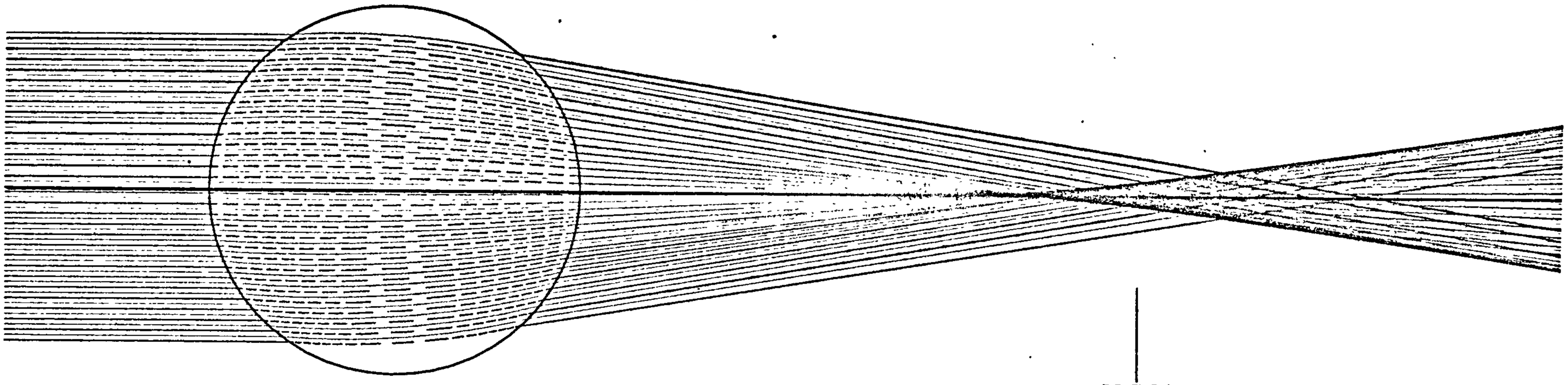

MIN
RMS
SPOT

SPHERE: H=C-SQRT(C*C-R*R)
CURVE RADIUS C= 1.866

Figure 2.8 Geometrical trace of rays from infinity through a spherical section geodesic lens, illustrating spherical aberration.

the lens depression) shows that the focal distance becomes longer as rays enter the lens further from the axis. Figure 2.8 shows a typical example close to the lens design required for the IOSA (lens diameter 10mm, focal length 18.66mm).

A computer programme was written to establish the radius of curvature of a spherical geodesic lens depression c_1 which would provide the minimum image size (estimated by the root-mean-square value of the transverse aberration) at a focal distance of 18.5mm. The following table shows the focal distance b for a series of input heights K for rays from infinity. It also shows the minimum cumulative r.m.s spot size and the distance at which this occurs. The lens diameter c = 5mm, its radius of curvature c_1 = 9.28mm and the entrance heights of the rays (half the aperture values) are up to 3.5mm.

TABLE 1: ABERRATION OF A SPHERICAL GEODESIC LENS

RAY ENTRANCE HEIGHT K mm	FOCAL DIST OF SINGLE RAY mm	DIST OF SMALLEST IMAGE mm	R.M.S. SPOT DIAMETER mm
0.0	15.850	15.850	0.000
0.5	15.910	15.910	0.000
1.0	16.095	16.055	0.005
1.5	16.415	16.285	0.020
2.0	16.920	16.620	0.050
2.5	17.675	17.065	0.105
3.0	18.815	17.675	0.195
3.5	20.635	18.510	0.355

It is clear that the image size becomes as large as an 8μm wide detector element for beams of height greater than about 1mm, that is aperture width more than 2mm. Since apertures greater than 2mm are required to meet diffraction criteria, spherical lenses would clearly give a performance below that required.

Several workers have attempted to overcome the above difficulties by making simple modifications to the spherical lens profile. In order to counteract aberration in a spherical geodesic lens Spiller and Harper [88] superimposed a mode index lens on the depression. This had aberrations in the opposite direction to the spherical aberrations of the geodesic lens. The variation in mode index required of the correction lens is of the order of a few percent, which cannot be achieved with titanium-diffused waveguides on lithium niobate. Vahey [64] used an aluminium layer over the waveguide as a correcting lens in series with a spherical geodesic lens. The lens was of about 16mm radius of curvature with the edge rounded (from the action of the flexible polishing pad) to about 1.2 mm radius of curvature. The aluminium layer was shaped with the profile of a biconcave lens with its optical axis along the direction of the 3mm wide light beam which entered the geodesic lens. The aluminium layer modified the mode index of the waveguide by about 3.10^{-4}. The near-spherical geodesic lenses were corrected to give images in which the full-width of the central peak was 13 μm, only 17% wider than the expected diffraction limit for the 3mm beam aperture.

A second, and probably even more critical, reason for not using spherical lens depressions is that the edge of the lens forms a very sharp boundary with the surrounding plane region of the substrate. In the example of Table 1, the angle at which the lens meets the plane is 33 degrees. It would be impossible to confine light within a waveguide which folds over such a sharp boundary.

2.3.2 Edge-rounding of spherical lenses

Many workers have designed lenses with an inner spherical region and an outer toroidal annulus which gently merges into the plane surrounding region [91, 94]. Southwell [94] showed that such a lens could be diffraction limited at f/4 with a 2.5mm aperture when the edge region

had a circular profile with radius of curvature one-tenth of the radius of curvature of the spherical part.

The author made a lens of this form with a 16mm radius of curvature in the inner (spherical) part and a 1.5mm radius of curvature in the toroidal section. The total depth of the lens was 0.8mm, the diameter of the inner part was 9.565mm, and of the whole lens, 10.461mm. The fabrication and testing of this lens is discussed in Chapters 5 and 7, where it is referred to as the "two-arc" lens. Using equation 2.18 (and ignoring the toroidal region) the paraxial focal length of this lens should be 52mm.

Although edge-rounding is expected to allow waveguided light to pass freely into the lens depression, the data presented by Southwell suggests that edge-rounding cannot correct spherical aberration sufficiently for wide aperture lenses. Ray-tracing (by N.Finlayson, using a similar computer programme to that mentioned in the previous section) shows that the paraxial focal length of the "two-arc" lens should be 51mm, and that the focal length increases to 55mm at the radial position of 4.8mm where the inner part of the lens meets the edge-rounding part. For a light beam of uniform intensity profile and of width equal to that of the central part of the lens, 9.565mm, the focused spot has a width of about 50μm r.m.s. The aperture for which the lens focuses with the smallest spot is expected to be approximately that for which the r.m.s. spot-width is the same size as the diffraction-limited spotwidth. This occurs at an aperture of 3mm, at which the spotwidths are about 12μm. The combination of diffraction and aberration spotwidths may be estimated by using their root-mean-square value [122], i.e. about 17μm.

2.3.3 Numerical optimisation: aspheric lens profiles

One approach to correcting the lens aberration is to modify the spherical inner profile of an edge-rounded lens

to an aspherical shape. Some work has been done on simple conic sections [92, 101] showing that elliptical cross-sections may be found which provide considerably better lens performance than spheres, but with image spreading comparable to the diffraction limit for large apertures.

Bulk optical lenses are frequently designed by starting with a spherical profile which provides approximately the desired performance, then modifying it by a numerical algorithm which compares changes of local profile with a merit function such as r.m.s. image diameter and such a procedure is also possible with geodesic lenses. Betts et al [103] started with a spherical lens profile and modified it using a numerical algorithm so that ten ray paths (spread equally over the semi-aperture of the lens) were of the same length. Their lens profile was expressed as a sixth-order polynomial. Later the same group [104] incorporated an edge-rounding region of circular profile, with radius of curvature 0.05 of the average radius of curvature of the whole geodesic lens depression. They designed a lens which focused 14 rays (again equally spaced over the semi-aperture) at 6.125 times the semi-aperture. Iterations ceased when the r.m.s. spot size became small relative to the diffraction limit for an aperture of 90% of the lens diameter.

2.3.4 Transformation of Luneberg lens designs

Another approach to the design of aspherical geodesic lenses is to transform the profiles of ideal lenses which have been derived in optical path-length space to profiles of geodesic lenses (i.e. in Euclidean path-length space). One such ideal lens was designed by Luneberg [123] where a collimated beam of radiation is focused perfectly onto the opposite rim of a lens in which the refractive index (relative to the surrounding medium) is an axisymmetric function $n(R) = (2 - R^{1/4})^{0.5}$, where R is the normalised radius of the lens. The refractive index of this lens ranges from 1 at the edge to $\sqrt{2}$ at the centre. This was

transformed by Rinehart [73] from a plane surface lens of variable refractive index to a geodesic lens of uniform index. Kunz [74] and Toraldo di Francia [75] later introduced families of gradient-index lenses similar to the lens type derived by Luneberg. Cornbleet and Rinous [109] introduced a generalisation which described an even wider range of refractive index profile lenses and went on to transform their generalised formula to describe geodesic lenses as well.

Southwell [71] used a similar transformation to derive geodesic lenses for integrated optics. Other workers have defined a geodesic edge-rounding function (circular [99], and a third-order polynomial [98]), transformed the function from physically-curved space into refractive-index space, used the explicit expressions of Rinehart and Luneberg to derive a gradient-index lens to fit within the "rounding function" region, and then transformed the composite lens into a geodesic lens. Chen and Ramer [98] were particularly careful to avoid waveguide scattering and insertion losses by constraining the edge rounding function and its junctions with the plane and the inner lens regions so that the slope of the lens edge was zero, and the functions and their first and second derivatives were continuous at these boundaries.

2.3.5 Exact solution for lenses with perfect ray traces

During the same month as the author began the work of this thesis, Sottini, Russo and Righini [83] published a method which avoids numerical optimisation computations or Luneberg transformations by deriving an exact expression which describes a family of geodesic lens profiles in terms of their slopes. Using these lens designs, all rays which cross over the edge-rounding boundary into the inner region are perfectly focused. The lens profiles themselves are obtained relatively quickly and simply from their slope functions by using any standard numerical

integration algorithm. Because of its apparent simplicity, this method was adopted to design the lens profiles required for the IOSA.

The method may be summarised with reference to Figure 2.9. An outer edge rounding region of arbitrary width is chosen and its profile is defined by a specific function for its slope. The particular function which is used by Sottini has appropriate boundary conditions, and possesses useful mathematical properties which allow the profile of the inner part of the lens to be determined analytically (in terms of its slope) by a solution of Abel's integral equation.

Referring to the lower sketch of Figure2.9, circle P is a latitude on the lens. The shape of the lens is defined by a surface of revolution S. A geodesic passes through the point M of longitude ϕ = O at an angle ψ on the surface to the tangent to the latitude. The geodesic continues around the lens to cross the latitude P (again at angle ψ, by symmetry and Equation 2.11) at a longitude ϕ. This longitude is expressed as a function $F(\psi)$ of ψ. The same function applies to all geodesic rays passing through circle P. The definition of this function depends on what is required of the geodesics on the surface. For the present needs the function is such that rays from one circle of radius a (Figure 2.9) which pass into the inner region of a lens (i.e. within the edge-rounding boundary at radius d) are focused onto another circle of radius b. The slope of the lens profile depends on this function $F(\psi)$ according to an integral equation.

The derivation of the expressions for lens profile slope is presented in Appendix I. A brief summary of the procedure is as follows. Using equation 2.14 the longitude function $F(\psi)$ is related to s', (the differential of distance along the lens generating surface with respect to radial position R) by an integral equation. Various boundary conditions are chosen, i.e. the radial positions

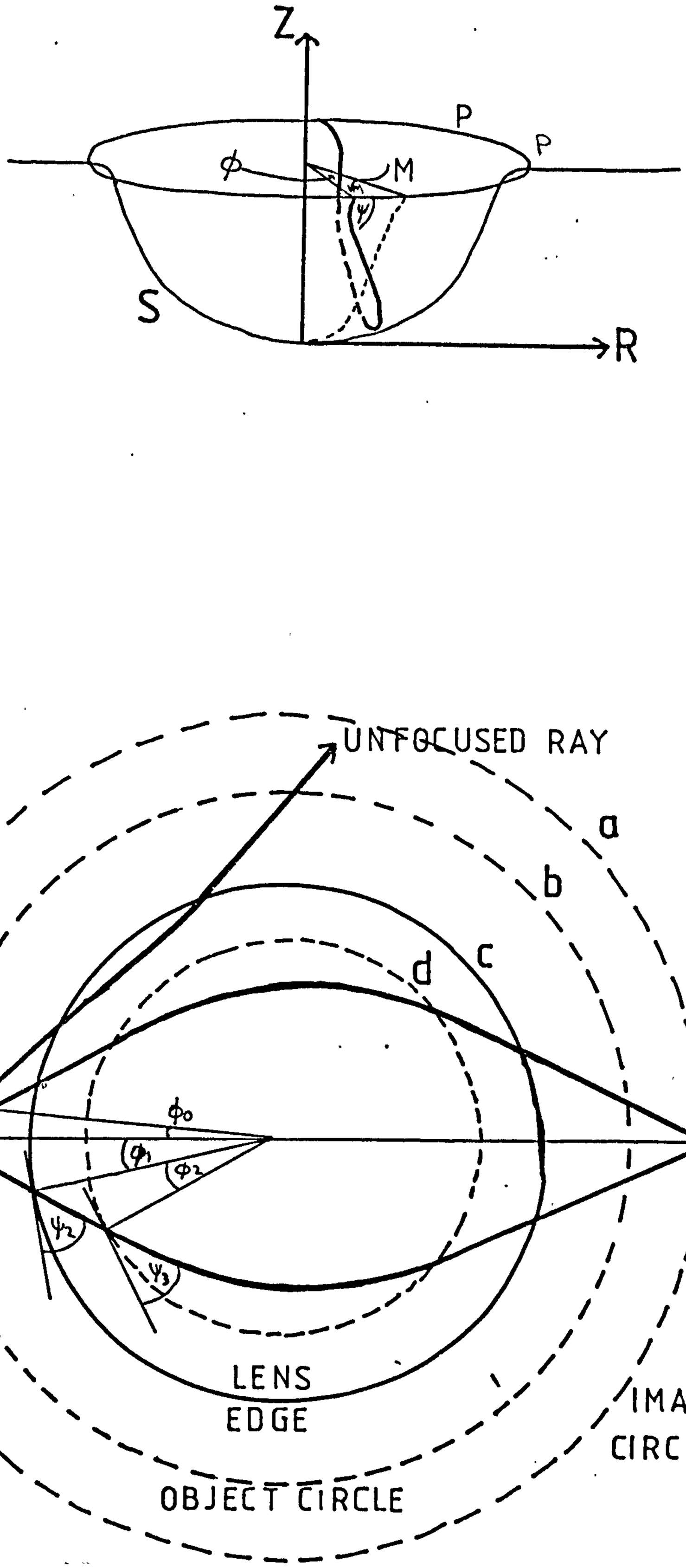

Figure 2.9 Definition of terms used in SRR derivation of perfectly focusing geodesic lens profile.

of the object, the image, the lens edge and the edge-rounding boundary. A function is used for the slope of the edge-rounding region which may be inserted into the integral equation for $F(\psi)$ and integrated to determine another function which describes the inner region of the lens which is continuous in slope with the outer region.

Figure 2.10 shows a family of lens profiles which has been calculated using a NAG library numerical integration subroutine in a programme written for the GEC 4070 minicomputer. Although the four lenses have different proportions of the inner region radius to the whole lens radius (d/c), the lenses have identical relative apertures (defined as the ratio 2d/F where d is the edge-rounding boundary radius and F the focal length). Therefore the image widths (as defined by Equation 2.3) produced by the family of lenses are all 12μm. As might be expected, the weaker, longer focal length lenses are shallower than the more powerful lenses.

Figure 2.11 shows a lens profile calculated to meet the design criteria of section 2.1. This lens is 1.315mm deep and is of overall diameter 10mm. The position of the edge-rounding boundary is, to a large extent, arbitrary. For this lens it has been chosen at 3.7mm radius. The width of the inner region of the lens within this boundary is large enough to allow assessment of focusing through a very wide aperture of the lens (wider than 4.9mm, the value specified in section 2.1), while not being so wide that all of the edge-rounding region of the lens would require to be of very small radius of curvature. This lens design forms the basis of most of the practical lenses that are reported in this thesis.

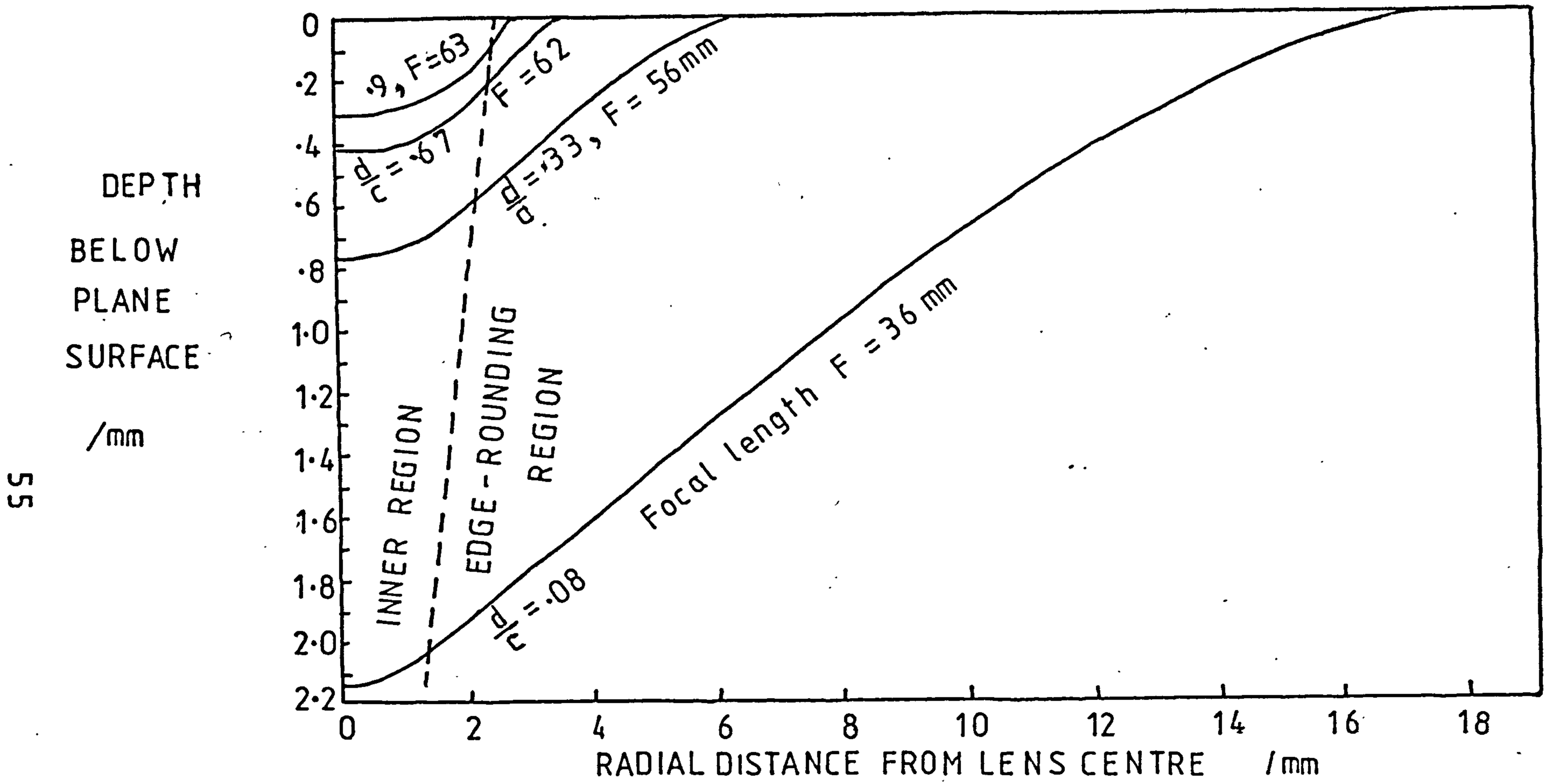

FIG. 2.10 A FAMILY OF LENS PROFILES WITH F/12·7 REL. APERTURE

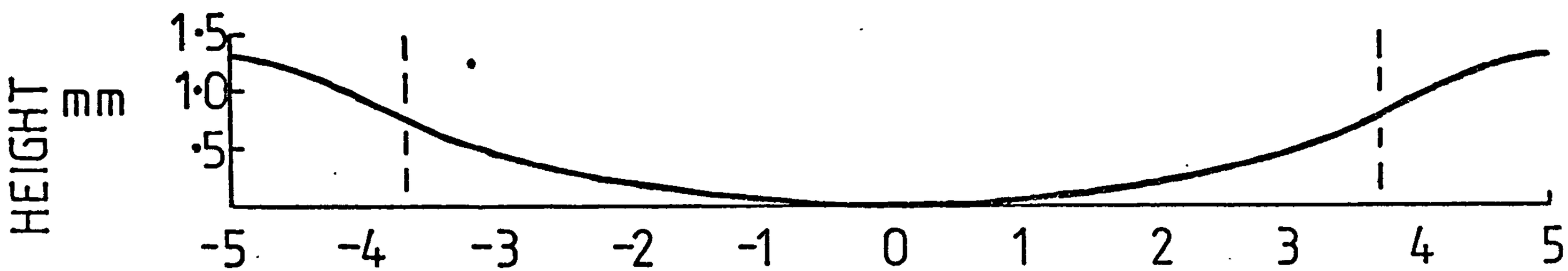

Figure 2.11
A geodesic lens profile derived by the SRR method, with diameter 10mm, and edge-rounding beyond 3.7mm, for conjugates infinity and 18.5mm

2.4 MODIFICATIONS TO THE EXACT SOLUTION PROFILE OF SOTTINI, RUSSO AND RIGHINI

2.4.1 Problems with small radii of curvature

When the author attempted to fabricate a lens which was designed using the procedure of the previous section, it was found (see Chapter 5) that a diamond-turning tool of small radius of curvature, 0.76mm, would not fit within the lens profile at the position where the edge-rounding region met the inner region. The local radius of curvature of the lens surface was clearly less than 0.76mm at this position. This presented two important problems:

- it would be impossible to either fabricate or measure the lens precisely using cutting tools and measuring probes of the smallest radii of curvature available.

-light would be likely to leak out from very highly curved regions of waveguides on lenses.

It was therefore essential to modify the lens designs to avoid regions of great curvature. The procedure used is described in section 2.4.2. Firstly in this section the local radius of curvature of lenses designed by the method of Sottini, Russo and Righini is discussed.

Using a well-known expression, the local radius of curvature C may be calculated as

$$C = \frac{(1 + z'^2)^{1.5}}{z''} \qquad \text{.....2.19}$$

where z', z" are the local slope and second differential of the curve.

Since the Sottini, Russo and Righini method derives the local slope z', it is only necessary to differentiate the expressions for z' to obtain z" and then C. This must be carried out for both of the lens regions. The derivations are given in Appendix I.

The local radius of curvature of the inner region of the lens profile is given by

$$C = \frac{\pi h^2}{R} \frac{z' (z'^2 + 1)}{P(R,a,b,c,d)} \qquad \text{.....2.20}$$

where P(R,a,b,c,d) is a function defined in Appendix I.

At the edge-rounding boundary, where R = d, it can be seen that P(R,a,b,c,d) is infinite and therefore the local radius of curvature is zero. At all other points along this inner region of the lens profile, the local radius of curvature has a finite value. At the centre of the lens where R = z'(O) = O, equation 2.20 may be evaluated using L'Hopital's rule for the quotient z'/R.

This leads to $C = h.\left(\frac{\pi}{P(O,a,b,c,d)}\right)^{1/2}$, which is finite.

As shown in Appendix I, the local radius of curvature in the edge-rounding region of the lens is given by

$$C = -\frac{h^2}{2R} z'(z'^2 + 1) \qquad \text{.....2.21}$$

This has a finite value for all parts of the curve except where R = c, where z' = O and therefore C = O. No problem would be encountered when fitting the diamond-turning tool or measuring probe to this highly-curved part of the lens profile, because contact would be on the outside of the curve. Severe problems with waveguide propagation would, however, be anticipated.

Figure 2.12 plots the local radius of curvature of the lens design of Figure 2.4, with values computed using the above expressions (a is at infinity, b = 18.5mm, c =5.0mm, d = 3.7mm) . The radius can be seen to be less than 3mm (a common value for tool and probe radii of curvature) over two regions of the lens profile with widths of a few tenths of a millimetre.

2.4.2 Bridging over locally highly curved regions

Dashed lines in Figure 2.12 indicate the general form of changes which are required to the lens profile in order

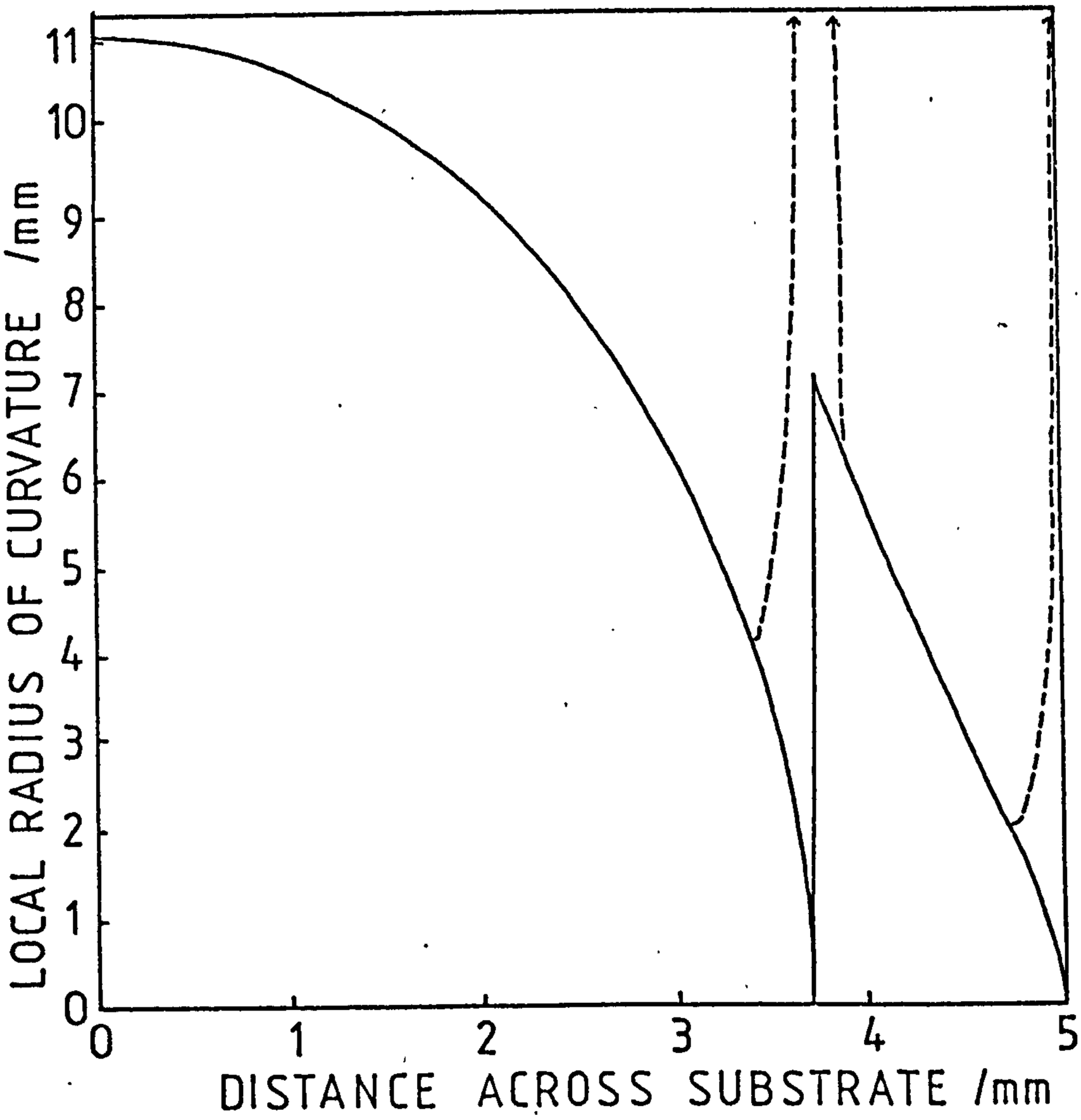

Figure 2.12 Local radius of curvature of an SRR designed geodesic lens.

to diminish the fabrication, measurement and light-loss problems. At the edge of the lens the curvature must become of infinite radius in order to merge into the plane region surrounding the lens. At the edge-rounding inner boundary the curvature must not have a radius below some value such as 2mm. Mergerian et al [106] indicate (experimentally and theoretically) that for losses due to mode mismatch to be less than a few dB the inner region must not be of less than a few millimetres radius of curvature and the edge-rounding region should not be less than about 0.2mm.

A method was devised which modifies lens profiles in the regions of extreme curvature so as to increase the local radius of curvature in these regions to at least certain chosen minimum values. For the lenses which were later fabricated (Chapter 5) these minima are set at 2.5mm radius of curvature for the inner region and 0.6mm for the edge-rounding region. The highly curved regions are bridged over with the least possible deviation from the Sottini, Russo and Righini profile. Elsewhere the modified profiles are within 0.1μm of the Sottini, Russo and Righini profile.

Figure 2.13 illustrates the method. The lens profile is approximated by a series of arcs of circles, whose centres are located at the intersections of normals to the original curve. This representation is particularly useful because the CNC machine controllers used to fabricate practical lenses can be programmed in terms of such arcs. The data are also in a very compact, portable form (only about 20 arcs were needed) which may be taken to a machine in the form of a short paper tape, or even quickly entered manually into its controller.

The algorithm reads a large number (e.g. 501) of sets of depth and radial distance values for the lens profile which are previously calculated by the Sottini, Russo and Righini programme and stored. Starting at the centre of the lens, the routine steps through the sets of positions,

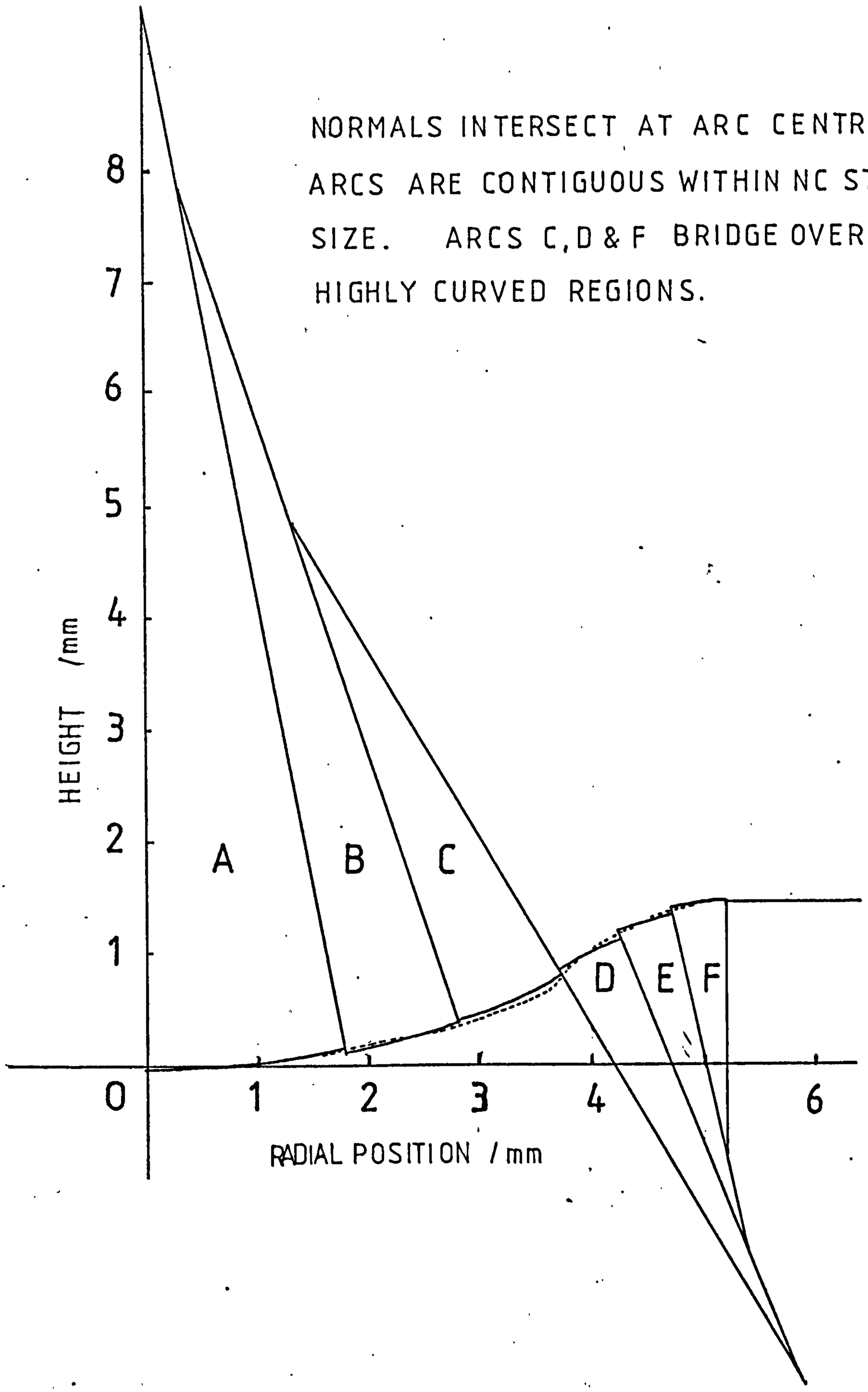

Figure 2.13 Method of fitting circular arcs to an SRR lens profile.

calculating each time the distance from the profile along the normal to the point of intersection with the axis of rotation of the lens. This is compared with the distance calculated from the centre of the lens to the point of intersection.

When this distance exceeds a preset value, typically 0.15μm, the first arc is defined. The radius of the arc is taken as the mean of the two most recent distances from the profile to the point of intersection. The centre about which the arc is drawn is taken as this point of intersection. The limits of the arc are taken as the radial (R) positions of the lens centre and the most recent data set, and the corresponding height coordinates on the arc itself.

The next arcs are determined by the same stepping routine, but use the normal which concludes the previous arc as its starting point, rather than the normal at R =0.

When this algorithm is used without any attempt to bridge over the highly curved regions, the Sottini, Russo and Righini curve can be fitted within better than ±0.2μm in height using only 22 arcs. The results are tabulated in Table 2. It can be seen that three of the arcs are of smaller radius of curvature than desired.

When the algorithm is used with bridging sections, the permitted difference between distances along the normals must be relaxed for the arc which steps over the boundary between the inner and the edge-rounding regions of the lens profile. The arc must be constrained to be of greater than e.g. 2.5mm radius of curvature. At the edge of the lens, the final arc must be chosen to be of greater than e.g. 0.5mm radius of curvature, and to meet the plane surface surrounding the lens within e.g. 0.5μm of the exact Sottini, Russo and Righini height. In practice the arc always becomes parallel to the plane surface at a greater height and at a larger radius than the exact design.

TABLE 2: CIRCULAR ARCS FITTED TO SOTTINI,RUSSO AND RIGHINI GEODESIC LENS PROFILE.
Without bridging over highly-curved regions.

NO	END POSITION OF ARC /mm		CIRCLE PARAMETERS/mm			HEIGHT ERROR/μm
	R	Z	R	Z	RADIUS	
1	0.0000	-.0001				
2	.8600	.0338	.0000	10.9326	10.9326	.08
3	1.4500	.0971	.0370	10.4633	10.4621	.08
4	1.9300	.1745	.1289	9.7895	9.7822	.08
5	2.3300	.2588	.2802	8.9817	8.9605	.08
6	2.6700	.3464	.4932	8.0753	8.0296	.08
7	2.9600	.4348	.7717	7.0864	7.0024	.09
8	3.1900	.5155	1.1076	6.0653	5.9275	.08
9	3.3800	.5913	1.4947	5.0336	4.8258	.09
10	3.5200	.6540	1.9264	4.0165	3.7211	.09
11	3.6300	.7091	2.4174	2.9803	2.5746	.12
12	3.6900	.7429	2.9913	1.9054	1.3564	.16
13	3.7000	.7489	3.4962	1.0651	.3762	.03
14	3.9000	.8730	7.3790	-4.9616	6.7930	.09
15	4.1000	.9869	6.7748	-3.9483	5.6134	.09
16	4.2900	1.0844	6.2914	-3.0563	4.5990	.10
17	4.4600	1.1616	5.9087	-2.2646	3.7199	.09
18	4.6100	1.2204	5.6156	-1.5713	2.9673	.09
19	4.7400	1.2631	5.3931	-.9536	2.3110	.09
20	4.8500	1.2918	5.2262	-.3870	1.7205	.11
21	4.9300	1.3071	5.1103	.1302	1.1907	.10
22	4.9800	1.3132	5.0385	.5986	.7170	.10
23	5.0000	1.3142	5.0001	1.0674	.2468	.13

TABLE 3: CIRCULAR ARCS FITTED TO SOTTINI,RUSSO AND RIGHINI GEODESIC LENS PROFILE.
Bridging over highly-curved regions.
minimum radius: concave part 2.50mm, convex part .58mm

NO	END POSITION OF ARC /mm		CIRCLE PARAMETERS/mm			HEIGHT ERROR/μm
	R	Z	R	Z	RADIUS	
1	0.0000	-.0001				
2	.8600	.0338	.0000	10.9326	10.9326	.08
3	1.4500	.0971	.0370	10.4633	10.4621	.08
4	1.9300	.1745	.1289	9.7895	9.7822	.08
5	2.3300	.2588	.2802	8.9817	8.9605	.08
6	2.6700	.3464	.4932	8.0753	8.0296	.08
7	2.9600	.4348	.7717	7.0864	7.0024	.09
8	3.1900	.5155	1.1076	6.0653	5.9275	.08
9	3.3800	.5913	1.4947	5.0336	4.8258	.09
10	3.4200	.6084	1.7690	4.3872	4.1238	.02
11	3.7700	.7933	2.3688	3.0235	2.6338	-2.5
12	3.7800	.7998	7.4391	-5.0462	6.8967	.09
13	3.9900	.9256	7.0949	-4.4962	6.2479	.09
14	4.1900	1.0345	6.5421	-3.5309	5.1357	.10
15	4.3700	1.1220	6.1036	-2.6798	4.1784	.09
16	4.5300	1.1902	5.7661	-1.9396	3.3651	.09
17	4.6700	1.2412	5.5086	-1.2876	2.6642	.09
18	4.7900	1.2771	5.3142	-.7013	2.0467	.09
19	4.8800	1.2982	5.1772	-.1844	1.5121	.08
20	4.9500	1.3100	5.0820	.2907	1.0278	.10
21	5.0235	1.3149	5.0235	.7349	.5799	.10

Table 3.1 shows a set of 20 arcs which fits the Sottini, Russo and Righini exact profile within ±0.1μm height except near the inner edge-rounding boundary (where the error reaches 2.5μm and the local radius of curvature is 2.63mm over a small radial range of 10μm) and near the edge of the lens (where the error reaches 0.5μm and the local radius of curvature is 0.58mm over a radial range of 75μm). This set of arcs was used to programme the CNC machines as described in Chapters 5 and 6.

2.4.3 Profile tolerances related to spectrum analyser performance

It is important to estimate whether the errors in profile introduced by the bridging and arc-fitting routine lead to any significant deterioration in lens performance compared with the exact-profile lens. Various authors have published estimates of the effects of lens profile errors.

Chen and Ramer [98] concluded that an error of 1% (or 8μm) in overall lens depth could be tolerated without noticing any loss of diffraction limited performance for a f/1.5 lens of 10mm diameter, provided that a little less than the full aperture is used, and that the image is measured at the focus - which may not be at the original design position for a perfect lens profile. Betts et al[103] draw a similar conclusion, and comment that the error must be less than about 1μm if the lens may only be used at the focus position of the ideal profile.

Sottini, Russo and Righini [84] published an empirical approximation for the change Δz_o in overall lens depth z_o which could be tolerated without exceeding a given image broadening D due to defocusing. The expression is

$$\Delta z_o = \frac{z_o\,(\lambda.F + 2dD)}{1.9\,(2d^2 - \lambda.F - 2dD)} \qquad \text{.....2.22}$$

where λ is the wavelength of light in the waveguide, F the lens focal length and d the radius of the edge-rounding circle, assuming that the aperture of the lens that is

used extends to that radius. For the main lens design reported in this thesis, with wavelength in the waveguide 0.38μm, F = 18.5mm, d = 3.7mm, and z_o = 1.315mm the following estimates arise:

TABLE 4: SOTTINI, RUSSO AND RIGHINI RULE-OF-THUMB APPROXIMATION FOR TOLERABLE LENS DEPTH ERRORS

DEFOCUSING WIDTH μm	LENS DEPTH ERROR μm
0.25	0.2
0.5	0.3
2.5	0.6
5.0	1.1
7.5	1.6
17.0	3.4

From this table it may be estimated that since the lens has a diffraction image width of about 2.5μm a depth error of over 1μm may be tolerated before defocusing increases the image width to fill a detector element of 8μm width.

All of the above estimates assume that the errors take the form of changes of the whole profile in proportion to either the height, the radius or both. Errors in fabricating lenses in practice could perhaps take these forms, but there could be other types of systematic error as well as random errors. The arc-fitting errors certainly do not have the form of proportional errors. In Chapters 5 and 7 it is shown that errors measured in fabricated lens profiles could be greatest at the inner edge-rounding boundary.

Figure 2.14 shows the results of ray-tracing for an aperture of 6mm for the exact Sottini, Russo and Righini profile lens and for the bridged-over lens defined by the set of arcs given in table 3. The exact-profile lens has the expected zero image width at the planned focal length 18.5mm. The bridged-profile lens has a spotwidth of about 1.4μm at about 3μm shorter focal length. The diffraction-

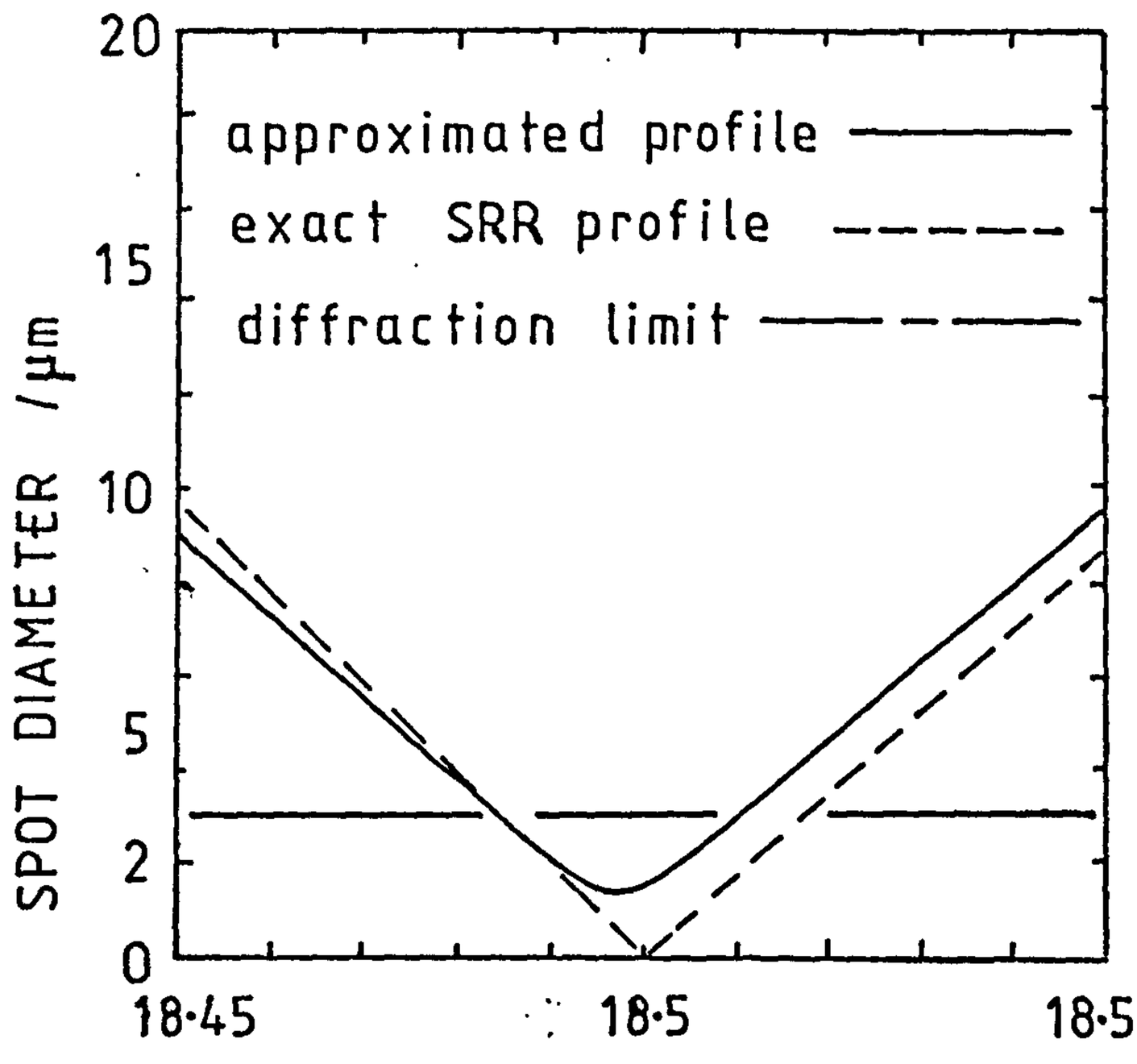

Figure 2.14
Ray-traced spot-size around the position of the designed focus of a circular-arc-approximated geodesic lens profile, compared with the perfect SRR profile and the diffraction limit.

limited spotwidth for 6mm aperture is about 3 μm for wavelength 0.85 μm in air. The total image width of the bridged-profile lens, adding together the diffraction and the profile-error contributions, is still much less than the 8μm detector element width. Ray tracing calculations therefore indicate that deviation from the perfectly focusing profile by the amount due to bridging and arc fitting would not seriously degrade the image size.

Wave theory analysis, which includes both the effect of diffraction and of geometrical aberrations, has been carried out on several geodesic lens designs using a beam propagation method (BPM) [27,54,61]. An analysis of the effect of profile errors [27] indicates that small periodic fluctuations of the profile can considerably enlarge the focused spotwidth if the combination of frequency and amplitude of the profile errors result in a significant lengthening of the path traversed by a beam or ray. Such periodic fluctuation errors may be important in practical lenses fabricated with the use of tools which are smaller than the lens diameter (Chapters 5,6, and 7). In an example from reference 27, sinusoidal variations in height of only 10nm amplitude and 125μm period produce double the spotwidth obtained for a perfect Sottini, Russo and Righini-profile lens.

2.5 CONCLUSIONS

The Sottini, Russo Righini lens-design method is conveniently simple to use, but lens profiles include regions with zero radius of curvature. Ray traces show that bridging-over the highly-curved regions by arc-fitting can modify the profile by a sufficiently small amount that the modified lenses should focus with spotwidths which are tolerable in the IOSA. However since this method of modifying the exact profiles does not ensure continuity of the second (and higher) differentials of the profile function, nor guarantees continuity of slope at the two bridging points, then potential loss of waveguided light is not completely avoided.

CHAPTER 3: REVIEW OF LITHIUM NIOBATE COMPONENT FORMATION PROCESSES AND METHODS USED FOR PLANE SUBSTRATE PRODUCTION.

3.1 INTRODUCTION

Apart from the present requirement for geodesic lenses, polished lithium niobate surfaces are needed in other applications of integrated optics and also more extensively for surface acoustic wave devices and for bulk acousto-optic and electro-optic systems.

The combination of shape, dimensional accuracy and surface smoothness required for the IOSA substrate and its lenses is probably more critical than for any other integrated optics application. Processes likely to achieve these demands have therefore been reviewed thoroughly, and are presented in this chapter.

Lithium niobate substrates, in the form of thin plane parallel components (e.g. surface acoustic wave wafers) or rods (e.g. ultrasonic transducers) are prepared routinely in industry by variations of processes used for general optical and crystalline materials [124,125,126]. Aspheric surfaces are also being produced for general optical applications, using many different processes. The discussion will therefore outline all of these processes, and indicate where particular variations are desirable or essential for $LiNbO_3$. The method to be described was used in the present work to prepare a large number of substrates (at least 25) for lens formation and other evaluations.

3.2 ASPHERICAL SURFACES

The use of aspherical rather than spherical surfaces on lenses and mirrors in bulk (i.e. not integrated) optics offers several advantages:

-eliminating image distortions, especially in wide angle systems;

-reducing the number of components for a given system performance level, thus reducing absorption, scatter and physical bulk.

The most common applications of aspherical surface are projector condensers (which are usually of such low quality that they may be moulded inexpensively), and components with conic section profiles such as parabolic astronomical mirrors (which may be formed and tested by relatively simple geometric means)[126,127,128]. In general, aspherical surfaces are so much more expensive and time-consuming to produce than spherical surfaces that the advantages are seldom strong enough to justify their use. The few applications where more complex aspherical surfaces are felt to be justified are in Schmidt corrector plates, and in military laser and thermal imaging systems, where expense is of less importance than performance. Only for unusual mirror shapes and for geodesic lenses are aspherical surfaces absolutely essential to successful system operation.

3.3 CUTTING LITHIUM NIOBATE CRYSTALS

Single crystal boule sections are oriented, then sawn into parts just bigger than the required component, commonly using diamond-coated peripheral-wheel tools on conventional machines such as horizontal grinders. Sometimes specially built saws are used such as the wire saw [126] which is claimed to be the most gentle method available for fragile materials, leaving the least depth of sub-surface damage. The wire saw passes wire between

spools, or in a continuous loop across the material being cut. The wire is either coated with diamond particles, or used with a free abrasive slurry. A commercial wire saw was purchased (South Bay Technology Inc model 850) and used in the present work to cut $LiNbO_3$ blocks. The 0.25mm diameter continuous-loop wire took about an hour to cut through 10mm depth of a crystal section 25mm wide, and tended to wear out and break before much more depth of cut could be achieved. Its use was therefore not continued.

Fynn [129] developed an annular saw specifically for cutting electro-optic crystals. This saw cut along the **inside** diameter. The thin blade was coated with 200 grit diamond, and was rotated at a speed of 200 rpm. An annular saw blade may be held more accurately in its plane of rotation than the blade of a (less expensive) peripheral saw of the same thickness and cutting width. The stability of an annular saw blade results in a narrower width of cut, a smoother surface finish, and perhaps less subsurface damage depth than can be obtained with a peripheral saw. All of the substrates used in the present work were cut from boules by annular saws (at Barr & Stroud Ltd.) then sliced by a thin peripheral saw (at the Electronics and Electrical Engineering Department of Glasgow University).

3.4 MACHINES FOR GENERATING AND POLISHING COMPONENTS

Machines for producing optical components of plane, prismatic and spherical shapes have been developed in several forms, and many methods of producing aspherical optical surfaces have been proposèd [130] since the early interests of Wren and Descartes. The methods may be broadly classified as

-removing surplus material;

-moulding or pressing;

-adding extra material.

Although processes of the third class, such as molecular beam epitaxy, could perhaps be eventually useful for thin waveguide lenses on single-crystal substrates, only the first class were considered appropriate to the relatively great depth of the lenses of the present study.

Ion-beam etching has been used to generate aspheres by material removal [131,132] and can also produce a polished surface, but erosion rates tend to be very slow and are only appropriate for removing a few micrometres. This technique was therefore not considered for the present work. The review only considered methods which involved material removal, whether by cutting or by abrading.

A scheme devised by the author to classify the various machine principles is illustrated with examples in Figure 3.1. Machines are grouped according to two attributes. The horizontal axis represents the area of the tool cutting surface relative to the area of the substrate (or substrates if more than one are processed simultaneously). The vertical axis represents the proportion of the cutting tool area which is always in contact with the substrate(s).

The top right-hand corner of the figure illustrates point contact machines, where the tool is of small area relative to the aspherical surface. Precision depends on the tool wear and the accuracy of its path over the surface, which is generally controlled by mechanisms such as cams [133,134,135] or by numerically-controlled motor driven cross-slides. Tool wear is potentially very rapid.

The use of turning with a single-point polished diamond cutting tool for generating (and to a large extent also producing an almost-polished surface) lithium niobate surfaces was first reported by Mergerian [105]. This technique has been well-established for generating plane and curved polished optical surfaces on the softer metals (particularly aluminium and copper) and plastics (such as acrylics for contact lenses), [136-147], but has not been

Area of cutting tool surface relative to substrate(s) area

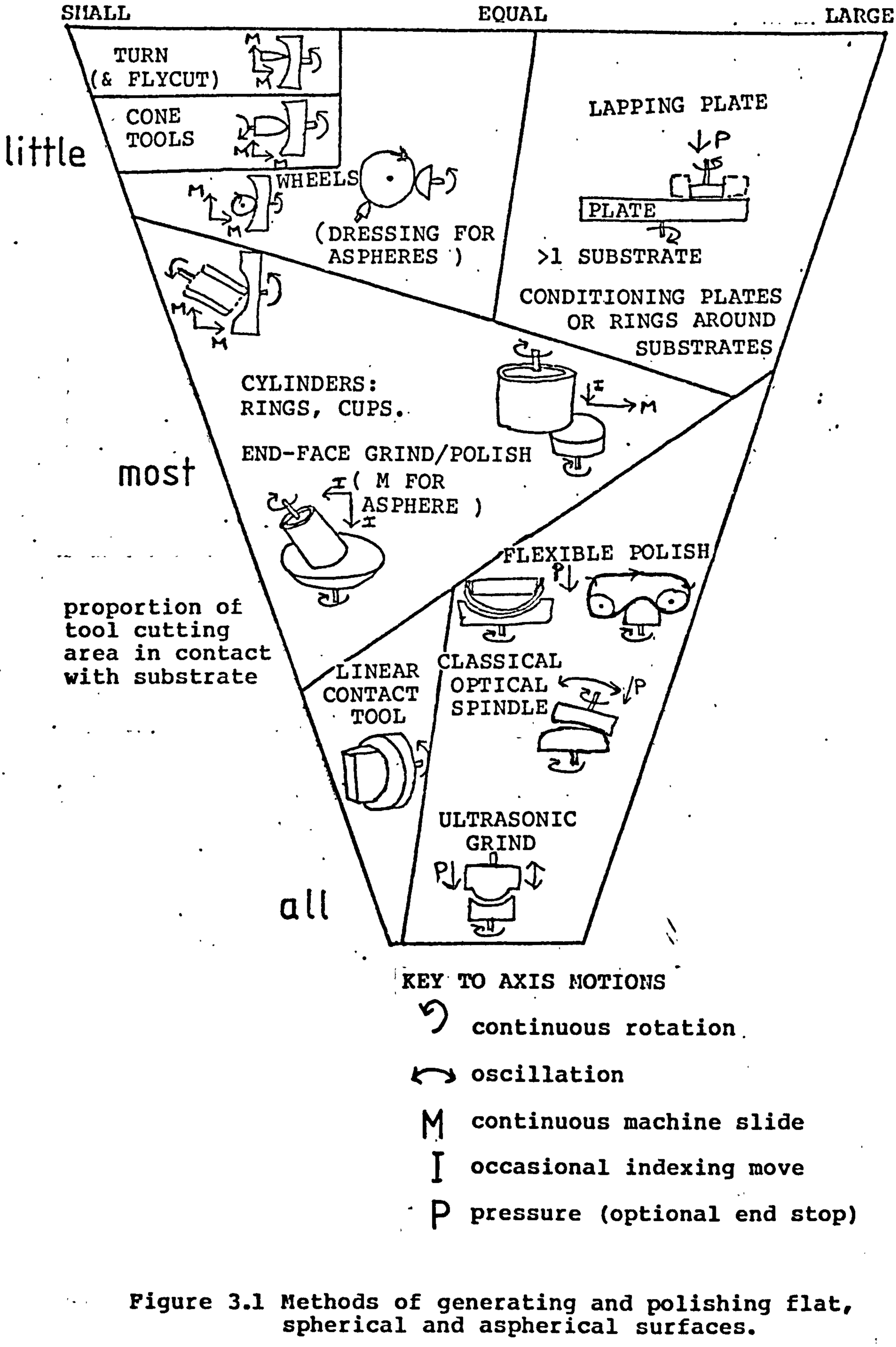

Figure 3.1 Methods of generating and polishing flat, spherical and aspherical surfaces.

successful in general on harder or more brittle materials [148]. More recently it has become a practical technique for single-crystal and polycrystalline materials such as germanium which are used at infrared wavelengths (e.g. 10μm) where the roughness and form errors produce smaller diffraction and scattering effects than for visible wavelengths. The techniques are discussed more fully in Chapter 5.

Rotating conical-shaped tools which have been dressed to a sharp point (i.e. very small radius of curvature at the tip) may also be used on the same or similar machines to those used for diamond-turning. Using suitable materials, tools of this shape may be used for grinding or for polishing (see Chapter 6).

Several types of grinding machines (illustrated towards the left-hand side of Figure 3.1) employ cutting tool contact along a line and most of these machines use tools of hollow cylindrical form with abrasive action at a circular end (these are commonly called ring or cup tools). They may be used with the tool in contact only at a point (in a similar way to the machines already discussed above), or over most or all of their abrasive ends. The latter type of contact is very commonly used to generate plane or spherical optical surfaces [124,149], but the same machines may be adjusted to produce a range of aspherical geometries [150,151], although not those needed for geodesic lenses. A machine employing a linear tool of a non-circular profile (see the bottom left hand side of Figure 3.1) has been used to grind the corresponding aspherical profile by total contact with a substrate of the same diameter [128].

A further type of machining employs contact over the whole surface of the substrate, e.g. using continuously dressed grinding tools of opposite profile to the surface [130,152]. This process is usually limited to about 10μm precision and to convex shaped substrates.

The sketch at the top right of Figure 3.1 illustrates the principles of the Draper type of machining process [124,126,153]. A lapping plate rotates, and a substrate is held in contact by the pressure of gravity so that friction causes it also to rotate. The substrate is made to sweep across a portion of the lapping plate by an independently oscillating arm. The shape of the lap and substrate surface may be controlled by adjusting the relative wear of each part of both substrate and lap. This depends to a first approximation on the average position, and the amount of sweep of the substrate. A conditioning ring is often placed around the substrate(s) to increase the wear of the lap, accelerating changes of shape. This kind of machine was used to prepare the plane parallel lithium niobate substrates for the present work. The angular and thickness accuracy of this process depends very much on holding the parts in special tools [154,155] which combine a conditioning ring, precise substrate location, and indication of the amount of erosion. In a further elaboration of this type of machining process, substrates are driven by geared carriers in a planetary motion between two lapping plates. This method quickly produces a batch of several parallel substrates of constant thickness, and is particularly useful when both sides require identical processing.

The final class of machining methods involves most or all of the cutting area of the tool being in contact with most or all of the substrate(s). Examples are sketched in the bottom right hand of Figure 3.1. These include ultrasonic impact grinding (the subject of Chapter 4), various flexible polishers (to be discussed in detail in Chapter 6) and the classic optical spindle, which performs a similar (Draper) motion to the lapping plates discussed above. This is normally used to produce plane or spherical surfaces: only the sphere and the plane coincide without any change in their positions on the surfaces. The oscillating motion of lapping, which is essential for uniform material removal and surface finish, cannot

generally be utilised for forming aspherical surfaces.

For small deviations from spherical, one can produce spherical surfaces on normal optical polishing spindle machines, then make the corrections required by the same methods as routinely used for making corrections towards spherical, e.g. by local figuring using cut-away laps [126]. The geodesic lenses required for the present work depart by far too much from spherical for this process to be employed.

There are certain types of surface of revolution which may be polished by Draper-type machines using very flexible laps, since they possess the property of mapping themselves (from substrate surface to lap) at all positions with constant Gaussian curvature [128]. The lengths of all lines drawn along the surface, and the angles between them are maintained. Thus a flexible lapping tool remains in full contact with the surface, without fractures or folds. However none of the nine types of surfaces of constant Gaussian curvature appear to approximate to the form required of geodesic lenses.

Figure 3.2 summarises the possible combinations of these machining methods which seem most appropriate to making $LiNbO_3$ geodesic lenses of the size and profiles required for the IOSA. Lenses may be generated by a surface contact method using an ultrasonically vibrated tool and loose abrasive, the tool being generated by other means such as the linear contact method. A large area polishing pad may be made flexible to fit into the concave profile. A point contact method may be used, with a rotating grinding or polishing tool on a multi-axis computer-controlled machine such as a jig grinder. Single point turning with a diamond tool may be used on a computer-controlled lathe-type machine. These will be discussed in great detail in later sections.

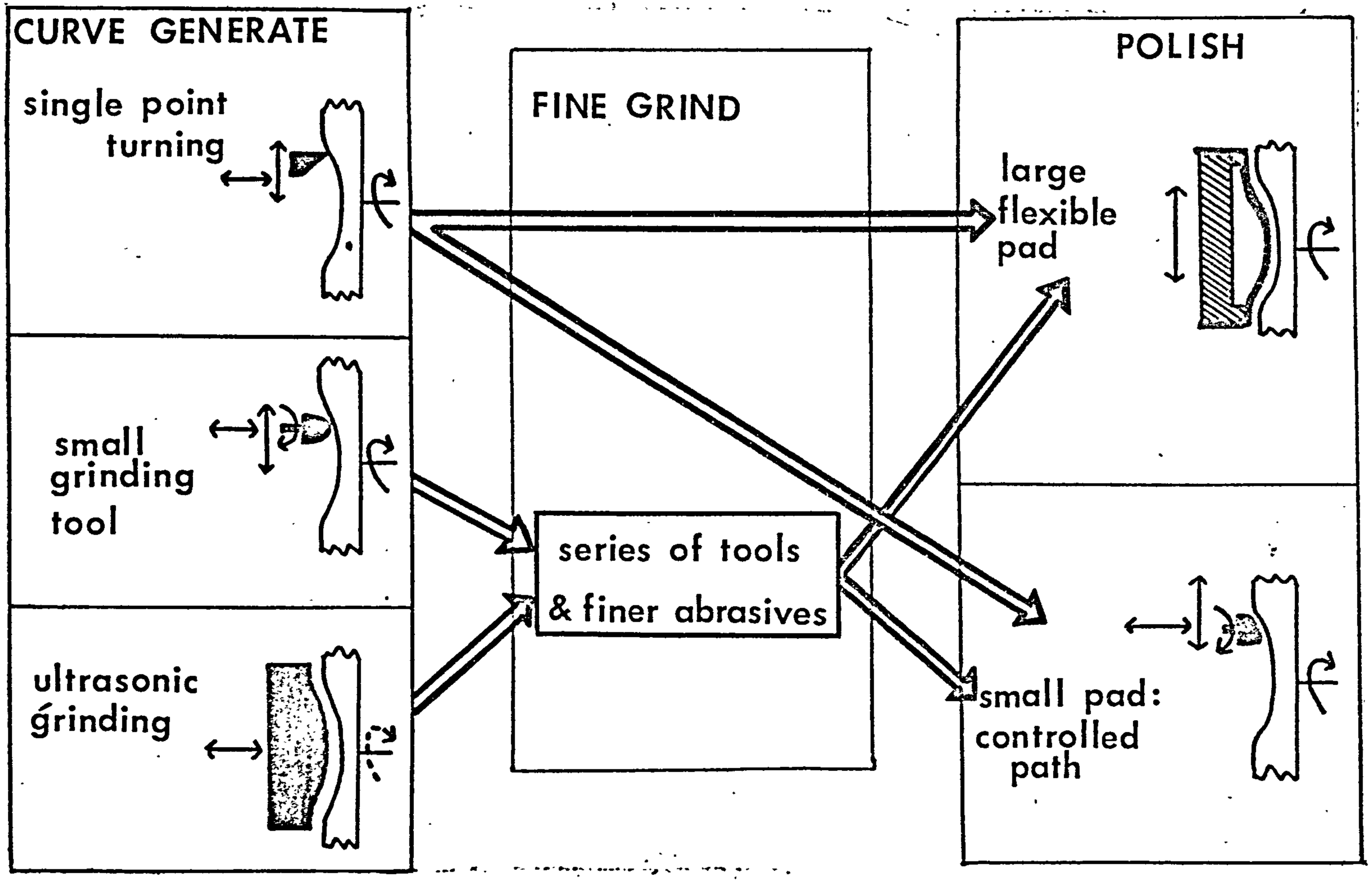

FIG. 3.2 Methods of fabricating aspheric depressions in $LiNbO_3$

3.5 GRINDING AND LAPPING

Apart from the special case of single-point diamond turning, the bulk of the material to be removed in forming any component is ground away by using small abrasive particles. The mechanism of material removal, for relatively brittle materials such as lithium niobate, is basically that of locally deforming the surface beyond the elastic limit until fractures occur [124,135]. Subsequent passes of the abrasive particles cause further fractures and/or push away broken fragments, which are washed away by the lubricating/cooling fluid. Surfaces are ground to a progressively smoother finish, using a series of abrasives of decreasing size to produce a progressively smoother surface and to remove most of the subsurface work damage produced by the previous stages [156].

Abrasive particles may be "free", i.e. not restrained from being pushed or rolled by the tool and substrates, or "quasi-free", i.e. partly restrained by being pressed into a soft lap material during use. The former case includes laps of cast iron and glass, and the latter case laps of tin and solder. The latter tend to be used for reasons of cost (with very expensive abrasives such as diamond particles) as well as to permit rapid conditioning of the shape of the lap.

Plane and spherical components may be made satisfactorily (and with low tooling costs) using free abrasive grinding methods. However, more rapid grinding may be achieved by using abrasives bonded rigidly into a matrix of a softer material. For high accuracy and fine surface finish these tools are usually metal formers with diamond particles coated in a thin surface layer. Wear of diamond-coated tools is usually slight compared with that of substrates (e.g. better than 2000:1 [149,157]). Tools coated with alumina (Al_2O_3) or carborundum (SiC) may be used, but being less hard they generally wear faster, (and are reputed to leave more surface damage [158]. Diamond-

coated tools require accurate and reproducible machine operation, and are costly to manufacture. They are particularly useful with the CNC grinding machines suitable for generating aspheric profiles.

Diamond grinding tools are made from a preformed metal shape, coated with diamond particles bonded in a metal or an organic layer. Tools of the latter type tend to wear more rapidly, but may be made thicker and may be redressed many times. The diamond grains, depending on their shapes and the depth of penetration, can shear the surface being worked, deform it plastically or cut it [157]. With free-abrasive grinding, the surface roughness and cutting speed depend mainly on particle size. For bonded diamond tools, the nature of the binder (and the concentration of diamond particles in it) affect the amount and wear of particles protruding, hence the surface texture and cutting speed [157]. For example, the total depth of surface damage produced by a metal-bonded diamond tool of 600 mesh (i.e. average particle size about 30μm) on glass was about 3μm, which was the same as produced by quasi-free-abrasive grinding with diamond particles of average size 15μm [156].

Noda [159] discussed the free-abrasive grinding of lithium niobate, relating particle size and grinding pressure to the erosion rate and surface roughness, and reported anisotropy effects between opposite faces of substrates. The Z-face is softer (Knoop hardness 380), has faster stock removal, and rougher surface finish than a Y- or X-face. Noda found that ground $LiNbO_3$ surfaces were smoother than glass of a comparable hardness, because cracks are able to propagate in up to three directions along cleavage planes, rather than in the single direction due to tensile stress in glass.

A wide variety of grinding tools and series of abrasive particles has been recorded in the literature on preparing lithium niobate surfaces. The techniques have probably been selected by intuition rather than by controlled

experiments on all the combinations of variables. Different emphases have been placed on the three main criteria which apply when preparing a surface - the surface microstructure (roughness and subsurface damage), the macrostructure (overall surface form) and the rate of material removal.

Schumacher [30] used 14.5µm alumina on a soft glass lap to remove about 0.1mm of $LiNbO_3$ in one hour (the last 20 min at zero pressure), then 9.5µm powder to remove about 0.05mm, taking about one hour with zero and then negative pressure. This process was used to smooth ends of substrates for end-fire coupling to a uniform appearance under 625x magnification, prior to polishing. Fynn and Powell [129] reported using cast iron laps with 600 grit carborundum, followed by solder, tin or indium laps with 3µm diamond paste, the pressure being 100g cm^{-1}. Esdaile[36] ground $LiNbO_3$ surfaces on a brass lap with alumina powders in the grit order 240, 400, 600 and 800 before polishing with Syton colloidal silica. He found that if the surface was lapped with 1µm diamond paste (on a solder lap) after the alumina stage, some subsurface damage existed after polishing. Although the surface appeared to be free of scratches, chemical etching with HF/HNO_3 (1:2 @ 100°C) revealed linear defects.

The author believes that the choice of abrasives should be governed by the following considerations. A coarse abrasive should be used first, to remove geometrical irregularities such as wedge, bow or saw steps in the sawn wafer. For fast material removal, the abrasive particles should be as large and harsh as possible. For economy of material, the size and type of abrasive should be limited so that it does not cause subsurface damage to penetrate below the lowest level of damaged caused during cutting. Damage penetration by annular sawing can be as deep as 0.1mm for single-crystal materials [129,160], although no data could be found for $LiNbO_3$. Using data obtained from reference 159, damage penetration depth for a typical

alumina abrasive is approximately 0.03 $P^{1.5}$, where P is the average particle diameter, and the size unit is μm. Thus the particle size of the first abrasive should not exceed about 220μm, i.e. about 80 grit. For the present work, where speed was not of primary importance, the author used a safety factor of ten, i.e. 800 grit alumina powder (average particle size about 9μm) on a brass roughing lap. Grinding was stopped when the surface became of apparently uniform roughness (about 0.5μm Ra) with no scratches.

The total time of grinding and smoothing would be least if a series of abrasive particle sizes were used such that each one was just smaller than its predecessor, and removed a depth of material such that its own damage penetration just reached the lowest level of damage in the crystal (i.e. that due to the saw). However the time taken to clean off all traces of abrasive before moving on to the next stage must also be included in any calculation of an optimum series of abrasive sizes. The author estimates that with alumina lapping of $LiNbO_3$ there is no time-saving advantage at all in using any more than a single stage of abrasive.

Since the most suitable method of polishing $LiNbO_3$ requires a flexible lap, which tends to lead to a worsening of the surface flatness with the amount of material removed (see the section 3.6.2), it was important to restrict the amount of polishing to that corresponding to the largest degree of non-flatness that could be tolerated. It was found that this could be achieved by the last lapping stage using 5μm diamond paste on a solder lap, until the surface was of uniform visible roughness. The flat-lapped surface was of low enough damage penetration and roughness (about 20nm Ra) that it could be polished by the method discussed below without departing from flatness by more than was specified for IOSA lens fabrication (see Chapter 5).

It did not seem likely that surface quality could be

improved nor processing time saved by using any more stages than (i) 800 grit alumina (about 9µm particle size), (ii) 5µm diamond then (iii) polishing with Syton.

3.6. POLISHING

3.6.1 Surface finish.

Polishing is carried out on machines similar to or identical to those used for smoothing, but with different materials for the tool surfaces and 'abrasives'. Although material is usually removed by the same process as in lapping, other mechanisms can also contribute, or even dominate. In the case of polishing metals and glasses some surface melting occurs, or folding over of the peaks of the lapped surface leaving voids beneath. These mechanisms are of little value in preparing single-crystal surfaces with no damage below the surface. However a mechanism that can be of significant usefulness in polishing single-crystal materials is that of chemically etching.

A polishing abrasive must generally be harder, and of higher melting point than the surface of the substrate [124]. Of the hardest-known materials, diamond powders are frequently used, while carbides and nitrides are seldom used in fine enough sizes for polishing. Oxides such as ceria, alumina and silica are the most common polishing abrasives, particularly for glasses, where there is evidence of some significant chemical action involving hydrolysation of the abrasive as well as the substrate[124]. Friability and particle size (eg in the 0.005 to 5µm diameter range) are often important. The common oxide polishing materials have been reported as generally unsuccessful with $LiNbO_3$. Esdaile [36] found orange peel or relief polishing when using 0.05µm alumina (Linde B) or ceria on a microcloth lap. Other workers have reported similar problems: 'flaking' with Linde A (0.3µm),

'ineffective' with Linde B, 'galling' with ceria [64].

Little information is available on the surface finish required for the $LiNbO_3$ IOSA. There is some literature on the surface quality required for surface acoustic waves, but it is expected that the requirements of optical waveguides are more critical. Slobodnik [23] concluded that scratches less than 0.1μm wide caused no substantial performance degradation of 1.9GHz waves, and that SAW attenuation was proportional to surface roughness: 200nm roughness caused about a 50% increase in the attenuation of SAW's at 1.9 GHz. Williamson [161] commented that Slobodnik's results could have been due to scattering at the surface or by absorption in subsurface damage layers. He suggested that surface irregularities and damage layers of a few nanometres size would explain the observed SAW dispersions of 10^{-3} over a bandwidth of 1GHz, which would be unacceptable for high time-bandwidth product devices such as reflective array couplers [162]. He concluded that the polishing processes that had been used for these substrates (whose details were unknown to Williamson, but described as "standard") were unreliable and only just adequate, and recommended further work using processes such as bowl-feed polishing.

It seems from the above considerations that as well as specifying the surface roughness, the polishing process itself must be chosen carefully.

Diamond pastes have been reported as satisfactory [30] for polishing lithium niobate: a series of 1, 0.5, and 0.25μm diamond powders on a pitch lap with an embedded nylon fibre cloth was used for polishing the edges of $LiNbO_3$ substrates for end-fire coupling. For this particular application the use of such a close series of particle sizes, together with such a soft lap material was perhaps appropriate to avoiding edge chipping, but following this procedure would be unnecessarily slow for polishing larger area surfaces.

Glass and fused silica have been polished to a better finish than obtained with conventional free-flow fresh abrasive slurry feed by "bowl feed" or "submerged polishing" [158]. The polishing compound is continuously reduced in physical size (and embedded in the lap if soft). In a similar way a pitch lap may be charged with compound, worked against a dummy workpiece (or used at an earlier stage with the real one), then washed throughly and used submerged in water. The embedded and worn particles give a fine finish with good surface form, but are small in number and in size, and the polishing rate becomes very slow.

Although fine polishing agents can remove very small pits and scratches, they cannot generally remove all subsurface damage propagated by the previous lapping stages even if used in a very carefully planned series of decreasingly fine abrasives taken to precise depths. Such processes are difficult to arrange and slow to perform. Attempting to continue fine polishing into the subsurface damage layer is usually unsuccessful. The abrasive material has insufficient abrasive power to cut below the surface roughness, and instead often produces an unwanted waviness called "orange peel" after its appearance.

However, for many single-crystal materials it has been found possible to arrange a significant chemical action. In chemical-mechanical polishing [129,158,163-165], dilute etchants such as NaOH, NaOCl, H_2O_2, K_2FCN_6, and Br are added to the polishing slurry to assist in the removal of the subsurface damage layer. The role of the abrasive is then more that of smoothly wiping away loose reaction products. In the case of some III-V semiconductor compounds, a smooth surface may be obtained by etching alone [164]. For polishing silicon wafers an alkali silica organo-aquasol was introduced [166] under the trademark Syton [167] for polishing silicon wafers, and has subsequently been found successful with other single-crystal materials [158,168] including $LiNbO_3$ [36,129,169], and

most glasses which are readily oxidised or hydrolysed.

Alkali silica sols can have a concentration up to 50% by volume of silica, and particle size in the range 1nm to 5μm. A typical sol, Syton W30, is a milky white liquid of average particle size 125nm, pH 10.2, specific gravity 1.2, viscosity 2.5 centipoise, and 30% silica by weight [167]. McIntosh [168] suggested that small particle sizes (1-4nm) polish silicon faster than larger sizes, probably due to the larger surface area available at maximum concentration. In order to obtain very flat (e.g. 1/34 wavelength) as well as very smooth (0.6nm rms) silicon surfaces, he used a bowl-fed pitch lap with a conditioning plate. The pitch was pre-charged with a conventional abrasive (composition not specified) to retard its dissolution in the silica sol.

Submerged polishing helps to avoid the coagulation and hard setting of silica sols which are accelerated if the slurry is drying out. Some workers [129] regularly scrape the lap with a razor blade to remove the hardening skin, but this may free agglomerates of particles which despite careful washing may remain in the contact region, and therefore cause scratching.

The surface finish of $LiNbO_3$ substrates polished on a polyurethane lap with Syton W30 was assessed by several methods (see Chapter 7, section 4) as better than 1nm rms. Another sample was reported as having only 0.1-0.3 nm rms roughness [170]. These values are as smooth as the very best so far published, which are for fused silica [171,172].

Colleagues in the Department of Electronics and Electrical Engineering appear to have been reasonably satisfied with waveguides formed on plane substrates polished as described below when polishing continued until no defects were visible under 100x magnification.

3.6.2 Laps and surface flatness

The material on the surface of the lapping tool or plate is required to hold the abrasive and to remain flat during polishing. Materials commonly used are pile or woven fabrics, plastics (with holes, grooves or other structure), and other organic solids such as wax, lacquer and pitch. In order to limit the wear rate of the tool, the last three materials are often loaded with a filler material or are covered with a fabric outer layer which becomes bonded into the material. Abrasive may be either dispersed throughout the bulk of the polisher material during its formation, or held by embedding into the soft tool surface, or constrained by a rough surface texture.

Of the various materials mentioned above, plastic laps are usually too stiff and cloth laps too flexible to be conditioned flat by the polishing tool. Wax and pitch laps can be used to polish samples to the highest attainable level of flatness since they may be readily conditioned to shape during polishing. However, the preparation and maintenance of pitch laps require more time and skill than plastic and cloth laps, and polishing with Syton on pitch in the Electronics and Electrical Engineering Department at Glasgow University has been found to give a scattering appearance ("milky") to $LiNbO_3$ surfaces.

Plastic laps such as those made with polyurethane sheet have been used with Syton to form $LiNbO_3$ substrates [129]. Flatness errors of 5μm over 100mm diameter have been reported to be possible [168]. During routine interferometric testing the author found errors for smaller sizes to be consistent with the shape of the lapping plate being spherical, that is the errors were proportional to the square of the component diameter [129]. The author found that it was only just possible to prepare substrates to the flatness required for the IOSA (see Chapter 5) using these relatively stiff plastic laps. For such flatness the author found it necessary to turn or grind the base plate of the lap within about 2μm flatness

over its 200mm diameter (a convex error being preferred), attach the plastic lap by a spray adhesive, allow to set under a heavy flat plate, then true the plastic surface by diamond grinding at the relatively high linear speed of about $5ms^{-1}$.

Laps used for submerged polishing usually have edge lips to contain the slurry. This precludes sweeping the substrate jig over the edge of the lap (as is commonly required to achieve flatness) unless the diameter of the plastic sheet is cut to be significantly smaller than that of the lap plate. Whatever compromise is used, the result may be that jigs are too large relative to the lap and have insufficient sweep over it. These limitations tend to produce a convex surface on the substrate, whatever shape is the lap. It is believed that by using an adjustable, flexible lap base-plate to control the overall curvature, the tendency towards substrates being convex can be prevented.

3.6.3 Rate of material removal in polishing.

The depth of material removed by lapping and polishing machines tends to follow an empirical law first proposed by Preston [173]. This law states that the removal rate dh(r)/dt at a radial position r is proportional to the product of the local pressure P(r) and relative lapping speed ds(r)/dt, i.e.

$$\frac{dh(r)}{dt} = k.\ P(r).\ \frac{ds(r)}{dt}$$

This law has more recently been derived from a model of the polishing of metals (and confirmed to a limited extent experimentally with some particular metals) where the constant k is the inverse of the elasticity of the substrate [174].

Contact between tool and substrate is usually maintained by a weight, so that local pressure is constant over the component radius, except at the edges where

overlapping may not always be complete. Local pressure is also a function of microstructure (thus also of time) since as the surface becomes less rough (and if bowl-feeding, as the particles become smaller by wear) the contact area increases.

Lapping speed depends on radial position and on the motions controlled or allowed by the machine. When polishing with a freely rotating jig, the relative speed is often difficult to predict, since the rotation depends on the distribution of pressure and friction over the contact area, and this varies with the lap shape and the changing substrate figure. Fig 3.3 (taken from Fynn and Powell [129]) shows the removal rate as a function of time for $LiNbO_3$ on polyurethane with Syton. The removal rate is clearly not constant with time, the decrease being probably explained by the changes in contact area and local pressure. Making simple assumptions about the relative speeds on Fynn's lapping machine, his data can be used to estimate the constant in Preston's expression for this important combination of materials. For polishing times of 12 hours or more it is about $0.5 \times 10^{-12} m^2/kg$. In the Electronic and Electrical Engineering Department of Glasgow University, plane components are usually polished on Logitech PM2 machines at pressures of about 50 kPa at average relative speeds of about $0.3 ms^{-1}$ to remove about 6μm per hour. This data gives a value for Preston's constant of $6.10^{-6}/3600/50.10^3/0.3$ i.e. 0.1×10^{-12}, and therefore fairly close to the value estimated from Fynn's results.

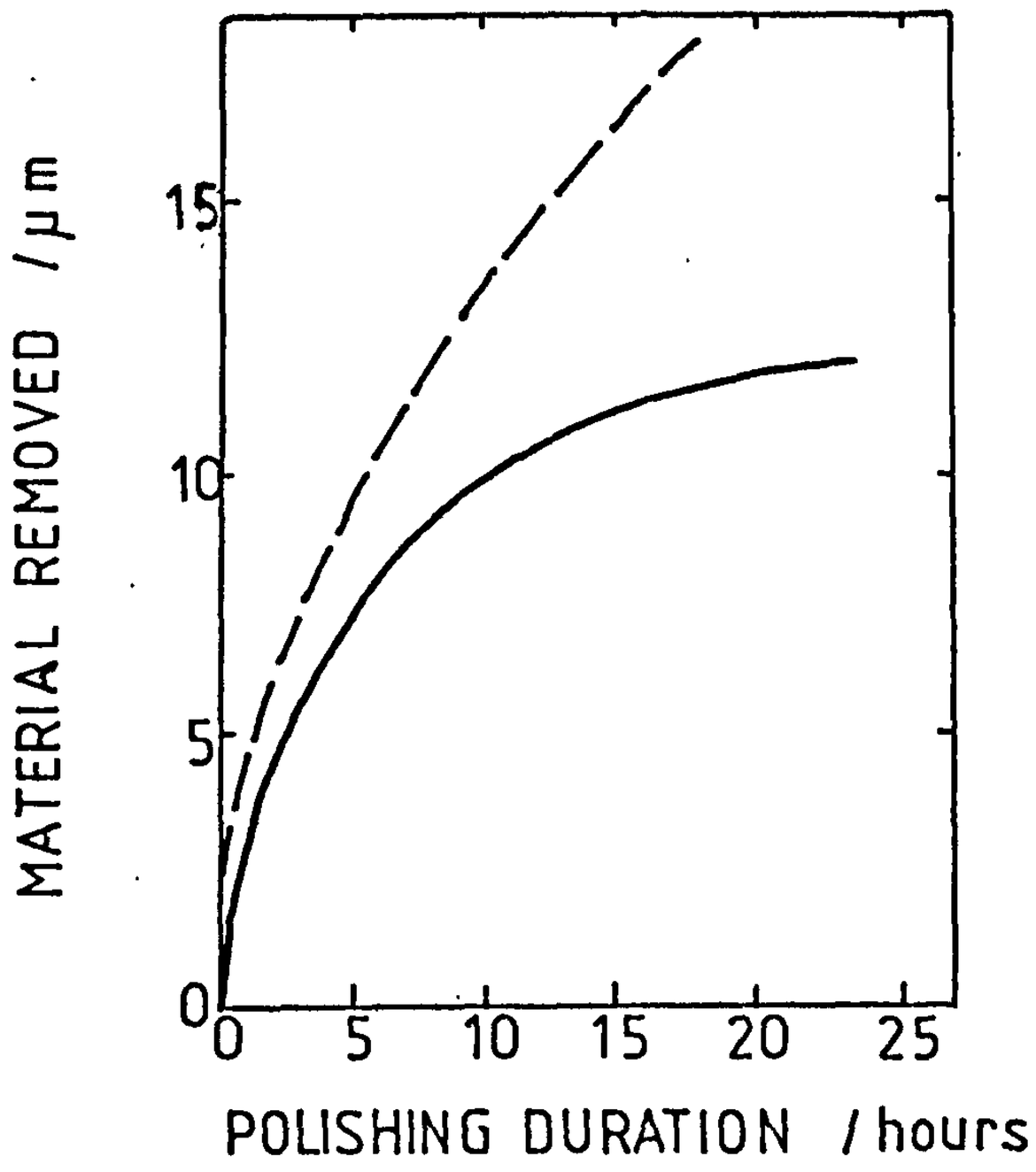

Figure 3.3
Graph of removal rate against time for alkaline silica sol on a polyurethane foam pad rotating at 60 rev/min at pressures of 100 g/cm^2 (full line) and 200 g/cm^2 (dashed line).

3.7 PREPARATION OF PLANE PARALLEL SUBSTRATES FOR THE PRESENT WORK

Two boules of lithium niobate were obtained from Barr & Stroud Ltd. They were grown along the Y-axis, and were of approximately 65mm diameter. The two Z-faces had been ground and polished to leave 30mm thickness, and inspected by measuring the extinction ratio between crossed and uncrossed polarisers. The boules chosen had ratios greater than 100, which indicated that they were of the highest quality currently available. The boules were X-ray oriented within 3 minute of arc to the Y-faces and mounted for cutting on annular saws within a tolerance of 0.5 degrees. The tapers on substrates from one of the boules were measured as being only between 17 sec and 2.4 min of arc. Fifteen substrates were obtained from a boule of length 51mm. These substrates were of average thickness 2.954mm with standard deviation 0.024mm. The sawn wafers were of sufficient area that two IOSA substrates could be cut from them at a later stage.

Various machines and mounting arrangements were used for preparing substrates. The most convenient and successful were as follows. One face of each substrate was lapped flat when held down by red dental wax in groups of six onto a steel block, using a slurry of 800 grit alumina powder in water, on a cast iron lap mounted on a Logitech PM2 lapping and polishing machine. Because of variations in the thickness of the wax bond, between 10µm and 76µm of material was removed. The surface roughness average (as measured on a Talystep 10) was about 550nm. The substrates were then demounted, reversed and held individually onto the vacuum chuck face of a Logitech PLJ2 lapping jig to remove 60µm of material (or more if the surface was not of uniform roughness). The lapping jig, its chuck face and the lapping plate were all conditioned to ensure substrate parallelism within about 4µm.

The substrates were next sliced with a peripheral diamond-blade saw into 55mm x 14mm rectangular IOSA substrates, and the corners and edges chamfered to reduce the chance of damage in subsequent processing.

Substrates were cleaned, remounted individually using red dental wax on Logitech PP5 polishing jigs, and lapped with 5µm diamond paste on solder laps, removing about 40µm of material. The surface finish became smooth enough (about 25nm Ra) to allow flatness to be assessed by observing Newton's rings between the substrate and a contacted optical flat under a monochromatic lamp. Roller arm positions were adjusted until the systems produced surfaces of regular curvature (i.e. spherical) within a flatness of 2µm over the longest dimension. The substrates were demounted, reversed and their other sides lapped in the same way. For this second side of the substrate, the jig chuck face was adjusted in angle so that an autocollimator indicating the angle between the rear (waxed) face of the substrate and the conditioning ring face of the polishing jig were within 10 sec arc parallelism. This side of the substrate was lapped with diamond paste until free of most scratches, flat within 2µm, and parallel to the rear face within 10 sec arc.

Without demounting, the substrate was then polished on a polyurethane lap submerged in a bowl of Syton W30. The material removal rate was about 6µm/hour, and the time on the machine was between about 8 hours and 20 hours. Polishing was stopped when the surface was clear of any defect visible under 100x magnification, the flatness was within 2µm (7 fringes of Helium-lamp light) and the parallelism better than 10 sec arc. Because the autocollimator and jig adjustment arrangements were at the limit of their accuracy the substrates were usually set and reset again many times before reaching the required parallelism. Only five out of the many substrates polished were within 10 sec arc: the remainder were tapered by up to 1.5 min arc, although a wedge angle of about 20 sec arc

was most common.

Before releasing a substrate from the polishing jig chuck face its surface was of an almost flat but spherical shape. After demounting, the polished surface was often found to no longer be of any regular form. The wax bond had apparently not held the rear face parallel to the chuck face in many cases, and the substrate was twisted. On demounting, the substrates could relax so that twists of up to 2μm magnitude were tranferred across to the polished face, and could be seen interferometrically. The use of more recently available commercial lapping and polishing jigs which are capable of more accurate bonding of the substrates would have allowed the tolerances on both flatness and parallelism to have been reached easily.

3.8 CONCLUSIONS

Plane, parallel lithium niobate components may be produced with the accuracy and surface finish required for the IOSA by the methods summarised in the previous section.

Aspherical depressions in the IOSA substrate may be generated by a variety of means: ultrasonic grinding, CNC jig-grinding and CNC diamond-turning seem particularly appropriate. It was not clear from the existing literature which of these three methods, if any, would produce a sufficiently accurate geodesic lens profile which could be subsequently polished to a satisfactory surface finish. Nor was it clear which would be the most economic, should more than one method prove technically satisfactory. The bulk of the work reported in the next four chapters was devoted to evaluating these various lens fabrication techniques.

CHAPTER 4 : GEODESIC LENS GENERATION BY ULTRASONIC GRINDING

4.1 INTRODUCTION

The use of ultrasonic grinding for the generation of geodesic lenses was first reported in 1977 by Chen [95, 97], who used a 100W ultrasonic impact grinder to which was fitted a specially made tool (whose fabrication method was not discussed). Ultrasonic energy transmitted agitation to an aluminium oxide abrasive slurry, removing material from the $LiNbO_3$ substrate. The method was claimed to be of low cost, and capable of generating multiple geodesic lenses with automatic alignment, since it is possible to use a multiple head grinding tool.

Ultrasonic grinding has been discussed in great detail by L.V.Popov in reference 128. The method has been widely used since around 1955 for generating shaped surfaces in brittle materials such as glass, ceramics and hardened alloys, and has been particularly useful for drilling blind holes (i.e. not completely through a component) and complex shaped slots. Using an electromagnet, a transducer formed from a magnetostrictive material is oscillated at its resonant frequency along an axis normal to the direction of grinding. This frequency is usually in the range 18-25 KHz. Vibrations of amplitude up to about 10μm can be produced. These may be magnified by a "velocity transducer" or "concentrator". The substrate is eroded by impacts of the vibrating abrasive particles, which must be of harder material than that of the substrate.

Popov has claimed that, for 1 Kw power input and boron carbide abrasive, the material removal rate for glass was $1500mm^3/min$. The drill used by the author was of much lower power, about 100W, and was claimed to be able to erode 55 $(mm)^3/min$ of glass, using 220 mesh silicon carbide abrasive and a 9:1 concentrator. At this rate, the geodesic lens profiles of the author's work would have

been generated in about three minutes. As will be discussed later, the lenses took rather longer to grind. This difference is probably explained by the different substrate material, and the difficulty in continuously supplying fresh abrasive.

In ultrasonic drilling machines, longitudinal vibrations are induced in single rods or multirod systems. For a single rod the length for resonance l=c/2f for frequency f, and longitudinal sound velocity c. To avoid the less transmittive higher modes, the greatest distance across the radiating surface must not exceed half a wavelength. At the optimum frequency (about 20 KHz) the acoustic velocity of the common transducer material, nickel, is 5.63 Km/s. This imposes the limit of 140mm on the radiating surface dimensions. This is well in excess of any likely geodesic lens dimensions, while a multiple head tool for precise relative location of two or more lenses should be possible. Velocity transformation is arranged by tapering down to a smaller cross-sectional area at the abrading end of the transducer, the total length being such as to have an oscillating node at that end. The required taper profile may be simplified to an exponential or hyperbolic cosine function [128], or to a series of parallel-sided cylinders. The last is clearly more easily made, but has the mechanical disadvantages of being more highly stressed, and more easily laterally deflected (as well as being less efficient in transmitting vibrations). Two-stage cylindrical concentrators with area ratios (hence vibration amplitude ratios) of say 4:1 and 9:1 are typically supplied with an ultrasonic machine. The transducer with the tip area closest to the required tool area is chosen for use. The Mullard machine used in this work quotes 8μm peak-to-peak vibration amplitude at the lower face of the transducer, giving amplitudes of 30μm and 70μm respectively for the two concentrator faces.

The choice of efficient grinding parameters is governed by several effects and constraints. Popov [128] showed that

the disintegration rate increased with frequency, but beyond about 20KHz electrical and mechanical losses caused decreases in efficiency. Commercial machines usually allow tuning to resonance in a small band around 20 KHz. The disintegration rate is proportional to a power of the vibration amplitude, which in practise is generally below the theoretical value of 2 unless all conditions, especially slurry feed, are ideal [128]. For brittle materials there is an optimum pressure: machines allow fine tuning of counterbalanced loading in the 1000 Kg/m^2 range.

Kumanin [128] found that the grinding rate of glass increased with the abrasive particle size up to a limit where the particle dimensions just exceeded the vibration amplitude. He also found some evidence that grinding rate is proportional to particle hardness. Silicon and boron carbides are the most commonly used materials. The grinding particles must be suspended in a slurry based on a fluid which has good wetting properties and low viscosity so that there is easy particle motion and removal. Vibration, friction and abrasion contribute significant amounts of heat, which is unlikely to be conducted away well by the kinds of materials being ground. It is therefore essential that the slurry provides good cooling. Water has been found to be the optimum fluid [128], and has been used to give a slurry of 30% to 40% abrasive concentration by volume [128,175]. This should be fed continuously through holes or slots in the tool, or by frequently lifting the tool.

4.2 MODIFICATION OF AN ULTRASONIC DRILL

For the author's experiments, a Mullard type E7685/2 ultrasonic drill was modified (under the direction of Dr. R.B.Wilson) to permit more accurate location of the grinding tool over the substrate (Figure 4.1). Stiffening struts of welded aluminium box-section were added,

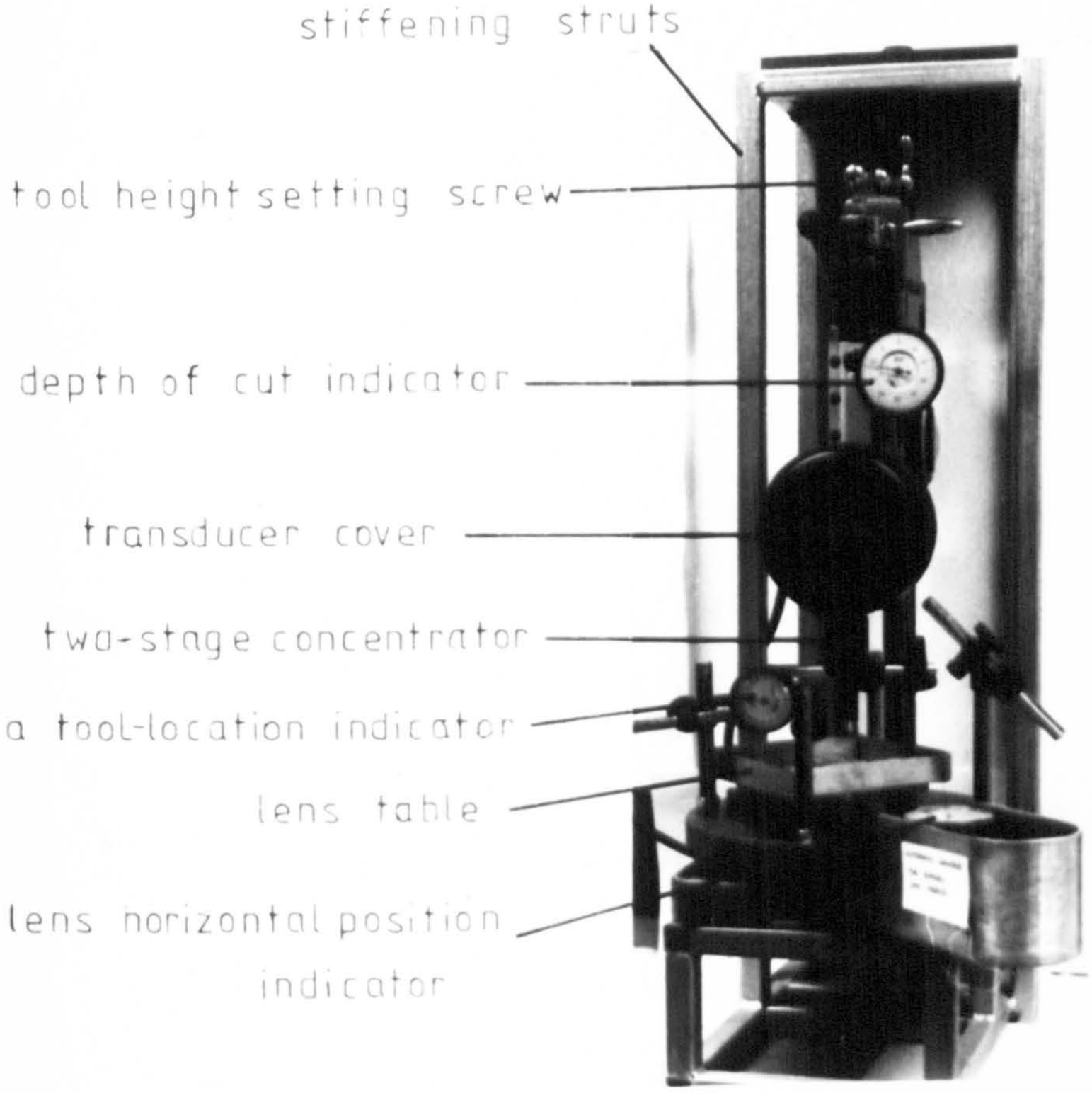

Figure 4.1 Ultrasonic drill as modified to grind geodesic lenses.

together with a vacuum-held substrate table which could be positioned under the grinding head by sliding over a horizontal base plate. A guide rail was provided which constrained the substrate table to slide along one axis only. A dial gauge indicator capable of reading to 1μm was attached horizontally to the base plate, reading the distance of the sliding table along its axis of motion to allow the desired lens positions to be located sufficiently accurately below the grinding head. Four other dial gauge indicators (capable of reading to 2μm) could be fixed horizontally on posts to define the position of the grinding tool vertical axis. These indicators could therefore be used to adjust each successive tool to grind in the same location on the substrate.

4.3 METHODS OF PREPARING ULTRASONIC TOOLS

An ultrasonic grinding tool was made of soft steel (KE672, as recommended by Mullard) to the drawing of Figure 4.2. The aspheric profile was turned by the author on a Harrison lathe with Baty C15 dial gauge indicators reading to 2μm fixed to the two moving slides. The first cuts were made to a seven-step approximation of the profile. Final cuts were made to a 58-step approximation to the mirror-image of the lens profile, which had been computed directly by the Sottini, Russo and Righini lens-design programme (see Chapter 2.3.5), with no allowances for the finite size of the lathe cutting tool, or for wear of the ultrasonic tool during grinding, or for any change in the lens profile during a subsequent polishing stage. Without disturbing the centring of the aspheric profile, the outer diameter of the whole grinding tool was turned concentrically (to an arbitrary diameter of 19.050mm), to provide a locating surface when fitting into the drill.

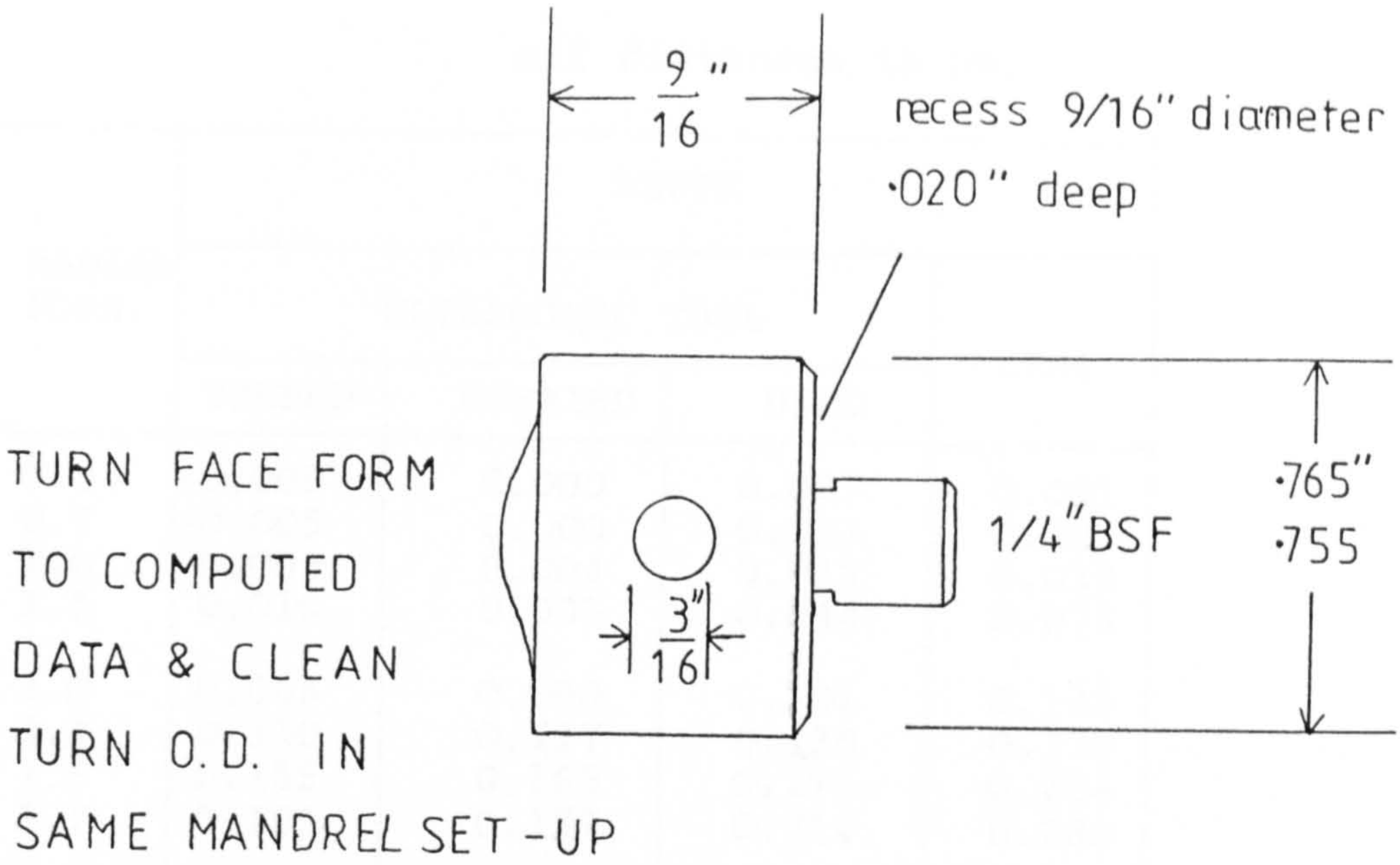

Figure 4.2 Drawing of tool for ultrasonically grinding lens depressions.

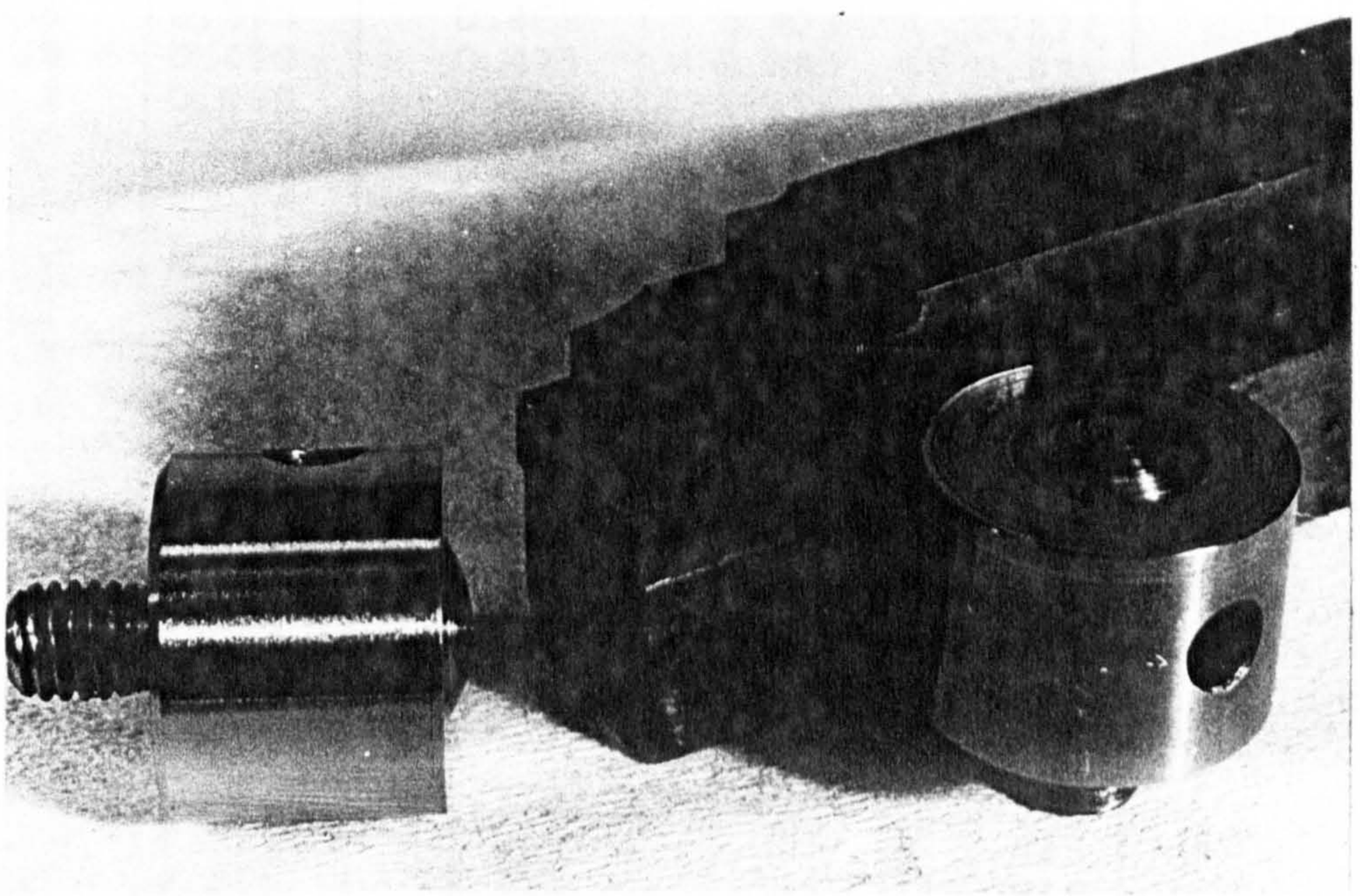

Figure 4.3

Two ultrasonic tools which were turned by a tungsten carbide profile tool (centre), which was in turn cut on a numerically controlled spark eroder.

TABLE 5: MEASUREMENT OF ULTRASONIC TOOL AND LENS PROFILES

all distances in mm.

RADIAL POSN.	DEPTH			
	ULTRASONIC TOOL			LENS
	TURNED	EMERIED	USED	
0.0	-0.005	0.000	0.007	0.021
0.7	-0.005	0.000	0.011	0.024
1.0	-0.005	0.004	0.015	0.033
1.5	0.010	0.033	0.044	0.073
2.0	0.065	0.090	0.101	0.143
2.2	0.110	0.117	0.130	0.178
2.5	0.155	0.165	0.177	0.234
2.7	0.185	0.197	0.214	0.280
2.9	0.225	0.242	0.253	0.334
3.1	0.265	0.285	0.290	0.410
3.3	0.315	0.334	0.345	0.469
3.5	0.365	0.389	0.398	0.536
3.6	0.395	0.408	0.425	0.577
3.8	0.450	0.475	0.485	0.696
3.9	0.480	0.507	0.516	0.750
4.0	0.510	0.540	0.553	0.806
4.1	0.545	0.577	0.586	0.849
4.2	0.595	0.614	0.622	0.901
4.4	0.660	0.685	0.692	0.990
4.6	0.745	0.763	0.773	1.062
4.8	0.845	0.858	0.865	1.102
5.0	0.955	0.966	0.977	1.144
5.5	1.245	1.240	1.243	1.315
5.7			1.315	1.315
5.73		1.315	1.315	1.315
5.88	1.315	1.315	1.315	1.315
6.0	1.315	1.315	1.315	1.315
7.0	1.315	1.315	1.315	1.315

Using the same dial indicators, the axial rotational symmetry of the turned tool appeared to be maintained within 2μm, and the total height of the profile had been machined within 2μm of the intended 1.315mm. The profile was measured at 25 radial positions using the dial gauge indicators (Table 5).

The faceted nature of the tool surface was clearly visible. In order to make the profile a more continuous curve, a light manual abrasion with emery paper was carried out. This process removed 5μm from the peak of the profile. Table 5 gives the radial profile measurements.

The point of contact between the measuring probe and the ultrasonic tool was displaced in height and in radial position from the tip of the probe, because of the curvature of the tool profile. Since the radius of the measuring probe tip was large, 1.5mm, it was necessary to make large corrections to the indicated position - up to 0.8mm radially and up to 0.2 mm in height. Methods of calculating these corrections are discussed in Chapter 7. For the work of this chapter, the data of Table 5 was corrected graphically. A graph was plotted of indicated height versus radial position. A template having the shape of the measuring probe was placed with the tip at each measured point, and traced around. The tool profile was taken to be the envelope of the measuring probe tracings. Profiles are plotted in Figure 4.7, which will be discussed in section 4.4.

Later, grinding tools (figure 4.3) were turned at the Department of Production Management and Manufacturing Technology at the University of Strathclyde with a tungsten carbide form-tool, which was itself cut with an Agiecut numerically-controlled spark eroder. The eroder programme was prepared from a table of lens design coordinates computed by the lens-design programme of Chapter 2.3.5, taking steps to the nearest 2μm, and allowing for an offset of 0.14mm corresponding to half the width of cut which was eroded by the 0.2mm diameter wire.

PAGE NUMBERING AS ORIGINAL

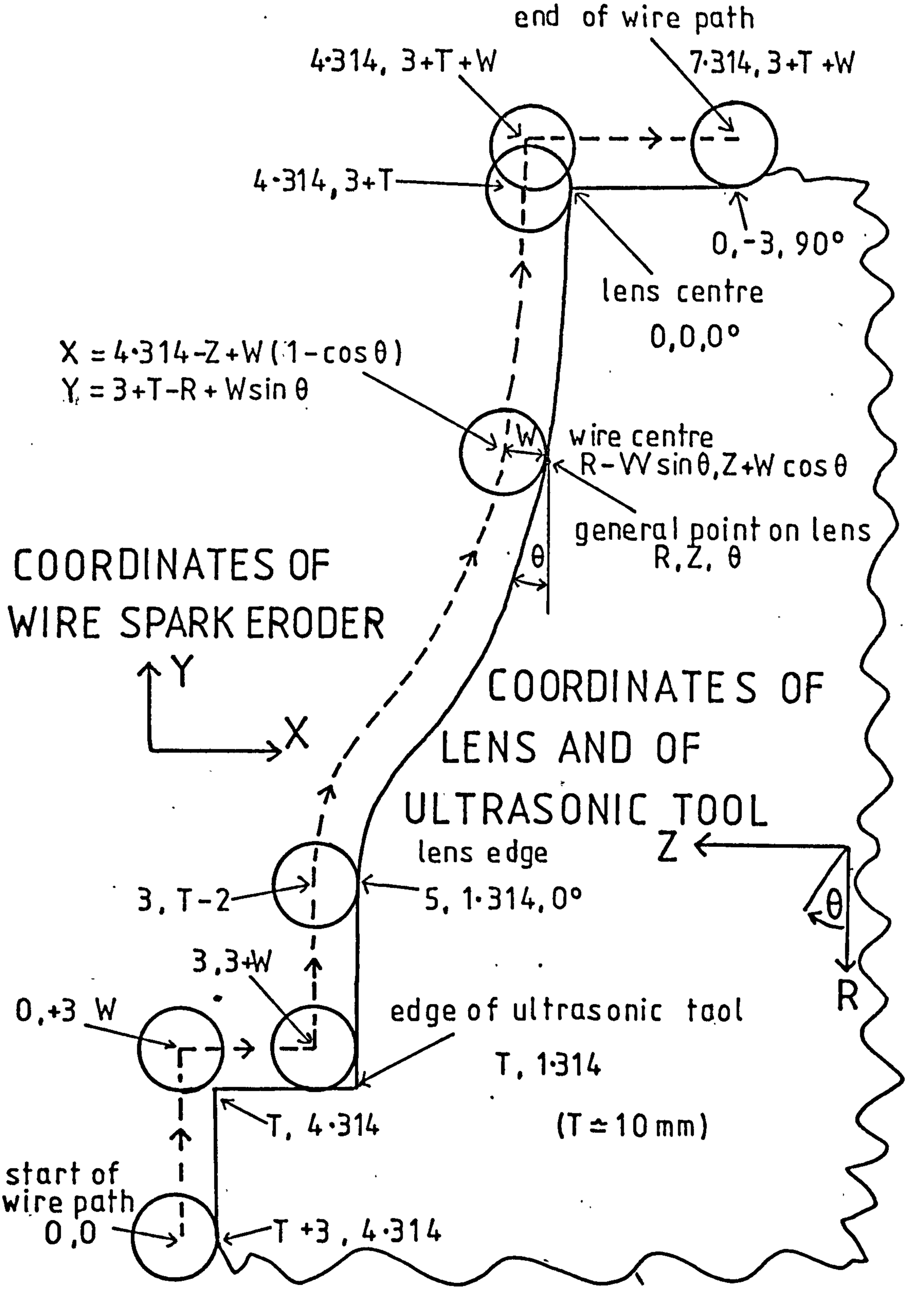

Figure 4.4 Profile of tungsten carbide tool, and coordinates of wire spark eroder path.

Figure 4.4 shows how the wire eroder path was related to the carbide cutting tool profile and ultimately to the geodesic lens profile.

It is unlikely that the carbide cutting tool could have been cut to an error less than about 4μm difference from the required profile, and its location when turning the grinding tool was probably of similar inaccuracy. These estimates, together with an allowance for the very uneven wear of the carbide tool after cutting two tools (see figure 4.3), indicate that the profiles of the grinding tools produced were probably no closer than 10μm to the required profile. This inaccuracy is too large for the geodesic lens performance specified for the present work. Because of a shift in emphasis in the work, these tools were never used, and results of their machining not obtained.

4.4 TOOL WEAR

Mullard Ltd.[175] suggest that to allow for the finite size of the abrasive particles and their oscillations, grinding tools should be smaller than the required hole (presumably laterally) size by three to four times the size of the abrasive particles. This allowance would be about 0.2mm for 220 mesh (UK) grains. However allowances in the opposite direction would be required for wear of the tool during grinding. Popov [128] showed that when machining glass, the sides of a cylindrical ultrasonic grinding tool wore about one-fifth of the amount of the wear at the end. The end of the tool suffered impacts of greater amplitude, and for a longer period than the sides. In a similar way, one would expect that the wear of an aspheric lens tool would not be uniform. The central part, which would be in contact with the substrate for a longer period than the edges, may wear most.

Since the amount and distribution of wear could not be

predicted, no correction was made to the profile of the ultrasonic tool discussed in section 4.3. Measurements of the amount of wear found in use are presented in the next section.

It is expected that a bonded-diamond tool would wear less than a steel tool used with loose abrasive, but the bonded tool would not vibrate grains so freely as with loose abrasive. Nevertheless Popov has reported that under some circumstances a bonded tool gave only 25% less grinding rate than a corresponding free-abrasive tool.

4.5 LENS GENERATION

Using the ultrasonic grinding tool which had been turned by hand (section 4.3), an aspheric geodesic lens profile was ground in a Syton-polished Y-cut lithium niobate substrate. (Later the same tool was used to grind a pair of lenses in a glass model of the IOSA. Fig.4.5 shows grinding of the second lens of this pair.) A one-step concentrator was used. This comprised two cylindrical sections, the upper being of the transducer diameter, and the lower of the grinding tool diameter, 20mm. The concentrator was screwed to the ultrasonic generator and to the grinding tool using copper washers. To promote high acoustic transmission, these washers were taken from a stock of annealed washers for each grinding run.

A slurry of about 60% water and 40% 240 grit (average particle diameter 50μm) Buehler aluminium oxide powder was applied by a small brush every half minute. After 30 minutes, the depth indicator on the drill read 1.26mm. Another half hour was needed to grind to an indicated 1.29mm (with ±0.05mm uncertainty when not perfectly clean of slurry). The tool felt very hot to touch. After waiting 20 minutes to allow it to cool to room temperature, the indicator (which was located against the transducer rather than at the grinding tool) was again read. Its value was

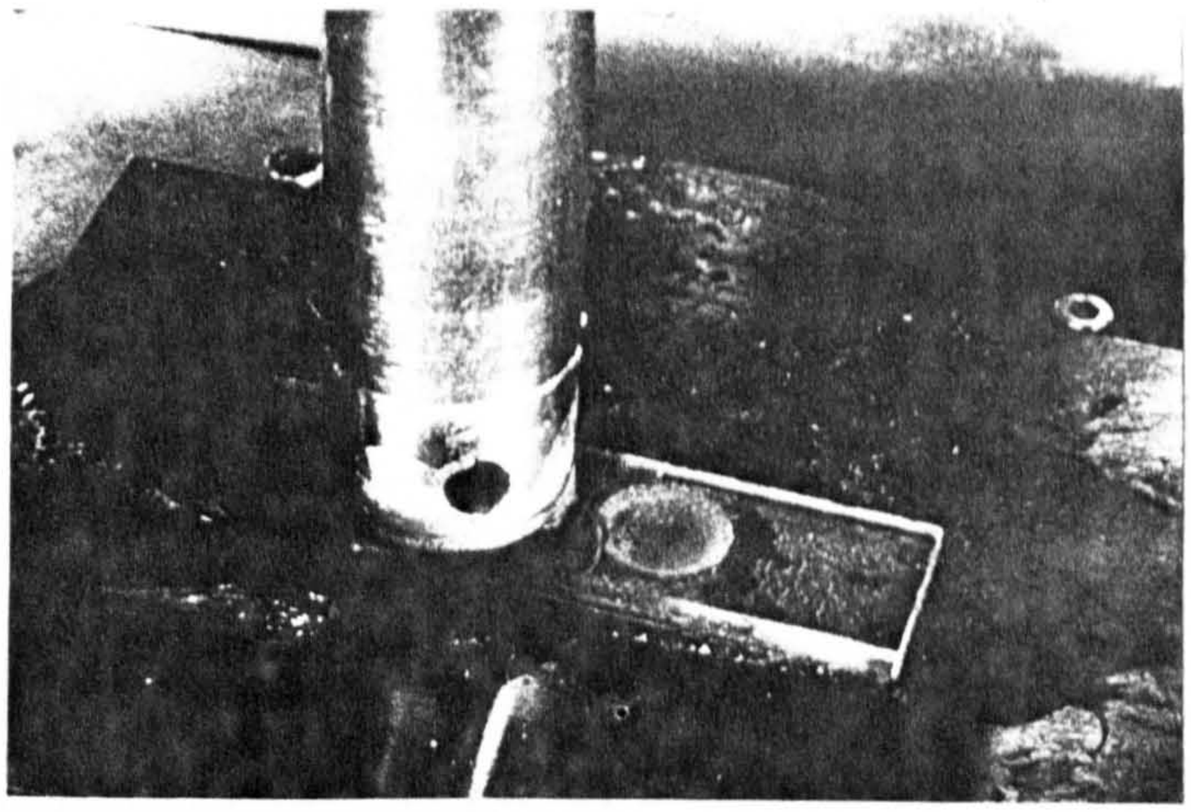

Figure 4.5 Ultrasonic generation of a geodesic lens in progress.

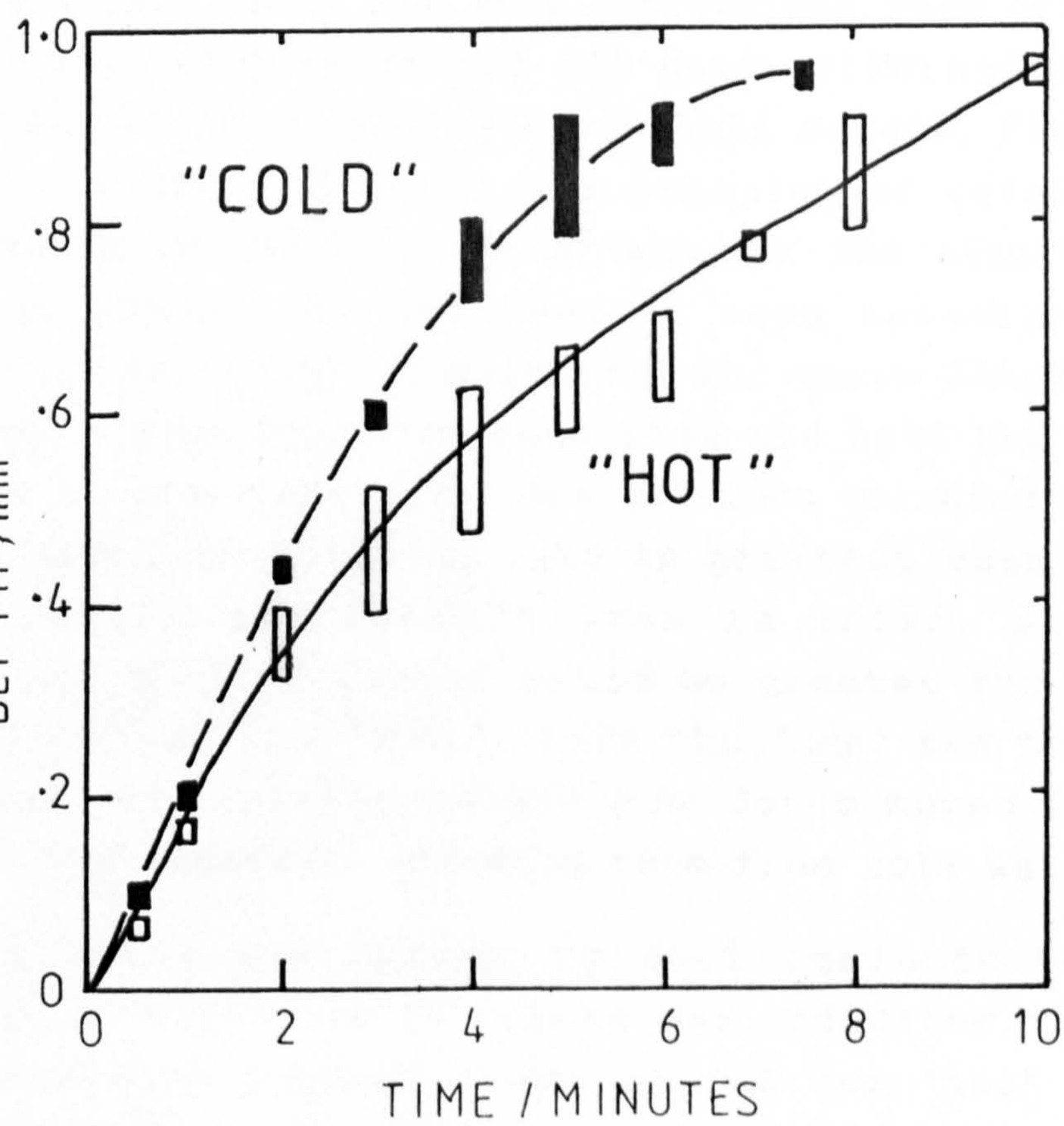

Figure 4.6 Effect of temperature on rate of ultrasonic penetration.

1.345mm, which showed that the transducer and tool assembly had expanded by about 60μm during use, and that the lens was now 30μm deeper than the planned final polished value.

A further 10μm depth of material was removed using 12.5μm powder in an attempt to reduce the surface roughness. Monitoring this grinding depth was very difficult since the tool expansion with the heat generated by grinding was greater than the planned change. It was necessary to allow cooling periods of about 20 minutes for every few minutes of grinding.

An investigation was made into the effect of heat generated during grinding on the amount of tool expansion and on the grinding rate. Six lens depressions were ground in float glass, using about 40% 150 grit carborundum in water, feeding in fresh slurry every half minute. Figure 4.6 shows the indicated depth as a function of grinding duration. The curve labelled "cold" was for the situation where the grinding tool had been at room temperature (about 20°C) at the start of grinding. The curve labelled "hot" was taken from grinding runs when the tool had not been allowed to cool down after the previous grinding run. It is clear that the grinding rate is greatest when the tool penetration and contact area is least. Since transducer and tool expansion would be greater for the "cold" runs than for the "hot", then the "cold" run total depth changes were under-recorded (the datum moved down with the tool) and therefore grinding rate from cold was faster.

After allowing the system to cool again to room temperature, an expansion of 0.14mm was indicated. This was the difference between depth of cut for "hot' and "cold" after only a few minutes of grinding. If the expansion had been uniformly distributed over the 15mm of steel grinding tool and 87 mm of brass transducer and concentrator, then this would have been due to a temperature rise of about 80° to reach the boiling point of water in the slurry. This estimate is consistent with

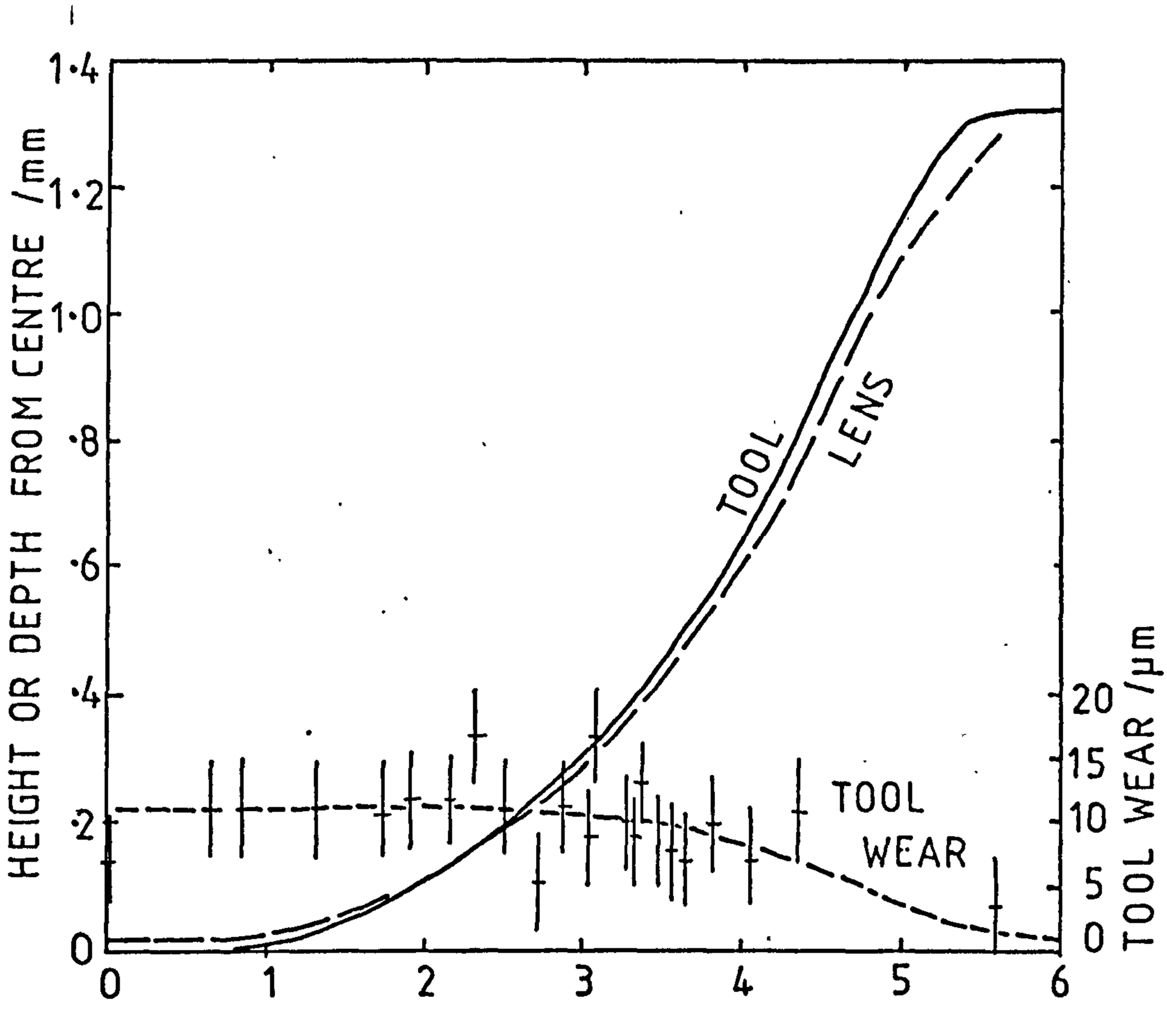

FIG. 4.7 Measured profiles of ultrasonic tool and a generated lens, and amount of tool wear from generating the lens.

the observation of steam rising from the slurry during grinding.

The need to clamp the transducer-concentrator-tool assembly at nodes other than that of the grinding end determines that not only is it free to expand considerably but that it is also free to be deflected sideways. The Mullard drill transducer is only clamped at the centre, in other machines the transducer may be clamped at more than one of the upper nodes [128], a design feature which should decrease the susceptibility to deflection.

The ultrasonically-ground lens was mounted in a chuck on the Harrison lathe and its profile was measured in the same way as was the profile of the ultrasonic tool. Table 5 shows the results. It is clear that the depth gauge on the ultrasonic drill had not given a true reading. Two factors affected its reading of lens depth. The ultrasonic tool had penetrated deeper than required for the aspheric profile, so that 67μm depth had been ground into the surrounding plane region. On the substrate, this region was also tilted with respect to the surrounding polished region. The amount of tilt was 0.126mm over 13mm, i.e. 0.6 deg arc.

The corrected measured profile of the lens is shown in Figure 4.7. This is plotted to a datum of 1.315mm at the lens edge (the region just inside the edge had ambiguous readings). The profiles of the ground lens and the ultrasonic tool (before grinding) differ by up to about 30μm, if measured normally to their profiles. The Baty C15 dial gauge indicators used for these measurements had been made to British Standard 907 which allows errors of linearity of 2μm over a 30μm distance, and 10μm over 1mm distance. The gauges were therefore sufficiently accurate for measuring small differences, but the 30μm difference indicated between lens and tool profile could have been in error by ±10μm since the dial gauge plunger moved in the opposite direction when measuring the lens to when measuring the tool profile.

The wear of the hand-turned ultrasonic tool was calculated by subtracting columns of table 4.5, and is plotted in Figure 4.7. Over most of the tool, the wear had been 11μm(±4μm) which is 0.8% of the total depth of lithium niobate that had been eroded. (After generating one lens depression in glass, the wear of the tool centre was measured as 7μm (± 4μm)). This amount of wear is large compared with the tolerance on lens dimensions.

4.6 CONCLUSIONS

Errors in continuously monitoring grinding depth with the Mullard ultrasonic drill can be about 0.1mm due to expansion by heating, and to the distribution of grit particles under the tool. Other manufacturer's drills which feed cooling slurry through a rotating drill face may generate less heat during grinding, but the author believes that uncertainty due to expansion is unlikely to be reduced to less than about 10μm. To allow sufficient accuracy of depth measurement, it would be necessary to use a separate depth gauge which would have the substrate surface as datum. This could only be used intermittently, and the substrate would have to be thoroughly cleaned of abrasive before each measurement.

Tool wear was measured as about 11μm after grinding one lens depression. If several tools were used, the wear per tool could be reduced, but this procedure would contribute to greater location and depth errors.

The lens profile was within 30μm ±10μm of the pre-grinding profile of the tool, and within about 20μm ±10μm of the grinding tool profile measured after use. During grinding, it had been observed that the tool tended to push the abrasive particles away from the centre towards the sides: this could explain why the wear of the lens which can be seen in Figure 4.7 is greater near to the edge than at the centre. The lens was not worn

proportionally more towards the centre than towards the edge, as would have been expected by the longer exposure to grinding of the central regions.

These profile errors were too great for lenses in the spectrum analyser, and the accuracy of locating lenses relative to the substrate edges was inadequate. However, if a considerable amount of profile correction were possible during polishing, ultrasonic grinding would seem an attractive method, since ultrasonic equipment is considerably less expensive than the machine tools required for the other methods investigated.

CHAPTER 5: GENERATION OF GEODESIC LENSES BY COMPUTER-CONTROLLED MACHINES

5.1 REVIEW OF COMPUTER-CONTROLLED ASPHERIC GENERATORS.

There were two major reasons why the ultrasonic generation method of the previous chapter was regarded as inadequate: inaccurate tool profile cutting, and large (and probably excessive) tool wear. The former problem could have been largely overcome by forming the tool profile on a computer numerically controlled (CNC) machine. Indeed early plans were made to use this method of tool generation, but it was realised that, even if an adequate tool precision could be obtained, the problem of large and unpredictable tool wear would probably be very difficult to overcome. In any case, the feasibility of using a CNC grinding machine could be tested by grinding lenses themselves in lithium niobate. Furthermore, it was hoped that direct grinding of lenses on a CNC machine could become a satisfactory method, and the use of intermediate tools would then become an unneccesary complication.

Chen & Ramer in May 1979 [98] reported CNC machining of lens depressions in lithium niobate to be inadequate. They found that when using a CNC machine with a diamond-coated grinding tool, chips came away of greater size than the diamond grit, and the peak-to-valley roughness of the surface was 6-10μm. They also reported trials with a CNC machine which turned lenses in lithium niobate with a single-point diamond tool. They found that high tool pressure was a problem (of unexplained nature) and that, in unfavorable regions of the crystal, the peak-to-valley surface roughness was as great as 5μm. However, later in the same year Mergerian [105] reported successful single-point diamond turning of geodesic lenses in lithium niobate on a CNC machine of the same manufacture (Moore Special Tool Co.). Several properties of single-crystal natural diamonds lead to the possibility of turning smooth

surfaces of accurate profile: extremely high hardness, hence low wear rate; single-crystal structure allows sharpening to a finer cutting edge than polycrystalline materials; the very low friction coefficient enables chips to move freely over the tool without bonding to it; the high thermal conductivity allows heat energy to dissipate well rather than heat-up and damage the tool tip.

It was clearly necessary therefore, for the present work, to investigate CNC machining, preferably both by grinding and by turning lens depressions in lithium niobate. There was already an extensive literature on the fabrication of aspheric components in glass by CNC grinding [124,130,176,177] and in metals and infrared transmitting materials by CNC diamond turning [124,139,141,145,178].

Machines for CNC generation of optical components have been designed to make all moving parts (e.g. workpiece spindles, tool slideways, and grinding heads) move with a precision one or two orders of magnitude better than the average toolroom machines for metal working. This has been realised by attention to the accuracy of the machine parts, and often by using fluid or gas bearings, rather than bearings with rolling metal parts. With several of these machines the cutting or grinding tools were originally made to follow aspheric profiles under the control of cams [124,152]. However, as computing power, positioning drives and feedback systems developed, the greater versatility of CNC control was built into the machining processes. These features are discussed in the following sections on the experimental evaluation of CNC lens generating techniques.

5.2 LENS GENERATION ON A JIG-GRINDER

5.2.1 Introduction.

Nicholas and Boon in 1979 [177] reported on the generation of aspheric lenses in glass or synthetic silica using a Moore G18 CP-4 continuous path CNC jig grinder, with four axes all of which could be moved in small steps. Although these lenses were relatively large and flat compared with the IOSA lenses (110mm diameter, and approximately 130mm radius of curvature), the process seemed appropriate to generating geodesic lenses since the surface finish was finer than had been found with the common optical generating processes, and the profile accuracy was of the order of one micrometre. Nicholas reported that the ground lenses could be polished (on the same machine) by using a felt mop with 5μm alumina slurry sufficiently, in about one hour, to obtain an interferogram.

Further enquiries by the author showed that Henri Hauser Ltd (Switzerland) had similarly ground glass aspheric lenses with a surface shape tolerance of 2μm, using their S3 CNC311 two-axis continuous-path jig-grinding machine which was controlled in 1μm steps. It has been claimed that Bostomatic 300 four-axis CNC milling machines have produced aspheric lenses in glass and plastics, including multifocus opthalmic lenses which are not axially symmetric. However the accuracy claimed by the manufacturer was not better than 10μm.

Arrangements were made by the author to use the machine at R.L.Smith Ltd. (Billinshurst,Sussex) which had been used to make the lenses for Nicholas & Boon [177]. The operator provided to work under the instructions of the author had experience of making the Nicholas and Boon lenses. The machine (Figure 5.1) has been very fully discussed in Ref. 179. The machine has two horizontal cross-slides (X- and Y- axes) moving on hardened, ground

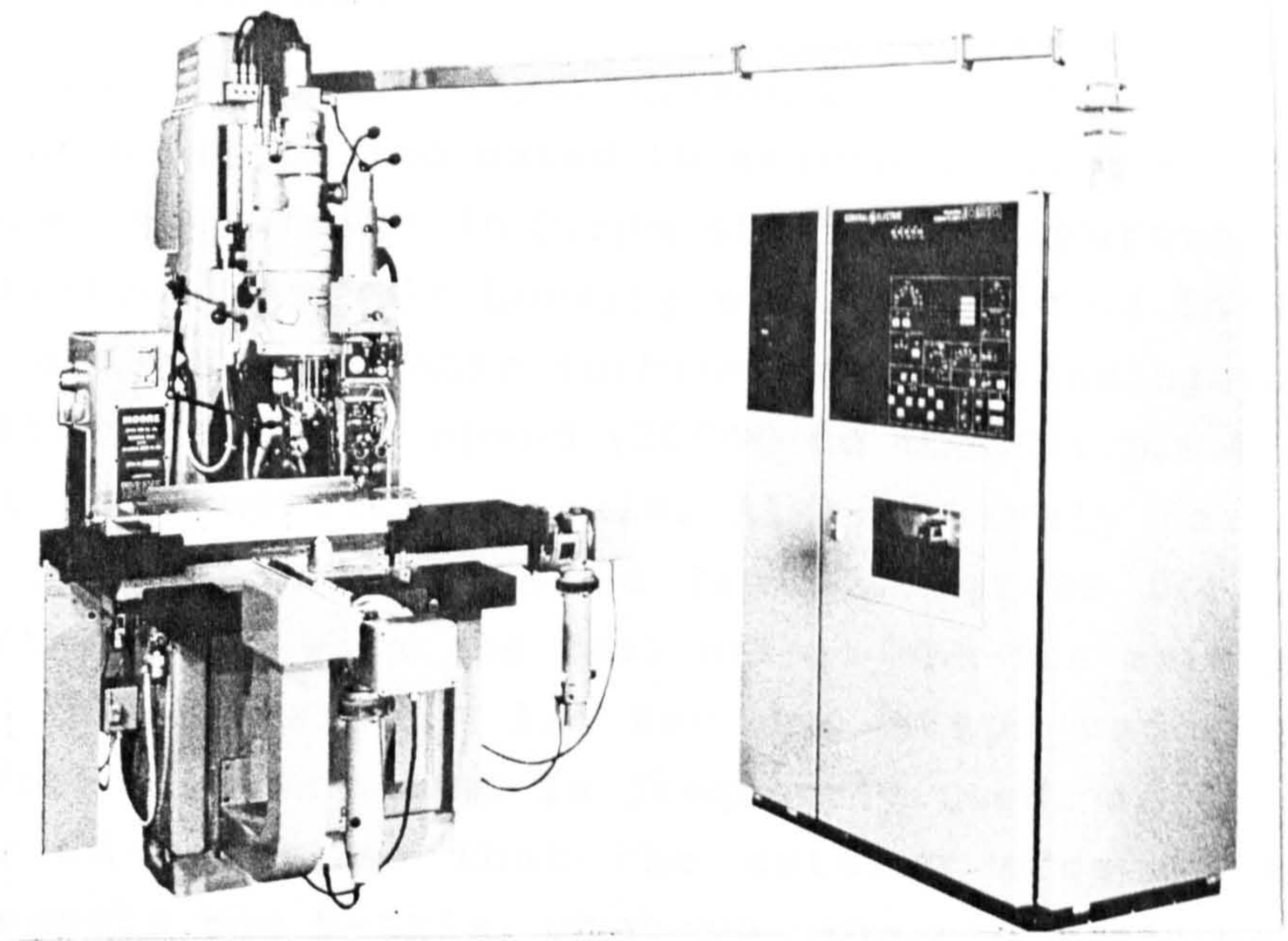

G 18 CP MACHINE

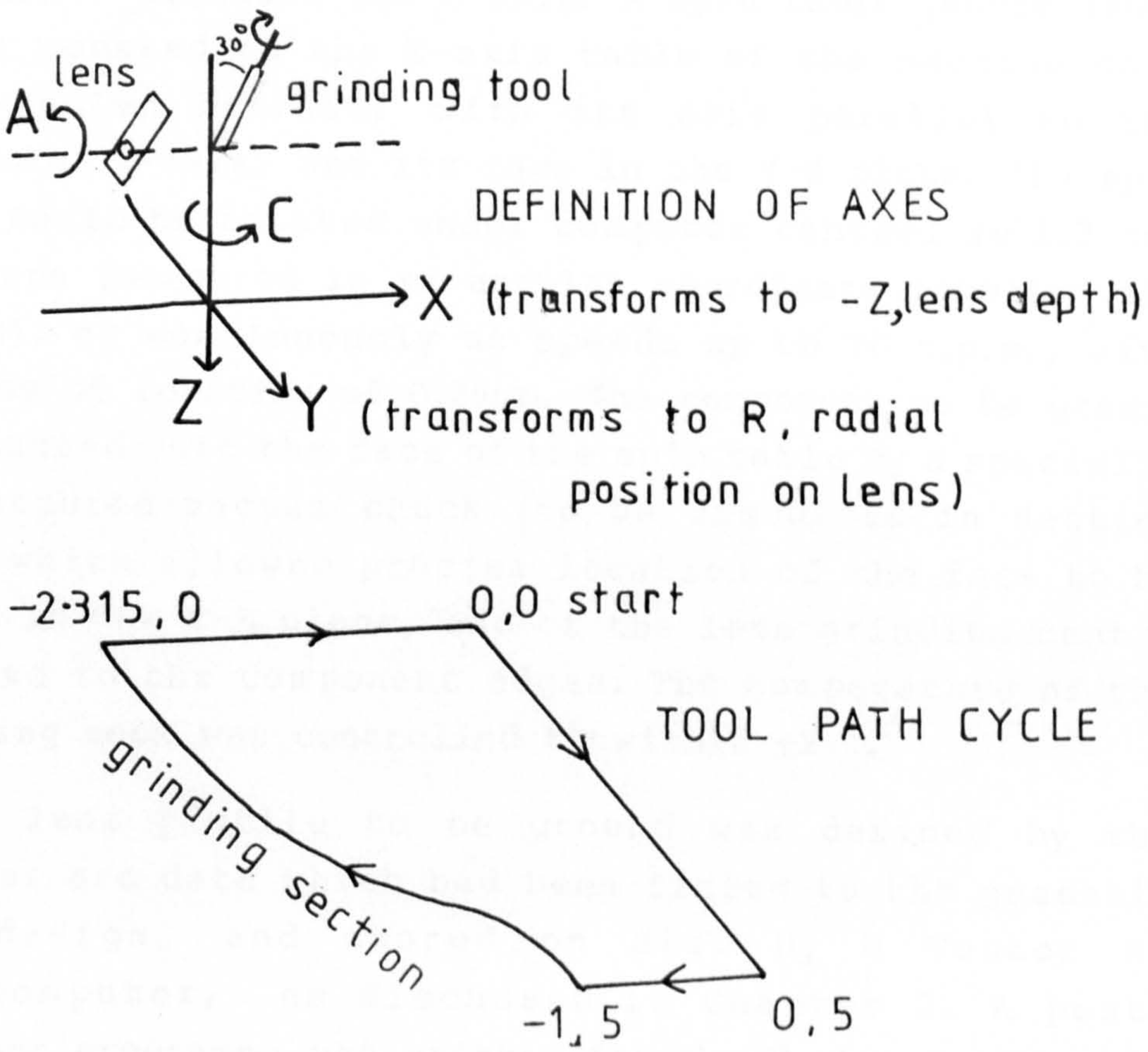

DEFINITION OF AXES

TOOL PATH CYCLE

FIG. 5.1 MOORE JIG GRINDER

and lapped double V-ways, driven by lead screws which have been hand-lapped and mated to aluminium-bronze nuts. These slides were driven in 0.2μm step under computer control. The vertical spindle housing was constructed in a similar way, and the pneumatic turbine-driven grinding tool could be rotated at high speed (20000 to 40000 r.p.m.) directly about this vertical Z-axis. Alternatively the grinding tool axis could be tilted (at 30 degrees for the work reported here) with the tool offset and its axis precessed about the Z-axis in 1.2 sec arc steps under computer control. The movement is frequently used, as in the work reported here, so that the cutting edge of the tool intersects the Z-axis, whatever the slope of the profile being cut. These steps are measured along an angular coordinate labelled the C-axis. A spin table (Moore 3900-A) was mounted on the X-axis table of the machine on a right-angled bracket, with its axis parallel to the horizontal X-axis, and its face in the Y-Z plane. The spin table could be rotated under computer control in 1.3 sec arc steps (measured in an angular coordinate labelled the A-axis), or continuously at speeds up to 70 r.p.m., with trueness of rotation of 0.25μm. The component to be ground was mounted onto the face of the spin table by a specially manufactured vacuum chuck (to be discussed in section 5.4.2) which allowed precise location of the face to be ground in the Y-Z plane, and of the lens grinding centre relative to the component edges. The temperature of the machining room was controlled to within $\pm 2^{\circ}$.

The lens profile to be ground was defined by the circular arc data which had been fitted to the geodesic lens design, and stored on disc by a Vector MZ microcomputer, as discussed in Chapter 2. A post-processor programme was written for the Vector computer to specify the grinding tool path required to generate the lens profile. This was output as a paper tape generated by a punch machine,controlled by the Vector computer in the format required for the General Electric GE 1050 computer which controlled the Moore grinding machine. (A similar

post-processor programme was used to prepare a paper tape for the GE 550 computer used to control the Moore aspherising machine to be discussed in a later section of this chapter.) Fig. 5.1 defines the axes and the transformations from the lens design coordinate system. Table 6 lists the tape data.

The GE 1050 computer required a set of codes in a particular format to define each arc. These codes defined: the block identification number N, the type of movement (linear (G01), clockwise arc (G02) or counterclockwise arc (G03) interpolation), starting point coordinates X and Y, angular sector of arc C, distance of arc centre from the starting point I and J, a calibration factor for arc length K, and the nominal feedrate of the Y-axis F (in mm/min). Each tool cycle started at position X,Y and C = 0.0, the X zero being preset 1mm away from the workpiece face in the positive direction. After a traverse to Y = -5.0mm the tool moved in towards the substrate above the lens edge position, then ground along the profile to the lens centre, before returning to the zero coordinates position to be manually fed in towards the substrate for another cycle. The first pass cut only at the lens centre. Subsequent cuts removed material from a progressivly wider area around the centre. The Y-axis feedrate was varied so that the tool traverse speed tangentially to the surface was constant,. using an expression given in the instructions for programming the GE1050 computer for use in metric units with an imperial dimensioned lead screw.

The grinding tool chosen was in the form of a cylinder initially of 4.7mm diameter, with 150 grit diamond particles resin-bonded to the cutting edge in 50 concentration (i.e. 12.5% by volume of diamond particles). The coolant used was as recommended by Moore, and was described as 1% in water solution of a lard oil (Quaker grind 101NS). The substrate was rotated slowly at 1 rev/sec.

TABLE 6: FORMAT AND DETAILS OF DATA REQUIRED
TO CONTROL A MOORE G18 JIG GRINDER WITH A GE1050 COMPUTER
FOR PRODUCING A 20-ARC LENS

```
N1001 %
N1002 G17
N1003 M07
N1004 G90
N1005 G01 Y-5.0238 F125.00
N2001 G01 X-1.0000 Y-5.0238 C0.00000 F030.00 M00
N2002 G02 X-1.0050 Y-4.9500 C-.02019 I  .5830 J0.0000 K.31831 F125.00
N2003 G02 X-1.0166 Y-4.8800 C-.03149 I 1.0192 J .1320 K.31831 F 72.40
N2004 G02 X-1.0378 Y-4.7900 C-.04122 I 1.4826 J .2972 K.31831 F 50.92
N2005 G02 X-1.0736 Y-4.6700 C-.05096 I 1.9784 J .5242 K.31831 F 39.50
N2006 G02 X-1.1246 Y-4.5300 C-.05986 I 2.5288 J .8386 K.31831 F 32.42
N2007 G02 X-1.1928 Y-4.3700 C-.06809 I 3.1300 J1.2362 K.31831 F 27.89
N2008 G02 X-1.2804 Y-4.1900 C-.07572 I 3.8018 J1.7336 K.31831 F 24.82
N2009 G02 X-1.3894 Y-3.9900 C-.08277 I 4.5654 J2.3520 K.31831 F 22.70
N2010 G02 X-1.5150 Y-3.7800 C-.08901 I 5.4218 J3.1050 K.31831 F 21.25
N2011 G02 X-1.5216 Y-3.7700 C-.08928 I 5.8460 J3.6592 K.31831 F 20.68
N2012 G03 X-1.7064 Y-3.4200 C-.06534 I 2.2302 J1.4012 K.31831 F 32.68
N2013 G03 X-1.7236 Y-3.3800 C-.06388 I 3.7788 J1.6510 K.31831 F 24.98
N2014 G03 X-1.7994 Y-3.1900 C-.05713 I 4.4424 J1.8852 K.31831 F 23.27
N2015 G03 X-1.8802 Y-2.9600 C-.05058 I 5.5498 J2.0824 K.31831 F 21.59
N2016 G03 X-1.9684 Y-2.6700 C-.04369 I 6.6518 J2.1884 K.31831 F 20.60
N2017 G03 X-2.0560 Y-2.3300 C-.03673 I 7.7288 J2.1768 K.31831 F 19.97
N2018 G03 X-2.1404 Y-1.9300 C-.02947 I 8.7228 J2.0498 K.31831 F 19.57
N2019 G03 X-2.2178 Y-1.4500 C-.02156 I 9.6150 J1.8012 K.31831 F 19.30
N2020 G03 X-2.2810 Y -.8600 C-.01253 I10.3662 J1.4130 K.31831 F 19.13
N2021 G03 X-2.3150 Y 0.0000 C-.00000 I10.8986 J .8600 K.31831 F 19.02
N3001 G01 X 0.0000 F125.00 M00
N3002 M09
N3003 M30
N3004 %
```

5.2.2. Plane grinding and polishing.

In order to establish suitable grinding and polishing parameters for lithium niobate, a programme was entered manually which was expected to produce a 10mm diameter flat region. A highly polished Y-face substrate was chosen to avoid confusion with any damage from a previous machine such as the saw used to cut the substrate. Resonant vibration between the grinding tool and the substrate caused an uneven surface finish, which showed as annular bands of differing roughness. Several grinding cycles were made, with a tool (X-axis) infeed between cycles of 2.5μm. The tool rotation speed was adjusted until one was found which gave an evenly-ground appearance. This speed (approximately 33000 r.p.m.) was used for all subsequent grinding operations.

It was necessary to restrict the maximum grinding tool crossfeed (Y-axis) so that there was no tendency to grind a significant spiral groove. The crossfeed F was set to 1mm/min, and the substrate was rotated at 60 revolutions/min. Thus the crossfeed per substrate revolution F_r was 1/60 = 17μm/rev. As illustrated by Figure 5.2, this crossfeed together with the tool radius of curvature r, would produce peak-to-valley "groove roughness" $p=F_r^2/8r$ (from the geometry of a circle). The The r.m.s. roughness would be $p/\sqrt{5}$ [180]. In the present case roughness would be 7nm r.m.s., which was negligible, being far smaller than the roughness expected from any grinding tool. The radial profile of the ground surface was measured by tracking a linearly variable differential transformer (LVDT) probe (Federal EHE 1083), which could resolve 0.1μm, across the surface using the driven Y-axis, but without rotating the substrate. Measuring over the step between the ground region and the surrounding region which remained polished showed that 30.7μm of material had been removed. The ground surface was indicated as concave, being 4μm deeper at the centre than at the edge. Since tool wear would be expected to remove relativly less material at the centre than the edge when feeding inwards

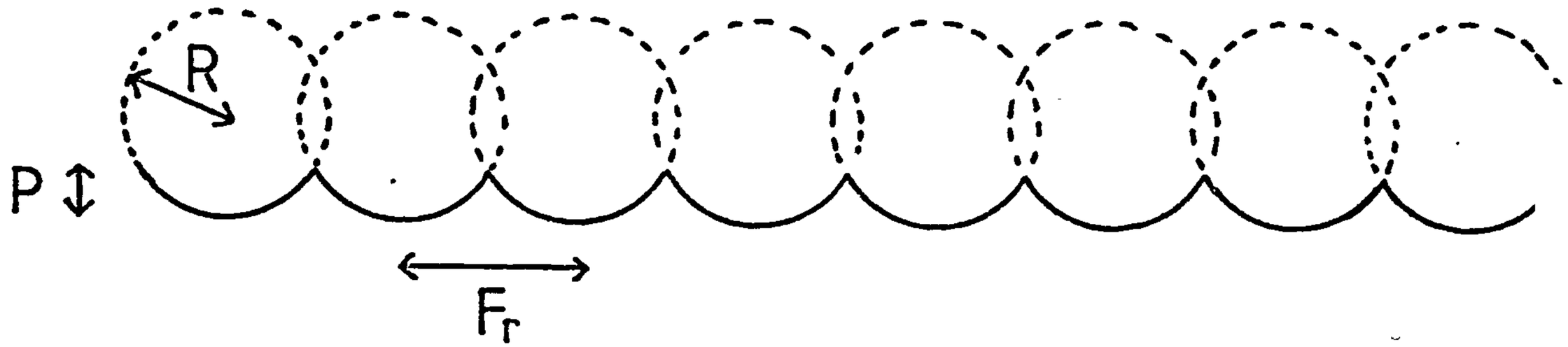

$$\text{PEAK TO VALLEY} \qquad P = \frac{F_r^2}{8R}$$

$$\text{RMS} \qquad = \frac{P}{\sqrt{5}}$$

Figure 5.2 Surface roughness due to turning tool radius (R) and feedrate (F)

towards the centre, it is difficult to explain this effect.

When rotating the substrate on the A-axis (Figure 5.1) the LVDT probe detected a slight anisotropy, there being a radial groove along a direction at about 10 deg to the crystal Z-axis. Visual inspection of the surface could not detect this groove, but three narrow radial bands with different roughness to that of most of the surface, at 120 deg angular separation, were just apparent.

A better compromise between tool wear and surface smoothness could perhaps have been obtained by using smaller diamond grit size in very much greater concentration. If a smaller depth than 2.5μm had been used for the final few cuts, then it may have been possible that the anisotropy effect would have been smaller.

The substrate was then polished, using an Engis hard felt mop which had been turned down to a cylinder of 5mm diameter. As with grinding, it was necessary to restrict the maximum tool feed so that there was no tendency to polish a significant spiral groove. As for the grinding tool, which was of the same diameter, the groove roughness would in theory be 7nm r.m.s. Although this was an order of magnitude greater than the ultimate surface finish which can be obtained with lithium niobate (see 3.6.1), this particular experiment was not intended to reach such performance. The contribution of this spiral-grooving effect was therefore regarded as negligible, especially since the deformation and wear of the felt tool would effectively increase its local radius of curvature, thus decreasing the groove roughness. The polisher was frequently loaded with Hyprez 1μm diamond paste. Fibrous material polishers such as the Engis felt mop must not be used at high surface speeds [124] because a regular surface structure ("orange peel") may be formed, perhaps because of resonant vibrations of the fibres. Unfortunately the slowest possible speed of the grinding spindle was very high (i.e. 20000 r.p.m.). The polisher was brought into

contact with the surface, then indexed-in by 100μm to produce some pressure. To polish a uniform amount from the entire surface, it was necessary in the first approximation (to Preston's law) to vary the radial feed at a rate inversely proportional to radial distance from the centre of rotation of the substrate. Because of lack of time, the area was divided into only four zones, the speed being constant within each zone. The zones and speeds were:

TABLE 7: VARIATION OF POLISHING FEED-RATE WITH RADIAL ZONE POSITION

ZONE mm	SPEED mm/min
0 to 2	10
2 to 4	3
4 to 5	1
5 to 6	0.5

28 polishing cycles were made, indexing in the polishing tool by 50μm after the second, fourth, sixth and sixteenth cycle. Most of the large grinding pits were removed, but the zones were clearly of unequal roughness. The last six polishing runs were made after slowing the feedrate in the roughest zone, 2 to 4mm, to 1.8mm/min. The LVDT gauge was tracked across the surface to measure the depth of material removed and the extent of the departure from flatness. 3.8μm had been removed at the rim (i.e. 0.13μm per polishing run on average), but only 1.3μm at an intermediate radius, and 2.8μm at the centre. The felt cylinder had worn considerably at the contact edge, thus being in contact with the central region for a longer relative time in the outer zones than planned. This would explain greater material removal at the centre of rotation. The surface was visibly rippled, as expected from polishing at a very rapid surface speed with felt material. The roughness average was measured by a Rank Talystep 10 stylus instrument as between 35nm and 85nm.

The region of greatest roughness was about 3mm from the centre in a crystal Z-axis direction.

5.2.3 Lens generation and polishing.

A second polished parallel $LiNbO_3$ substrate was mounted on the vacuum chuck for generating a lens. The LVDT probe was mounted in the grinding tool position to align the system (see Figure 5.1 for definition of the axes). The front face of the substrate was adjusted to be within 0.25μm of the Y-Z plane, the vacuum chuck was recentred on the spin table axis, and the Y slide moved until the probe indicated that the Z-axis intersected the A-axis. The Y-axis zero was set at this position. The LVDT probe spherical tip was then centred on the Z-axis by moving the probe tip and the X-axis until no change of reading was indicated when rotating the C-axis with the probe in contact with the vacuum chuck face near to the A-axis. The X-axis was set to zero at this position, then moved away from the chuck (and the probe moved down the Z-axis so that its tip was on the A-axis) to measure the position of the front face of the substrate and also therefore measure its thickness. This setting of the X-axis was called the "front face position".

The grinding tool was remounted and dressed to be of cylindrical shape with a sharp edge. Its axis was adjusted into the X-Z plane as indicated by the probe when mounted on the spin table. Its cutting edge was set on the Z-axis by moving the X-table to the front face position and adjusting the tool on a rack attached to the vertical slide until it just cut into a thin layer of engineer's blue tool-setting paint which had been applied to the surface. Finally the cutting edge was set on the A-axis by adjusting vertically until it cut a point into the paint rather than a circle.

Grinding was started with the X-table positioned so that, during the first cutting cycle, the tool only contacted the surface at the lens centre position. Surface

crossfeed was set to about 1mm/min. After making five cuts of 30μm each it was clear that tool wear was excessive - a flat of 3mm to 4mm had been worn onto the cutting edge of the tool (Figure 5.3). The radius of curvature specified at the lens centre is 10.933mm. For a grinding tool penetration depth of five 30μm cuts, i.e. 0.15mm, the diameter of the abraded region can be estimated using the expression of Appendix II as $(2x.15x10.933)^{0.5}$ = 3.6mm, which corresponds to the size of the flat on the tool. It seemed therefore that the tool was wearing at the same rate as the lithium niobate substrate, and that cutting was taking place over the entire surface of contact.

The resin-bonded tool was replaced by a 4mm diameter 120 mesh diamond-plated grinding tool, which was expected to wear less rapidly. Using cuts of 40μm depth, most of the lens depression was ground out. The circular boundary between the ground region and the previously polished regions of the surface was very badly chipped. The X-slide was fed in a further 300μm in cuts of 10μm depth each, with the crossfeed reduced to about 0.6mm/min. This change of parameters decreased the incidence of chipping, but the surface was still very rough. The previously used resin-bonded diamond grinding tool was redressed, set back in position, and three cuts of 10μm made. The LVDT gauge was fitted, and it was found that the lens was 280μm too shallow, rather than the 70μm expected from the X-table total movement. The underestimate of material removal by reading X-table travel was clearly because of wear in the tools, which in terms of total depth removed during this series of cuts was about 20%, considerably less than for the resin-bonded tool alone. For this depth of wear, the plated tool would have a flat of about 0.5mm width, which would, fortunately, fit into even the most curved part of the lens (2.6mm radius of curvature) with little profile error. The LVDT gauge was refitted to check the profile. Rather surprisingly, the probe did not deflect by more than 3μm when tracked with the same programme which was used when grinding the lens.

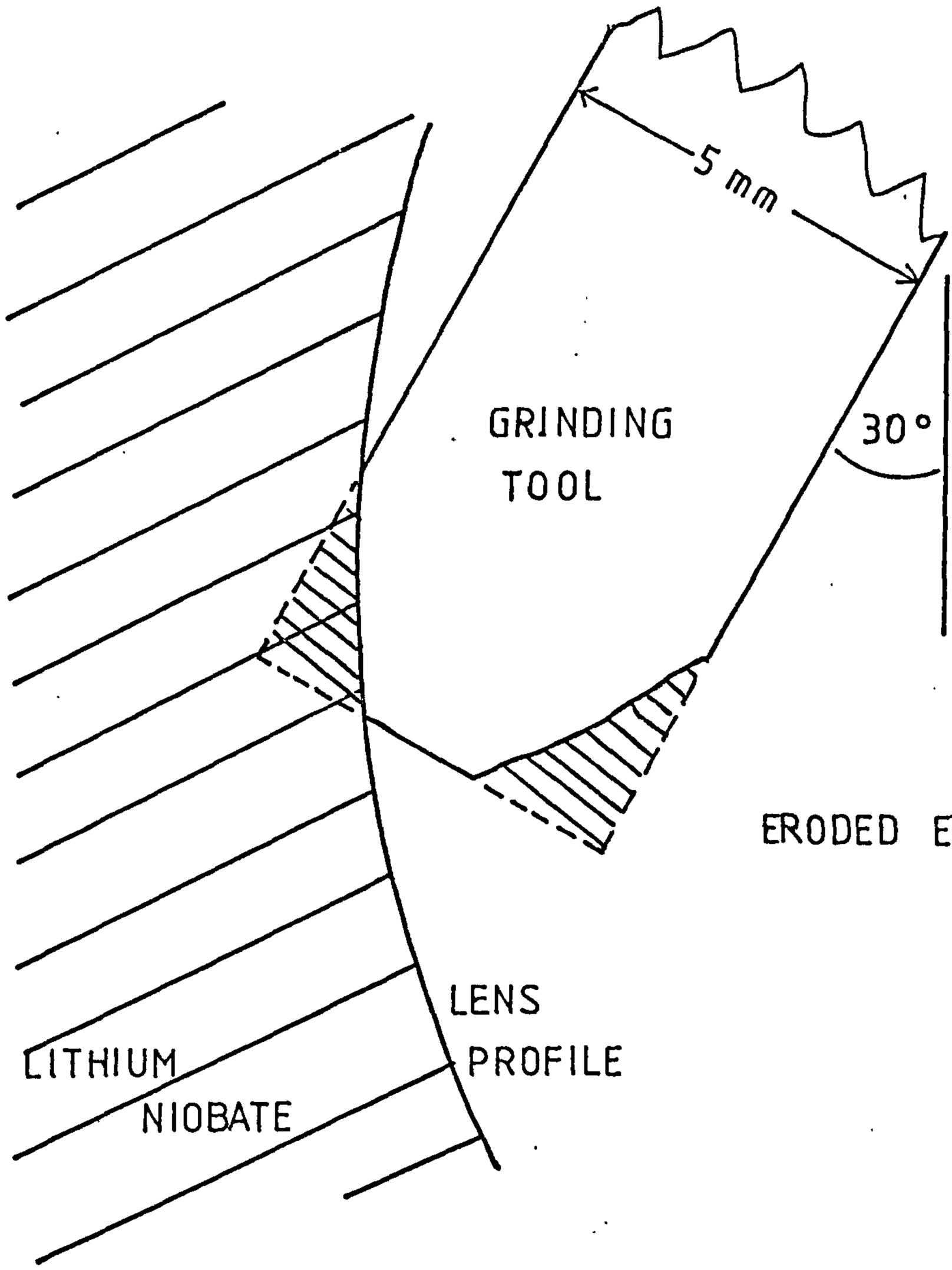

Figure 5.3
Wear of resin-bonded diamond grinding-tool when forming a lens depression in $LiNbO_3$.

Although the plated tool was expected to give much greater profile accuracy than the resin-bonded tool, the benefit of this greater accuracy would be lost because of the larger amount of polishing that would be required to remove the greater surface roughness. It was felt that it would be more useful to revert to grinding with the resin-bonded tool and obtain a surface finish which would require only a relatively small amount of polishing. A further 200μm depth was ground away using the resin-bonded tool, leaving 10μm for polishing. The last few cycles were taken at 0.4mm/min surface crossfeed, and the last cut was "sparked out", i.e. with no further feeding in of the tool, to remove some of the material which may have been elastically deformed by the tool rather than cut during the previous cycle. Although the surface appearance was generally of low roughness, several grooves and abrupt changes of roughness could be seen. These probably occurred where the flattened resin-bonded tool was cutting into regions next to the more highly curved parts of the lens profile.

A short time was available to attempt some lens polishing on the machine. This was carried out in the same way as described in section 5.2.2 for the flat component. The programme tape specified 20 annuli (corresponding to the circular arcs) rather than only four as used when polishing the flat substrate. This allowed finer resolution of the crossfeed rate required by applying Preston's law for uniform material removal. 20 cycles were made at 2 minutes each. The surface became smoother. An approximate check on the lens profile showed that the probe deviated less than 1μm over the surface, except for a 5μm depression in the region from 3.75mm to 3.78mm radius. This was the least-curved zone of the edge-rounding region, which was next to the most-curved zone of the inner part of the lens. The extra wear during polishing was probably due to flattening of the felt polishing tool. Since at least another 50 cycles would have been required to reach the correct lens depth, it

would clearly have been necessary to redress or renew the tool frequently to avoid increasing this source of error. Measurements made by a Talystep 10 instrument in the central region of the lens showed roughness averages between 150nm and 300nm, which confirm that a great deal more polishing was required.

5.3 SINGLE-POINT DIAMOND TURNING OF PLANE LITHIUM NIOBATE SURFACES.

Following the work of Mergerian et al [105], a review was made of machines which were potentially able to produce geodesic lenses. Those identified are summarised in Table 5.8. Of the few which could possibly have been available for the author's use, it was felt that the Hardinge CHNC lathes (e.g. at Barr and Stroud Ltd in Glasgow, and at Fife Autocam Ltd in Glenrothes) were not quite precise enough, the Moore aspherising machine at Bridgeport, Connecticut, was expected to be satisfactory (it was used by Mergerian et al), and the other machines (Bryant Symons, Heliotrope and Ealing-Beck) all required the development of at least one feature. However, since the last three machines were available within the U.K., the author attempted to make arrangements for carrying out such development. This work did not progress further than diamond-turning of plane samples, but this provided useful information on the ultimate degree of surface finish which could be expected of diamond turning of lithium niobate.

A study of the turning of plane $LiNbO_3$ components of different orientations was made using a 17F8A facing lathe at Bryant Symons Ltd. This lathe was equipped with a Westwind air-bearing spindle which was driven by an in-line AC motor, and used triply-filtered air at a pressure of 56×10^3 kg m^{-2} to maintain its axial and radial

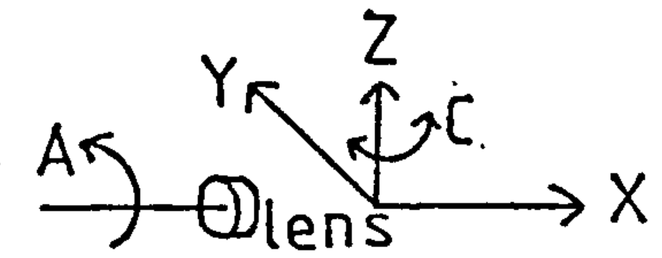

TABLE 8A: MACHINES WHICH COULD POSSIBLY DIAMOND-TURN GEODESIC LENSES, WHICH MAY BE PURCHASED.

MACHINE	AXES	CONTROL	ACCURACY OVER 50mm μm	ROUGHNESS nm Ra	SMALLEST NC STEP μm	COMMENTS
Harrison M300 lathe	X,Y,A	manual	15			used for ultrasonic tools
Hardinge lathes	X,Y,A	manual	<2			have made metal aspherics
contact lens lathes (City Crown, Nissel, Chase, etc)	R,θ,A	cam	<10			
Hardinge CHNC	X,Y,A	CNC	1		0.25	diamond-turning of metal and plastic optics
Bryant Symons MF58A facer	X,A	manual	<0.1	10		diamond-turning of metal, germanium and plastic optics
Pneumoprecision MSG 325	X,Y,A	CNC	0.1	25		aspherics in metal, Ge etc
Moore aspheriser	X,Y,A,C	CNC	0.1		0.2	$LiNbO_3$ geodesic lenses, etc

TABLE 8B: MACHINES WHICH COULD POSSIBLY DIAMOND-TURN GEODESIC LENSES, NOT AVAILABLE FOR PURCHASE.

MACHINE	AXES	CONTROL	ACCURACY OVER 50mm µm	ROUGHNESS nm Ra	SMALLEST NC STEP µm	COMMENTS
Heliotrope Aldershot	R,θ,A	CNC cam	<<1	1.5	0.025	flat,aspheric metal mirrors. Subcontract only.
Rank Optics Taylor Hobson Leicester	R,θ,A	cam NC CNC	0.75			aspheric mirrors, lenses in metal, Ge etc. Subcontract only if not busy.
Ealing Beck Watford	R,θ,A	cam		4		off-axis metal parabaloids of long radius of curvature. Subcontract only.
Philips "Colath" Holland	X,Y,A	NC	0.5	<10	0.016	"bi-asphere" plastic lenses for video disc reading. In-house use only.
Honeywell USA			0.3	40		aspherics in metals, plastics, semiconductors. Subcontract only.
Bell and Howell USA	X,Y,C,A	NC	<0.7			aspheric components. Subcontract only.
Battelle ΩX USA	R,θ	CNC	0.075	1.2	0.004	In-house and subcontract only.

position within a claimed tolerance of 0.12μm. The cross-slide was driven from an air-pump motor on a hydro-dynamic oil bearing with straightness quoted by Bryant-Symons Ltd to be within 0.25μm over any 125mm of travel. 3mm and 4mm thick Y- and Z-face lithium niobate substrates had been made flat for vacuum chucking by lapping one side with a 12.5μm alumina slurry. They were mounted on a vacuum chuck, and the whole spindle assembly was dynamically balanced when rotating at 1032 r.p.m. using a Shenck vibration indicating instrument. All substrates but one were turned using white spirit coolant, fed as an air-mist spray at 550 x 10^3 kNm^{-2}. Table 9 summarises the results of several turning experiments. The depth of cut was progressively reduced from 25μm for roughing through 10μm or 5μm to 2.5μm for the final cuts. Three Shaw diamond cutting tools were used. They were of circular shape, two of radius 0.76mm and one of radius 0.5mm. The tools had 12 deg arc clearance, and no top rake (Figure 5.4). The diamond tools frequently chipped at the cutting position after cutting very little material (e.g. 100μm) producing grooves which were rough enough to show obvious diffraction colour on the $LiNbO_3$. The tools were rotated as often as was possible to expose fresh sharp cutting parts of the edge.

Surfaces which had been cut with a fresh unchipped diamond had areas of surface roughness close to the 6nm Ra expected from the tool feed (12μm/rev) and diamond radius of curvature (0.76mm). However this only occurred in certain sectors, radiating from the centre of rotation of the spindle (Figure 5.5). Other sectors, particularly those centred on the X-axis, exhibit 5 to 10 times greater roughness. Varying the spindle rotation speed between 1000 and 3000 rpm made no discernible difference. Diamond turned Z-face substrates showed a more uniform surface finish, but they were rougher than the roughest parts of Y-faces. On the several Y- and Z-face substrates which were turned the number, directions and angular extent of the smoother sectors seem to depend very

TABLE 9

DIAMOND-TURNING OF PLANE LITHIUM NIOBATE SUBSTRATES ON BRYANT SYMONS FACING LATHE

SAMPLE CUT/NO.	SIDE	DIAMOND	SPINDLE SPEED, COOLANT	CUTS TAKEN	RESULTS
Y/3A	polished	K439	1032rpm white spirit	8x10µm 1x 5µm?	cut into metal, diamond chipped.
Y/3B	polished	K439 moved	"	6x5µm	Rough & smooth sectors 7.5nm to 35 nm Ra. Surface not flat.
Y/10A	smoothed	not moved	"	13x5µm 4x2.5µm	to clear scratches. diamond chipped. Sectors:30-150nm Ra. Not flat.
Z	front smoothed	not moved	"	12x5-12µm (=100µm)	roughing cuts 190nm Ra.
Z	back	not moved SA437	" "	1x25µm 3 x 5µm 1x2.5µm	roughing cut 125nm Ra.
Y	front sawn	SA439	"	9x25µm	roughing.
Y	back ground	not moved SA437 moved round	" " "	1x25µm 3x 5µm 1x2.5µm 2x 5µm 1x2.5µm	roughing 100nm Ra,but very regular-chip seen on diamond. Rough & smooth sectors:typically 100nm Ra. Another chip.
Z	back	SA437 only good part	" soluble oil +few % lard oil	1x5µm 1x 5µm 1x2.5µm	230nm Ra. 205nm Ra.
Y/10A	same side as before	SA437 0.5mm radius tool	" white spirit 3000rpm	3x2.5µm 2 x 5µm 2x2.5µm 3 x 5µm 2x2.5µm 3x2.5µm	only now cut over whole face. 160nm Ra. Much diffraction colour. Probably not clear of diamond chip areas. now cut all over. Sectored; along better X direction- 90nm Ra. Above sector is now 75nm Ra.

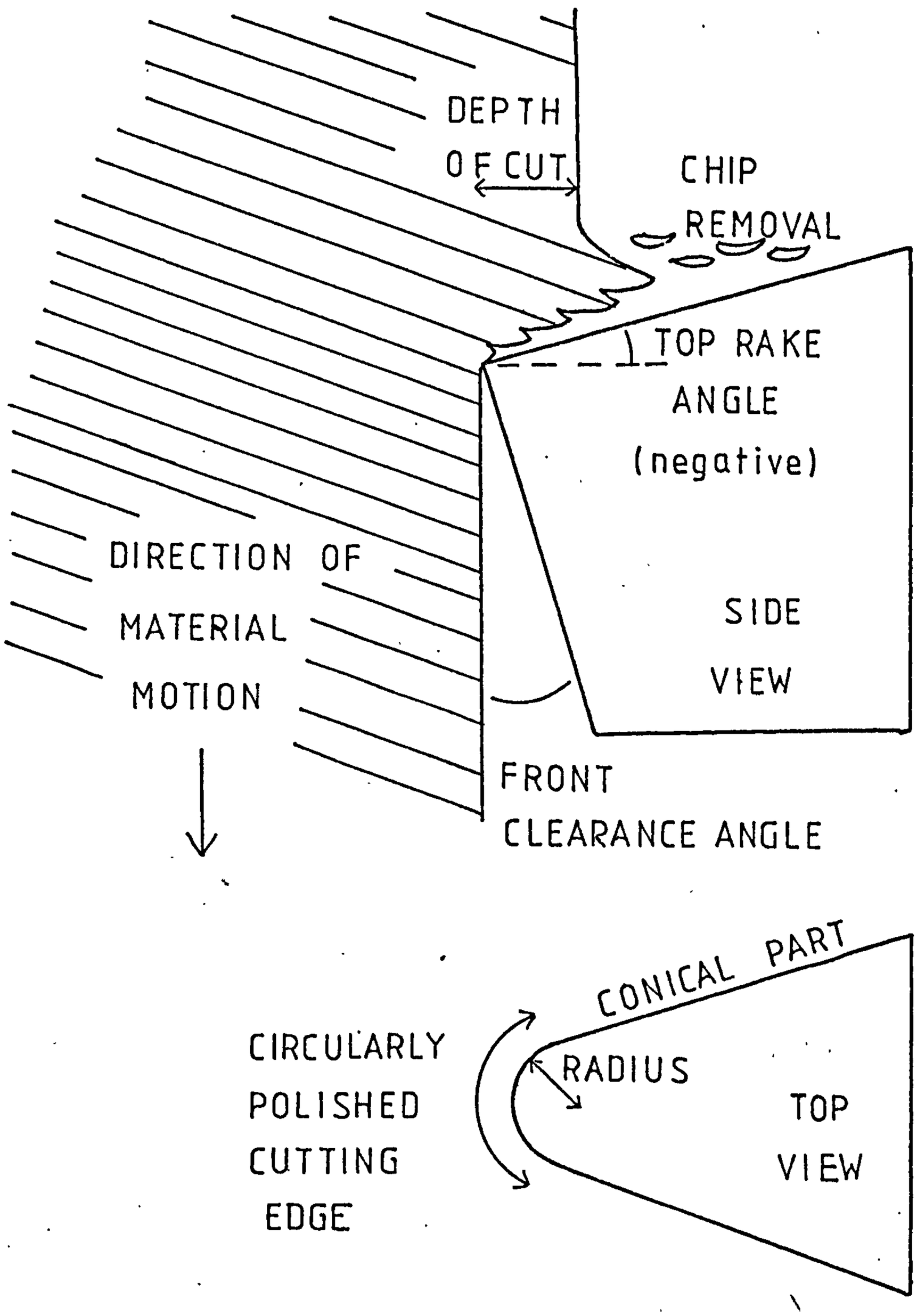

Figure 5.4 Single point diamond-turning tool: definition of parameters.

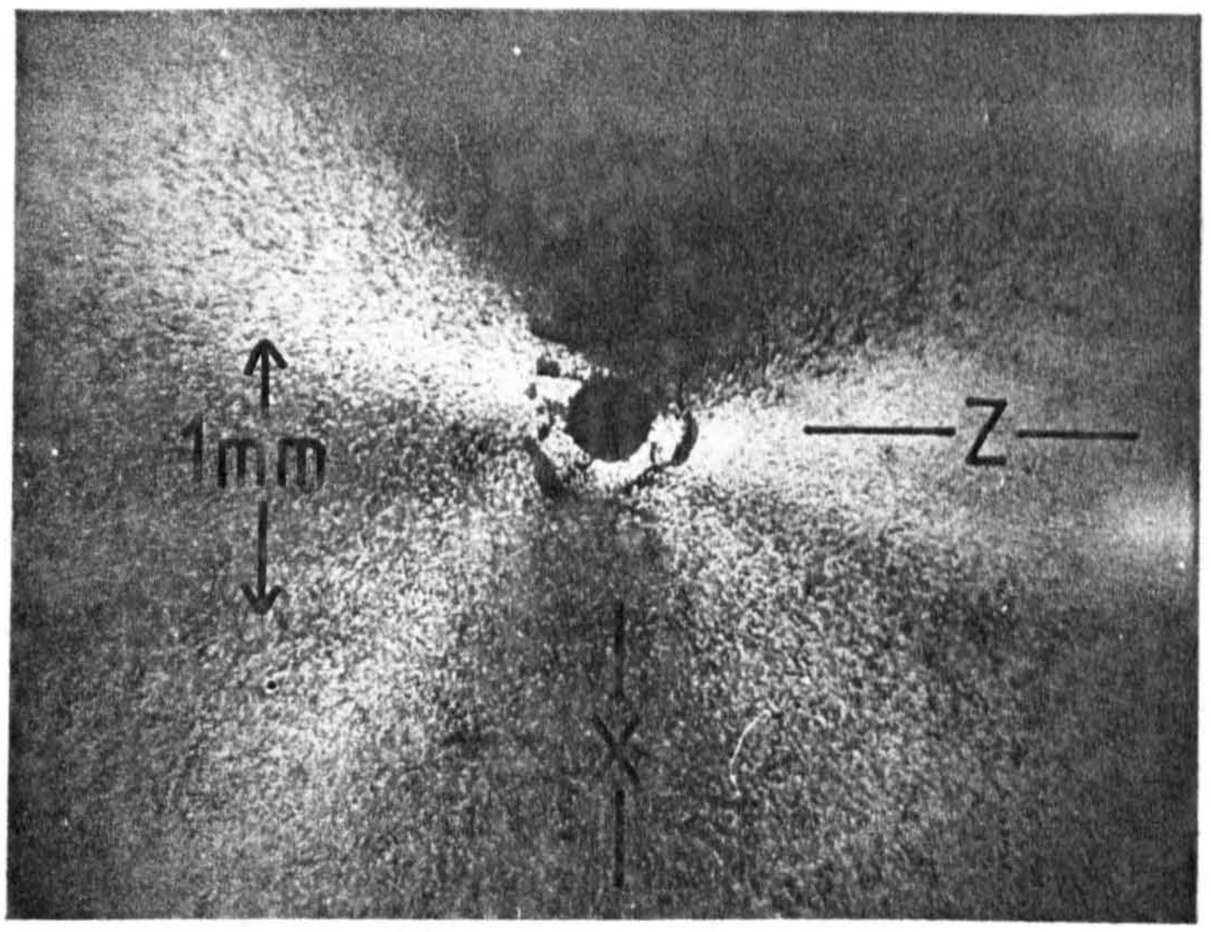

Figure 5.5 Photograph of plane, diamond turned $LiNbO_3$ Y face.

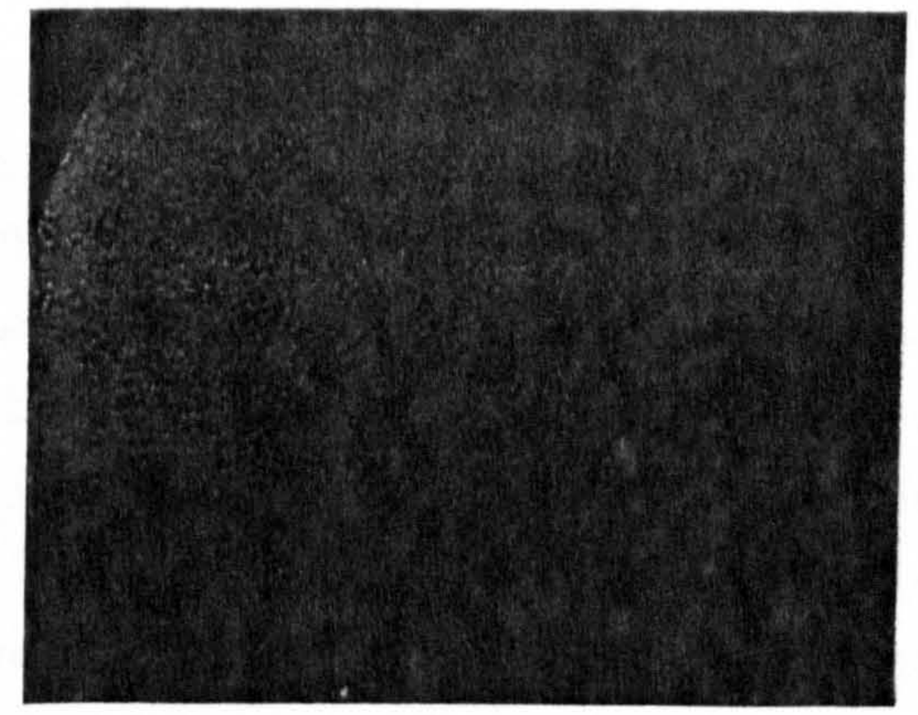

BRYANT SYMONS LTD.
1μM TOOL FEED
OPTICAL MICROSCOPE 310X

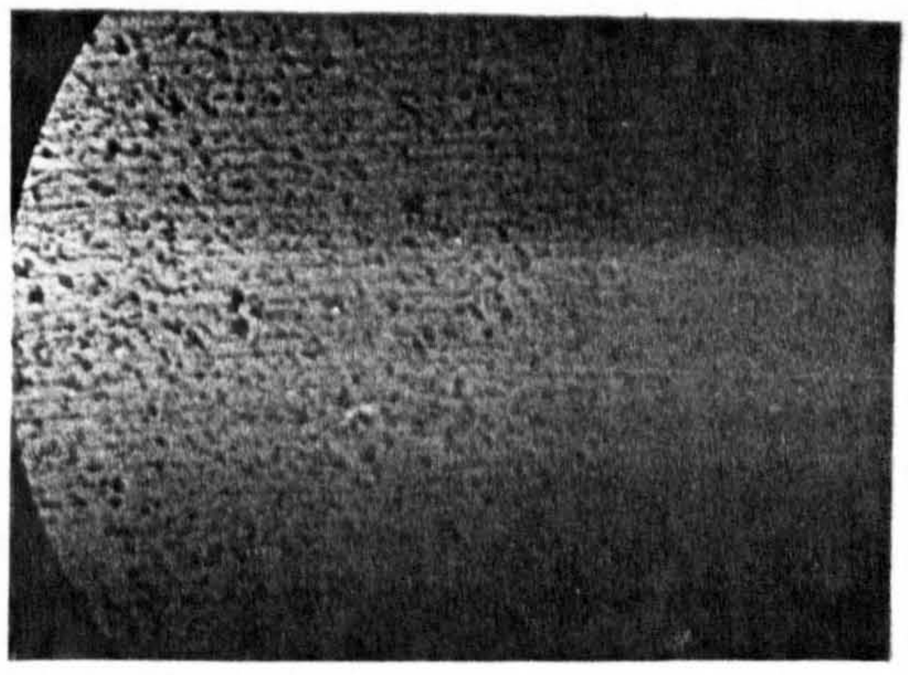

EALING BECK LTD.
3μM TOOL FEED LINES VISIBLE
OPTICAL MICROSCOPE 310X

Figure 5.6 Photomicrographs of plane, diamond turned $LiNbO_3$.

critically on precise orientation of the surfaces to the crystal planes (Figure 5.5). Variation in face angle of a few minutes of arc gave rise to different numbers of sectors. These effects may be related to the mechanical constants of the $LiNbO_3$ in an analogous way to the variations in wear of diamond tools when turning with small changes in angle from planes of symmetry [181].

The surface profiles of the turned faces were assessed with a Fizeau interferometer working at 633nm wavelength (at Barr & Stroud Ltd), and by stylus tracing on a Talysurf 4. These instruments indicated that saddles and grooves existed in the turned surfaces. Some of this lack of flatness was probably due to the vacuum chuck pulling the sealing face down from a convex profile to flat, so that the turned face would spring away from nominal flatness when released from the vacuum. There would probably be similar distortions due to small dust particles being trapped between substrate and vacuum chuck, and other distortions related to the non-uniform vacuum hole pattern. However one departure from flatness seemed due to the turning process. It took the form of a narrow groove, about 20 deg wide, and about 0.15µm deeper than the surrounding area. The groove radiated from the position on the substrate which was at the centre of rotation of the spindle along the sector which was smoothest. On the Y-positive face, this sector was in the direction of about 15 deg arc from the positive Z-direction towards the positive X-direction, when the face had been rotating clockwise as seen from the cutting tool.

Fig 5.6 shows the microscopic appearance of plane diamond-turned $LiNbO_3$ surfaces. The upper photograph shows a Y-face Bryant-Symons sample discussed above. The lower shows one diamond-turned at Ealing Beck Ltd, using the greater tool crossfeed of 3µm/rev., a diamond of 0.5mm radius of curvature, and 10µm final depth of cut. The substrate was mounted about 120mm away from the spindle axis. The surface roughness is about 50nm Ra. The figure clearly shows tool track marks.

5.4 DIAMOND-TURNING OF GEODESIC LENSES.

5.4.1 Diamond-turning on a contact-lens lathe.

The use of small, moderate precision, special purpose lathes for diamond-turning of plastic contact lenses has been well established (see e.g. manufacturers literature from City Crown Ltd., Nissel Ltd, Chase Ltd). Although these lathes are only capable of about the 10μm precision needed for opthalmic lenses, they are well-suited for producing small-radius curved surfaces and lenses of the size required for the spectrum analyser.

Diamond-turning of spherical depressions in several small sample pieces of Y-cut $LiNbO_3$ was performed by J.F. Smith on a CLM (Robertson-City Crown) lathe (Figure 5.7) at the premises of Dominion Contact Lenses Ltd. The spindle speed used was 3500 r.p.m. Three samples were machined. Sample A was cut with a 'Dominion Contact' diamond having a tip radius of approximately 0.75 mm. A nominally spherical surface with an 8.0 mm radius of curvature was machined. No coolant was used. Samples B and C were cut with a Triefus diamond tool having a tip radius of approximately 1.5 mm, no top rake and clearance angle 18 deg. Drip-fed white spirit was used as the machining coolant. In all cases the tool was hand-fed into the work-piece. The somewhat rougher surface finish obtained on sample C was attributable to slight chipping of the diamond tool.

The finish obtained in all cases was specular: this commonly indicates a surface finish with less than 0.5 μm roughness. As with the plane samples turned at Bryant Symons, significant sectoral variations in surface roughness were obtained. This is evident in the magnified photograph of sample B, Fig. 5.8. Periodic machining marks are also clearly evident. (The pronounced demarcation into inner and outer zones is an artefact due to the presence of a similar lens depression on the opposite face of the sample).

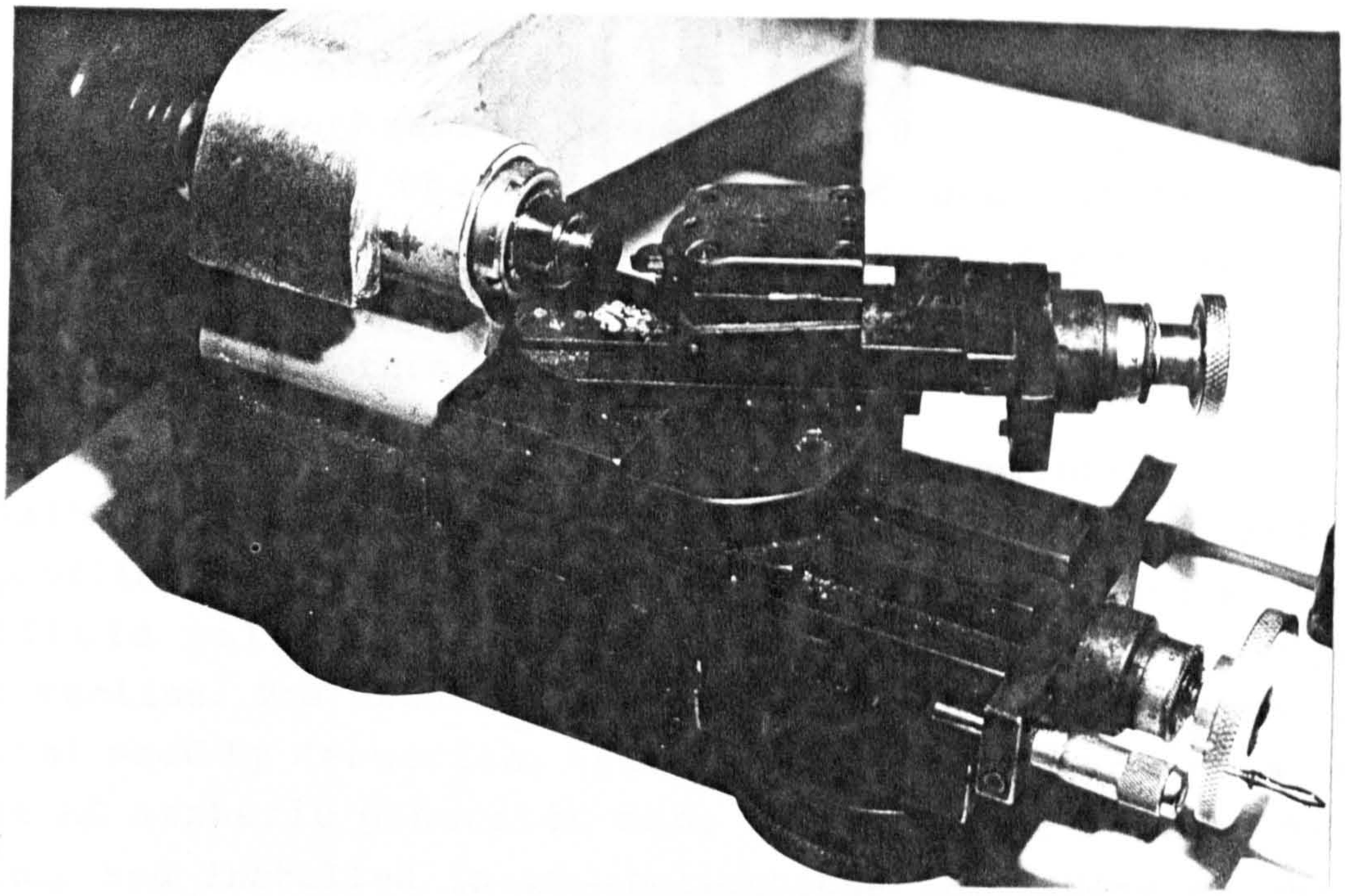

Figure 5.7 Diamond turning lathe for opthalmic contact lenses.

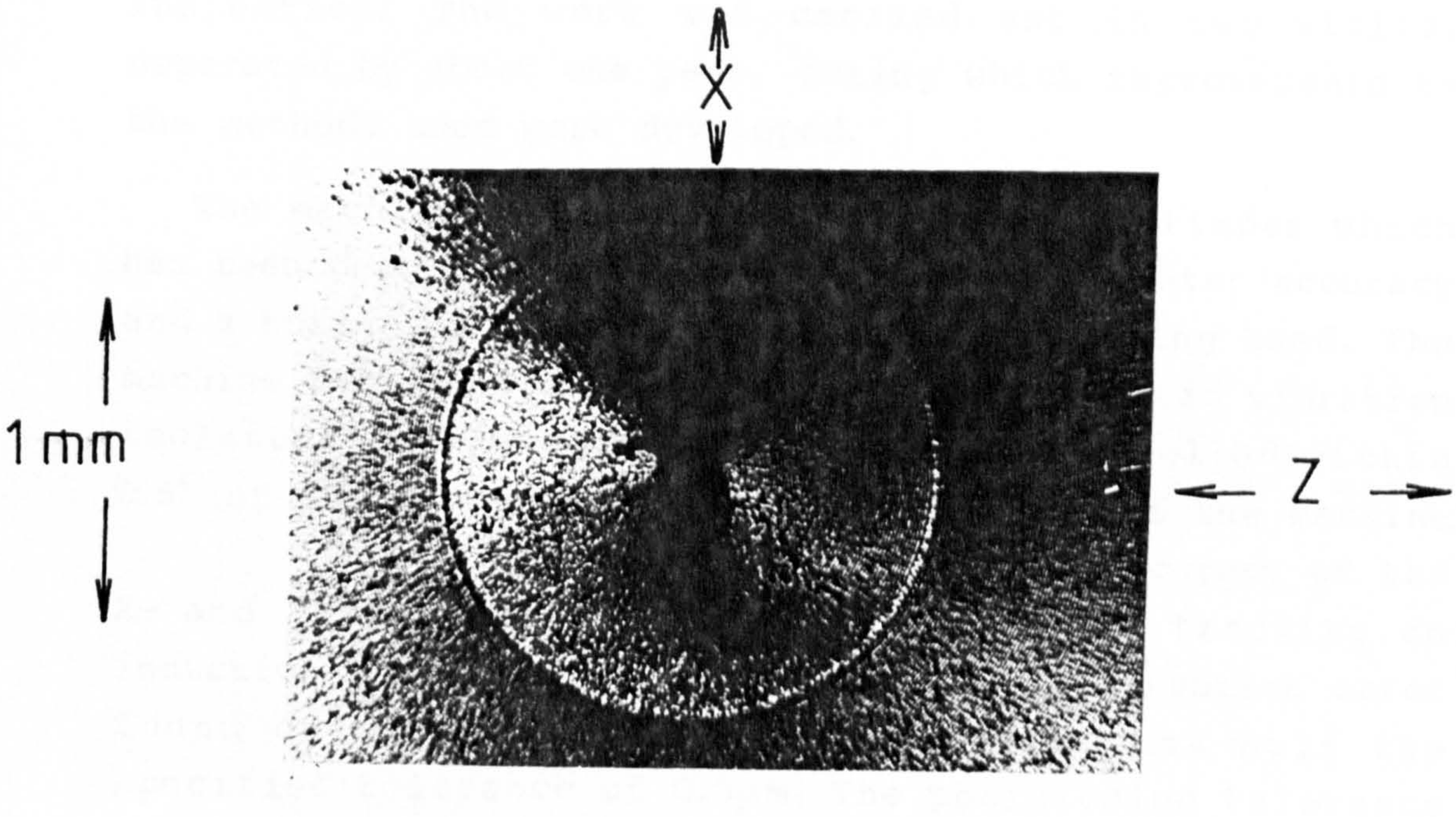

Figure 5.8

Phase contrast photomicrograph (35x) of central part of a spherical lens which was diamond turned on a contact lens lathe

Measurements carried out with a Talystep machine indicate roughness as low as 100 nm Ra, - only about five times rougher than obtained over most of the plane samples, using a much more massive and costly machine.

5.4.2 Diamond-turning on a high-precision machine.

According to Mergerian [105,106], diamond-turning of lithium niobate geodesic lenses provided sufficient profile accuracy and a surface finish which required very little polishing until smooth enough for waveguide formation. The author arranged to use the same machine as that used by Mergerian, this being the prototype of the M-18 AG aspheric generator made by the Moore Special Tool Co., and installed in an applications laboratory at their premises. The author prepared CNC data tapes and Y-cut $LiNbO_3$ substrates, supervised the Moore operator to produce geodesic lenses, and carried out in-process inspection. The work was carried out in two visits, separated by about one year, during which improvements to the methods used were developed.

The machine was similar to the G18 jig grinder which has been described in section 3, but with greater accuracy and a turning tool post rather than a grinding head. The machine was mounted on self-levelling pneumatic vibration isolators, and housed in a clean room, controlled within 0.5^{o} of $20^{o}C$. Figure 5.9 shows a photograph of the machine.

The straightness accuracy of the X- and Y-axis cross slides was tested by tracking an inductive probe along an optical flat. The greatest error found over any 25mm section was less than half the specified tolerance of 0.5µm. The positioning tolerance over any 25mm was also specified as within 0.5µm. The A-axis movement was provided by a model 1230 rotary table with truth of rotation specified as less than 0.4µm. This axis was used to rotate the turning tool about its cutting point so that it was always normal to the profile being cut, and so that the same part of the diamond was always

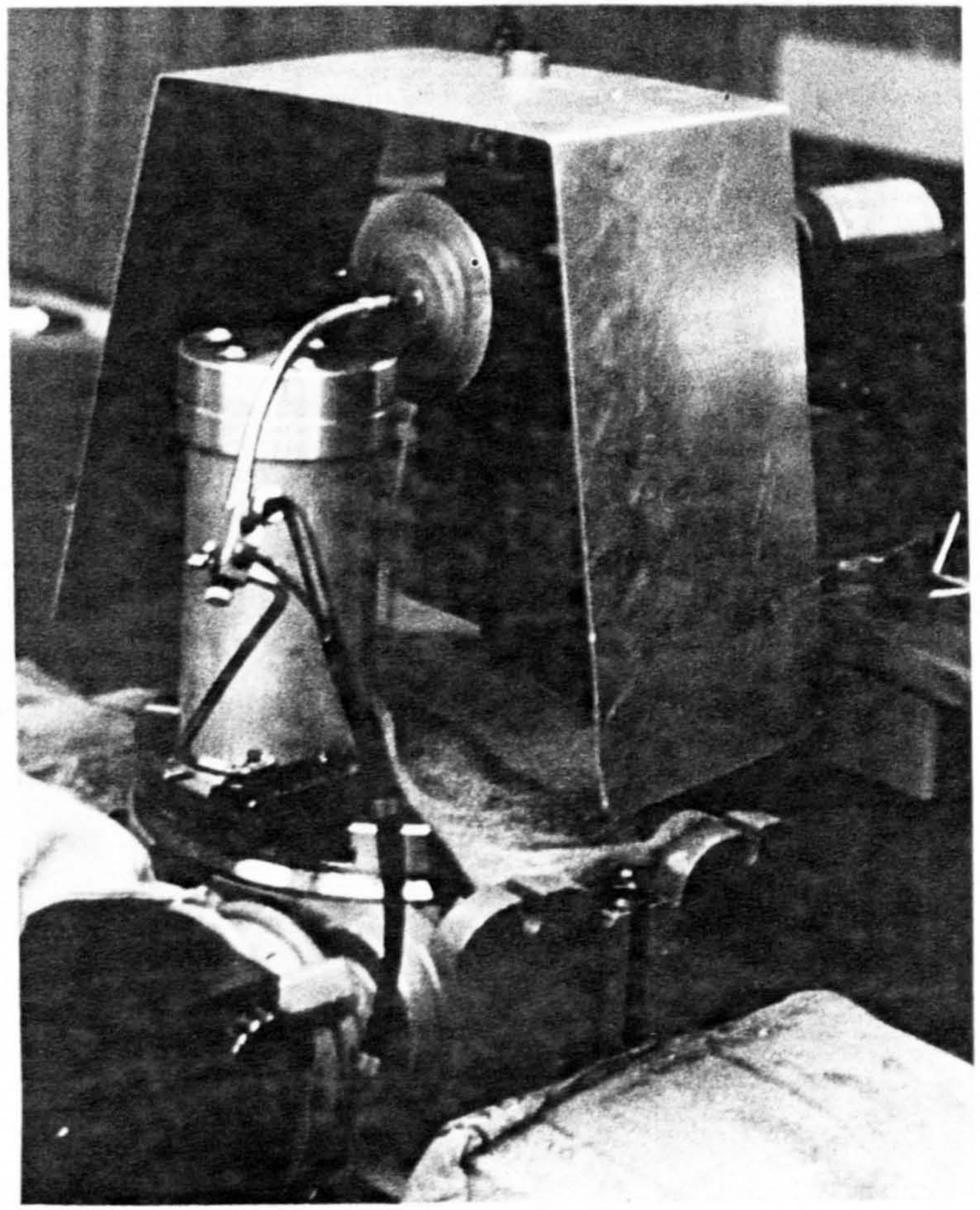

Figure 5.9 Moore aspheric generating machine

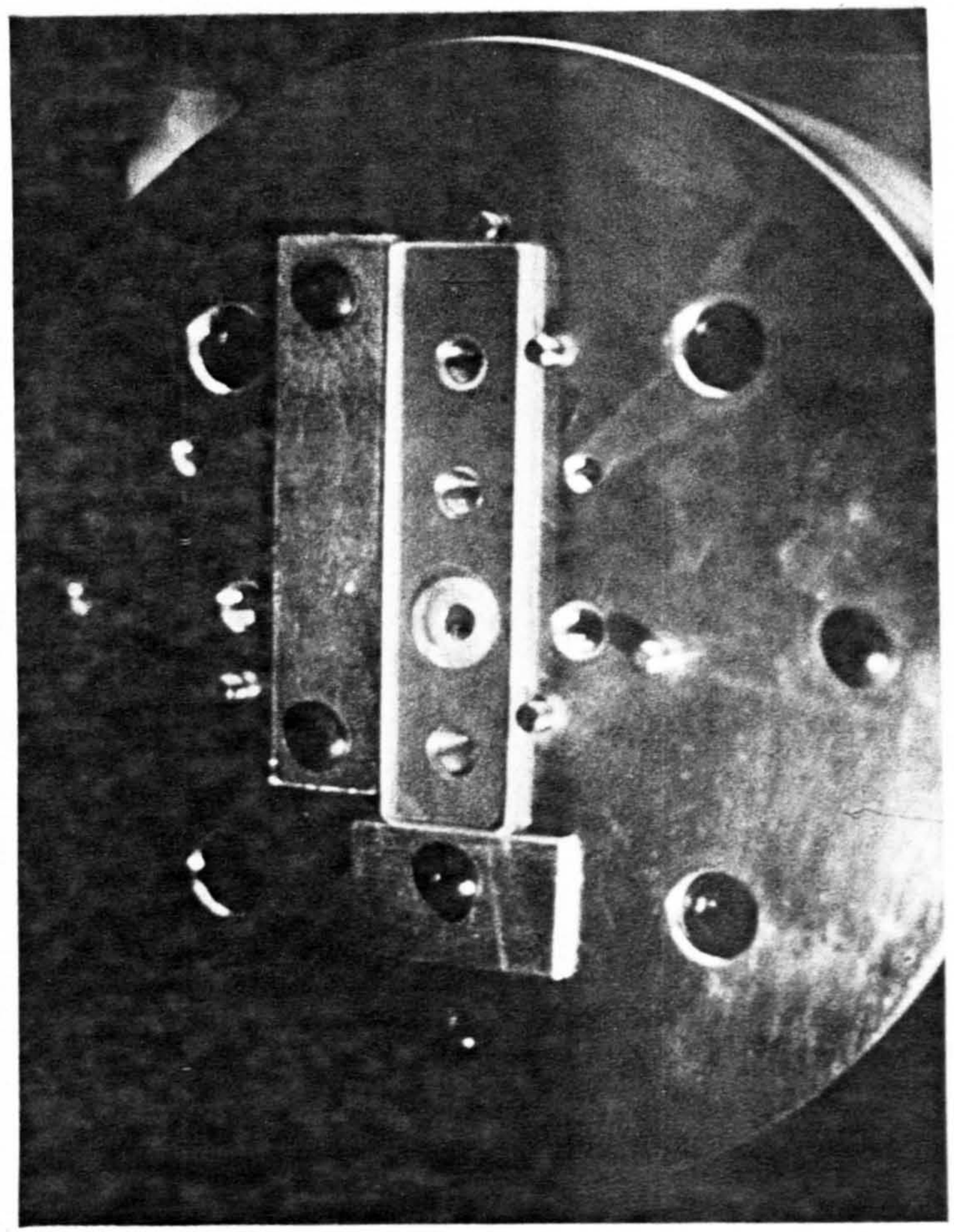

Figure 5.10 Vacuum chuck for holding IOSA substrate

used and no corrections to the X- and Y-axis positions were necessary for the shape and size of the diamond tip.

The toolpost consisted of an aluminium tube of about 100mm diameter bolted down to the model 1230 rotary table. A steel head was mounted onto the top of the tube and held the measuring probe of a Federal model EHE 1048 gauge, a diamond for rough-cutting and another for fine-cutting. The holders were adjustable, those for the tools being manufactured by the M.A.Aloris Company. The tips of the tools and the probe were set to the same radius on the toolpost head, and the whole toolpost mounted onto the A-axis spin table with this radius 248mm above the centre of the table. The head could be rotated and precisely located by dowel pins so that the two tools and the probe tip could be indexed in turn to be above the centre of rotation of the A-axis. The diamond tools were made by J.Robert Moore Co. The diamonds were mounted on 6.3mm square shanks, and had been polished to a circular edge of radius 0.76mm over 50 deg with clearance 10 deg and negative rake 1 deg. The cutting edge was free of chips and waviness as seen under at least 500x magnification. An air-mist oil spray nozzle was fitted to the tool post so that it blew a mineral lubricant/coolant (Mobil Mobocut 34) upwards and across the top of the diamond at an angle of about 30 deg to the X-Y and Y-Z planes to remove the $LiNbO_3$ chips.

The spindle was a Professional Instruments Co. model 4B 100mm diameter air bearing spindle, run at 760 x 10^3 Pa pressure of filtered and dried air, and driven by a DC servo motor via a phosphor-bronze universal coupling during the first visit, and by a flexible copper bellows during the second visit. The spindle radial runout was specified by its manufacturer as less than 0.1μm, and the axial runout 0.05μm.

5.4.3 Additions and setting adjustments to aspheriser

A substrate-holding chuck was designed by the author and made in an aluminium alloy at Moore using a Moore jig grinding machine and the aspherising machine (Figure 5.10). A central hole and four mounting holes were drilled into an aluminium disc 114mm in diameter and 37mm thick to enable mounting onto the air-bearing spindle. Using a diamond tool on the aspherising machine both sides were faced flat and the edge turned concentrically. The chuck was 114.219mm in diameter. Using the jig grinder seven holes were bored to allow substrates to be held down by vacuum, and five holes were bored and fitted with steel locating pins. The positions of these pins relative to the centre of the chuck were measured by a Moore Universal Measuring Machine within 0.5μm accuracy. A substrate could be mounted against three pins, two pins being in contact with the straight edge which had previously been a polished inspection face of the crystal boule, and the substrate was then held down by a row of four vacuum holes. In this position one lens could be turned at a distance of 18.9870mm from a short edge of the substrate - thus allowing about 0.5mm beyond the designed focal length for edge-polishing for end-fire coupling. By rotating the substrate by 90 deg it could be located against another set of three pins and held by the other row of vacuum holes to turn a second lens at a distance 17.9695mm from the centre of the first. The centre of each lens was positioned 7mm away from the polished edge of the substrate.

During the first visit, the substrates had to be parallel within 10 sec arc in order for the wedge across a lens diameter not to exceed one machine slide step of 0.2μm. It had not been possible to prepare all of the substrates to this standard, so on the second visit modifications were made to allow a limited amount of tilt to bring the front face of the substrate at the lens turning position as perpendicular to the Y-axis as could

be detected by the LVDT gauge (which was about ±0.1μm over a diameter of 12mm). A circular groove was milled into the rear face of the vacuum chuck and an O-ring fitted. Four levelling screws were added so that the chuck could be tilted in any direction relative to the air-bearing spindle face.

As with the jig grinding machine of section 5.2, the aspheric generator cross-slides could be moved in 0.2μm steps and the rotary table in 13 sec arc steps under the control of a General Electric Model 550 computer. Paper tapes were prepared in a similar way to that described in section 5.2. The data was required in a slightly different form and the lens design axes were transformed in a different way.

During the second visit to the Moore company the profile was approximated by a series of circular arcs as discussed in Chapter 2.4.2. This had not been developed for the first visit to use the machine: on this former occasion the lens design profile was described by an approximation using 96 linear interpolation steps. These steps were first computed using the Sottini, Russo and Righini lens-design programme on the GEC 4070 minicomputer, so that all interpolated points were within 0.2μm (the machine step size) of the ideal profile. Table 10 gives the machine coordinates for the ends of the interpolation sections. The A-axis coordinate was defined in terms of the proportion of a 360 deg anticlockwise rotation, i.e. $A = -(\tan^{-1}((R_i-R_{i-1})/(Z_i-Z_{i-1}))/360$, where the subscripted R and Z values are adjacent lens profile coordinates in the table.

Figure 5.11 illustrates a problem which was not realised until the first few cutting cycles had been made on a substrate. At the end of one linear path, the circular edge of the diamond tool cut beyond the next linear path to be followed. At the start of the next path, the diamond tool rotated to become normal, and penetrated into material along the previous path. The depth of

TABLE 10: LINEAR INTERPOLATION POINTS USED FOR DIAMOND-TURNING ON A MOORE ASPHERISING MACHINE

DEPTH mm	RADIUS mm	DEPTH mm	RADIUS mm
0.0000	5.0000	0.6644	3.5117
0.0013	4.9773	0.6897	3.4568
0.0042	4.9509	0.7239	3.3783
0.0120	4.9013	0.7585	3.2943
0.0160	408802	0.7829	3.2321
0.0202	4.8602	0.8026	3.1802
0.0248	4.8395	0.8222	3.1268
0.0370	4.7905	0.8470	3.0568
0.0432	4.7677	0.8698	2.9900
0.0534	4.7325	0.8890	2.9314
0.0608	4.7082	0.9117	2.9600
0.0671	4.6882	0.9306	2.7983
0.0746	4.6654	0.9528	2.7233
0.0892	4.6230	0.9639	2.6653
0.0974	4.6002	0.9856	2.6064
0.1099	4.5665	1.0071	2.5260
0.1201	4.5402	1.0240	2.4600
0.1280	4.5202	1.0413	2.3900
0.1378	4.4958	1.0572	2.3233
0.1549	4.4548	1.0741	2.2500
0.1649	4.4316	1.0917	2.1700
0.1796	4.3980	1.1065	2.0998
0.1923	4.3700	1.1236	2.0151
0.2015	4.3499	1.1356	1.9528
0.2135	4.3242	1.1473	1.8900
0.2330	4.2835	1.1630	1.8019
0.2446	4.2598	1.1768	1.7200
0.2615	4.2259	1.1912	1.6300
0.2765	4.1964	1.2033	1.5500
0.2874	4.1754	1.2160	1.4600
0.3014	4.1485	1.2274	1.3742
0.3233	4.1076	1.2379	1.2900
0.3365	4.0833	1.2484	1.2000
0.3554	4.0489	1.2580	1.1100
0.3728	4.0180	1.2659	1.0300
0.3852	3.9962	1.2741	0.9400
0.4013	3.9681	1.2815	0.8500
0.4255	3.9267	1.2881	0.7600
0.4402	3.9018	1.2934	0.6800
0.4613	3.8668	1.2986	0.5900
0.4809	3.8346	1.3030	0.5000
0.4948	3.8120	1.3066	0.4142
0.5129	3.7828	1.3097	0.3205
0.5393	3.7409	1.3114	0.2541
0.5556	3.7154	1.3128	0.1877
0.5768	3.6813	1.3140	0.0938
0.6007	3.6386	1.3144	0.0000
0.6230	3.5962		
0.6435	3.5554		

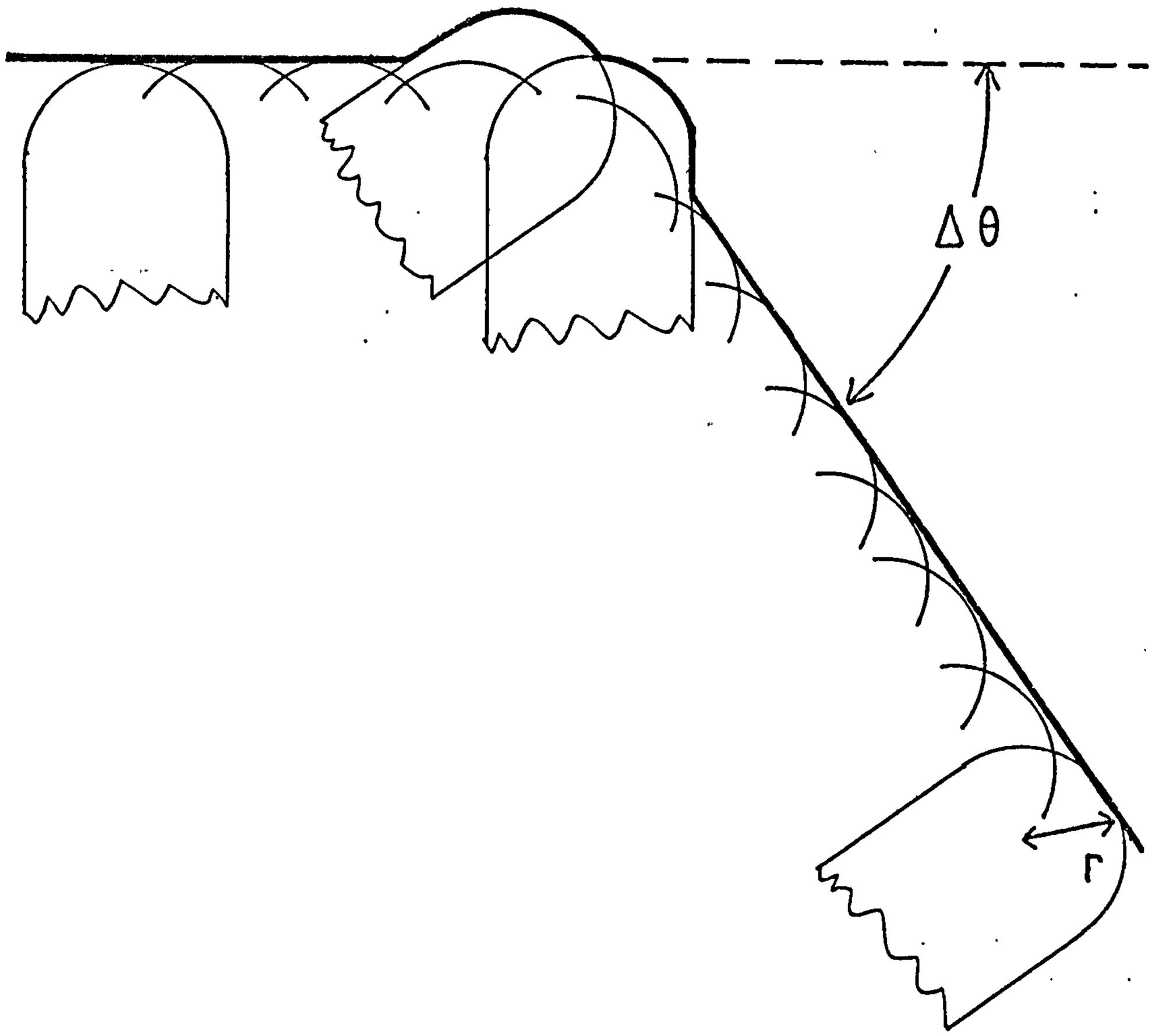

Figure 5.11
Envelope of diamond-turning tool-path at a junction between linear-interpolation sections.

penetration of these two grooves depended on the angle between the linear sections A and on the tool tip radius r according to the expression r(1 - cos A). When turning the first lens, a very conspicuous groove appeared near the edge-rounding boundary. Here the angle A was 2.6 deg, for which the calculated groove depth was 0.8μm. The data were changed so that the potential groove was just the same size as a machine step (0.2μm) - this point on the lens surface was made 0.5μm shallower than the Sottini design, and the angle A became 1.5 deg. After the next cutting cycle the groove could not be seen.

The various components of the machine were aligned as follows (see Figure 5.9). A tool setting stub had been previously made and checked by the measuring machine. This rod fitted onto the centre of the spindle, and by rotating it against the fixed LVDT probe it was adjusted to be central to the spindle within 5μm. A precisely semicircular part had been ground away from the end of the rod. A microscope was mounted onto a table set parallel to the X-Y plane. It was adjusted in height and direction until the cut-away diameter line of the stub always crossed the centre of the eyepiece graticule when the stub was rotated. The microscope was thus focused onto the centreline of the spindle. The stub was removed and the rotary table was rotated, adjusting the diamond tool height and position until all of its cutting edge could be focused at the microscope crosswires. The diamond tool was then set within about 5μm of the height of the spindle axis. The microscope was next set to view the diamond from above. The A-axis rotary table was moved around and the diamond horizontal-position adjusted until one part of the circular tip of the diamond was stationary at the centre of the eyepiece graticule. The cutting tip was then on the rotary table A-axis. Measurements showed that rotation and return of the toolpost-head to select another diamond or the testprobe was only reproducible within a sphere of about 2μm radius.

The X-axis zero was set by moving to the position where the probe tip gave the same reading on the left- and right-hand side of the spindle chuck edge when rotated 180 deg on the A-axis table. A tool-setting indicator was set by fixing a metal plate to the machine base, moving the diamond to touch it by recorded X- and Y-slide adjustments, and marking the position of the point of contact. This indicator was used to set the position of the other (roughing) diamond tool, and furthermore the positions of both tools were rechecked several times during the work. The final adjustment of the tool positions was made with their errors from the spindle axis being indicated by cutting into blue paint (of about 1µm thickness) on the surface of a substrate - a circular cut could be seen with the aid of the microscope if there was an error.

The LVDT test probe was put against the edge of the lens chuck to indicate how far it had been mounted away from the spindle centreline, and the error was reduced to below 0.5µm by tapping laterally with the mounting screws loosened. A substrate was mounted onto the chuck, taking great care to avoid any dust which would cause distortion, and with the unrequired vacuum holes blanked off by set-screws. Guard pieces were added to prevent the substrate from slipping sideways should the vacuum fail, and washers were added in appropriate places on the chuck face to balance the asymetrical weight distribution (within about the weight of one small washer) and reduce a potential source of vibration. The chuck was adjusted in angle until the testprobe indicated no deflection when held against the rotating substrate at the lens circumference position. Generally when changing substrates it was necessary to make several iterations between adjustment of the substrate face angle and the centre of rotation of the chuck until the latter was indicated as within 0.5µm of the spindle centre.

With the roughing diamond in place, and the X-axis set

to zero, the diamond was brought to be just in contact with the front surface of the substrate. The Y-axis was then withdrawn by 2.315mm and this position redefined as zero for the Z-,Y- and A-axes. The tool was now at a position such that, in a tool motion cycle, it would only contact the substrate at the lens-centre position.

Figure 5.12 indicates the lens profile errors which would arise from some of the major components of cutting tool position mis-setting (left-hand column of sketches). The dashed lines indicate the programmed, expected profile. The full lines indicate the profiles that are cut, or the indicated measurements of the profile. The approximate expressions for each type of error given below are derived in Appendix II. In practice these errors could be combined, and it was difficult to uniquely identify the cause of each error. Trial resettings of each type were made in the directions suggested by the Figure until the profile error was acceptable.

a) The cutting depth or probe measurement error ΔE for the case of the tip being above or below the spindle axis by ΔZ is given by the approximations $\Delta E = \Delta Z^2/2(C-T)$ at and near the lens centre, and $\Delta E = \Delta Z^4.\cos^2\theta/(8.X^2(C-T))$ over the remainder of the lens, where X is the X-coordinate, C is the local radius of curvature of the profile at position X, T the radius of curvature of the tool or probe tip, and θ the local slope of the lens profile. The limits to which this adjustment should be made can be specified by taking ΔE = 0.2μm and T = 0.4mm. Then, at the edge of the lens, where θ = 0 deg, C = 0.58mm, and X = 5mm, ΔZ = 0.4mm; at the steepest part where θ = 33 deg, C = 2.63mm, and X = 3.77mm ΔZ = 0.6mm, and at the lens centre where C = 10.933mm ΔZ = 0.07mm. The latter is clearly the accuracy to which the tip must be set. This value is well within the adjustment precision of the tool, but there was some difficulty with adjustment of the measuring probe.

ERROR OF TIP OF TOOL OR PROBE	DIAMOND TOOL	MEASUREMENT PROBE
not on spindle/ lens axis a		
A-axis to right of X=Ø b		
A-axis to left of X=Ø c	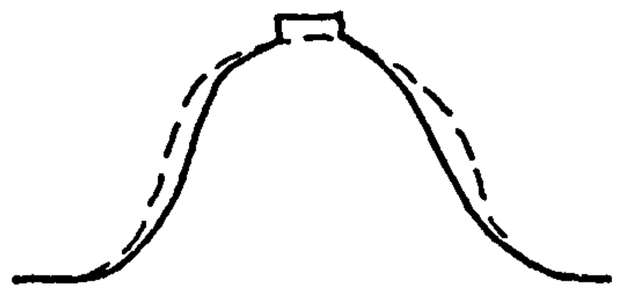	
tip to left or right of A-axis d	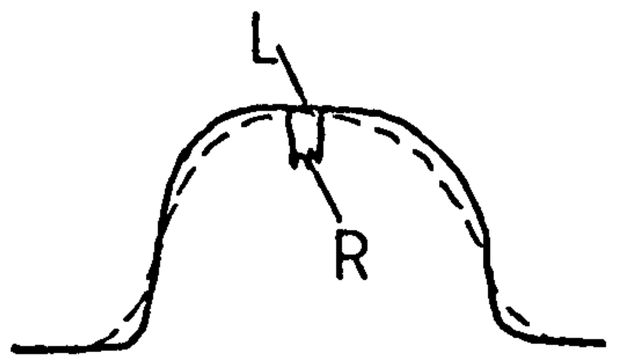	
tip towards lens from A-axis e		
tip behind A-axis f		

Figure 5.12
Qualitative effect of positioning errors of turning tool or measuring probe: dashed lines are the ideal profile, full lines represent the errors in the cut profile (left hand) or in the profile measurements (right hand).

b,c) If the A-axis is not centred above the X = 0 point, but is displaced by ΔX, then the profile error can be approximated by $\Delta E = \pm \Delta X(\sin\theta - \Delta X.\cos^2\theta/2C)$ where + applies to measurement, and - to lens cutting, and the sign of ΔX depends on the relative directions of the error and the tip. The second term only becomes significant at the very edge and centre of the lens. The smallest tolerable error for ΔE = 0.2μm occurs at the steepest part of the lens profile where θ = 33 deg: here ΔX = 4μm. This required tolerance is smaller than those discussed above, but it was within the accuracy of the setting method. The direction of the error is indicated by the central pip (b) or hole (c) which is visible (under a microscope) if its height or depth exceeds 0.2μm. This step occurs for ΔX greater than $(2C.\Delta E)^{0.5}$, i.e. 66μm (here C is the radius of curvature at the lens centre).

d) The distance ΔL by which the tip may be displaced parallel to the lens surface away from the A-axis is determined by the expression $\Delta E = \Delta L^2/2(C \pm T)$ using + for convex (edge-rounding) regions and - for concave (inner) regions of the profile. For ΔE = 0.2μm, the smallest value of ΔL is 20μm and occurs at the lens edge. It was quite possible to hold the tips within this accuracy.

e,f) The required accuracy of tip location away from the A-axis in the direction normal to the lens profile ΔL may be estimated by the approximation :
$\Delta E = \Delta L(1 - \cos\theta)$. For ΔE = 0.2μm and at the steepest part of the lens this tolerance is 1.2μm. This value was difficult to achieve, and was probably the largest source of error in the cut profile and its measurement.

5.4.4 Turning of geodesic lenses

Some of the lenses that were diamond-turned are shown in Figure 5.13. During the first visit one pair of lenses were diamond-turned on a single IOSA substrate, using the linear interpolation data. During the second visit a further nine lenses were made: three IOSA substrates had a

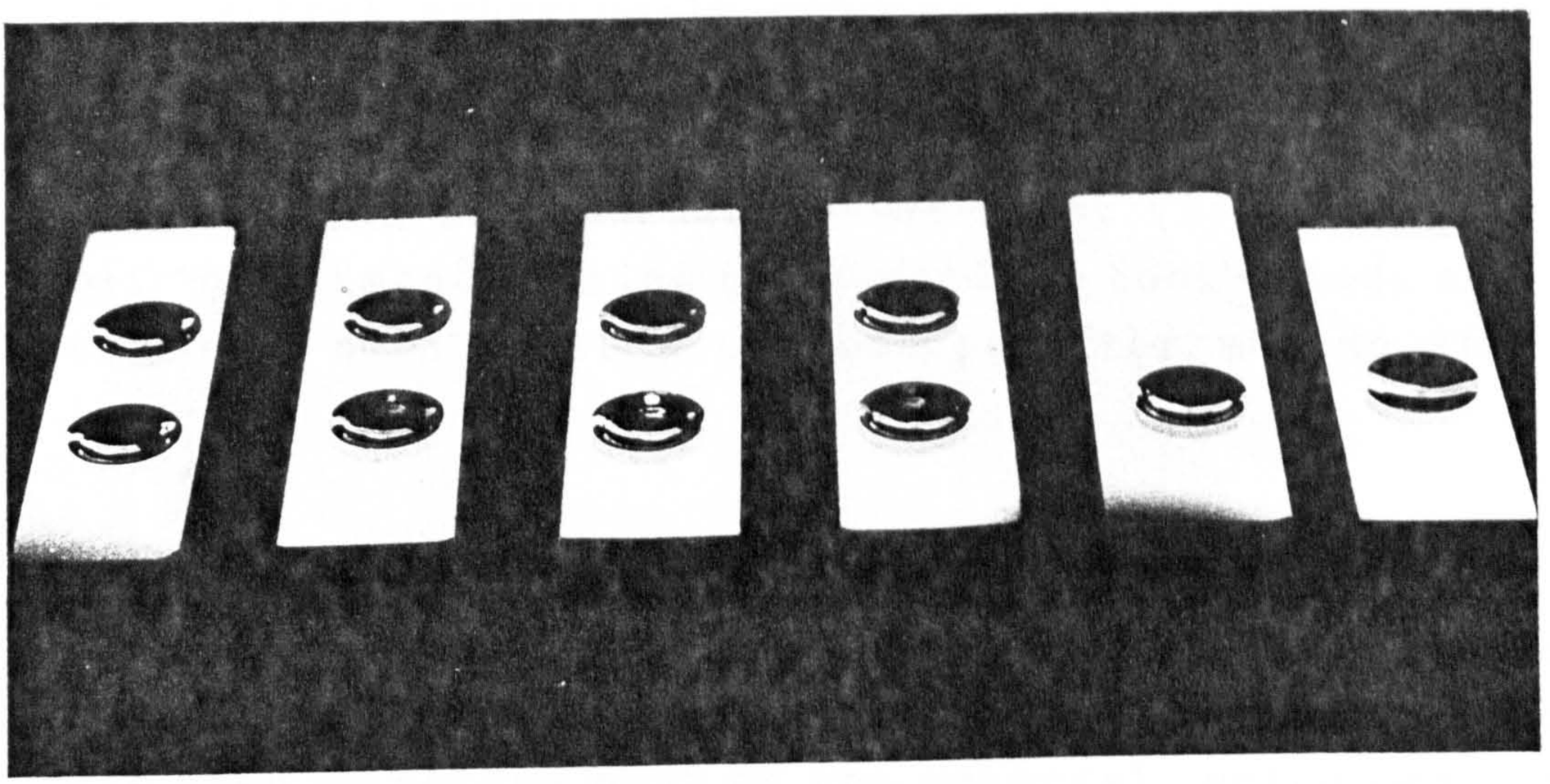

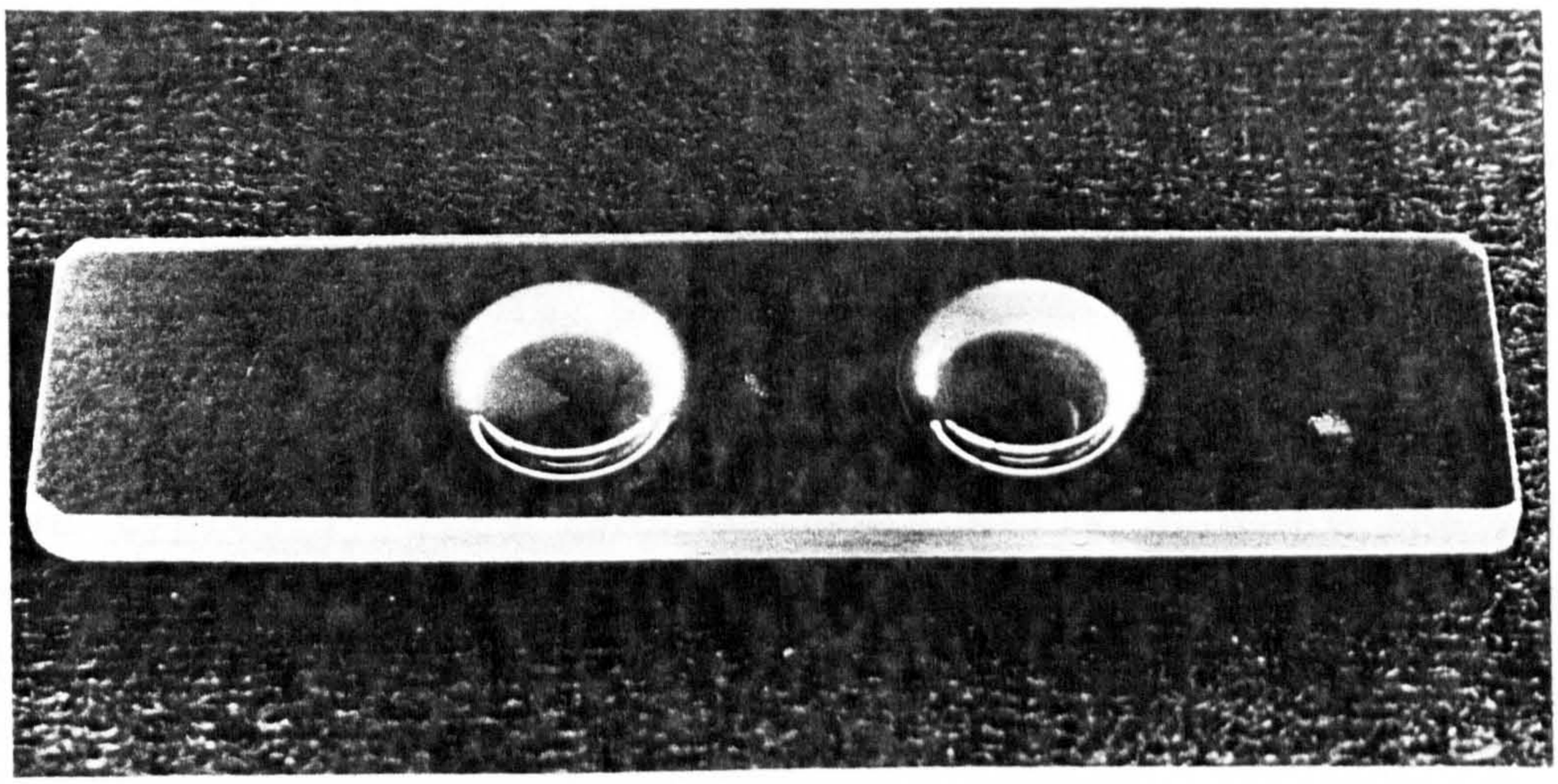

Figure 5.13

Photographs of geodesic lenses after diamond turning.

pair of lenses fabricated on them, the remainder had single lenses. One single lens was made to a simple two-arc profile (whose design was discussed in Chapter 2) and its central spherically concave region used to assess machining accuracy by using interferometry. The remainder were made to the twenty-arc profile. Only one diamond was used for all cutting during the first visit, and only a pair of diamonds during the second. No tool damage or wear could be seen under a microscope after making all the lenses.

The general procedure was to perform between 14 and 19 cutting cycles. The table below indicates a typical sequence of cuts and measurements. The roughing diamond was used to remove most of the material, using deep fast cuts. Four cuts were made with the fine diamond, and then the depth of the lens centre checked with the probe (recording the Y-axis shift for equal probe indication at the lens edge and at the centre). The depth was usually between 0.5µm and 3µm less than the sum of the series of cut depth settings. Using this new depth measurement, further cuts were made with the fine diamond to leave a nominal 3µm to cut, and the depth checked again. The error was typically less than 0.5µm. Finally another one or two cuts were made to a nominal depth of 1.314mm, to allow 1µm for material removal during polishing.

TABLE 11: TYPICAL SERIES OF CUTS AND TESTS DURING DIAMOND-TURNING OF A GEODESIC LENS

CUT NO.	DIAMOND	SPEED µm/rev	CUT DEPTH mm	ACCUM. DEPTH mm
1 to 9	rough	3	0.127	1.1430
10	rough	1.5	0.075	1.2180
11	rough	1.1	0.040	1.2580
12,13,14	fine	1.5	0.012	1.2940
15	fine	1.1	0.0012	1.2952
depth check				1.2934
16	fine	1.1	0.0126	1.3060
17	fine	1.1	0.006	1.3120
depth check				1.3124
18	fine	1.1	0.0016	1.3140
depth and profile measurement				1.3144

Lens profile measurements were made by tracking the LVDT probe tip around the lens using the same tool cycle as the diamond. The right-hand column of figure 5.12 illustrates the effects of the most important types of tip position errors.

a) The correct vertical position of the probe tip was indicated by the height which gave the greatest horizontal depth reading: this was not very sensitive. Apart from this vertical setting, the probe could be set more accurately than the diamond so the trace obtained for a lens profile mainly indicated the result of diamond tip location error.

b,c) These errors could be reduced by shifting the X-axis zero position until the trace of a lens was symmetrical in the positive and negative X-directions.

d) Adjustments onto the A-axis (in the X-axis direction) were indicated by rotating the A-axis equal angles either side of normal to a flat face, e.g. the substrate. The probe deflections would be equal if the

centre of the tip were on the normal to the substrate which passes through the A-axis. If in error by ΔL, the deviations would be $T(\sec\theta - 1) \pm \Delta L.\tan\theta$. The smallest noticable probe change of 0.2μm will indicate the required limit on ΔL, 20μm, at any angle above 0.3 deg. Rather than tap the probe sideways (no useful easily varied adjustment was available) the A-axis was rotated to a new zero where the deflection was zero. To reach this position the probe would have been been tilted by $\theta = 2\tan^{-1}(\Delta L/T)$, e.g. 5.7 deg for ΔL = 20μm. Such a tilt would only cause $(1 - \cos\theta) = 0.5\%$ errors in readings, which are negligable since the probe is used in the null mode, only indicating errors in profile of the order of a micrometre.

e,f) The probe tip could be adjusted on the A-axis in the Y-axis direction by obtaining a zero indication on the substrate face when Y = 1mm. The setting could have been made more accurate by rotating the A-axis around a rod of known diameter, adjusting the rod until on axis, removing the rod, and moving the probe or diamond tool with a micrometer adjustment holder by half the rod diameter. Because the micrometer adjustment holder wes not readily available, this setting was not attempted. The measuring probe was set to positions over a range of 1.2μm: this varied the apparent lens profile error at the steepest part between zero and 0.2μm (a sensitivity which was expected - see above). However a zero error reading merely indicated that the probe tip was located at the same position as the diamond tool tip.

LVDT measurements were made of the profile of every lens, and the errors indicated (as in the example of Figure 5.14) were within ±0.5μm in general as required. Profile measurements will be discussed in greater detail in Chapter 7. Measurements were also made of the concentricity of lenses, rotating the lens slowly with the probe tip near to the steepest part of the lens profile. Figure 5.15 illustrates an example. The concentricity was generally within ±0.1μm, but with some fine structure. A

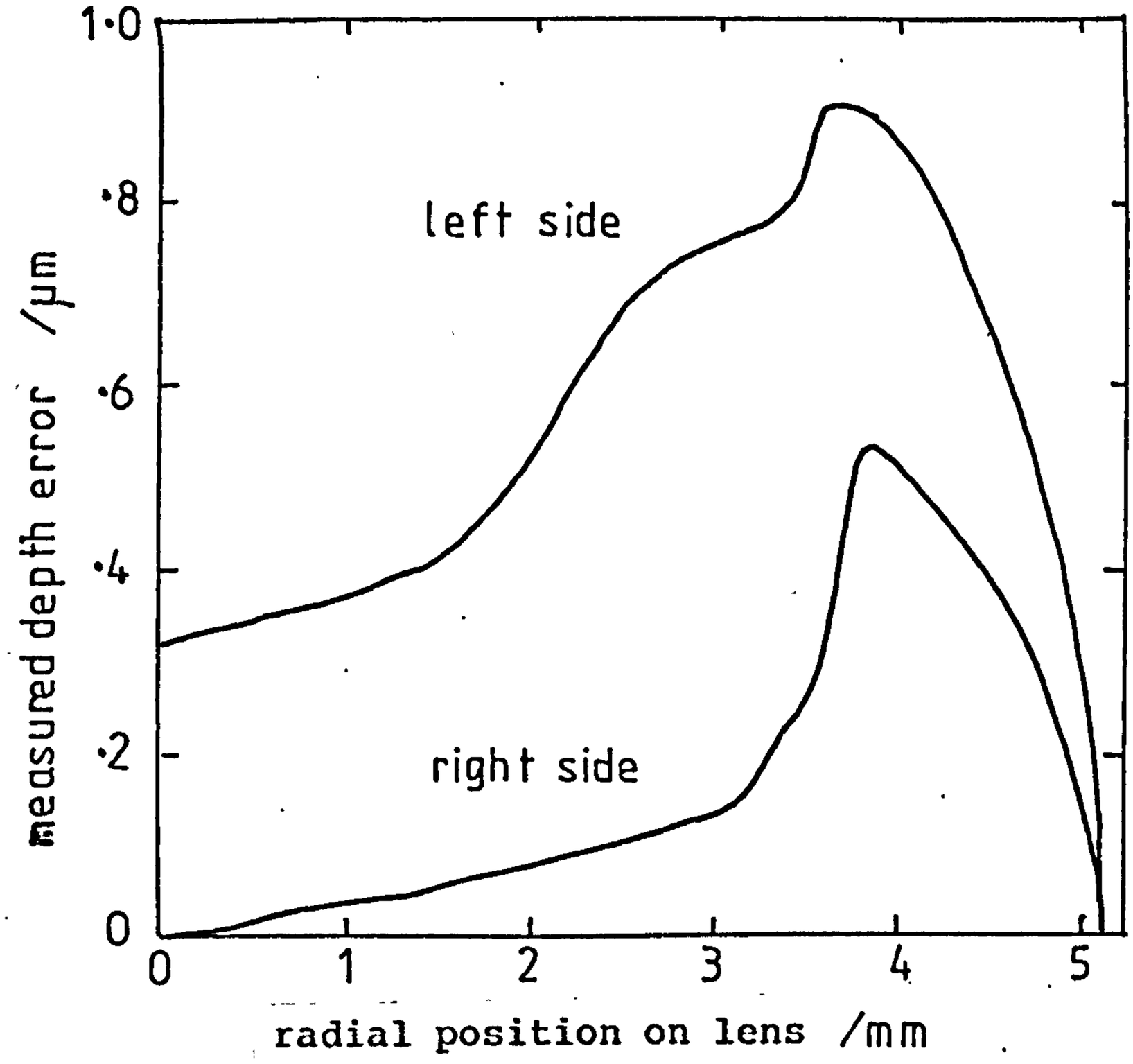

Figure 5.14 Lens profile errors indicated by LVDT probe measurement.

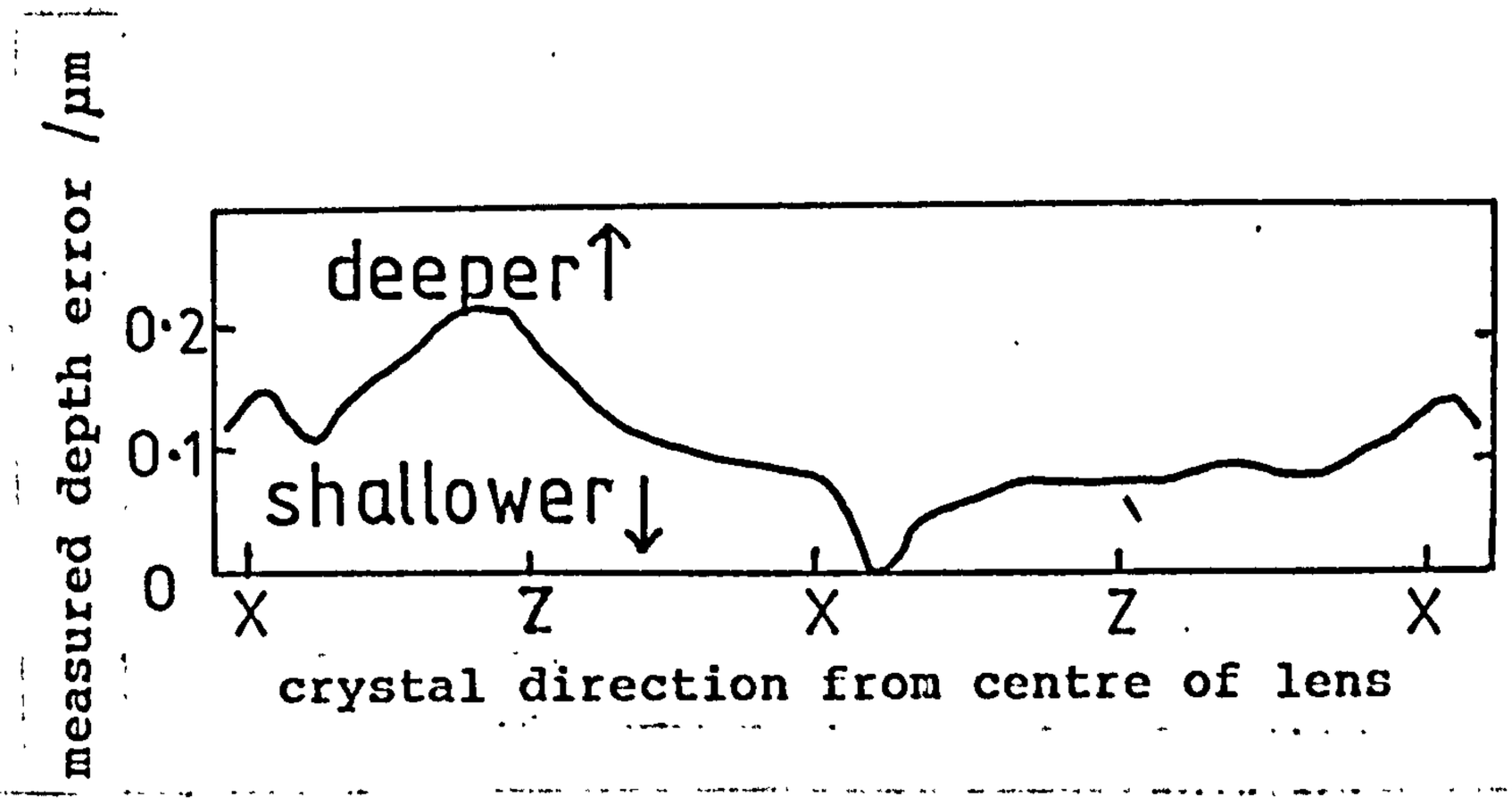

Figure 5.15
LVDT probe measurement around an annulus of radius 3.7mm, showing apparent anisotropy of diamond-turned depth.

deep broad groove appears close to a substrate Z-axis and narrow ridges appear near to both X-directions. Surface anisotropy can be seen in Figure 5.13: lenses exhibit sectors along the X axis of greater roughness. This can be seen more clearly in Figure 5.16 which is a Nomarski phase contrast micrograph of the central 1mm diameter of a lens.

Figure 5.17 shows a Talystep trace over the central 0.1mm of a lens; the dashed line indicating the programmed tool path. The general roughness average of about 15nm is seven times more than expected from the turning parameters, this probably being due mainly to machine vibration and to departures from continuous path movement. However even the roughest part of the lens is smooth enough for it to be possible to polish the turned lenses without removing more material than the profile tolerance, perhaps using the same machine, or on the machines discussed in Chapter 6.

The "two-arc" lens profile which was cut for accuracy tests had a central concave region of 16mm radius of curvature extending to 4.7824mm radius, and an outer edge-rounding region of 1.5mm radius of curvature which extended to 5.2308mm radius. The designed total lens depth was 0.8mm, and the measured depth was 0.6µm too deep. Chapter 7 presents the results of profile and curvature measurements.

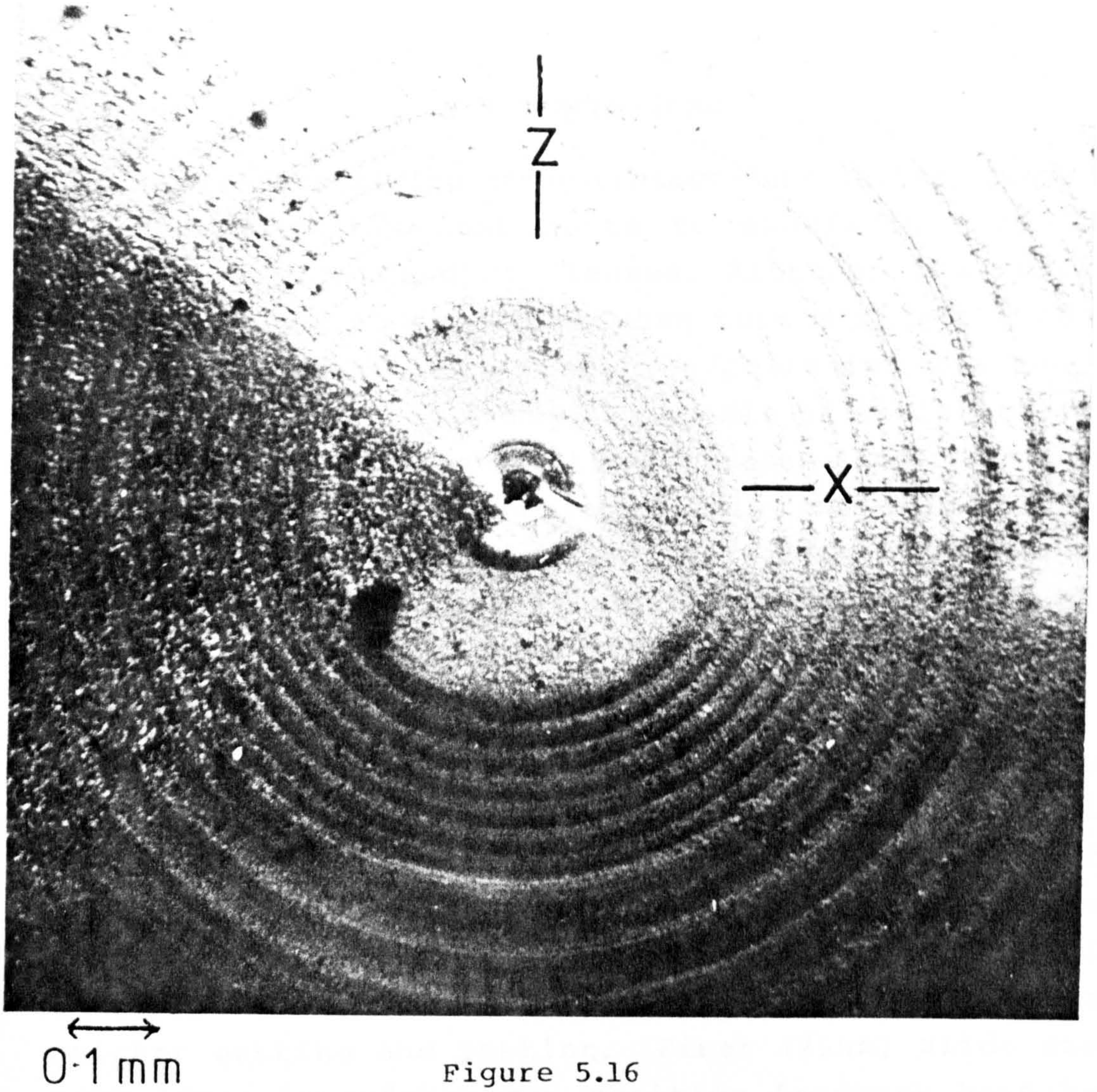

Figure 5.16

Nomarski phase constrast micrograph of central part of a diamond turned $LiNbO_3$ lens, showing anisotropy of surface roughness and annular ridges related to imperfections of machine slide motion.

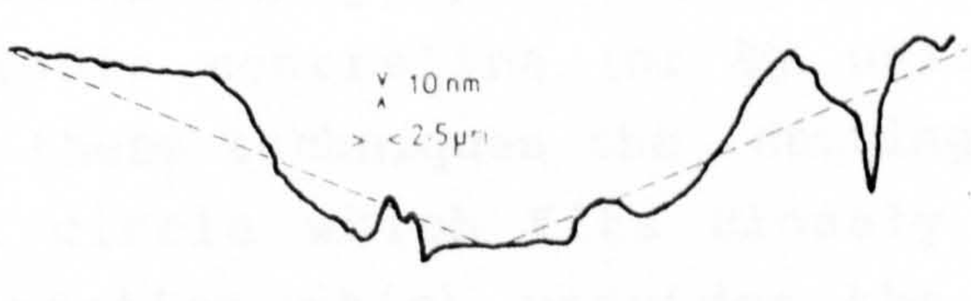

Figure 5.17 Talystep trace of profile over central 0.1mm diameter of a diamond turned lens (full line). The dashed line indicates the tool path which had been programmed.

5.5 CONCLUSIONS.

Diamond-machining using contact-lens lathes, provides a potentially low cost route to manufacture of IOSA substrates with geodesic lenses. Although the surface finish was not as smooth as when turned with the Moore machine, a subsequent smoothing/polishing process as discussed in Chapter 6 may be capable of satisfactorily completing the lens fabrication process. Aspheric surface generation on contact-lens lathes using cam-mechanisms is known to be available and it certainly also seems possible that a low-cost microprocessor based CNC approach, with the tool mounted on precision X,Y slides, could be established.

Diamond-turning with the Moore prototype machine showed that lenses could be made within the required profile accuracy. Several modifications have been built into the production models. A better toolpost and a flexible-reed tool/measuring probe adjustment system has been installed to allow much greater accuracy, and certainly easier and quicker setting and testing. Finer (25nm) slide steps with laser interferometer position feedback have been provided. These should allow even greater lens profile precision, and perhaps a slightly smoother surface finish.

The evidence so far indicates that diamond-turned surfaces, with their sectors of greater roughness, are not smooth enough for immediate waveguide formation. The existence of the sectors does indicate that plane surfaces of $LiNbO_3$ (unlike curved surfaces) could perhaps be produced quite smoothly by mounting the substrate away from the spindle centreline (or by using diamond fly cutting). In these techniques the cutting path may be a large radius circle which fits closely enough to the crystal orientation which provides the least surface roughness. However, a light polishing stage is almost certainly still required.

CHAPTER 6: POLISHING OF GENERATED LENSES

6.1 LARGE-AREA FLEXIBLE POLISHER

At first sight perhaps, the most simple method of polishing an aspheric lens is to use a flexible polisher of shape and size similar to that of the lens, on a standard polishing machine, with very small oscillations [124,182,183,184]. The polisher must be faced with a material suitable for the type of polishing action required, but it may be backed with any flexible material. The practical problem is to maintain contact between the polisher and the lens with a pressure and relative velocity distribution which provides uniform material removal. The problem is less easily approached for concave lenses such as the present geodesic lenses - for convex lenses a flexible sheet can be stretched over the lens as in Figure 3.1 [124] or the lens pressed into an elastic lap[182].

The author made several attempts to design an elastic polisher suitable for the very small and steeply sided geodesic lenses. A heavy weight was placed onto the arm of a polishing machine to press a flexible polishing tool onto the surface of a lens which had been ultrasonically generated in lithium niobate (Chapter 4). Flexible polishing pads were attached to steel bases (which were ultrasonic grinding tools as used in the work described in Chapter 4). These were bolted to a flexible arm. Lenses were wax-mounted onto the base of a glass Petri-dish for immersion polishing in Syton W15.

Several combinations of pad and flexible backing were tried and two are illustrated in Figure 6.1. The first used a finger of a rubber glove as the elastic backing, clamped over the metal tool by a Jubilee clip, with Melton cloth glued on as the flexible polishing pad. The stiffness of the backing was varied by filling alternatively with air, water or grease. The radius of curvature of the polisher (about 10mm) was approximately

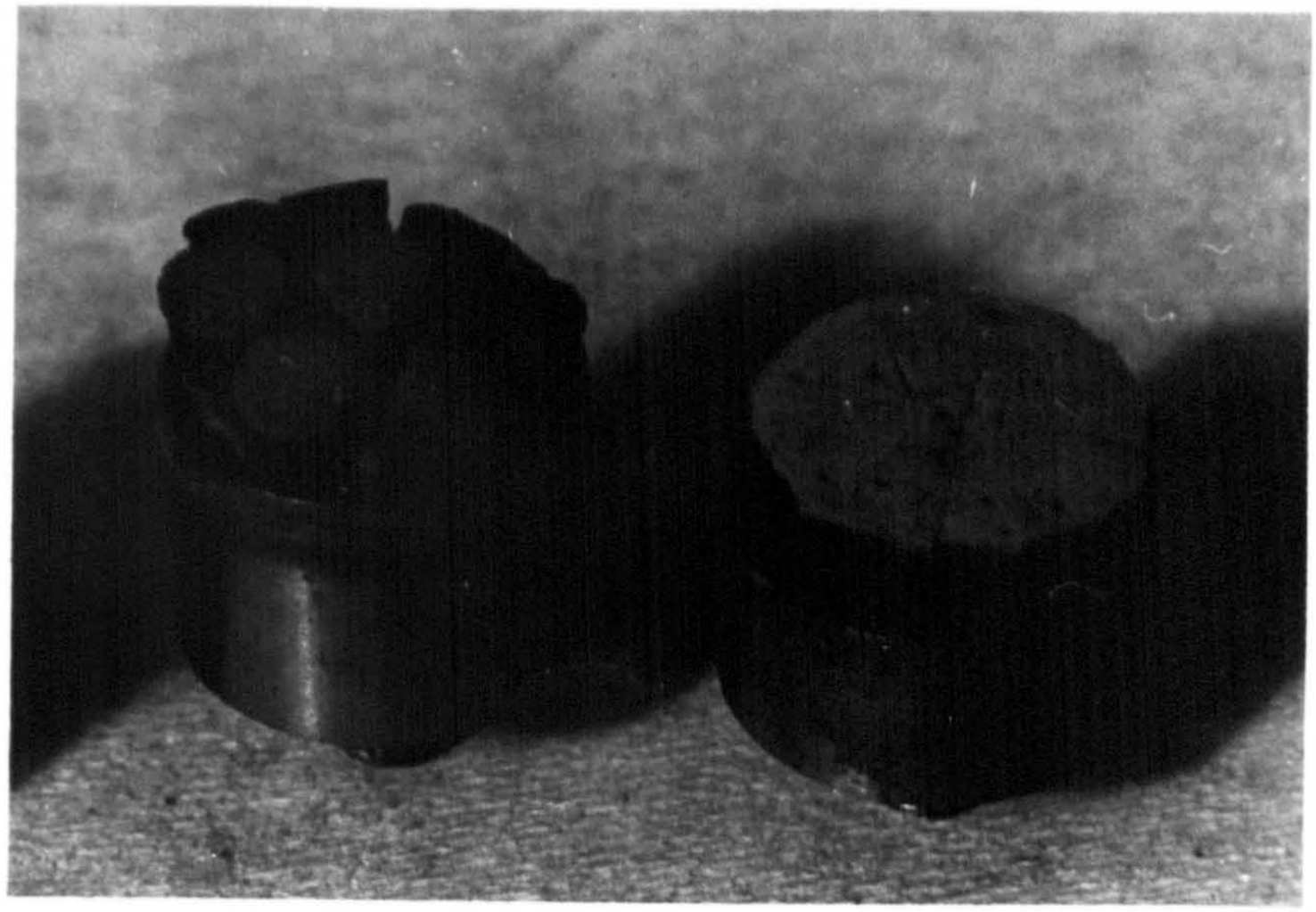

Figure 6.1

Flexible polishing heads for geodesic lens depressions.

the same as the best-fit curvature of the lens when not in contact but, when pressed against the lens with a suitable pressure for polishing, the polisher became too shallow and could not reach into the bottom of the lens. This design could probably be improved by using a valve to allow pumping of the gas or fluid to control the pressure and curvature.

The polisher arm was given a small oscillatory motion so that the metal base of the polishing head moved a few millimetres to either side of the lens centre position. The author's experience when polishing on the jig grinder (section 5.2.3) confirmed a well-known practical factor in lapping and polishing that has been investigated recently by Brown [185,186]. When using a full size polisher rather than a small area one, a transverse lapping action is essential: without it one tends to obtain concentric grooved scratches on the surface, with no lapping at the centre. This is because to a large extent the slurry and lap materials ball up, deepening and widening the grooves. There is no control to ensure continuity of the first and second radial figure derivatives. Minor variations in lap parameters and slurry concentrations soon make the process unstable [185]. This first flexible polisher was so flexible that it pivoted about the lens surface rather than following the set oscillations.

The second design of a flexible polisher used various foam rubber backings, with polyurethane rods glued on top (Figure 6.1, left). Rods were cut from 2mm thick expanded sheet using a a cork borer. Such polishing tools failed to slide well over the lens surface, and tended to break away from the backing after a short period of polishing.

The third polisher design used a 4mm thick foam rubber backing, glued over a 10mm diameter steel ball which was recessed into the flat face of the steel base, projecting by 1.3mm (the lens depth). 1mm thick expanded polyurethane sheet was glued using Evostik over the rubber and cut through in a random pattern to form a convex

approximation to the lens profile (Figure 6.1, right). The lens was polished at a pressure of about 2 kg cm^{-2} at 90 rev/min, with oscillations of amplitude 2mm offset from the lens centre by 2mm. The temperature of the Syton polishing slurry in the bowl rose to about 34°C. The grinding pits remaining from ultrasonic generation were so deep, and the polishing action so slow that even after 22 hours not all the pits had been removed.

Because of the small size of the tool relative to the texture of the polishing surface (particularily with expanded polyurethane foam, which contains randomly spaced holes as large as a millimetre), it was difficult to ensure reproducibility of tool dimensions and behaviour. The polisher was reconstructed using a plastic Polytron foil polishing pad which was not perforated, but had a regular groove pattern of 0.2mm pitch . Sectors were cut out to make it easier to curve the plastic sheet. The amount cut out could be used to make the polishing rate more constant with radius or to make profile corrections [185-187]. Test lenses were ultrasonically ground in glass rather than lithium niobate (for economy of the latter). Polishing times were shortened by a few hours by using a slurry of zirconia powder in water, but the polishing rate was not uniform, being slower at the steepest part of the lenses where the lens and polisher were probably at the least contact pressure.

Because it was difficult to arrange uniform material removal, and because the process appeared to be extremely slow, the development of a flexible polisher was deferred.

6.2 SMALL-AREA MICROCOMPUTER-CONTROLLED POLISHING MACHINE

Although polishing may be carried out on the generating jig grinder or the diamond-turning machine, and indeed was to a limited extent, there were several problems which could not be readily overcome by the author. Time on the machines was very limited and expensive, there were no suitable polishing heads available, and the programming computers available for grinding and turning were not appropriate to the frequent changes of feedrate (radial velocity) required during polishing. It seemed appropriate to develop a dedicated (and potentially less expensive) machine specifically for polishing geodesic lenses.

In the manual production of high-quality optical surfaces and of aspheric surfaces, the final figuring is frequently obtained by "local touching-in", that is polishing with a relatively small pad, typically one-fifth the diameter of the lens. In comparison with larger tools such as described in the previous section, a tool can be operated at greater pressure and velocity, remove material more rapidly, follow the curve of an aspheric more closely and therefore correct local surface errors more rapidly. The craftsman usually holds the polishing pad for longer periods over the areas requiring the most material removed. This tedious process requires the highest level of skill and experience, particularly for profile tolerances of less than 0.3μm. Several organisations have developed polishing machines with pads smaller than the lens or mirror workpiece diameter which have been controlled by a computer to follow similar paths to that used by a craftsman [130,137,138,174,187-192]. The pad may be programmed to pass over the lens with varying radial velocity to maintain constant polishing depth or provide correction to the profile.

These machines were all built to polish aspheric surfaces which were of much larger size and less curvature but requiring greater profile accuracy than the geodesic lenses of this study. The design and

construction of a small polisher for geodesic lenses would be expected to be less concerned with rigidity and accurate location over long distances, but to encounter more problems with the design of a suitable polishing pad to fit inside the very highly curved regions of geodesic lenses.

The following three sections discuss the main aspects of developing the geodesic lens polishing machine: the polishing head, the head positioning mechanisms, and the computer control. As far as possible the machine was designed around low-cost commercially-available components. The main components were DC motors, stepper-motors, optical tables, printed-circuit interface boards and a microcomputer. The machine is referred to as the Microcomputer-Controlled Polishing Machine (MCPM) in the subsequent text.

6.3 DEVELOPMENT OF A SMALL-AREA POLISHING HEAD

The design approach used was to employ a small polishing head consisting of various combinations of flexible material, with the polishing spindle driven by a compact motor drive. It was hoped to achieve high polishing speeds by using as fast a rotation rate as possible. Some experiments were carried out using a KaVo Type K9 dental drill with Electronic speed control unit. An adaptor was made to allow the drill head to be mounted on a Logitech PM2 polishing machine. Fig. 6.2 shows a photograph of the assembled polishing apparatus in use.

According to Balasubramanian [187] in a thesis on the "Development of an aspheric polisher", in order for the polisher to fit the surface, the yield point of the polishing layer should be just lower than the value of the shearing forces which develop between the surface and the polishing layer when polishing. The maximum polishing rate

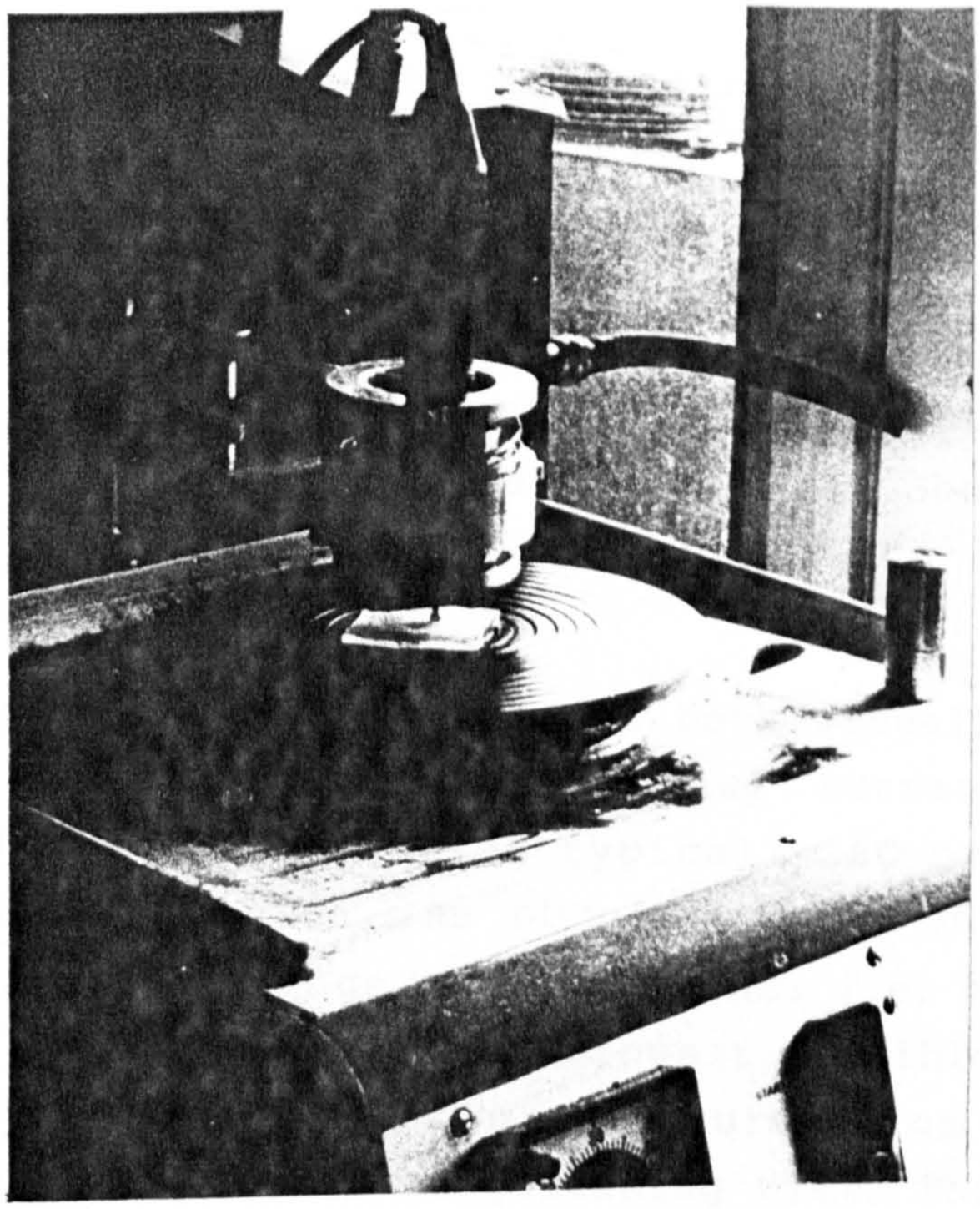

Figure 6.2 Polishing arrangement using a small pad on a Kavo K9 dental drill mounted on the reciprocating arm of a Logitech PM2A machine.

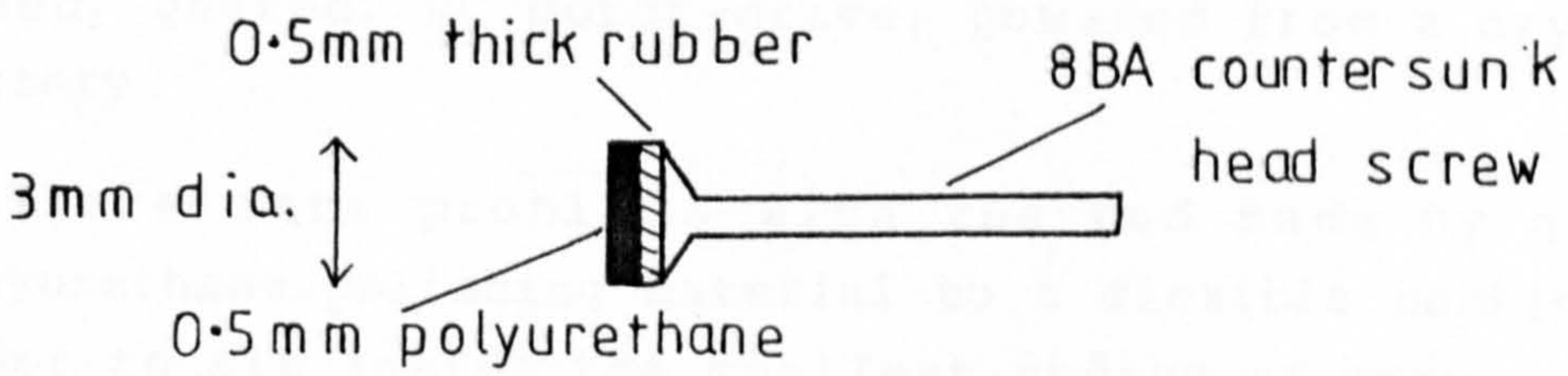

Figure 6.3

Small flexible polishing head used in the arrangement of Figure 6.2

occurs for materials with modulus of elasticity in the range 2.10^4 kg cm^{-2} [128,187]. For the present work, polishing mops were made (Figure 6.3) by gluing 1mm and 2 mm thick rubber sheets onto the head of an 8 BA brass screw approximately 20 mm long. The mop faces were made of 0.5 mm thick standard optical quality polyurethane lapping material (LP-57) of hardness on the Shore scale of 25 - 40. The diameters of the polishing heads were approximately 3 mm.

The principal result, evident both visually and with a Talystep machine, was an 'orange peel' surface roughness effect with roughness being typically 60 nm Ra. This type of surface finish was obtained both on glass and $LiNbO_3$ over a wide range of conditions: i.e. head speeds from 1,000 revolutions/min (the slowest possible with this equipment) to 20,000 rev/min, pressures from 100 to 500 gram, and up to one hour of polishing time. These results were sufficiently discouraging that after 14 runs over a range of conditions on flat samples this particular approach was abandoned. It was concluded that very much slower polishing head speeds were needed to obtain acceptable surface finish. Slower speeds were also desirable for contact to be maintained when polishing over the steeply contoured surfaces involved with geodesic lenses. The dental drill motor was replaced by a lower speed, geared, DC motor-drive, powered from a dry-cell battery.

There were problems with the pad made by gluing polyurethane polishing material to a flexible backing. In order to fit inside the smallest radius of curvature of the lens profile, the pad had to be of very small diameter. It tended to tear away or wear out before polishing away very much material. A new polishing head was made therefore which was intended to use the flexibility of polyurethane alone [193] and allow for rapid wear. Figure 6.4 shows the head mounted on the low-speed drive. To make this head a brass tool was turned and

drilled with a 2mm diameter central hole. Polyurethane sheet material was cut and punched to form a polishing rod which fitted tightly in the hole. The end of the whole assembly was turned to a radius of curvature of 2.5mm to allow the plastic polishing rod to fit into the lens at any point without the brass touching the surface. The plastic rod could be pushed down the hole as frequently as necessary to compensate for wear. In practice it was found that the rod wore away so quickly that it would have to be fed in at intervals shorter than the time needed for a polishing cycle, which would allow the surface to be scratched.

The brass tool design was made more elaborate. A hydraulic ram was constructed to continuously feed down the plastic polishing rod at constant pressure (Figure 6.5). Unfortunatly there was not enough time available to develop this approach to a sufficiently reliable stage for use in polishing lenses. The polishing pad used for all the lenses was therefore a hard felt mop (Engis Ltd) of conical shape and spherical tip profile, with initial radius of curvature about 2mm. These mops wore down to flatter tips (of greater hardness than before use) after a few hours of use (Figure 6.5). It was necessary to change the mop frequently, particulary just before the final stages of lens polishing.

It is clear that this machine removes material in a manner somewhat between two modes - (i) removal by a rigid tool, the final profile depending only on the tool shape and the path which it follows, and (ii) removal by a flexible lap, free to erode material at any position for as long as relative motion exists. Since the tool material wears away during use so that its contact pressure tends to decrease, these extreme modes could possibly be unified by considering the polishing action to follow Preston's Law, with the pressure decreasing as a function of time.

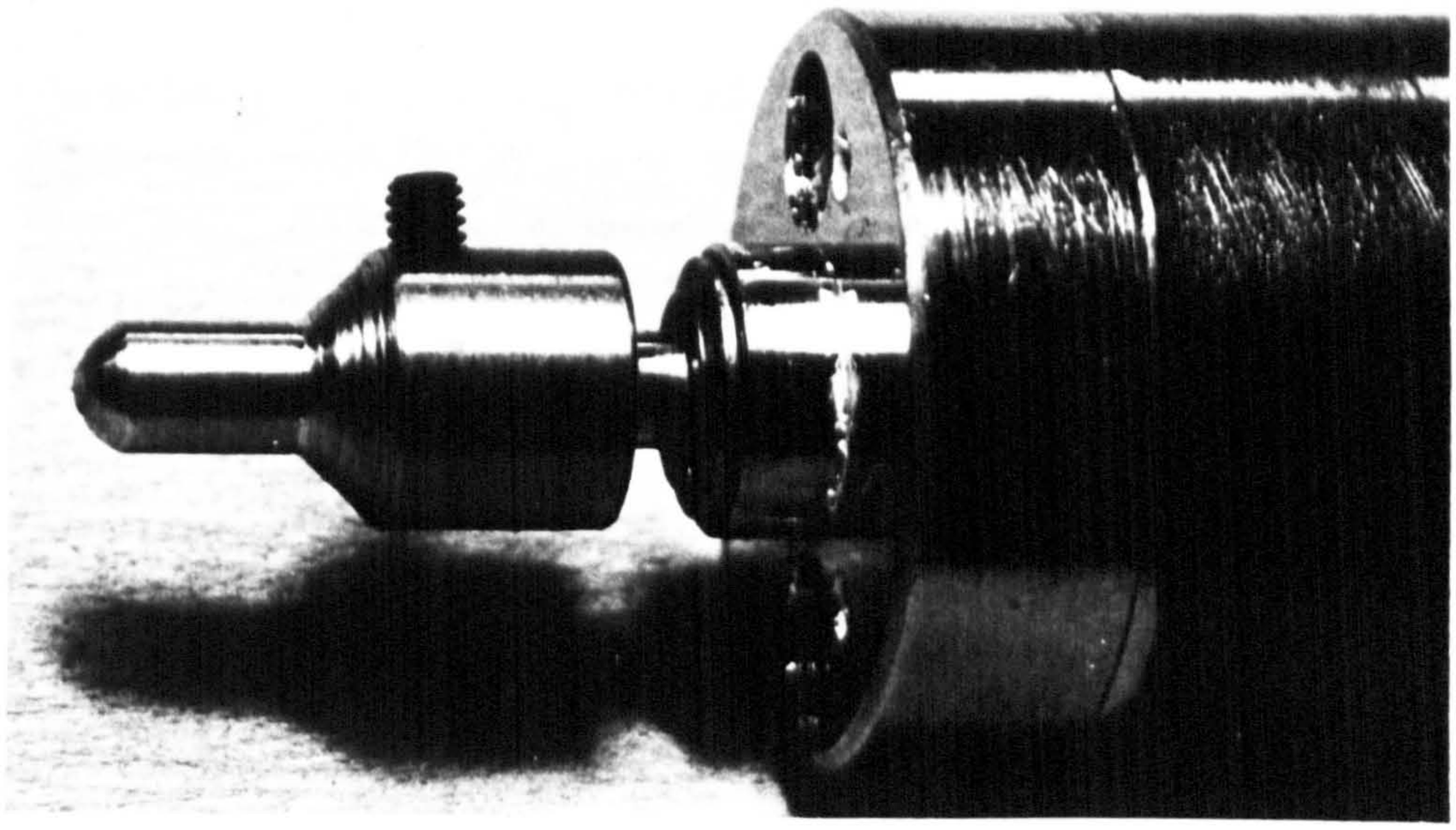

Figure 6.4

Polishing head containing a flexible polyurethane foam insert mounted on a motor & gearbox assembly.

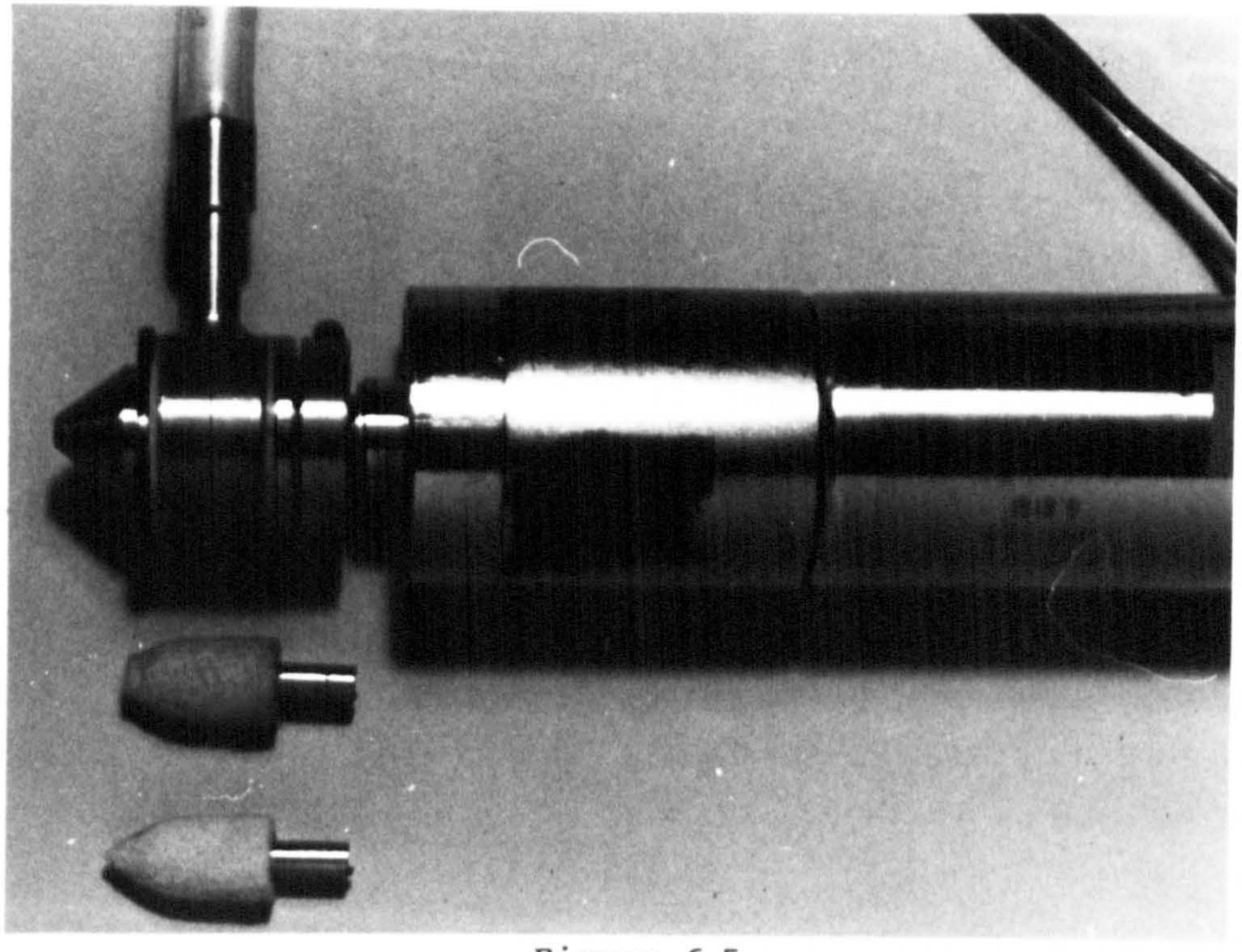

Figure 6.5

Hydraulic ram polishing head for use with polyurethane inserts, and (below) a worn and a fresh felt polishing cone.

6.4 CONSTRUCTION OF A MCPM - HARDWARE

6.4.1 Accuracy and design of mechanical components.

Air-bearing rotary spindles are a regular feature of precision machinery now being supplied and used for optical and other applications, e.g. machines supplied by, or available from Bryant-Symons, Moore, Pneumo-Precision, Ealing-Beck and Heliotrope all use air-bearing rotary spindles. Air-bearing spindles give, in practice, approaching five times less run-out than the best equivalent mechanical spindles. The other alternative, oil-filled hydrostatic bearing spindles, are (taking into account ancillary equipment required) typically ten-times more costly than air-bearing spindles. Air-bearing spindles can be rotated at high speeds but tend to be affected significantly by variations in loading conditions. They are also known to suffer, occasionally, catastrophic failures for reasons not clearly understood, but possibly due to cleanliness problems.

The air-bearing approach can also be applied to linear slides, but has not been applied to the same extent as for rotary spindles - e.g. mechanical contact linear slides are used in machines from Moore.

Enquiries about the availability and suitability of air-bearing spindles and slides were made, with two broad objectives: (a) application in the MCPM and in a geodesic lens profile measuring machine and, (b) possibly longer term development of a high-precision machine capable of diamond-machining and grinding as well as polishing and measurement. The latter machine was envisaged as being capable of fabrication to a level of precision comparable to that achieved with machines from Moore Co. but as being considerably cheaper because, in particular, of the much smaller distance required to be traversed, appropriate to the relatively small size of workpiece and machined region implied with the IOSA. The machine would be designed so that the use of CNC would be an essential feature.

The encouraging conclusion to be drawn from the above-mentioned enquiries is that, given sufficient time and money, equipment could be developed within the U.K. having the precision required for all aspects of geodesic lens fabrication. The time and money requirements are reasonably modest (£100,000 and two years on a fairly pessimistic estimate). However such resources were not available for the present work, and the MCPM was designed with the limited objective of at least being able to polish geodesic lenses which had been generated by diamond-turning. It was estimated that a positioning accuracy of about 10μm would be sufficient for this purpose. The MCPM was constructed as much as possible using equipment which was already available or could be purchased at relatively low cost and with rapid delivery.

6.4.2 Lens mounting and rotation spindle.

For convenience and speed of construction, the Logitech PM2A polishing machine which had been used for preparing the substrates was utilised to provide a rigid base for the machine and to provide the rotation drive system for the lens substrate (Figure 6.6). The polishing head positioning equipment was mounted onto the rigid cast aluminium baseplate. Lenses were mounted onto the same chuck as was used for the generating machines. This lens mounting chuck was drilled and tapped to allow it to be screwed down onto the spindle that usually drives a lapping or polishing plate. This spindle was extended (and required support by an upper bearing to maintain sufficiently accurate truth of rotation) because the polishing head was raised by its positioning equipment to a position well above the normal lapping plate height. Since the lenses were held down by gravity and the pressure of the polishing head, no vacuum was required.

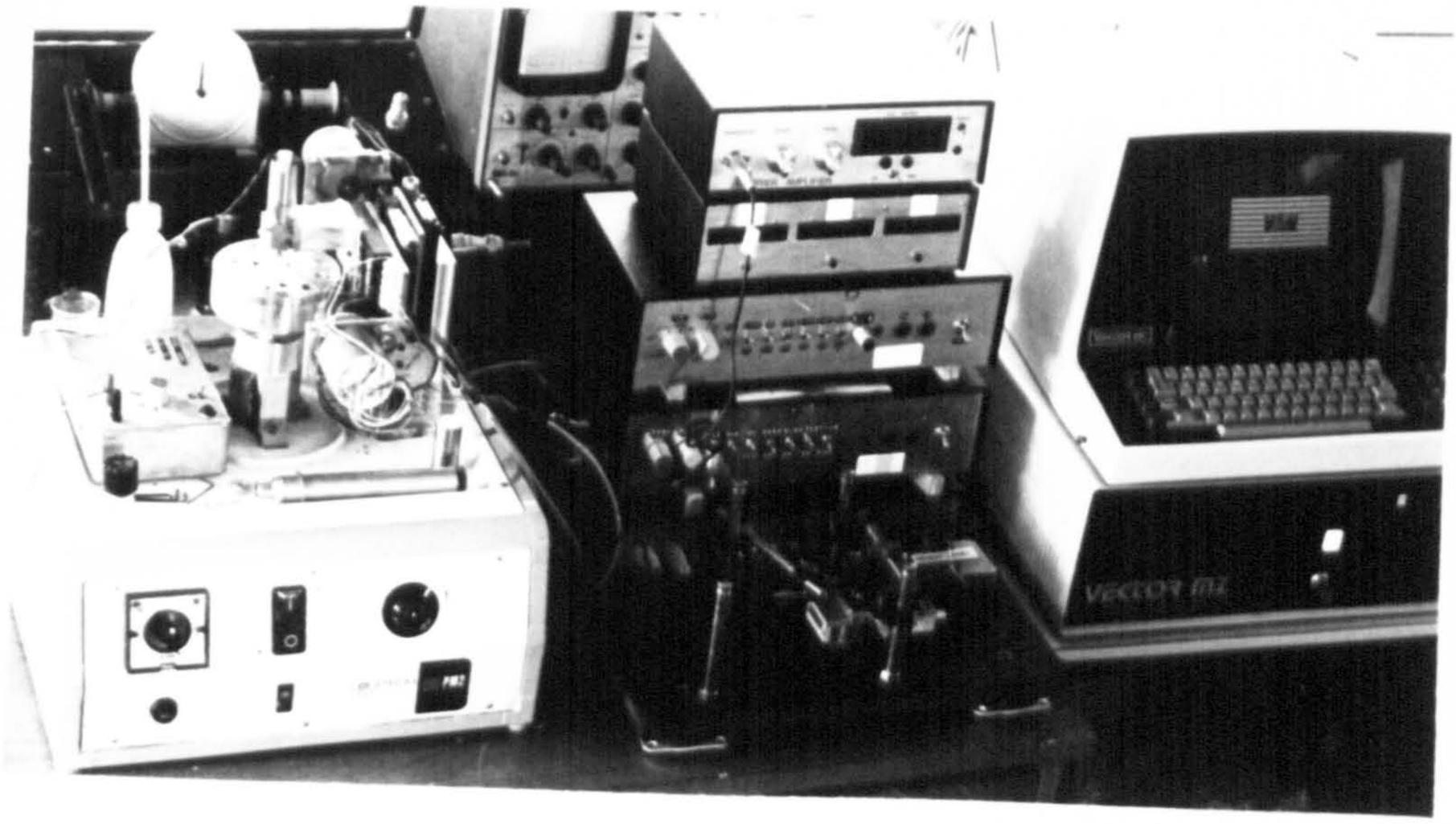

Figure 6.6 Microcomputer controlled polishing machine.

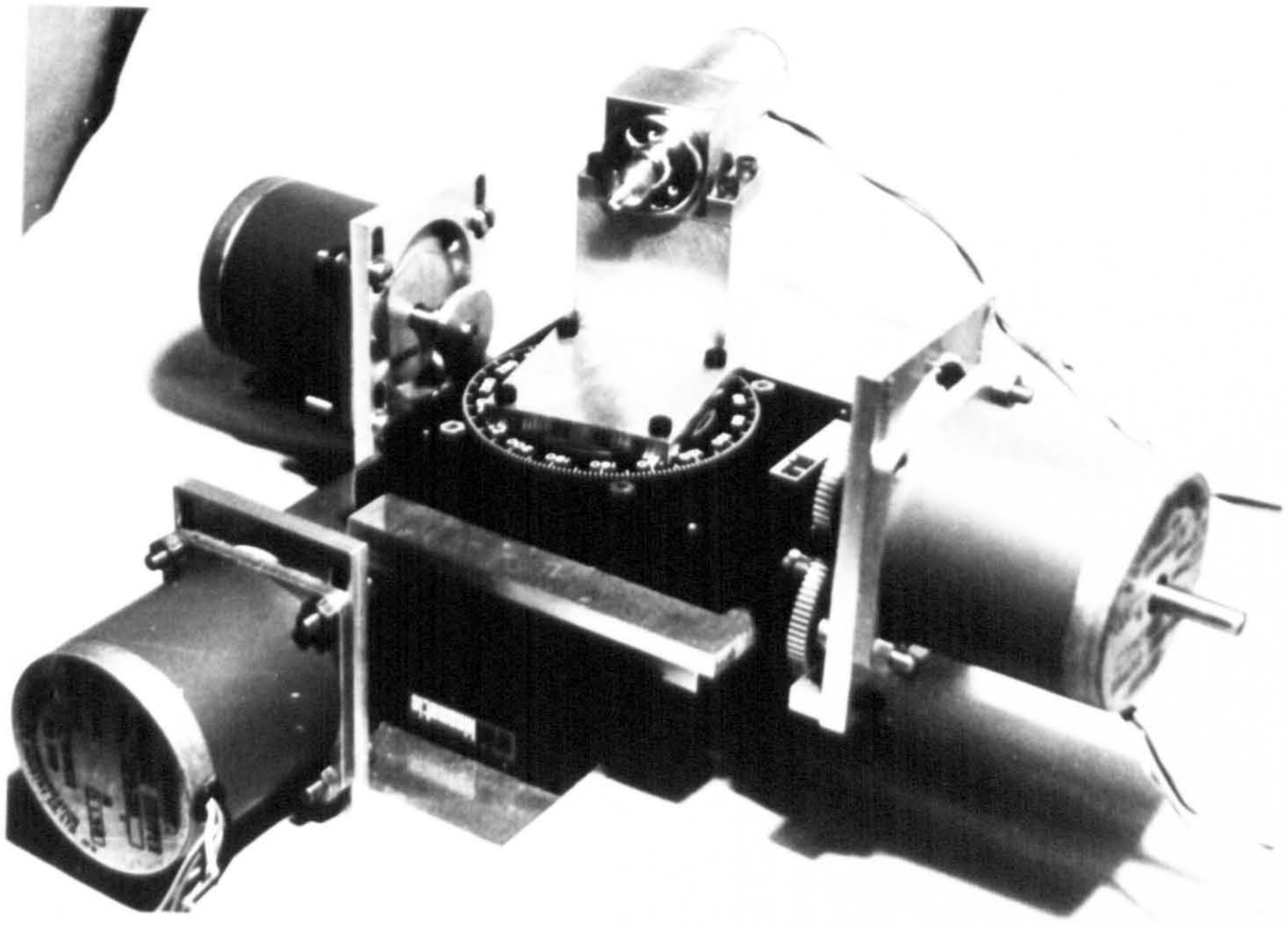

Figure 6.7 Three axis drive assembly for MCPM.

6.4.3 Polishing-head positioning-unit

Figure 6.7 shows the subassembly used for positioning the polishing head. Two linear translation tables (model T1005, manufactured by Ardel Kinematic Inc) and one rotation table (model RT-200) were combined into a single unit to provide two linear motions at right angles to each other and a rotary motion about an axis perpendicular to the linear axes. Stepper-motors were fixed to mounting plates to drive the tables through simple spur gear drives. The linear tables (horizontal X- and vertical Z-axes) were driven by Astrosyn Co. type 23PM-C005 12 volt stepper-motors, whose step angles were 1.8 deg ±3 min. The rotary table (A-axis) was driven by an Astrosyn Co. 23PM-C012 stepper-motor whose step angles were 5 deg.

In order to assess the linearity and reproducibility of the stepper-motor linear-table motion the LVDT equipment, electronic controllers and one stepper-motor driven table were taken to the Metrology Laboratory of the National Engineering Laboratories where a Hewlett-Packard laser interferometer system was available. The interferometer was used to measure the distance travelled by a corner-cube reflector placed on the linear table. The table movement was also measured by an LVDT probe so that an LVDT calibration was made at the same time. The calibration of the LVDT was used later to check the remaining Ardel table. It was clear that the table could be moved along any part of its range of travel in 0.5μm steps to be at a required position within 2.5μm accuracy over 5mm.

The gear ratios were chosen to produce linear motion of 0.5μm per step and rotary motion of 1.736 min arc per step. These ratios were chosen so that the radial motion of the polishing head would be as fast as possible, and that the slowest likely speed of the Z- and Y-axes would not be slower than the speed of the X-axis. The X-axis motion was required to be as rapid as could be driven by the stepper-motor system when near the lens centre. In this region the other two tables moved very little. Even

at the steepest part of the lens (about 33 deg) the rate of Z-steps was less than the rate of X-steps. The A-axis moved rapidly at the two regions of greatest local lens curvature, being most rapid at the edge of the lens. The gear ratio for the A-axis drive was chosen to make the A-steps large enough to be made within the time dwell prescribed for each X-position.

For the polishing runs made during this work, only in two small regions of the lens was more than one A-step required for each X-step. The arc-length of a step was given approximately by 0.5μm/cosθ, where θ is the local slope of the lens profile. The angle subtending this arc can be obtained by dividing the arc length by the local radius of curvature, C. The number of A-steps per X-step is then this angle divided by the A-step angle (which is 0.505×10^{-3} radians), i.e. $0.5\mu m/(C.\cos\theta.0.505.10^{-3})$. At the edge-rounding boundary of the lens this value is 0.45 (i.e. never more than one A-step per X-step) and at the lens edge the value is 1.7 (i.e. either one or two A-steps per X-step). However there were two larger jumps than expected within these two boundary regions. Where the arc fitting programme of Chapter 2 smoothed over the regions of great local curvature there were discontinuities in the lens slope between two pairs of adjacent arcs. These were equivalent to 2.3 and 4.9 A-steps at the edge-rounding boundary and the lens edge regions respectively.

A bracket was mounted onto the rotary table to hold the polishing head in a hole bored to a close fit (less than 2.5μm) with the nominal 26mm diameter of the polishing motor case (see Figure 6.6). This bracket could also hold other accessories which will be discussed in section 6.4.5. Several preliminary alignments of the equipment were required. The lens spindle and the polishing spindle (when vertical) had to be collinear and parallel to the vertical Z-axis table motion. The horizontal X-axis table motion was required to be at right angles to the Z-axis, parallel to the plane top surface of the IOSA substrate.

The rotary table had to rotate about a horizontal A-axis, in the plane of the lens surface, at right angles to the X- and Z-axes. Various slotted mounting holes and packing shims were used to adjust the positions of the components until an LVDT probe (sensitive to displacement smaller than 1μm) mounted in appropriate positions on the equipment assured these alignments were correct to within a few micrometres. To check the alignment, the LVDT probe was mounted in the polishing head bracket (Figure 6.8) and tracked around a spherical lens of known radius of curvature, using a programme to describe its circular profile. The deviations indicated were within the ±5μm accuracy expected of the MCPM.

The positioning tables were normally driven without any feedback other than a visual check of a motor step counter display. Dial gauge indicators were fitted permanently against the linear tables for coarse setting (within a nominal 2μm, although the British Standard for such indicators allows non-linearity up to 15μm). The rotary table could be set within 0.5 deg using its built-in protractor scale. This accuracy was considered adequate for polishing.

6.4.4 Position-unit electronics

Electronic subunits were used to drive and control each stepper-motor. A Digiplan Ltd type LD2 circuit board was used to drive each stepper-motor as a two-phase bipolar bridge. The four leads of the stepper-motors required the following energising sequences, where 1 implies energised and 0 implies no connection:

TABLE 12: SEQUENCE OF ENERGISING STEPPER-MOTOR COILS.

lead	1A	2A	1B	2B
	1	0	0	1
	0	0	1	1
	0	1	1	0
	1	1	0	0
	ETC, ETC			

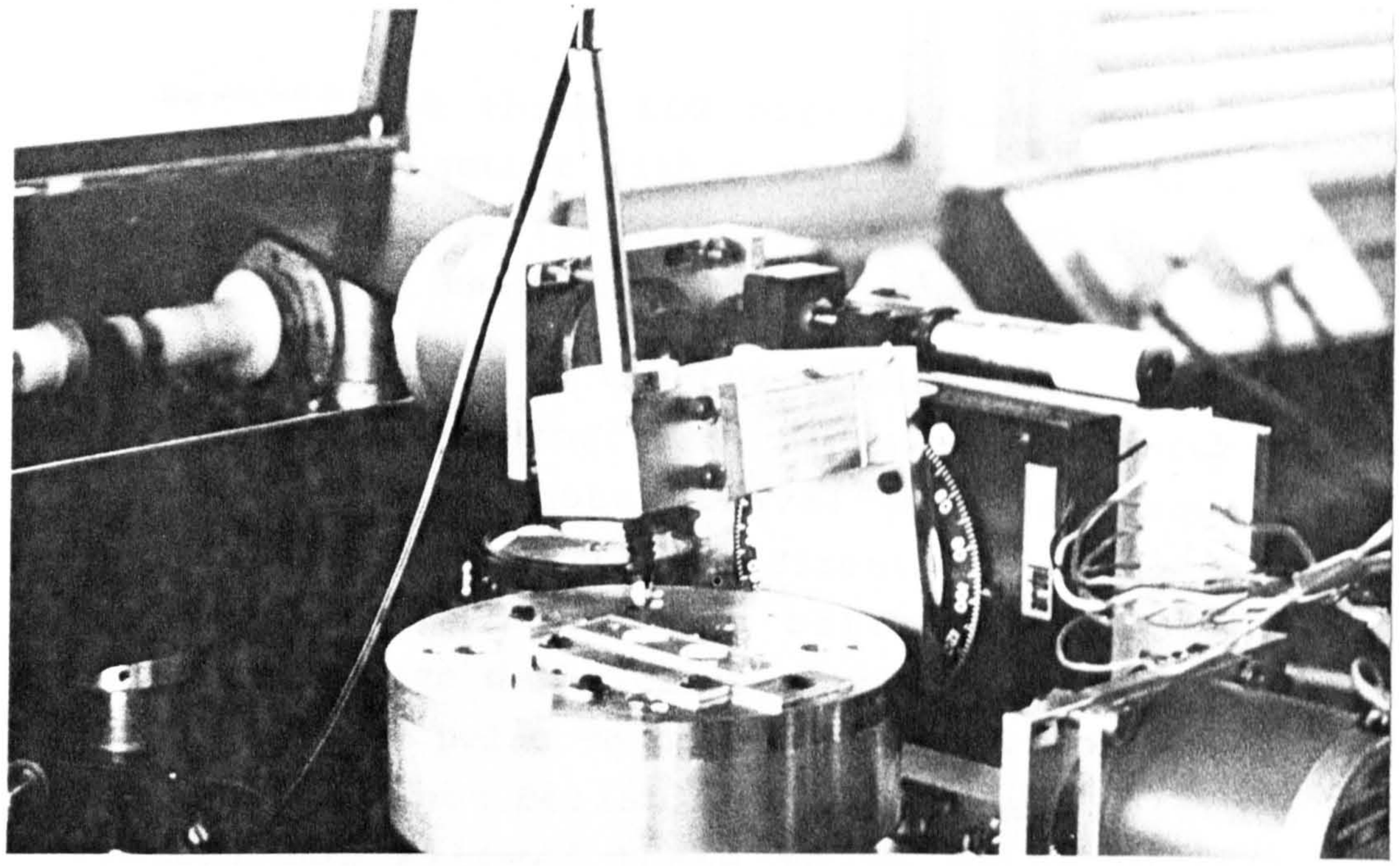

Figure 6.8

LVDT measuring probe mounted on MCPM for axis alignment.

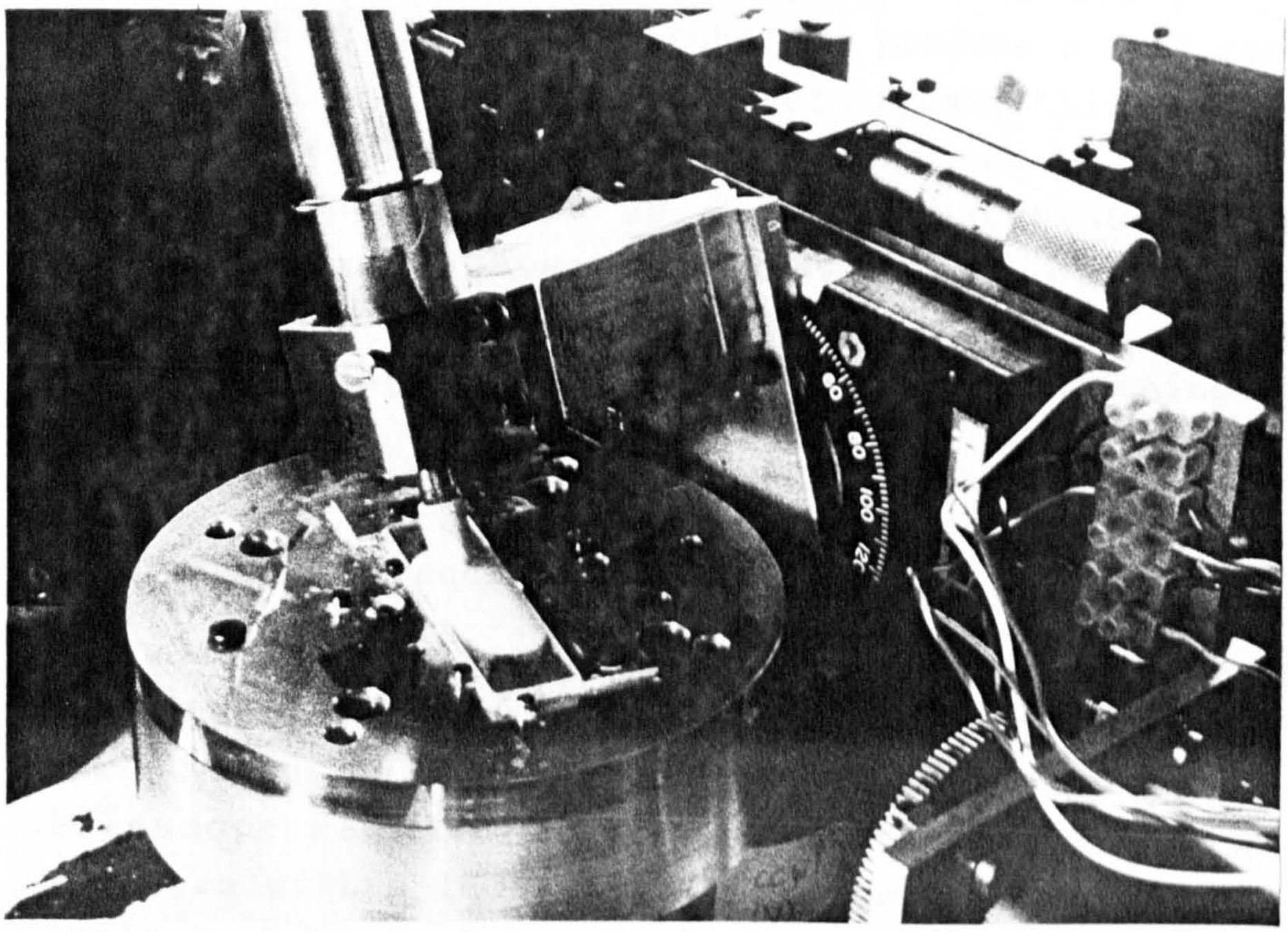

Figure 6.9

Felt cone polishing pad and pool of colloidal silica in a diamond turned geodesic lens depression mou nted on the MCPM

Each of the three LD2 boards was mounted in a box (Figure 6.6) together with a power supply, other auxiliary circuits switches for direct control and interconnections for control by the Vector MZ microcomputer.

Two 12V inputs to the LD2 circuit were supplied by the microcomputer via smoothing circuits. One input specified the direction of motor travel (and was required to be switched in the appropriate direction for the duration of the motor step plus 10μs before,to ensure that any direction change was clearly established). The other input instructed one pulse to occur each time it was switched on (for the shortest reliable time - 10μs). Switches on the control box allowed these to be manually overridden, either as single pulses or a train of pulses at a rate controlled by a clock subcircuit. The speed of this clock could be varied from zero up to faster than the motors could be driven by the setting of switches and potentiometer controls. The pulse introduced to the stepper-motor could be switched to produce a full step of the specified rotation, or a step of half this angle. The three tables could be set to any position by using these controls manually. An up - down counter (Radiospares 50395) and a seven-digit numerical display were constructed to indicate how far (in terms of the number of steps) each axis had been traversed since switching on or re-zeroing the display.

6.4.5 Auxiliary equipment.

Two important items of auxiliary equipment could be substituted for the polishing head, being fitted into the same cylindrical aperture. A 90x magnification inspection telescope was made, using a x9 objective and a x10 eyepiece with a 160mm tube. Once focused onto the lens surface at any point and firmly clamped, the telescope could be moved under a computer-controlled path to scan over the whole lens profile while the surface remained in focus. Side illumination from a fibre-optic light source

or from a remote tungsten lamp provided semi dark-ground illumination to reveal turning grooves which had not been polished away.

An LVDT could be fitted into an adaptor and placed into the same position as the polishing head (Figure 6.8). This was used for alignment of the axes as discussed above, and could also be used for coarse measurement (to about 10μm precision) of the lens profile after polishing, if required.

6.5 CONSTRUCTION OF MCPM - SOFTWARE

It was intended to control the movement of the polishing head over the lens surface in a manner which achieved uniform removal of material, or alternatively removed the amount of material needed to correct an inaccurate lens profile. The procedure was to track the polisher over the lens surface from centre to edge, dwelling for a precalculated time at each annular position as the lens rotated below the polisher. The relative times were initially calculated using a gross approximation to Preston's law, and subsequently modified by observation of the relative amount of material removed from the various zones.

If the rotational speed of the polishing head is V_p, and that of the lens is V_l, the pressure between polisher and lens is P, the effective radius of the polishing head is S, and the radial position of the annulus being polished is R, then the depth of material removed from this annulus during time T is given by:

$$Z = k.P.(S.V_p + R.V_l).T/(2.\pi.R) \qquad \text{.....6.1}$$

where k is Preston's constant (see Chapter 3 and references 173, 174). This approximation assumes that the integral over time T and over the area of contact of the

local relative velocity of polisher and lens is proportional to the sum of their (scalar) speeds. The speed at which the lens rotates under the polisher is simply $R.V_1$. The effective radius of the polisher was defined as a radius which best fitted the above approximation: its value could have been obtained by performing the appropriate double integration using a fuller expression for the polishing action [153,185]. Since there was little time to establish the various constants experimentally, and because it was expected that a few empirically-determined polishing runs would probably be required to correct for any non-uniformity of removal during the main polishing runs, it was felt that full evaluation would not be fruitful.

The above approximation determines the relative dwell times at every annular position of the lens. The absolute times are governed by the need to compromise between several considerations:

(i) Short times. The total time per cycle should be short enough to avoid significant profile errors due to tool wear during the polishing cycle. There should be a large radial velocity component of the tool motion to avoid spiral grooving, although since little material removal is needed this fault may be negligible. Analysis of many Talystep traces over polished lens surfaces failed to reveal any grooving of a frequency which could be associated with the polishing tool motion. The operator can only inspect the progress of polishing after each cycle, so therefore he needs sufficiently short cycles to end polishing before too much material has been removed.

(ii) Long times. The ratio of maximum to minimum dwell time must be capable of being large in order to allow a wide range of polishing removal rates. If the tool were of very small contact area, then its dwell time at the lens centre would be zero and the range of times would be infinite. To obtain the greatest possible range the X-table must be moved as rapidly as possible when the

polisher is near the lens centre. This immediately dictates that there is insufficient time for any arithmetic in the controlling microcomputer programme, since this may take up to several milliseconds. Therefore the dwell times must be precalculated, and the fastest programming language available must be used - in this case Intel assembler language. The speed limit of the system was governed by the LD2 stepper motor controller, which could not drive the tables at faster than 500 steps/sec without losing steps.

The value of V_l could be adjusted from about 10 rev/min to 90 rev/min. V_p could be from about 0.5 rev/min to 10 rev/min. The value of S was estimated as 0.5mm to 1mm, being clearly less than the contact area radius. The greatest range could be obtained with the fastest V_l and the slowest V_p. These were set to the most extreme values which were found to be reliable.

Four files were used. FIRSTPOL.FOR was a Fortran programme which read the lens design parameters from the CIRDATA.SMO arc-data file, calculated the stepper motor movements and dwell times and wrote them into POLDATA.DAT, a binary data file which specified which motors should step, which directions they should turn and how much dwell time should occur between steps. If it was required to polish or simulate polishing a plane horizontal surface, a prism face or a spherical lens (these were used for testing the machine) FIRSTPOL.FOR requested the appropriate parameters rather than read the CIRDATA.SMO file. POLISH.ASM was an assembler language programme which read the POLDATA.DAT file and followed its data to control the stepper motors. These programmes will be described more fully now.

FIRSTPOL.FOR considered each 0.5μm X-step from the lens centre outwards, using the arc-data to calculate the appropriate A and Z values. A- and Z-steps were specified if the incremental change in A- and Z-coordinates had

changed by 0.5μm or 1.736 min (or greater) since the previous steps. If the increments of A were two or more times 1.736 min then extra A-steps were specified at this X-position. Thus several combinations of steps may have been specified: X only, X & Z, X & Z & A, X & A and A only. The programme also noted the sign of each step. Two bits of information were required for each motor step: whether to step or not, and direction. The information for all three motors was combined into one 8-bit word, using six bits for the motor steps, and a seventh for starting or stopping the polisher (the eighth was not used).

TABLE 13: 8-BIT CODING OF POLISHING-MACHINE STEPS.

CODE 1		polishing	counterclockwise			step		
CODE 0		not polishing	clockwise			no step		
AXIS			A	Z	X	A	Z	X
BIT	7	6	5	4	3	2	1	0

For the aspheric lens (and any other monotonically curved concave lens) the directions of X-table and Z-table motions were always positive when the polisher was traversed from the centre of the lens to the edge. The A-table motion was positive at first (i.e. angle increased), then negative when in the edge-rounding region. The orientations of the stepper motors, gears and tables were such that positive movement of the A- and X-tables required clockwise turning of their stepper motors, whereas positive Z-table motion required anticlockwise turning. Since the directions of the X- and Z-tables were constant, their direction bits (4 and 3) were kept switched to the appropriate values (1 and 0) at all times, even if no step was required: it was expected that this procedure would lead to greater reliability than would be possible with very frequent switching. For the same reason, the A-table direction was kept switched to 0 for the inner part of the lens, and to 1 for the edge-rounding region. The following table lists all the possible combinations of steps. The decimal, hexadecimal and ASCII

(alphanumerical equivalents) codes are listed for convenience when testing a POLDATA.DAT file for errors. The arrows refer to forward (A>, Z^, X>) or reverse (<A) movements.

TABLE 14: ALL POSSIBLE STEP-VALUES

STEP	BINARY 76 543 210	DECIMAL	HEX	ASCII
X>	01 010 001	81	51	Q
Z^,X>	01 010 011	83	53	S
A>	01 010 100	84	54	T
A>, X>	01 010 101	85	55	U
A>,Z^,X>	01 010 111	87	57	W
X>	01 110 001	113	71	q
Z^,X>	01 110 011	115	73	s
<A	01 110 100	116	74	t
<A, X>	01 110 101	117	75	u
<A,Z^,X>	01 110 111	119	77	w

A subroutine (TIMER) within FIRSTPOL.FOR was used to compute the dwell time associated with each step. This used the approximation to Prestons's law, taking values from the keyboard. In a later version, a correction factor was applied to the edge part of the lens to specify polishing for a greater time, rather than use a separate polishing cycle to make the corrections which had been found necessary. The dwell time was coded as two 8-bit bytes (one byte was insufficient to provide the greatest ratio of times that was expected). Since these bytes were used by the assembler language programme to specify the number of times that a delay loop (of time T_b) was followed, the dwell-time was expressed in terms of an integral number of loops I_t after subtracting the time which the assembler programme needed to read and process the data, and perform switching, T_a. The real dwell-time per step is given by $T_a + T_b I_t$. The relative dwell-time is given by dividing the real time by $T_a + T_b$. Measurements of the total time taken for various values of I_t showed that T_a was 3.4725ms and T_b was 2.0756ms. The maximum speed at which the polishing head could be traversed was

1000/5.5481ms i.e. 180 Hz. Although it was possible to drive the tables faster (up to 500 Hz), severe vibration problems occurred at several resonant frequencies above 180z.

The POLDATA.DAT binary file was written in the following format. The first three bytes were all zero, signifying no step or dwell-time at the lens centre, but more importantly being used as markers for the start of the file (which is twice read in reverse during polishing). Then for each X-step there were three bytes: byte 1 - pulses & directions; byte 2 - time low-byte; byte 3 - time high-byte. The latter was often zero. The file was stored in a large number of "records" each of 128 bytes. Since 128 cannot be divided by three, there would be data lost at the end of writing each record. This problem was initially overcome by writing a dummy fourth byte for each X-step, but this resulted in data files being larger than could be stored in the 64 Kbyte available (together with the assembler programme and enough of the operating system). Eventually a subroutine (PUTPUT) was written in FIRSTPOL.FOR which sorted the 43rd pair of time-dwell bytes into individual low-and high-bytes which could be written separately at the starts and ends of the appropriate blocks. The various files written were typically about 40 Kbytes long, and took many minutes to read or write.

The absolute, execuble object file version POLISH.COM of the assembler language programme was loaded from disc to occupy memory from address 100H (hexadecimal) by a keyboard entered command such as POLISH ASPHERE. The argument of this command (in this case ASPHERE) was the name of the file containing the polishing data to be followed. The first subroutine of POLISH read the data file from disc into memory starting at address 1000H. The memory map when loaded is outlined below:

TABLE 15: MEMORY MAP OF LOADED SYSTEM
(Hexadecimal addresses)

LOCATION	FEATURE
FFFF	TOP OF MEMORY FDOS
C800 to 1000	POLDATA.DAT
0410	CYCLES
0405	TIME
0400 and below	STACK POINTER
02B6 to	POLISH.ASM
0100	TBASE
0000	BOOT

The programme read the number of polishing cycles required from the terminal. Each cycle comprised four traverses across the radius of the lens - out from the centre, back to the centre, across to the opposite side and return to the centre. This procedure was intended to diminish errors due to asymmetry of positioning and the gradual wear (or pressure decrease) of the polishing tool. The programme made four loops through the data file. "Forward" means starting at lens centre, "reverse" starts at lens edge part of data file. "True" means steps in the directions specified in the data file, "comp" means complements the direction of the file, i.e. going the other way. The four loops read as follows:

TABLE 16: SIGN RULES FOR THE FOUR LOOPS THROUGH THE POLISHING-DATA FILE.

LOOP NUMBER	DIRECTION READ THROUGH FILE	PULSE DIRECTION		
		X	Y	Z
1	FORWARD	COMP	TRUE	COMP
2	REVERSE	TRUE	COMP	TRUE
3	FORWARD	TRUE	TRUE	TRUE
4	REVERSE	COMP	COMP	COMP

When required, the bits to be complemented were selected, complemented by the CMA assembler language command then added back to the remaining bits. To avoid ambiguity, the direction bits were preselected and output onto parallel port number 8 in advance of the step commands with a 10μs delay obtained by the number of states needed for some programme steps. The three step command bits were output for 10μs (42 states with the particular 4MHz Vector MZ computer used), to make the appropriate motors step once. The programme then read the two bytes specifying the time delay. A delay loop was followed for this number of times. It was found more reliable (more immunity to electrical noise generated by the polishing machine DC motor) to use the motors in their half-step mode; each step and time dwell was therefore repeated. After all the specified number of cycles were finished the message "polishing finished" was displayed and the disc was rebooted to return the computer to CP/M control.

6.6 EVALUATION AND USE OF MCPM

Before using the MCPM, lenses were polished on the Moore machines, with poor results. Polishing of a lens which had been partly polished on the Moore aspherising machine was continued by hand with the lens mounted on the Logitech PM2A machine. A felt cone mounted on the drive motor which was also used with the MCPM was kept very wet with Syton W30 and was held for long periods with a small sweep over the regions of the lens which appeared most rough. It was difficult to polish out all diamond-turning marks, and it was also difficult to avoid losing a controlled grip on the polisher and breaking the substrate.

Many polishing runs were made as illustrated in Figure 6.9 on several different lenses. The Engis felt cone polishers wore flat quite soon (see Figure 6.5 centre).

They were frequently replaced from a large stock of fresh cones. The initial pressure was not great - the procedure in setting the polisher head was to apply a little pressure by one finger before clamping the polisher in place. The resulting pressure was estimated as about 0.5 kg. A pool of Syton was poured into and around the lens depression: surface tension kept it in place without any need to contruct a bowl.

Using the microscope, inspection showed grooves remaining near the edge of the lens even after the central areas seemed featureless. it was assumed that the approximation to Preston's law was inadequate in this area. A data file was computed using FIRSTPOL to make the polisher move as rapidly as possible over the central part of the lens, then dwell progressively longer towards the edge. This was found satisfactory. Subsequently FIRSTPOL used this correction subroutine within the run to prepare the main lens polishing data file. The routine made the polisher dwell for the greatest time at radius 5.01mm. For radii greater than 4.8mm the empirically-determined correction factor applied was $58.(0.12 - ABS(5.01-R))^{0.5}$ (where ABS means the absolute value). Using lens rotation speed 90 rev/min, polisher rotation 1 rev/min, and effective polisher dimension 0.5mm this corrected file had 10156 steps in each loop, taking 105.71 seconds - i.e. about seven minutes per cycle.

For the "two-arc" lens and for the last asphere polished, a better correction was made to the Preston's law approximation. This correction allows for the variation in contact area as the polisher passes over regions of the lens surface of varying local radius of curvature. An expression which approximates to the desired correction factor has been derived in Appendix II: this is $(.33 \pm 1/C)/(.33 - 1/C_o)$, where C and C_o are the local radii of curvature at a general position of the lens and at the centre of the lens, respectively.

Each lens required about six hours of polishing until

no pits or turning grooves could be seen (about ten cycles). Usually two felt cones were used for each lens.

As will be discussed in greater detail in Chapter 7, the surface roughness of lenses was assessed after each processing stage. Surfaces which were diamond-turned had peak-to-valley roughness of about 30nm, and 200nm steps at the centre. After MCPM-polishing and forming a titanium-diffused waveguide this roughness had been reduced to about 4nm. The Roughness Average for this measurement would be about 1nm, which is within an order of magnitude of the best smoothness which has been obtained (Chapter 3).

Although the surfaces were very smooth, the Talystep trace just indicated a periodicity of approximately 4µm. This same period could just be observed in corresponding traces over the lenses before polishing.

The profile accuracy after polishing was assessed in three ways. When the lens was inspected by tracking the microscope over the surface, it was always in focus (only dust and smears, once the turning damage had been removed). The depth of focus and the machine tracking errors probably totalled about 10µm, indicating less than 10µm error in the lens profile. The circular-section lens was photographed in a Fizeau interferometer (Zygo) before and after polishing (Chapter 7), and it was found that polishing had not introduced more than 0.5µm profile error. Talystep traces of the central (small area) regions of polished lenses showed that the steps due to the diamond-turning machine had been smoothed out, and that these small regions of the lens were within about 0.5µm of the design profile.

6.7 CONCLUSIONS

Although the MCPM was constructed with inexpensive simple components, was controlled by software which used a gross approximation to the polishing behaviour, and did not employ any feedback other than operator attention, it was still possible to polish diamond-turned lenses to a superb finish. On most lenses the profile accuracy was only assessed by the microscope focus technique. For some lenses, profiles at the central and edge regions were measured by tracking stylus gauges of short height range (Talysurf and Talystep). These measurements indicated less than 0.5μm errors. One spherical surface was polished (the "two-arc" lens) and it showed that the errors introduced were no more than about 0.5μm (Chapter 7). These errors are quite tolerable for IOSA lenses.

The time taken to polish each lens was about six hours, using two felt cones per lens.

CHAPTER 7: EVALUATION OF GEODESIC LENSES

7.1 MEASUREMENT OF LENS PROFILE

7.1.1 Interferometric methods

Optical surfaces are routinely inspected for profile errors by interferometry, for example using Fizeau or Twyman-Green instruments [127]. Before fabrication of lenses, the lithium niobate substrates of the present work were checked for flatness during polishing by double-beam interferometry, generally using a contacting optical flat. Interferometric assessment of surface profile is straightforward for plane or spherical surfaces, and can be performed fairly simply for most conic sections. For more general, aspherical, surfaces it is often possible to provide a system of "null optics" which cancels out the asphericity (or departure from a conic section) and therefore allows the surface to be evaluated [194].

The asphericity of a geodesic lens was calculated by comparison with a sphere which closely approximated to the lens profile. This was an osculating sphere, touching at the lens centre, and with the smallest possible range of radial departures between its surface and the lens surface. The asphericity of the lens design discussed in this thesis was computed as 77μm. This would produce 243 fringes of helium-neon laser wavelength light in an interferogram. Even if these fringes were evenly distributed over the surface it would be difficult to locate them accurately for profile error assessment: the fringes would need to be sharpened by forming a highly reflecting, partially-transmitting thin layer over both the lens surface and the comparison sphere surface to enable multiple reflections to have a significant contribution to finesse. But because of the asphericity, the fringes would not be evenly spaced. The fringes would be closest where the greatest difference in slope (about 32 degrees) occurs between the lens profile and the

osculating sphere, near the edge of the lens. At this position the fringes would only be separated laterally by about 2μm. The relative aperture at which an interferometer would have to operate in order to resolve this close spacing may be estimated, using the Rayleigh criterion that the resolution of a lens system with circular aperture is given by $1.22 \lambda.F/W$ [121], where λ is the wavelength, F is the focal length and W is the aperture. The value obtained is f/0.3: it would be very difficult and expensive to construct an interferometer with such a wide relative aperture.

The aspherical geodesic lens surface could perhaps have been tested interferometrically in comparison with an ellipsoid of revolution, using an appropriate null optical system. An ellipsoid could provide a better fit than a sphere to the central part of the aspheric profile [101]. This was not attempted since it would have involved a great deal of preparation of an accurate comparison surface, and, more importantly (since an ellipsoidal lens would not fit the edge-rounding region of the geodesic lens any better than would a sphere) the fringe separation would still be too close to be resolved satisfactorily near the edge of the lens, and it would not be possible therefore to measure the profile of the whole of the lens.

It would be more difficult to test a geodesic lens on a lithium niobate substrate by transmission normal to the plane of the substrate than by reflection. This is because the wavefront of light transmitted axially through a geodesic lens would be far more complicated to analyse than a reflected wavefront since it depends on the refractive index of lithium niobate (which is anisotropic), the thickness of the substrate and the shape of the rear surface. For the lens design of this thesis light cannot be transmitted through all zones of the lens because the steepest part of the lens (up to slope of about 32 degrees) is greater than the angle at which total internal reflection occurs (about 27 degrees).

Interferometric testing of a strongly aspherical geodesic lens should be possible using a pre-calibrated reference surface of the same profile as the lenses, perhaps diamond-turned in metal to provide a good mirror surface conveniently. With the present lens design there would be difficulty in collecting light reflected from both the inner and the edge rounding regions because the change of direction of reflected light does not follow an easily-managed, monotonic, function of lens radius. However even if these difficulties were overcome there would still be a need to pre-calibrate the profile of the reference surface.

It is possible to introduce a computer generated hologram into an interferometer wavefront to correct for asphericity [195-199]. Using an expression from reference 198, the number of lines that would be required to be drawn to compensate for 243 fringes of asphericity with a maximum slope error of 32 degrees and profile measurement accuracy of about 0.5μm would be many thousands. This number of lines is so great that plotting reliability and time-related costs would present great difficulties (although a machine under development [199] may eventually enable sufficient lines to be drawn with sufficient accuracy).

The profile of the inner spherical part of the simple "two-arc" geodesic lens (made by diamond-turning and MCPM polishing, as described in Chapters 5 and 6) was inspected interferometrically. The lens was tested by Fizeau interferometry using converging auxiliary lenses (on Zygo instruments at Moore Special Tool Co, and at Barr & Stroud Ltd). Before polishing, the lens radius of curvature was measured (within ±0.01mm) as 15.99 mm at the centre and the average over the whole concave spherical region was 16.00mm. As expected from the known precision of the turning machine at Moore, the Zygo instrument showed that the lens had been turned to its design radius of curvature within the accuracy of measurement. Figure 7.1 (A)

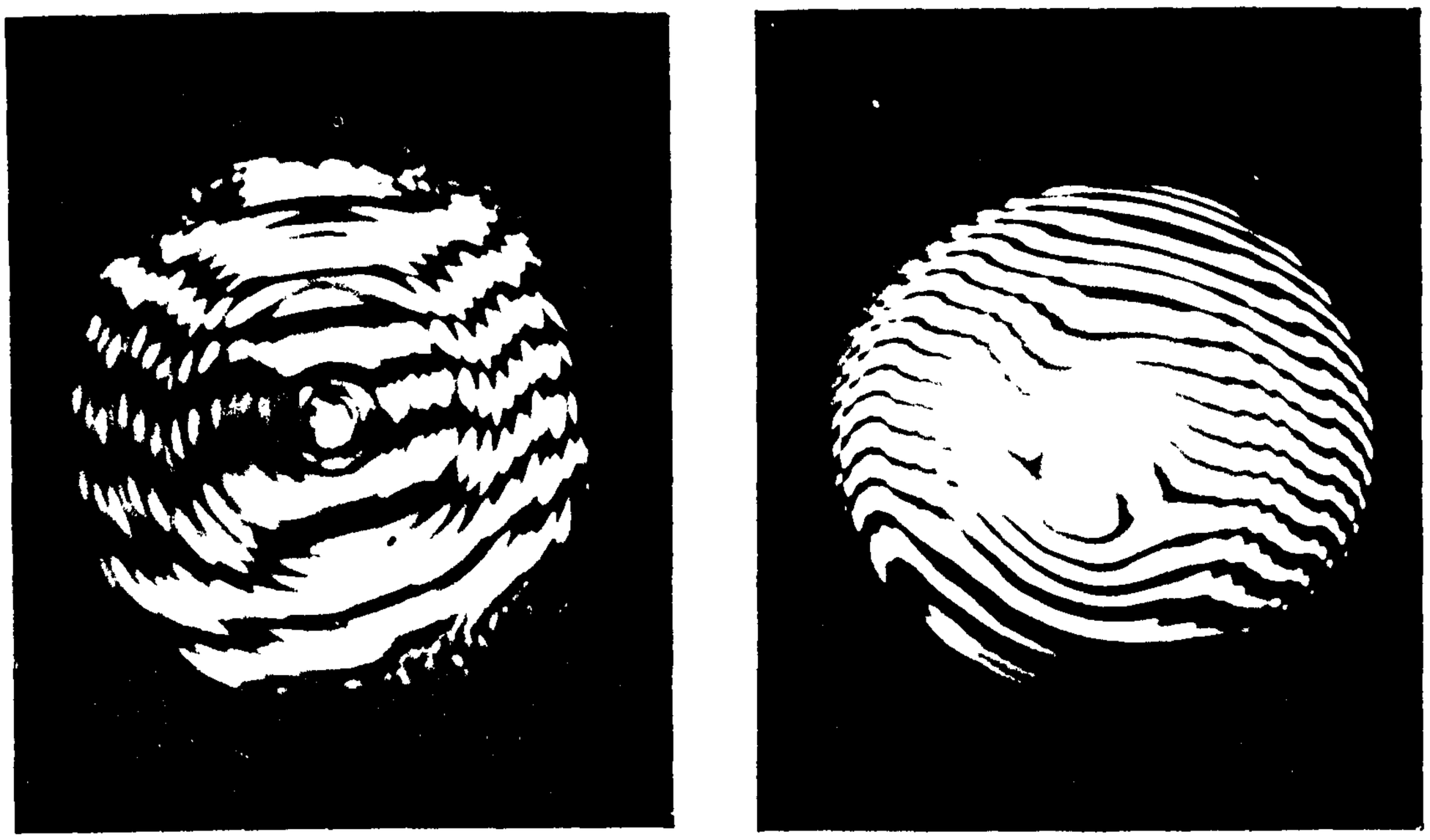

Figure 7.1

Interferograms of spherical part of a geodesic lens:
A after diamond turning
B after MCPM polishing

shows an interferogram of the lens centre after turning. The fringes indicate that the profile error after turning was less than one fringe separation (that is less than about ±0.3μm). Figure 7.1 (B) shows an interferogram of the same lens after polishing on the MCPM. Errors of 2·5 fringes (i.e. ±0.8μm) can be seen. The fine structure of the fringe pattern is due to further interference from the back surface of the substrate, and does not indicate diamond turning marks or any tendency of the turning machine to have produced errors in the form of stepped regions. This unwanted interference could have been reduced (but not eliminated) if reflection-reducing, absorbing paint for the back surface of the substrate had been available in the laboratories where these interferograms were made.

7.1.2 Scanning depth-probe methods

Several mechanical-probe measuring-machines have been constructed for measurement of aspheric lens profiles [200-204] but none are available yet commercially, except by hire as discussed below. In the present work, several mechanical methods were assessed for measuring geodesic lens profiles.

As described in Chapters 4 and 5, lens profiles were measured mechanically using tables which moved a recording probe on two or more axes relative to the lens.

The ultrasonically-generated lenses were measured by using mechanical dial-gauges (Chapter 4). One gauge was scanned across the radius of a lens by traversing the cross-slide of the lathe on which the lens and gauges were mounted. The measuring range of the gauges was long enough to record the full travel across the lens radius and the full depth of the lens profile. The dial gauges could only be read to within 1μm (by interpolating between scale marks), and were of limited accuracy. The British Standard to which they are specified (907:1965) allows errors of a few micrometres for short distances but up to

20μm for a long travel. These gauges, therefore, could not be used directly without accuracy being limited to ±20μm.

Profile measurements of lenses which were generated on the CNC grinding and diamond-turning machines were made directly on the machines themselves, with a probe stylus replacing the cutting tool (Chapter 5). The probes were used as null indicators, the machine-slide calibrations being used to indicate distances. Although these measurements were not independent of the accuracy of the machines, the machine slides and probes had been calibrated against known plane, spherical and length standards. Since the machines were not available after polishing the lens surfaces in Glasgow, other measurement equipment was clearly necessary.

To a limited extent, lens profiles may be assessed by instruments which are primarily intended for surface-texture measurement. Because the range of height measurement is usually very small (10μm for the Rank-Taylor-Hobson Talystep instrument which was available) it is not possible to produce a single scan of a lens profile. It is necessary to make many scans and join them together by calculation, and this procedure tends to be insufficiently accurate (about 4% [64]). Figure 7.2 shows a Talystep trace taken over the central 0.9mm diameter of one of the lenses which had been diamond-turned then MCPM-polished. For comparison a dashed line shows the designed profile for this portion of the lens - an arc of 10.933mm radius of curvature. The trace indicates a profile-height error of 0.7 ±0.2μm at radius 0.4mm, and implies that the radius of curvature in this region is 10.00 ± 0.25mm. Although this result gives little information on the whole profile of the lens, it is encouraging that the height error is of the same order of magnitude as the claimed accuracy of the Moore diamond-turning machine, and that polishing with the MCPM does not seem to have introduced significant errors into this small central region of the lens.

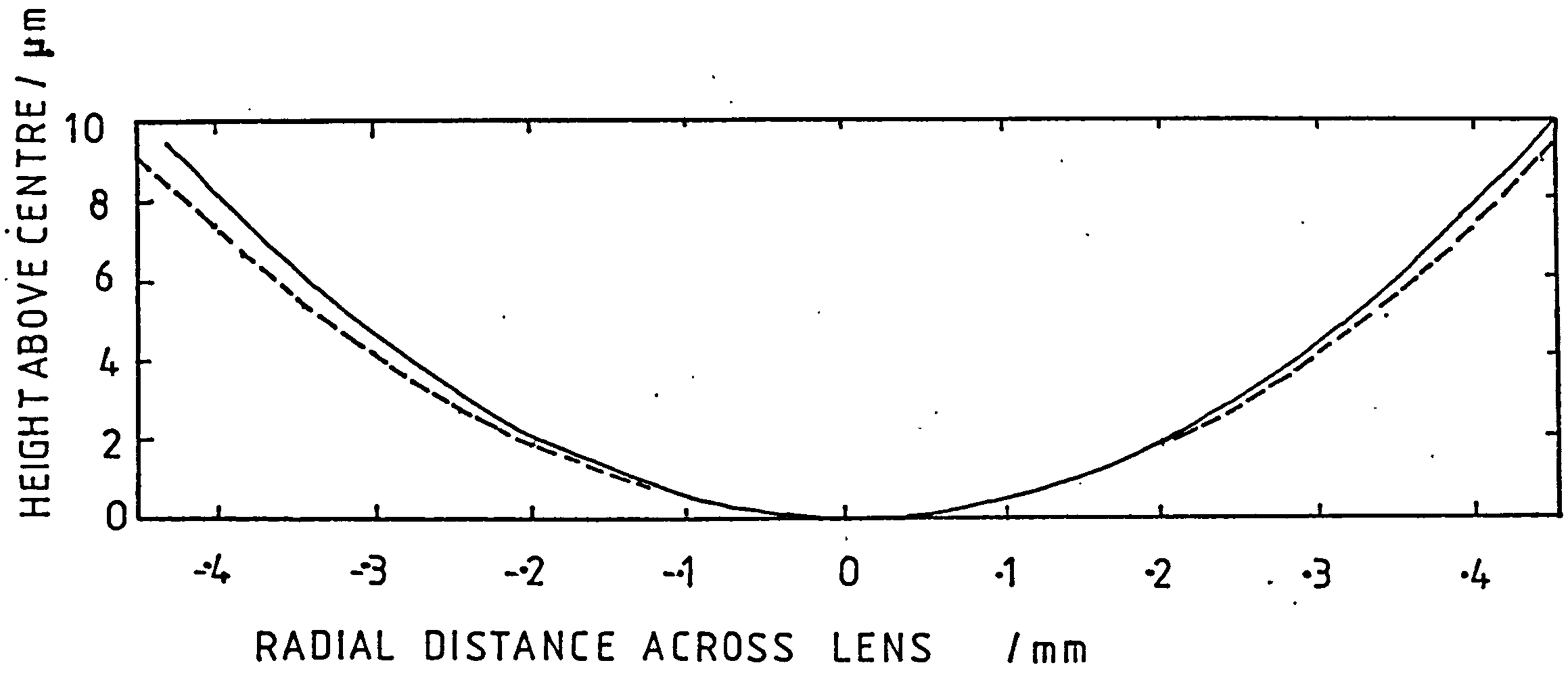

FIG 7.2 Profile of central 0·9 mm diameter of a polished lens.
Full line – Talystep trace, dashed line – 10·933 mm radius arc.

7.1.3 Sira surface-form gauge.

The only mechanical scanning gauge in the U.K. which was accessible to the author and seemed capable of measuring a complete geodesic lens was an instrument developed by Sira Institute Ltd [200] (Figure 7.3), and which was available (infrequently) for hire at their premises. The operating principle of the machine involves the measurement of radial deviation from a sphere. In this instrument a probe is mounted on a rigid arm which may be rotated about a horizontal air-bearing axis. The distance of the probe tip from the horizontal axis may be set to any length up to 1.2m. The surface to be measured is fixed below the probe on a very precise air-bearing vertical-axis rotary table. The locus of the probe tip is a circle, so that if the lens-bearing table rotates, the probe displacement measures the difference of the lens profile from a sphere. In the work carried out on geodesic lenses the instrument was used in a radially-scanning mode to measure deviations of the diamond-turned lens profile from a circle which closely fitted the lens profile. The rotary table was only rotated during initial setting-up, such as when arranging the axis of rotation of the lens to be precisely vertical, and along a line between the probe tip and the axis of the arm bearing.

Figure 7.4 shows the output from the machine for a scan across the diameter of a geodesic lens. "Positive radial deviation" refers to probe deviation towards the axis of rotation of the arm and therefore in the direction away from the substrate. The horizontal scale of Figure 7.4 is the angle of rotation of the arm with respect to vertical, zero degrees corresponding to the centre of the lens. The position of the probe assembly on the arm was adjusted until the positive and negative deviations were approximately equal.

The value of the comparison radius was measured by moving the measuring-probe assembly along the arm by a short distance until zero probe displacement was recorded

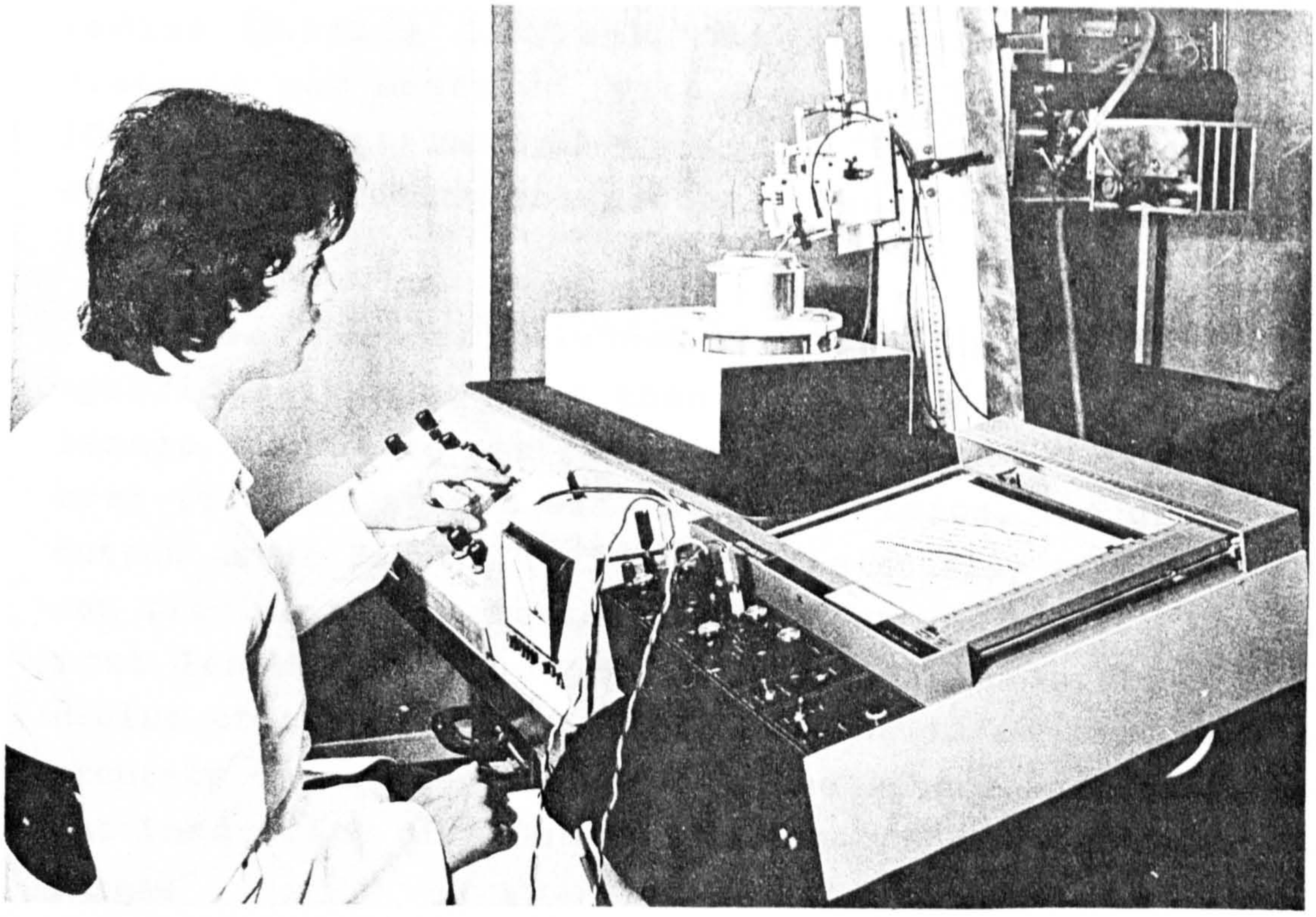

FIG. 7.3 SIRA aspheric profile measuring machine.

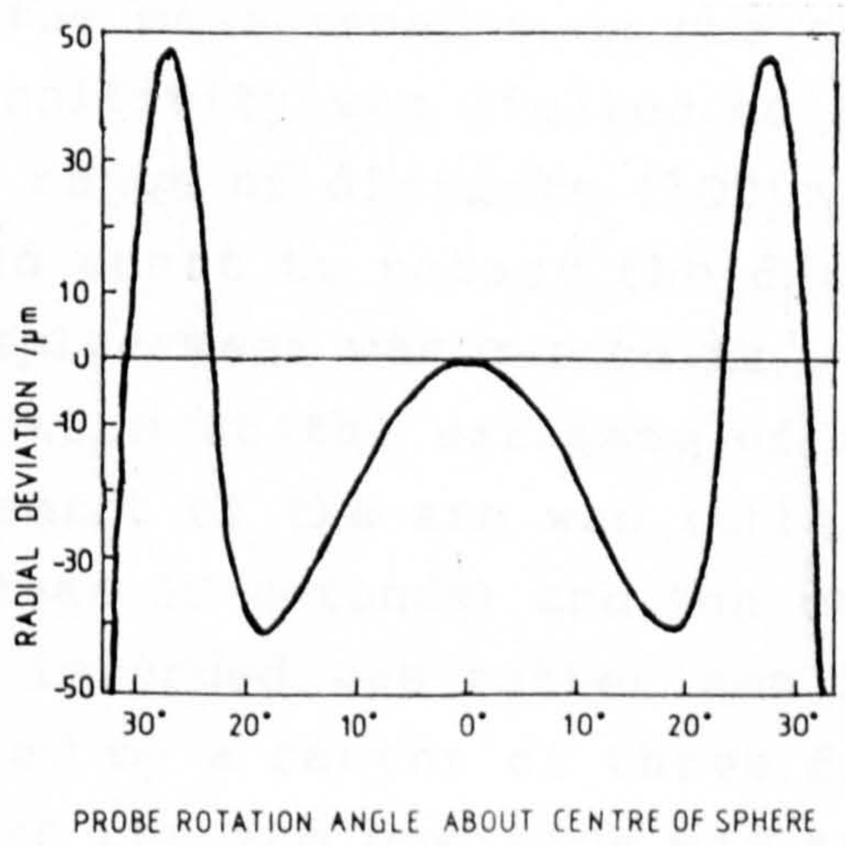

FIG. 7.4 Output from Sira machine for an diamond-turned SRR lens.

Radial deviation of a diamond-turned geodesic lens from 9.47-radius reference sphere, as tracked by a stylus with 2-mm radius tip.

when scanning over a concave lens of precisely-known radius (8.942 ± 0.005mm). The increase in probe-axis distance was measured (with a micrometer calibrated in 10μm divisions) as 0.53 ± 0.02mm. The comparison radius used for measuring the geodesic lens was therefore 9.47 ±0.02mm.

For most aspheric lenses the level of deviation from spherical is much less than encountered with geodesic lenses, and it is not required to know the radius of the best-fit base sphere with much precision. The graphical output as in Figure 7.4 is therefore usually adequate, and can provide measurements within 0.5μm of asphericity for most lenses. For the geodesic lenses, accuracy in the radius of the base sphere measurement is as important as accuracy in the deviations from the sphere, and therefore the inaccuracy of ±20μm in the base sphere radius is too large.

The spherical tip of the probe has a diameter of 2±.005mm and the limit of detection of its displacement is about ± 0.1 μm, the instrument being capable of 0.1μm resolution when measuring almost spherical lenses of radii of curvature similar to that of the geodesic lens [200]. However during the measurements on the geodesic lens, the displacement sensitivity was limited to ±0.8μm by the need to span a large range of distance (100μm) and by the need to use a pen and chart to record the data. The linearity of the probe displacement was quoted as within 1.5%, which is also about ±0.8μm at the extremes of this measurement. The angular movement of the arm was rather fast (the whole scan took less than 30 seconds) and the chart on which the deviations were recorded was rather small (Figure 7.4 had only been reduced by a factor of three from the original trace). Therefore the arm position was not recorded very accurately and an error of ±0.5 degrees was possible. Unfortunately the arm could not be traversed beyond 30 degrees without decreasing measurement sensitivity even more: it was not possible therefore for the probe to

measure the whole of the lens profile.

The data points from the Sira instrument were converted to lens profile measurements by using a computer programme which estimated the points of contact of the probe tip with the lens surface. The points of contact were calculated from the measured data using

$$Z = C - (C - T + \Delta C).\cos\alpha - T.\cos\beta$$

and $$R = (C - T + \Delta C).\sin\alpha + T.\sin\beta$$

where R, Z are the radial and height position of the point of contact relative to the centre of the lens depression, C is the radius of curvature of the probe rotation (9.47mm), ΔC is the probe displacement, T is the radius of the probe tip (1mm), α is the angle of the probe arm to vertical and β is the local slope of the lens profile (expressed as an angle) at the point of contact.

For a first approximation, the programme assumed that the local slope-angle of the lens, β, took the value of the slope of the path taken by the centre of the probe tip between the measurement points around each particular reading. The initially-unknown position of the point of contact was calculated using this value of the slope in the above expressions. Having calculated this estimated position, the designed slope at this position was calculated, using the arc-fitting data discussed in Chapter 2. The contact point position was then re-estimated using this new slope value in the above expressions. The procedure of this paragraph was reiterated as many times as was required until the height Z did not change with each iteration by more than 0.5μm.

Figure 7.5 is a graph of the errors in lens profile, expressed as the height above the ideal Sottini profile of the lens design versus radial position. The dashed lines indicate the limits to the inaccuracy of the points on the graph, estimated by running the computer programme with values of parameters at the extremes of their inaccuracies given above. The graph shows a small section at radius 3.5mm which is raised by about 2.5μm above the surrounding

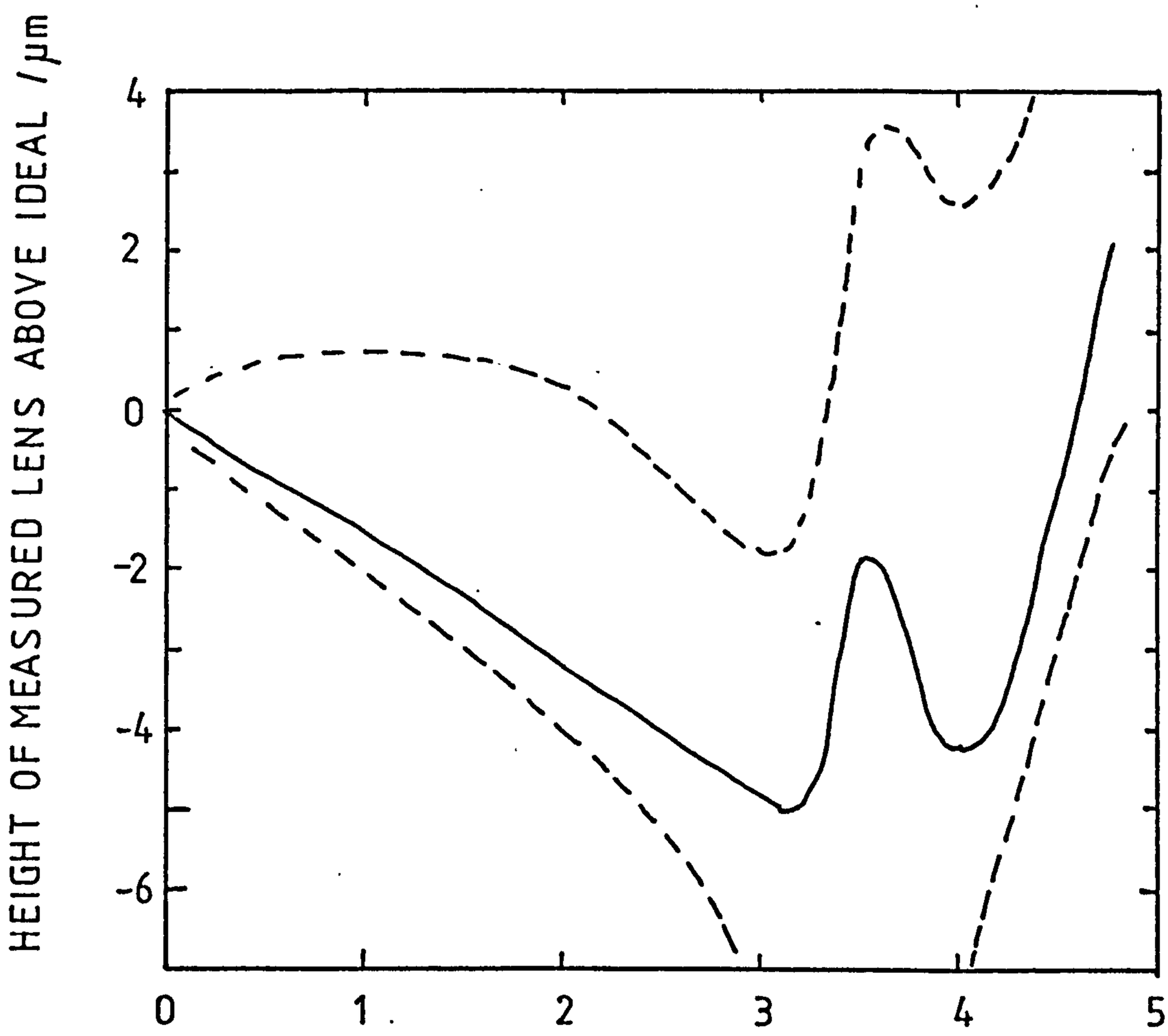

FIG 7.5 Errors measured in an aspheric geodesic lens by the Sira surface-form gauge.

part of the lens profile. Although this could perhaps be identified with the region where the practical lens design bridges over the ideal Sottini profile, the errors in the measurements are so large that such an identification cannot be certain.

Further errors in measurement were revealed when repeating the scan over the lens: drift in the plotted values of about 2μm was observed. It is believed that temperature instability affected the calibration of the electronic and mechanical systems in the Sira machine.

7.1.4 Development of geodesic-lens measuring-instrument

Work was carried out on a small machine to be dedicated to IOSA lens measurement. The machine operates in a similar manner to the equipment described above, and is based on a precision linear-table driven by a stepper-motor, together with two distance-transducer probes. A geodesic-lens substrate may be mounted on the linear table so that a vertically-mounted probe measures the lens profile as the table is translated beneath it. The second probe measures the position of the table. Control of the system and data analysis may be carried out by a micro-computer such as the Vector MZ which has been used to control the MCPM.

Although the use of an air-bearing slide would be preferred for the greatest available measurement-accuracy, it was believed that the use of a high-precision motor-driven table would be adequate, preferably with the table drive effected through a precision lead-screw (giving good positional stability under thrust and torque in all directions) rather than the more commonly available type which use a spring return-drive and push-rod mechanism.

Many types of distance transducers have been developed [200-204]. Position is sensed either by direct physical contact with a stylus or spherical probe-tip [201,204] or by non-contacting indication with a focused light-beam or

constant-depth air-cushion [200,202,203]. Other position sensors relying on capacitive or magnetic effects are inappropriate to geodesic lenses in lithium niobate. Distance is transduced by a differential transformer [200] as on the Moore machines , or optically by laser interferometer [202,204] or moire fringe-counting systems [201,203]. The electro-mechanical types are capable of resolving (linearly) 1000 levels, e.g. 1μm over 1mm travel, and the optical types can resolve 5×10^5 levels, e.g. 5nm over 2.6mm travel [204].

The only suitable distance-gauging transducer type which is commercially available at the time of writing is the linear variable differential transformer (LVDT), which may be obtained from several manufacturers. The A6G/1.0 mm transducer (for measurement of lens depth) and the AG/5.0mm transducer (for measurement of radial position) have been obtained from Sangamo Ltd. for evaluation. The inductance bridges operate at 5KHz at a nominal 5V. Their sensitivities are a few hundred mV/V/mm. The strokes were specified as linear within 0.3% over ±1mm and ±5mm respectively.

Evaluation of the LVDT at the National Engineering Laboratory, East Kilbride, showed that their performance was well within specification. Figure 7.6 shows the results of calibration of the AGG/1.0 mm LVDT and indicates that output voltage is linearly dependent on position to within ± 1.4 μm over a total travel of 2 mm. The calibration curve could be fitted by a third-order polynomial within +0.1μm, which would be more accurate than necessary for assessing the present geodesic lenses. To achieve this level of accuracy, temperature stability within 1° would be required.

There are two problems associated with using these LVDT. There is a backlash (of 1.1μm for the A6G/1.0mm transducer) which alters the zero setting each time the transducer reverses its direction of travel. Since the lens profile changes monotonically from the centre

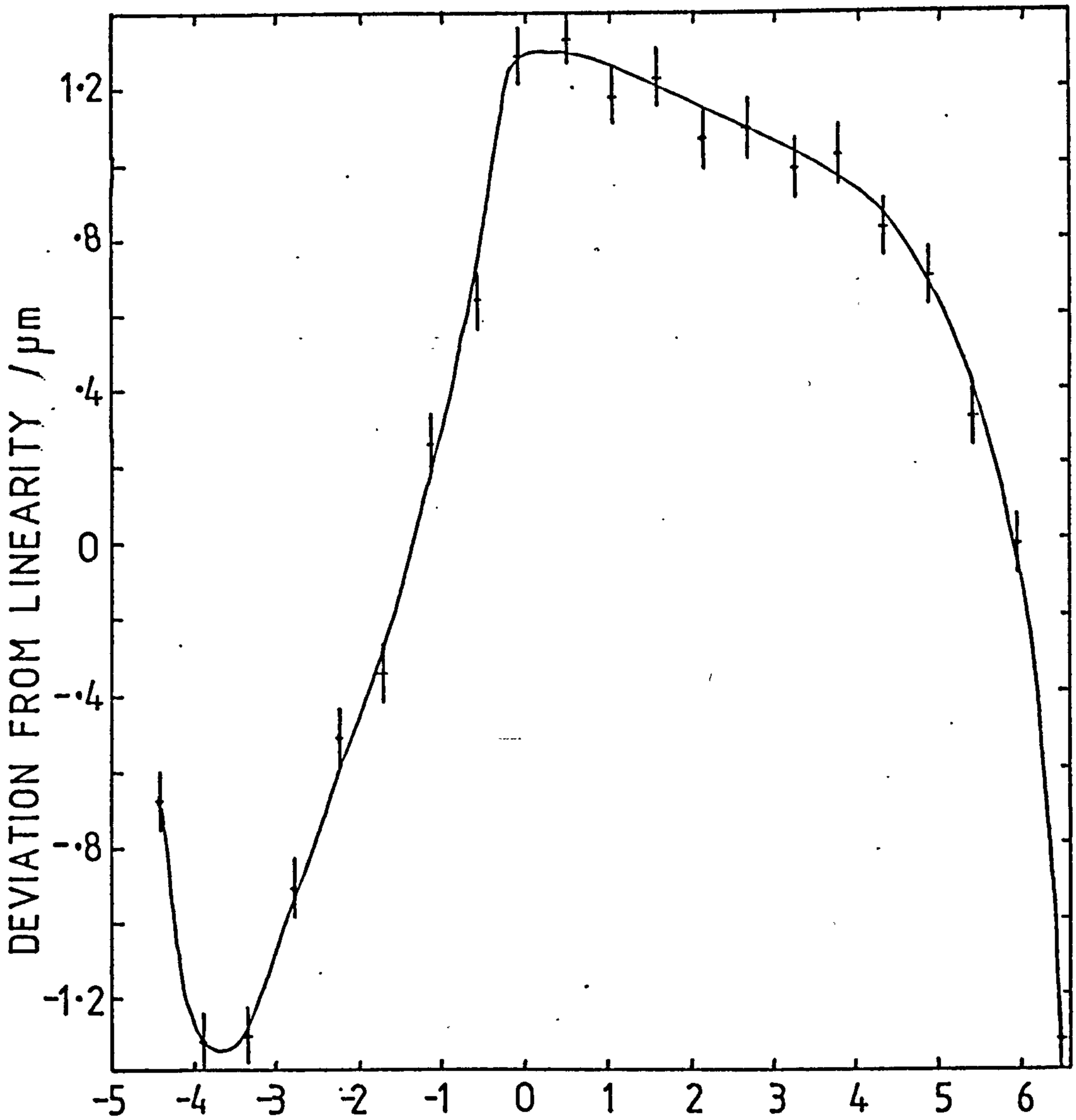

FIG. 7.6 DEVIATION OF DISTANCE TRANSDUCER FROM LINEAR CALIBRATION OF 183·2 μm/volt

outwards, this backlash should be recognisable, and may be calculated out. There is also a small amount of sideways movement of the probe within its bearings. The probe therefore cannot provide its greatest accuracy if scanning across the radius of a lens with the probe perpendicular to the plane of the substrate, since the variation in lens slope would impose a variable sideways thrust and therefore varied displacement of the probe tip. This problem could be eliminated if the probe were always presented normally to the lens surface (as on the Moore machines) or if an intermediate probe set in a very close tolerance bearing were employed.

The lens-profile measuring machine was constructed using these transducers (it can be seen at the centre of Figure 6.6). A small vibration-isolated table supports a stepper-motor driven table (Micro-controle MT 50-16PP) which can be moved in steps a small as 0.1μm. The table may be driven manually or under microcomputer control using the stepper-motor control boxes described in Chapter 6. An IOSA is held on the table, and traversed horizontally under an LVDT held vertically with the probe tip in contact with the surface of a lens. The output from this transducer therefore is related to the depth of the lens profile. A second LVDT is used to indicate the position of the moving table, which is related to radial position on the lens surface. It was planned to link the voltage output of the inductance bridge, which is used to indicate the LVDT movement, to the Vector MZ microcomputer, using a 12-bit analogue-to-digital converter circuit. However there was insufficient time to complete the assembly of this potentially useful instrument.

The LVDT transducers were, however, used in conjunction with dial-gauge indicators to set-up the positions of the axes and lenses in the microprocessor-controlled polishing machine which was discussed in Chapter 6.

7.2 FORMATION OF WAVEGUIDES AND COUPLING

7.2.1 Formation of titanium-diffused waveguides on plane and concave surfaces

The lenses which were tested for imaging performance used titanium-diffused waveguides (produced by J.Singh). The preparation methods for these waveguides are outlined in this section.

The substrate surface was first cleaned in warm trichlorethylene, then in ultrasonically-agitated methanol, then washed in warm detergent (Decon 90), rinsed in ultrasonically-agitated, filtered, deionised water and finally blown dry with filtered dry nitrogen.

The titanium layer was evaporated from an electron-beam heated source at a pressure of about $1x10^{-6}$ torr, the thickness being monitored by a quartz-crystal system. Because of the curved shape of the lenses, it was difficult to ensure a uniform-thickness layer over the lenses and over the plane surrounding area. To a first approximation the thickness, t, at any point on the IOSA is given by

$$t = k \frac{\cos \gamma . \cos \delta}{d^2}$$

where k is a constant for each evaporation, γ is the angle between the vertical line above the evaporation source and the direction of the point on the substrate, δ is the angle of incidence of the evaporant at the point on the substrate and d is the distance from the source to the point on the substrate.

If there is no relative motion between source and substrate during the evaporation, the most uniform layer of titanium which is possible is achieved by the source being at a great distance from the substrate. Then γ and d are effectively constant, and the thickness varies as the cosine of the lens slope. For the lenses in this study the least-possible non-uniformity is related to the steepest

slope of the geodesic lens, 33 degrees, by (1 - cos 33), i.e. 16%. In practice the evaporation source was much closer to the substrate, and the uniformity could not approach this value. For one lens pair a mask was used to coat an extra 20% (approximately) of titanium in a separate evaporation run. The mask took the form of an annular slot, which was placed under (and at a short distance from) the region of greatest slope on the lens.

About 35nm thickness of titanium was coated onto the plane regions of the substrates. This thickness enables a waveguide to be formed on a plane substrate which propagates two modes [35,43]. It was expected that the waveguide layer formed in the lens depressions would support at least one mode of propagating guided-light through the curved surfaces of the lenses.

For in-diffusion, the titanium-coated IOSA substrates were placed into an alumina tube in a furnace and held for a period (typically 9 hours) at about 980°C, with slow heating and cooling. Generally oxygen was continuously passed over the substrate during the diffusion.

7.2.2 Methods of coupling light into waveguides

Some of the IOSA substrates were polished along the input and output edges in preparation for end-fire coupling of laser light. Usually lapping and polishing of edges leaves chips and rounding which are at least of dimensions comparable to the depth of a titanium-diffused waveguide. Extreme care and very accurate holding are necessary to achieve satisfactory edges [30]. A reasonably rapid and high-yield procedure was developed and is described below.

The $LiNbO_3$ substrate is coated with shellac on the lens face and pressed against a datum face which has been ground on glass rod (Figure 7.7), with the long edge of the IOSA pressed against an alignment lip which has been left on the glass rod during grinding of the datum face.

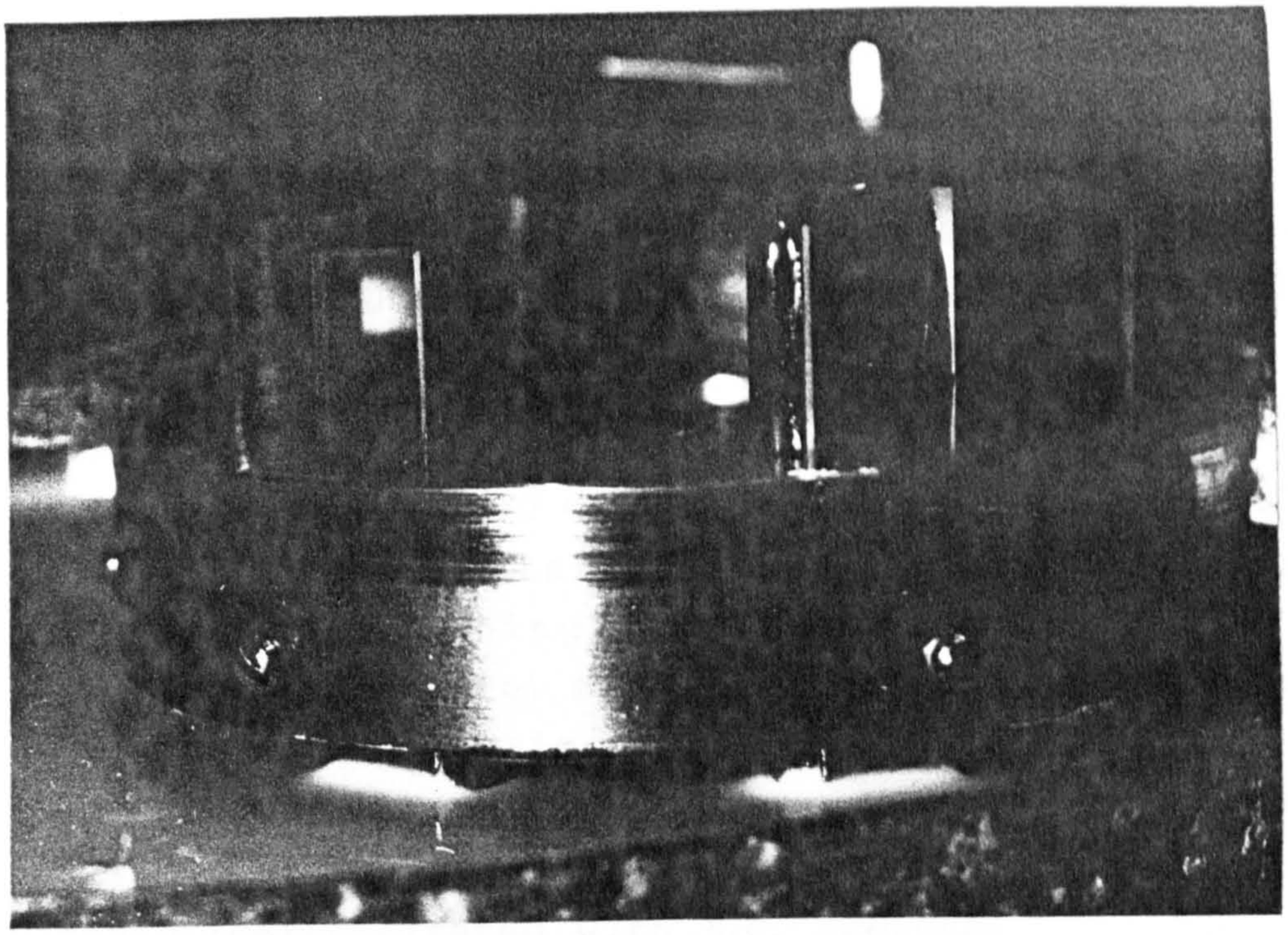

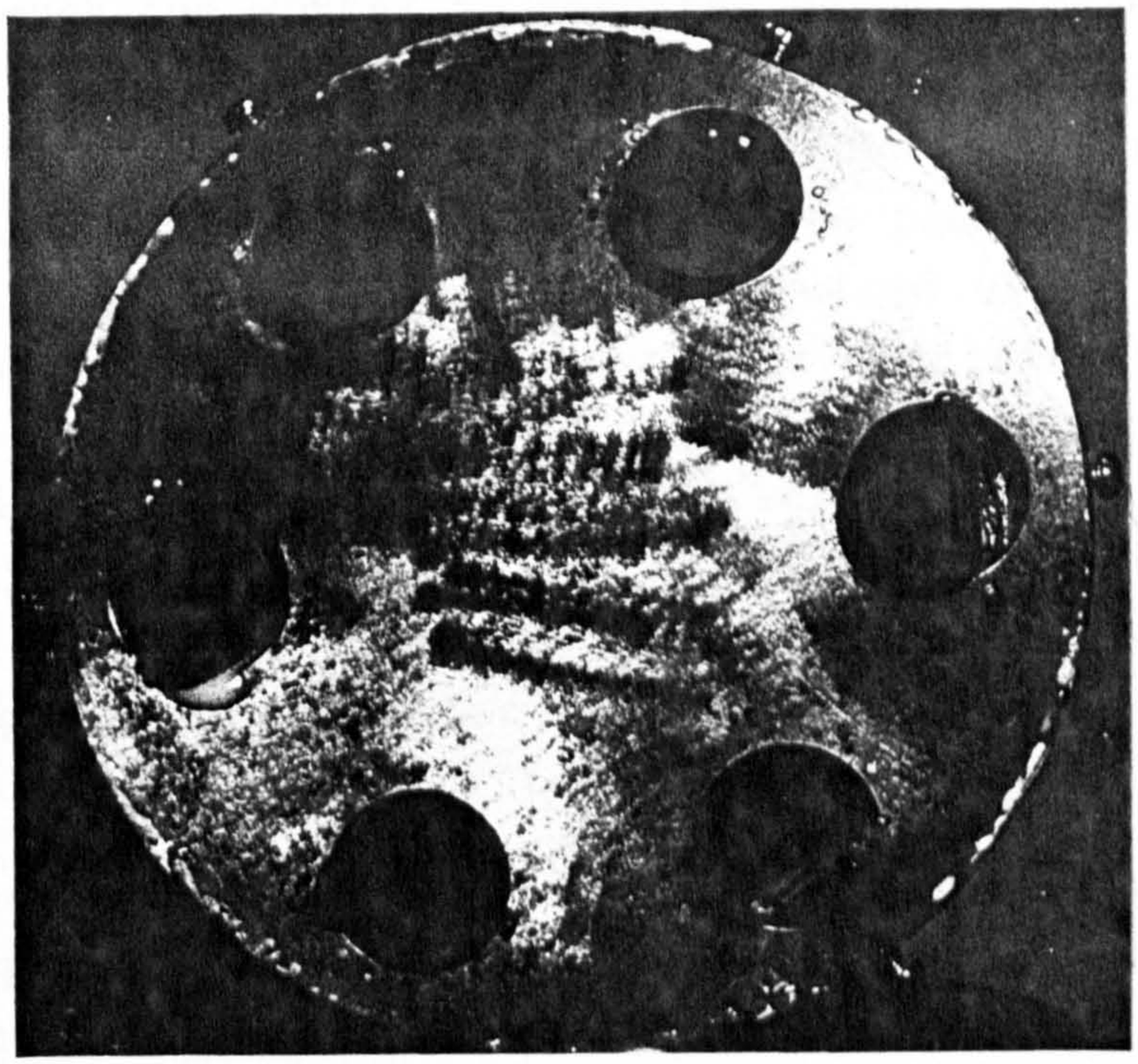

FIG. 7.7 Polishing edges of IOSAs.

The assembly is heated on a hotplate to melt the shellac uniformly. After cooling, excess shellac is cleaned off with methanol. Up to six assemblies of substrates with their glass rods are then mounted into a specially-constructed jig, each assembly being held in a bored hole by a rubber-faced pressure pad and set screw.

The ends of the glass rods and the attached IOSA substrates are lapped on a cast-iron plate with a slurry of 9µm - 15µm alumina particles in water, at very low pressure, inspecting under a microscope (at 100x magnification or more) every five minutes, until chips are no longer visible. This could take 15 to 120 minutes and remove 150µm of material, depending on the amount of initial chipping. The jig and the bonded substrate(s) are ultrasonically cleaned with e.g. acetone.

Although one worker [30] reported using a series of pitch laps with 1µm, 0.5µm and 0.25µm diamond pastes, it is much easier to produce satisfactory edges for end-fire coupling by polishing on a lipped polyurethane plate, submerged in Syton silica sol. Inspection is required every hour or so until no chips are seen (under 100x magnification) around the area which will be used for coupling light in or out. Any chips are considerably smaller than 1µm. The total polishing time could be about eight hours. Once satisfactorily polished, the assemblies are removed from the jig and the shellac bond is dissolved away using methanol, without damage to the polished edge.

Although end-fire coupling is the eventually preferred technique, prism coupling[1] was used for many of the lens assessments, especially on the input side of the lens. The test equipment using prisms for both input and output is illustrated in Figures 7.8 to 7.11. Rutile prisms (of greater refractive index than the waveguide) are pressed by clamps against the waveguide surface so that waves leaking across the air-gap are coupled between prism and waveguide.

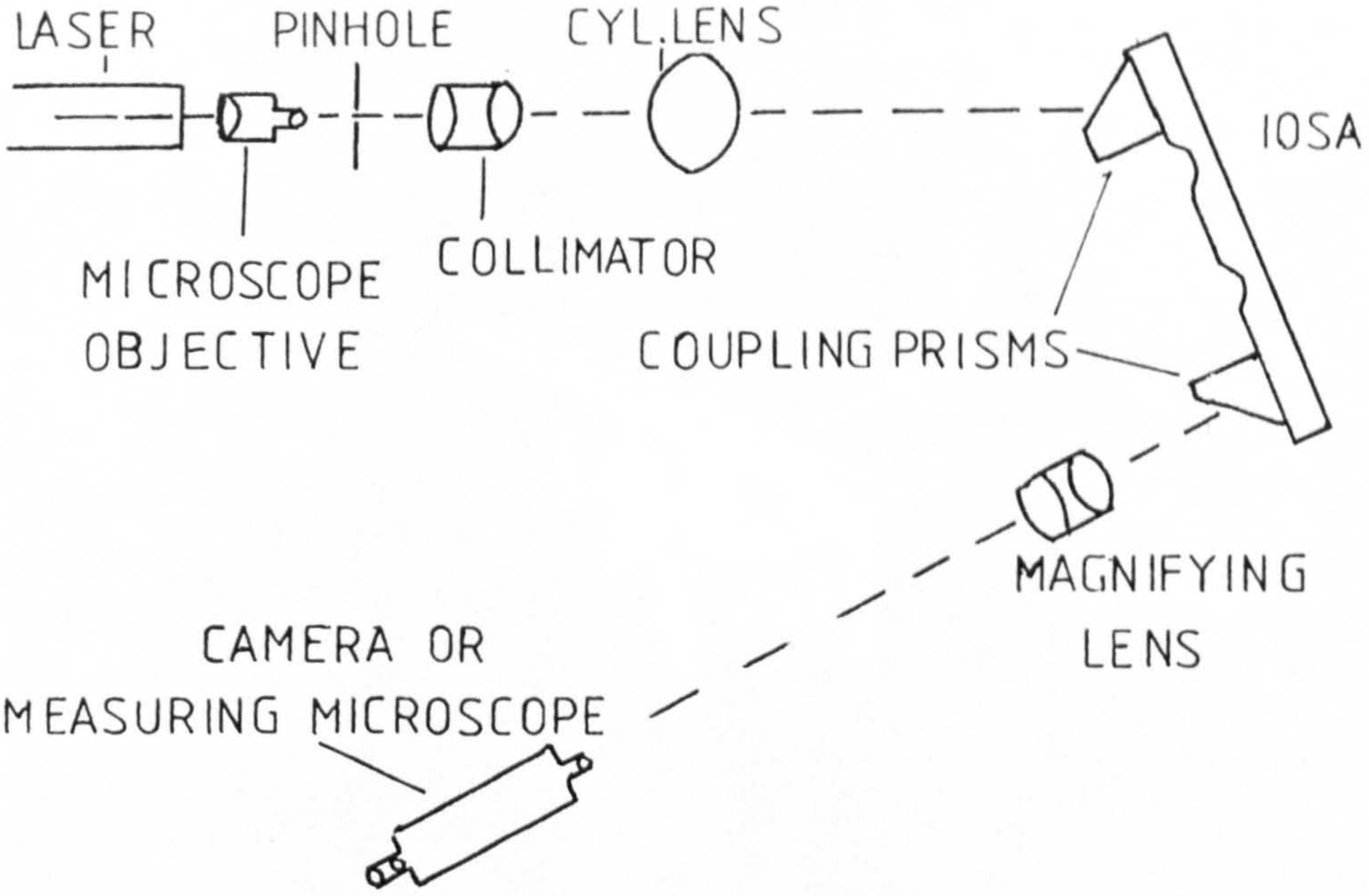

FIG 7.8 Sketch of lens-testing rig

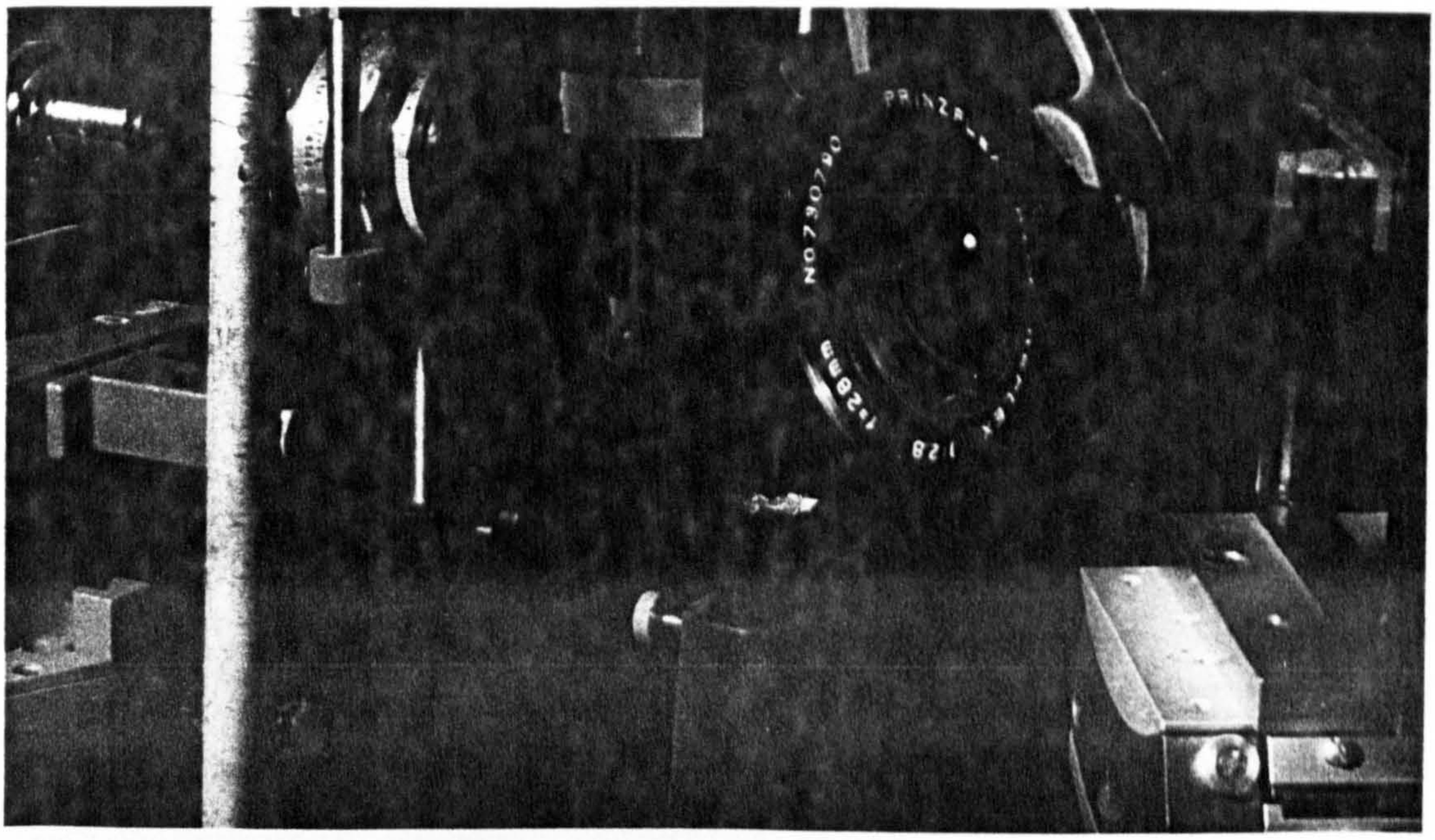

FIG. 7.9 Photograph of lens-testing rig

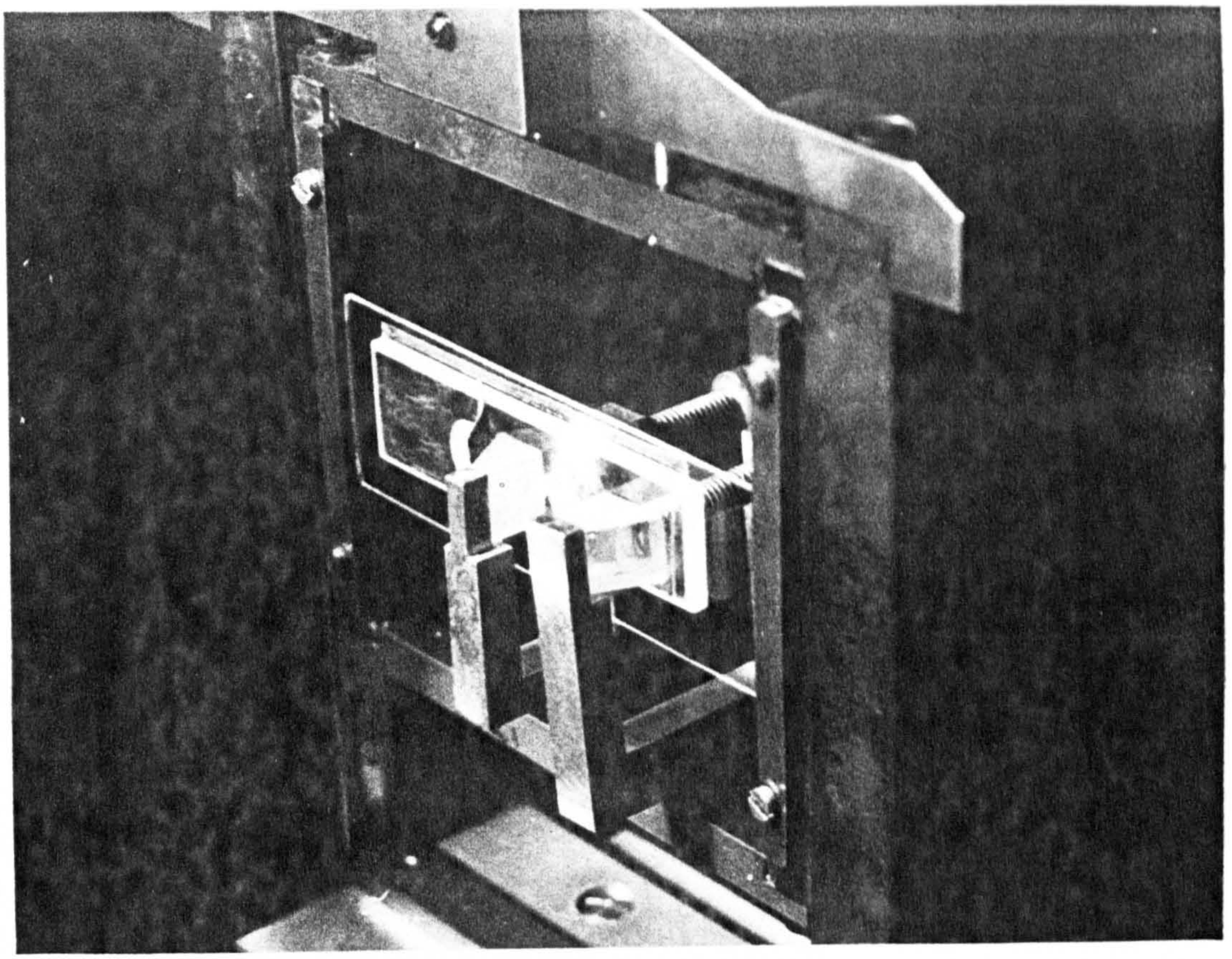

FIG. 7.10 Testing performance of one lens.

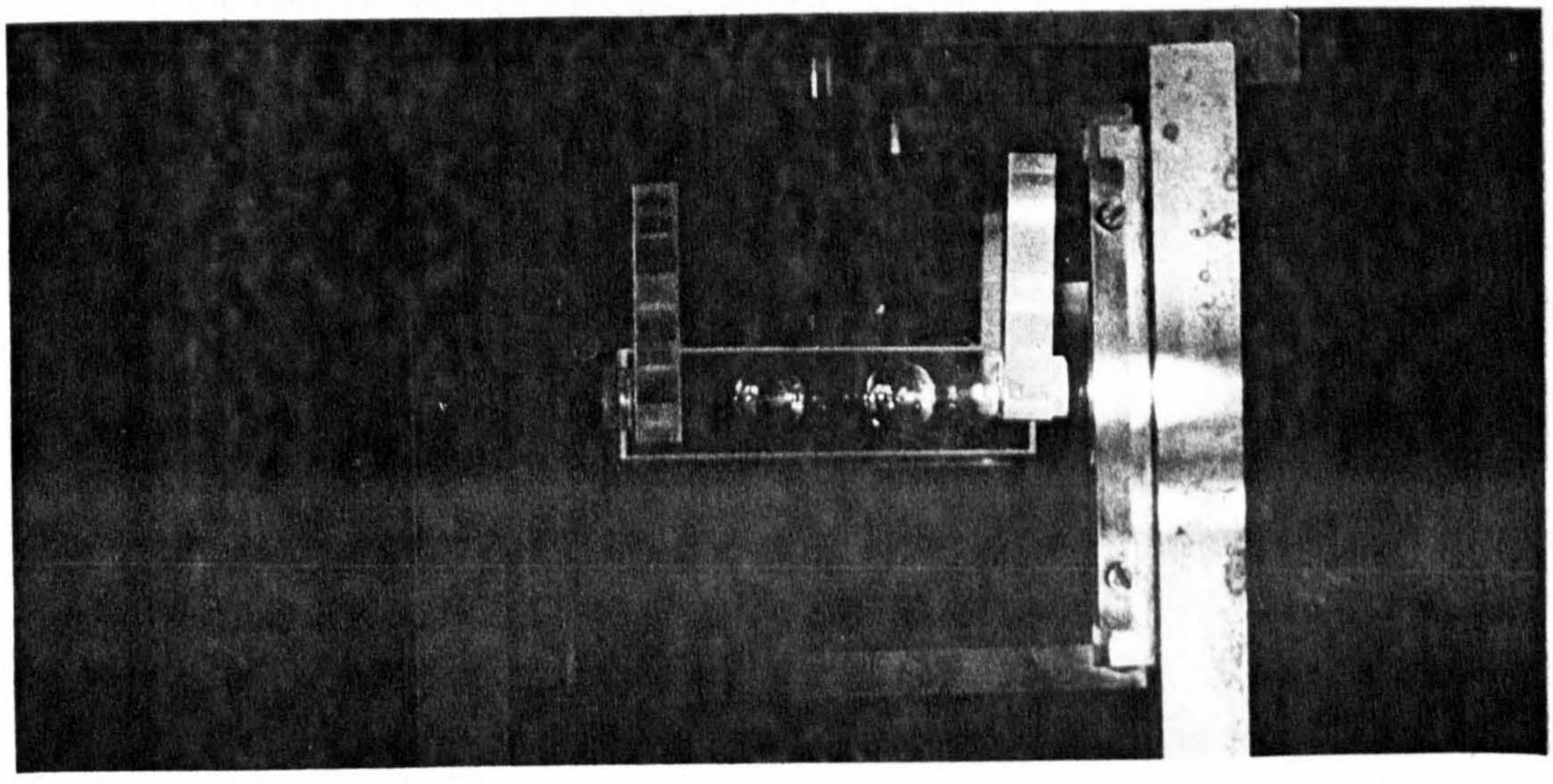

FIG. 7.11 Testing performance of lens pair.

7.3 ASSESSMENT OF SURFACE ROUGHNESS

7.3.1 Roughness of plane lithium niobate surfaces before and after waveguide formation

In-plane scattering of guided light is one of the parameters that has great significance in the operation of the IOSA [2,3,205-207], since it sets a limit to the potential dynamic range of the analyser. This scattering is affected by imperfections introduced by the Titanium deposition [208,209] and diffusion processes [210], by inhomogeneity in the initial crystal material [211], by roughness of the surface of the substrate [212], and by subsurface damage remaining after the generating and polishing processes. The last two imperfections are of concern in the work discussed in earlier chapters of this thesis.

The surface finish of lithium niobate substrates, before and after waveguide formation, has been assessed by stylus gauges, and by correlation with total integrated scatter measurements of light incident normal to the substrate [172,212]. A surface roughness of 0.5-1nm Ra may be achieved on plane lithium niobate substrates by polishing with alkaline silica sols on a polyurethane foam pad until no defects are visible under 400x magnification (Chapter 3, section 3.6.1). This surface finish has been found quite adequate to permit the subsequent formation of good quality waveguides [43]. In contrast, a waveguide which was formed on a plane diamond-turned surface of roughness 130nm Ra was apparently too rough to allow prism coupling.

Although the roughness of Titanium deposited films differs little from that of the underlying substrate, an increase in roughness is induced by the subsequent diffusion process. For example, after 6 hours diffusion at 980^{o}C, a 40nm thick Titanium film is converted to a waveguide layer with a surface roughness of 5nm rms. However for 36 hours diffusion, a film of the same thickness is diffused much further into the substrate,

leaving only about 1nm rms roughness on the surface. Thinner starting films result in smoother surfaces for any given diffusion time: a 23nm thick titanium film, when diffused at 980^{o}C for 6 hours has surface roughness of about 1.5nm rms, and when diffused for 25 hours has roughness similar to that of a starting substrate, about 0.6nm rms.

There is evidence that although long diffusion times lead to a reduction of surface roughness, other defects within the waveguide may occur [43]. The titanium films tend to include many defects and dust particles [43] which form discrete scattering centres, about 20nm in diameter, in varying densities over the waveguide surfaces. It is believed that the scattering effect of these centres predominate but that they can be diminished by improving the cleanliness of the fabrication processes.

The application of waveguides formed by long diffusion times are not suitable for the IOSA because the waveguides do not propagate close enough to the surface of the geodesic lenses. It is preferred to propagate only a single mode close to the surface, permitting an efficient acousto-optic interaction. However it has been found that polishing a very small amount from the waveguide after diffusion can reduce the surface roughness to a magnitude close to that of the crystal surface before coating the titanium layer [42,43]. It may therefore be possible to form low-scattering single-mode-propagating waveguide layers by whatever combination of initial titanium thickness and diffusion time produces the least amount of potential scattering at a deep level, and then polish away the top rough layer both on the plane region of the substrate and (using the MCPM) within the lens depressions.

Figure 7.12 shows the angular dependence of in-plane scattered light for a plane waveguide for which particular care was taken over substrate cleanliness prior to titanium film evaporation and waveguide diffusion. Angles

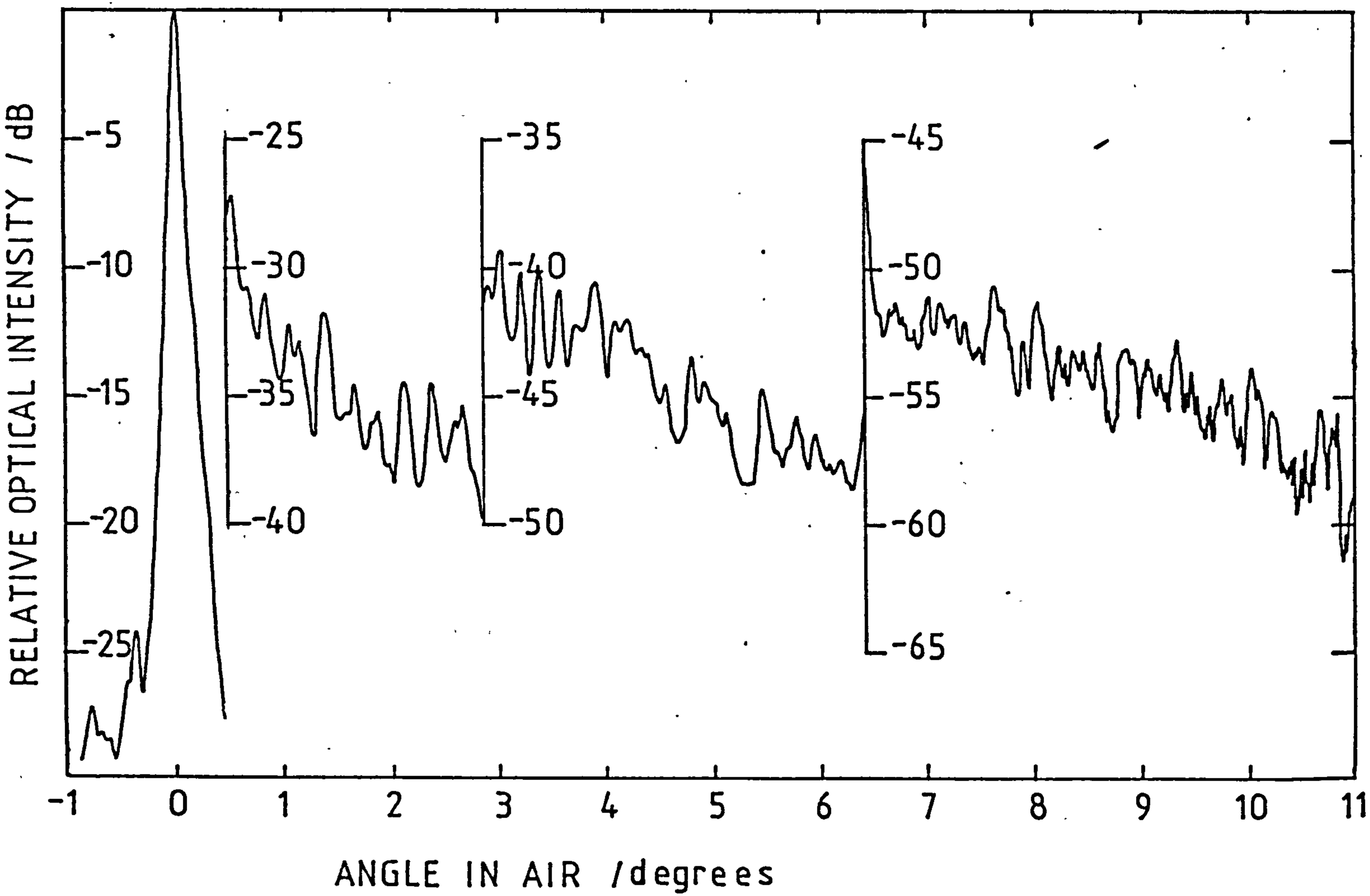

FIG. 7.12 Angular dependence of in-plane scattered light : Ti-Li NbO_3 guide

in air, used as the independent axis in this graph, are related to angle, β , within the waveguide layer by $\sin^{-1}(n.\sin\beta)$ where n is the effective refractive index of the waveguide mode. Using Equations 1.2 and 1.3, the deflection angle in air from the zero-order beam is about 15^{o} for a 1GHz signal using 820nm laser wavelength. Figure 7.12 indicates that the light scattered from the zero-order into the detector-element array where the microwave-derived signals are analysed would be about 60 dB below the intensity of the zero-order beam. But light scattered from a deflected signal into nearby detector elements is of more operational importance in the IOSA. Such small beam deflections correspond more to angles of less than 1 degree in air, for which the relative scattered light intensity may not be much better than 30 dB.

7.3.2 Measurements of roughness of lens surfaces

The roughness of lens-depression surfaces was assessed by means of a Talystep stylus-tracking instrument. Using the maximum magnification, a base-table free from vibrations and the finest stylus available (a pyramid truncated to 0.1µm x 2.5µm), the instrument is claimed to be capable of resolving 0.5nm peak-to-valley deviations from a smooth surface for spatial frequencies low enough not to bridge-over the stylus tip. For surfaces which are not flat (such as the geodesic lens depressions) it is difficult in practise to resolve deviations smaller than about 1nm.

In the diamond-turned depressions, if allowance is made for the 0.2µm machine-slide steps, the peak-to-valley roughness was generally 32 ±10nm, the variation within this range ocurring between different crystal directions (as discussed in Chapter 6).

During polishing with the microprocessor-controlled polishing-machine (MCPM) the progress towards completion of polishing was judged by the reduction of turning marks visible at 90 times magnification (section 6.4.5). At the

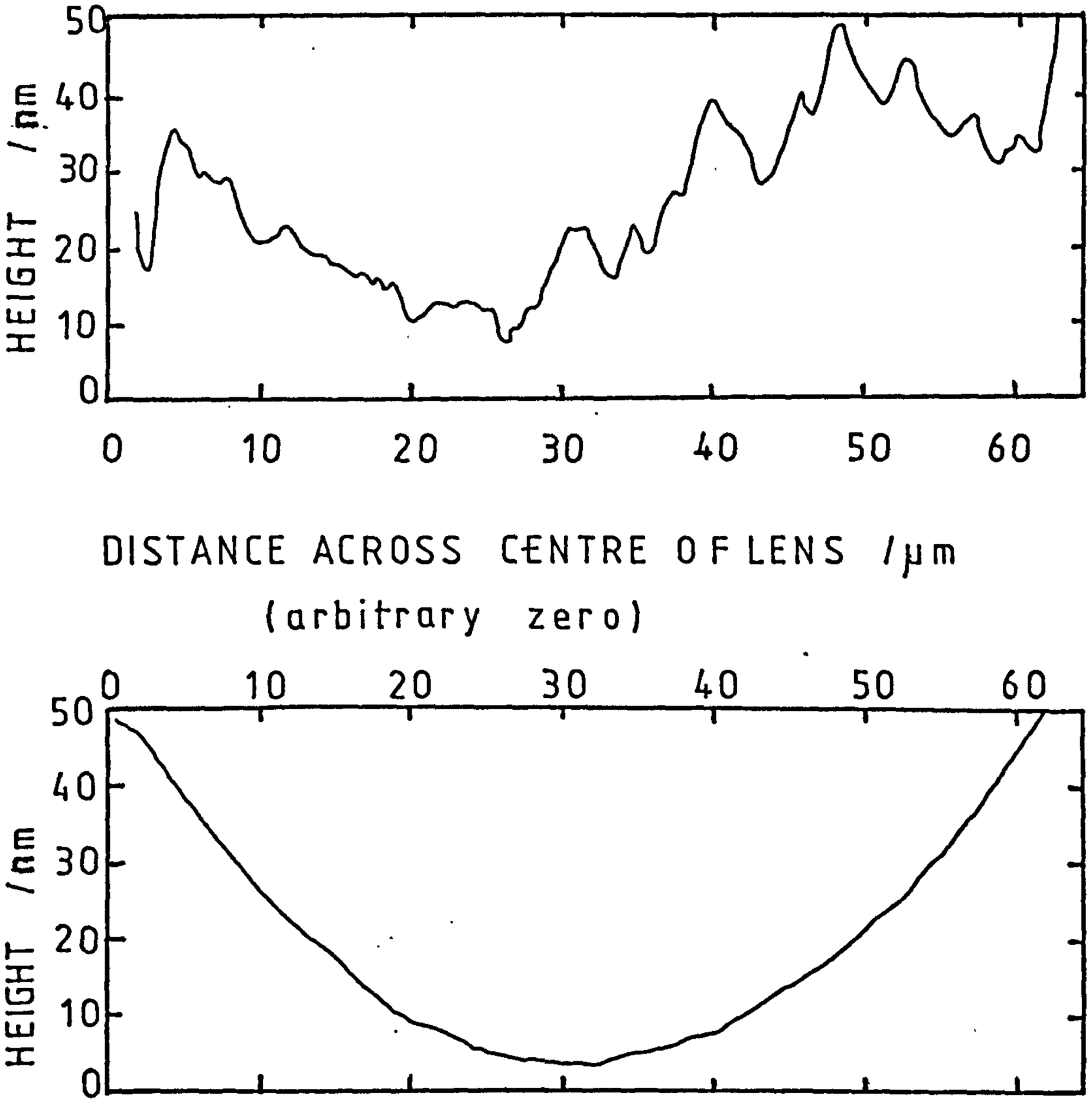

FIG.7.13 Talystep traces of central part of aspheric geodesic lens:
top - after diamond-turning
bottom - after polishing

stage where only isolated pits were observable, the Talystep instrument indicated peak-to-valley surface roughness of about 3nm. At the final stage where no pits could be seen the instrument could only just resolve surface roughness, indicating that the peak-to-valley roughness was between 1nm and 2nm, and that the roughness average, Ra, was therefore less than 1nm. Figure 7.13 illustrates the surface roughness for the central part of one particular lens before and after polishing.

The roughness of polished lens surfaces is about the same as has been measured for plane lithium niobate surfaces (section 7.3.1), and therefore is probably as smooth as may be expected to be achieved by the polishing process employed. This roughness is also less than the value, about 1.5nm rms, which has been measured for single-mode waveguides [43].

7.4 ASSESSMENT OF LENS IMAGING PERFORMANCE

7.4.1 Measurement of lens focal length

The "two-arc" lens, after diamond-turning at Moore and polishing on the microprocessor-controlled polishing machine (MCPM) at the University of Glasgow, was supplied to the Marconi Research Centre (Great Baddow, Essex) of GEC Research Laboratories, where a waveguide was formed and (after returning to Glasgow for edge-polishing) lens performance was evaluated. The focal length of the edge-rounded spherical geodesic lens was measured by N.Finlayson under the direction of Mr. S.C.Gratze at the Marconi Research Laboratories. The beam from a 5mW helium-neon 633nm laser was attenuated to diminish potential photorefractive damage, and expanded by twelve times. The beam was then restricted in size by a variable rectangular aperture and prism-coupled into the waveguide. After being passing across the single lens the converging light beam was end-fire coupled out of the polished edge of the substrate to reach a focus in air.

Because the substrate was short compared with the size of the lens and its focal length, the focus was expected (from design calculations) to be some distance into the air from the edge, therefore the focal distance was longer than it would be if entirely within the single medium of the waveguide. The distance from lens centre to focus was measured very approximately (with a rule) for an input slit aperture of 0.92mm. Then other slit widths up to 10mm were selected and the change in focal length was measured by noting the movement against the scale of a measuring-microscope which magnified and relayed the image produced by the geodesic lens. The changes in focal length could be measured within about 60μm accuracy, and the slit width within about 0.5mm. Figure 7.14 shows the measured variation of focal length with beamwidth. For comparison, the variation calculated by ray-tracing (Chapter 1) for a uniform intensity rectangular aperture is also given. The increase in focal length with aperture for the practical lens is very much less than expected.

7.4.2 Measurement of image profile and width

Measurements on the width of the image focused through the "two-arc" lens were made by N.Finlayson and A.G.Hodkin at Marconi Research Centre. Using the same equipment as for measuring the focal length, a grating of known pitch (about 4μm) was positioned at the focus to enable the image width to be assessed. For initial location of the focal position the image and grating were observed through a microscope system comprising a x40 objective and a x12 eyepiece. For measurement of the spot size the eyepiece was replaced by a Hamamatsu video camera. A line scan (viewed on a monitor screen) could be selected, giving a record of intensity versus position, which could then be plotted on a chart recorder.

A typical plot of the image in the focal plane is shown in Figure 7.15, in this example for an input beamwidth of 3.65mm. For comparison, the figure also shows a

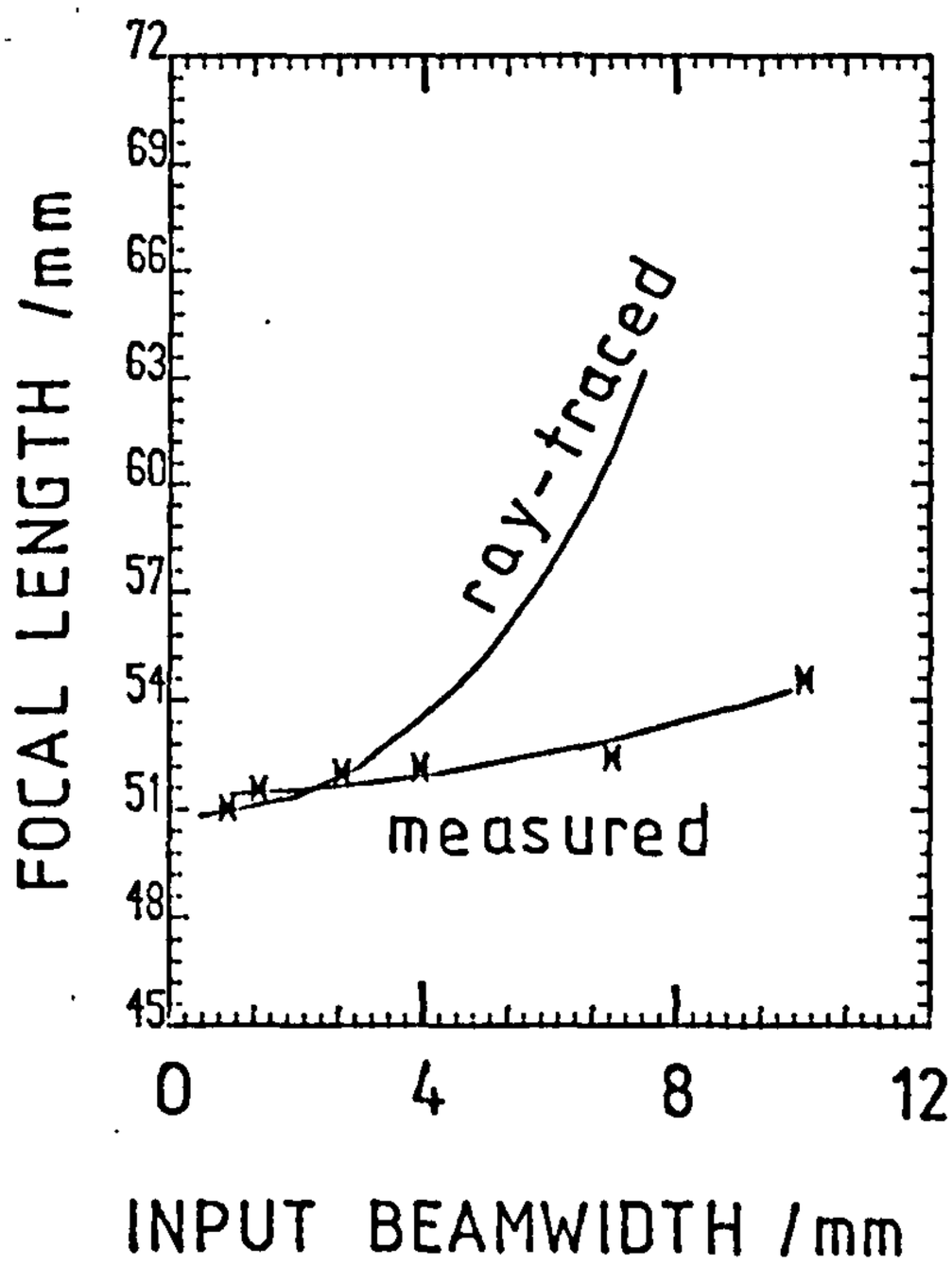

FIG 7.14 Comparison of measured and calculated variation of focal length with aperture for an edge-rounded spherical lens.

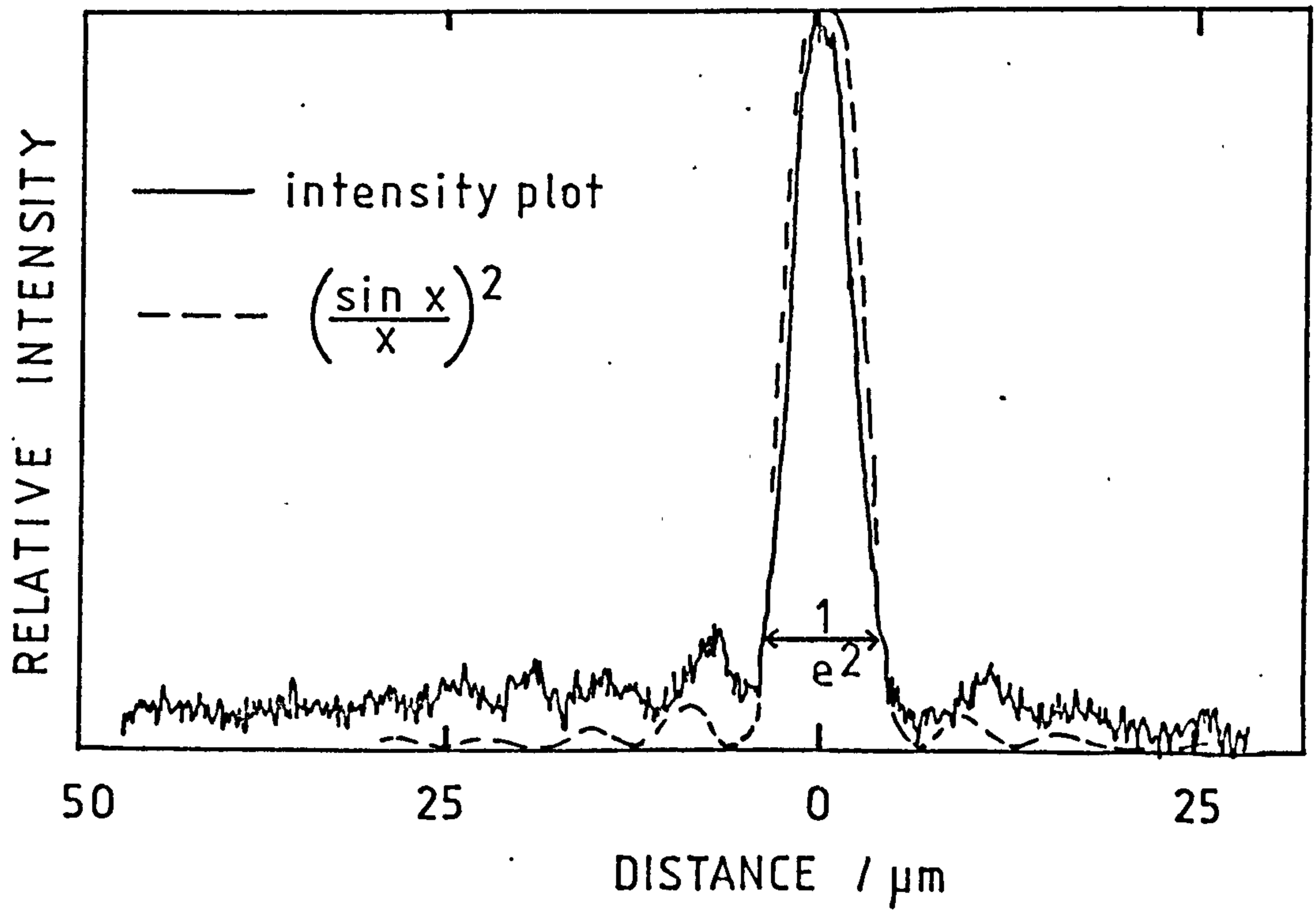

FIG 7.15 Plot of intensity (linear scale) of the image of an edge-rounded spherical lens for 3·65 mm input beamwidth.

rectangular aperture diffraction function (dashed line), $(\sin.x)^2/x^2$. Assuming that the camera measurement-system has a linear relationship between the output of this plot and input light intensity, and that the zero level of intensity occurs at the lowest recording on the chart, the 1/e and $1/e^2$ spot diameters were 5.4μm and 7.9μm respectively. Figure 7.16 shows plots (measured by N.Finlayson) of these two spot diameters versus the beamwidth of the laser light before entering the coupling prism. The spot size would be expected to be large for small beamwidth, to decrease to a minimum size at some larger beamwidth and then to enlarge again as spherical aberration degrades the lens performance. In anticipation of this expected trend, parabolic curves have been drawn through the experimental points. The dashed lines represent the expected theoretical diffraction spotwidths (using the simple expression for a truncated Gaussian beam) and the spotwidth due to aberrations alone. The measured results do not match the theoretical spotwidths very well, the lens performing better than expected at large apertures. Even at the widest beamwidth which was evaluated (7mm) the spot-widths were very narrow.

In an attempt to determine the reason for better than expected performance at wider apertures, measurements were made of the intensity of very narrow beams (simulating rays) which were transmitted through different heights on the lens from the central axis. Prism-coupling was employed for both the input and the output beam. The following table gives the relative intensities.

TABLE 17: MEASURED ATTENUATION OF NARROW LIGHT-BEAMS THROUGH LENS

RAY HEIGHT /mm	RAY INTENSITY /dB
2	-6.9
1	- 4.2
0	0.0
-1	- 0.6
-2	- 2.3
-3	-6.6
-4	-11.4

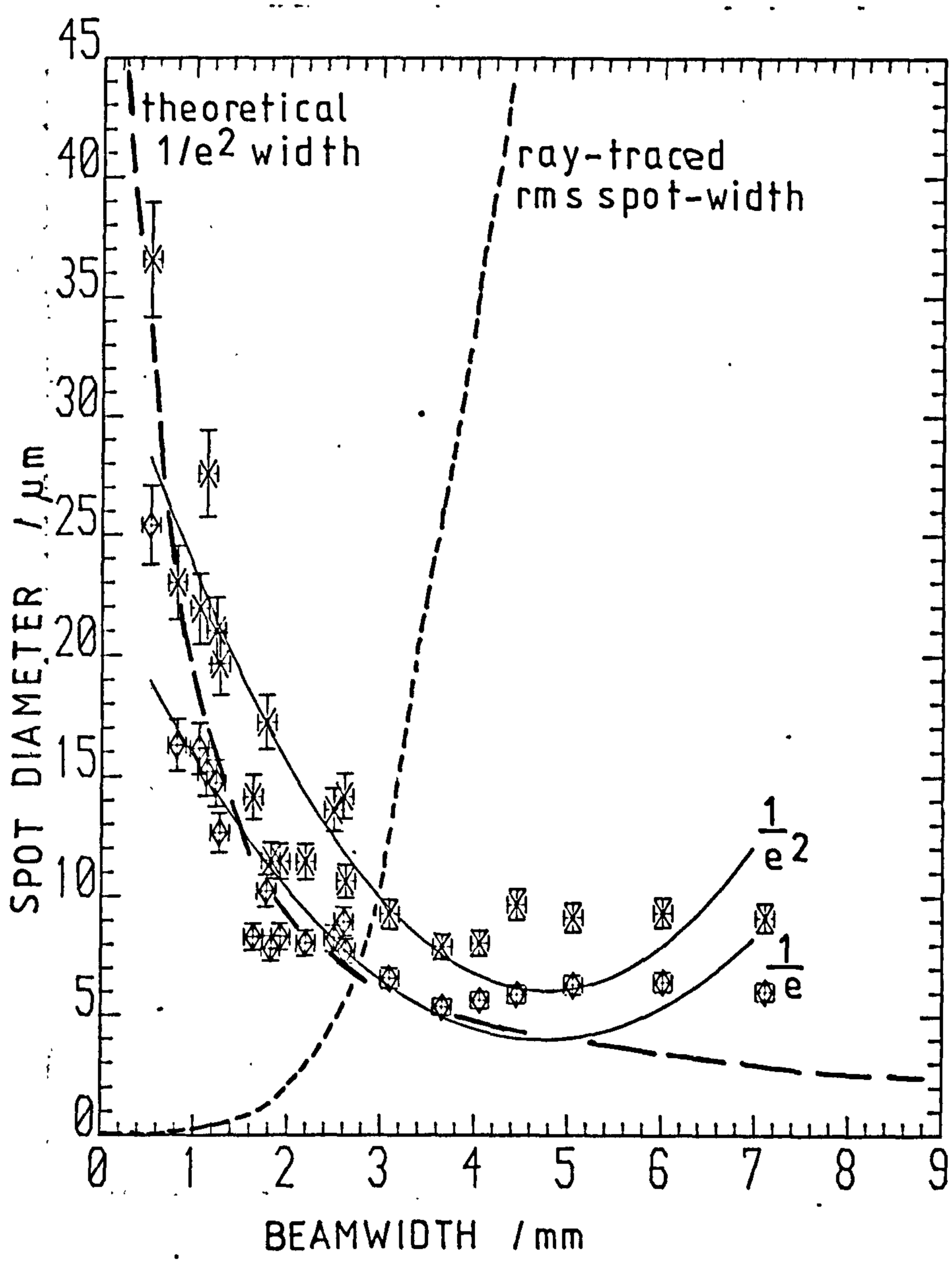

FIG 7.16 Variation of spot diameter with input beamwidth for an edge-rounded spherical lens.

The error in readings of transmission was estimated as about 1dB. There is, therefore, clearly a much lower intensity transmitted through the system towards the edge of the beam than would be expected from uniform prism coupling. The attenuation of rays towards the edge of the beam probably occured mainly at the prism-coupling stages, although some losses would be expected to occur within the waveguide on the plane and lens surfaces. The effect of this form of attenuation is that the contributions to image degradation and increased focal length due to the outer parts of the lens are very much diminished, and the lens appears to perform better in all respects (other than in total transmission), giving the observed result.

Several aspheric lenses and IOSA lens pairs were coated with titanium and waveguides were formed by the methods described in section 7.2.1. The imaging performance was assessed using the equipment layout shown in the sketch of Figure 7.8 and photographs of Figures 7.9, 7.10 and 7.11. Prism-coupling was used for both input and output.

The focusing performance of one particular geodesic lens was assessed under four different conditions - A,B,C, and D. Figure 7.17 shows a photograph of a typical image.

Condition A. The beam from the laser was not expanded or truncated, being coupled into and out from the substrate by prisms as in Figure 7.10. The image near to the output prism was magnified by an f/2.8 camera lens of 50mm focal length at a distance of 2.58m, and then measured with an eyepiece graticule in a microscope with a 5x objective, so that the combined magnification was 258. The image did not have a Gaussian profile, and intensity minima were observed, the closest to the main peak being of width 23μm ± 2μm. Using the same measuring microscope, it was possible to estimate the width of the laser beam in air as 1.6mm: this visually-measured width was probably at intensities below the $1/e^2$ level of the Gaussian profile.

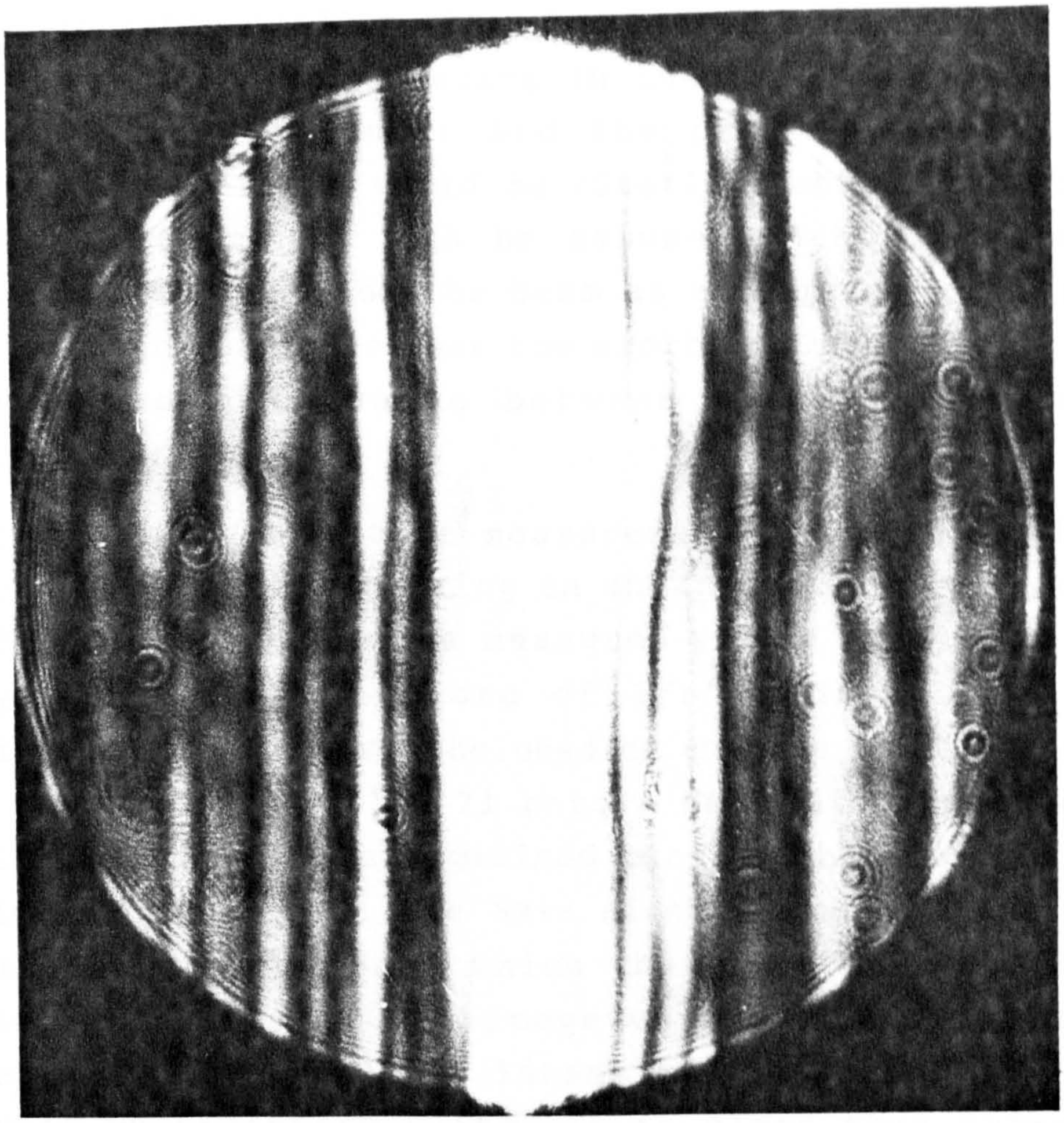

FIG 7.17 Projected image from IOSA lens

However the width of the laser beam was found to be considerably smaller after being coupled into and out from the waveguide (propagating in the plane waveguide region alongside the lens), and the profile was no longer Gaussian - minima could be clearly identified at a width of only 0.4mm. It can be assumed that light was lost towards the edge of the beam at each prism-coupling, as described above, so that the width of the beam through the lens was of a value between these extremes, i.e. 1.0±0.6mm.

Condition B. A further measurement was made on the same lens by N.Finlayson using an unexpanded input laser beam of 1/e-width 1.5mm (as measured with a Hamamatsu camera system), and therefore of $1/e^2$-width 2.1mm. A x40 microscope objective was used to enlarge the IOSA image by a factor of 292/4.1 = 71 onto a Hamamatsu video camera. Figure 7.18 shows a digitised plot of the whole field of view of the camera. The axis along the narrow part of the image is 9.6mm long, which therefore corresponds to a field of 135μm at the image on the IOSA. The contours represent intervals of intensity, separated on a linear scale by arbitrary units. It is clear that there is an intense central peak surrounded by several minor peaks.

Figure 7.19 shows an intensity scan through the narrowest part of the image in Figure 7.18. The figure has been plotted as intensity level in dB relative to the lowest intensity recorded in the field of view. From this graph the $1/e^2$-width was measured to be 8.0μm and the width between the first minima estimated to be about 11μm. The background intensity level was quite high, the highest sidelobe being only about 7dB below the peak.

Condition C. The laser beam was expanded in width, using a 10x microscope objective (focal length 16mm) of numerical aperture 0.3, focused onto a 20μm diameter pinhole, and collimated by an f/2.8, 50mm focal length, Tessar camera lens onto an input coupling prism. Although the beam, which was considerably attenuated, was about 4mm wide in

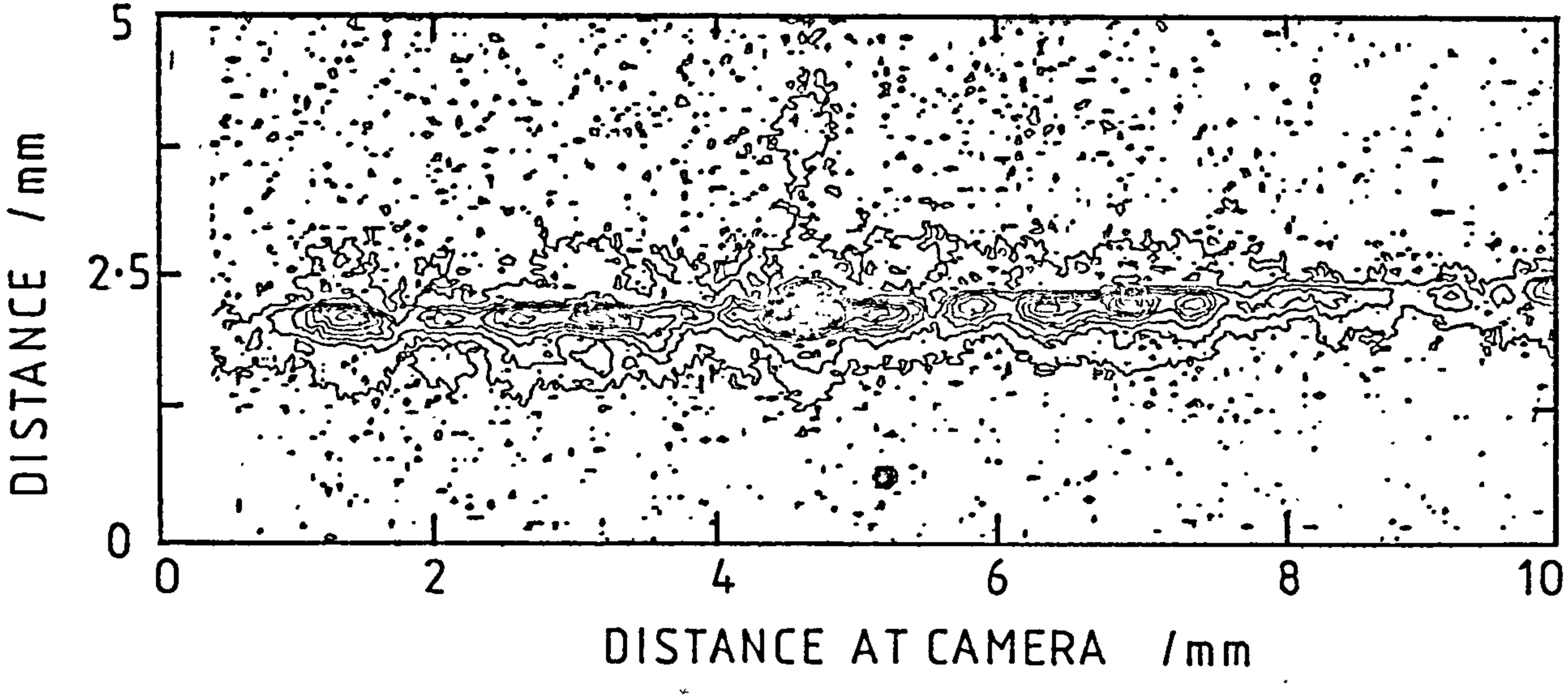

FIG 7.18 Plot of intensity contours of a geodesic-lens image as relayed to a video camera.

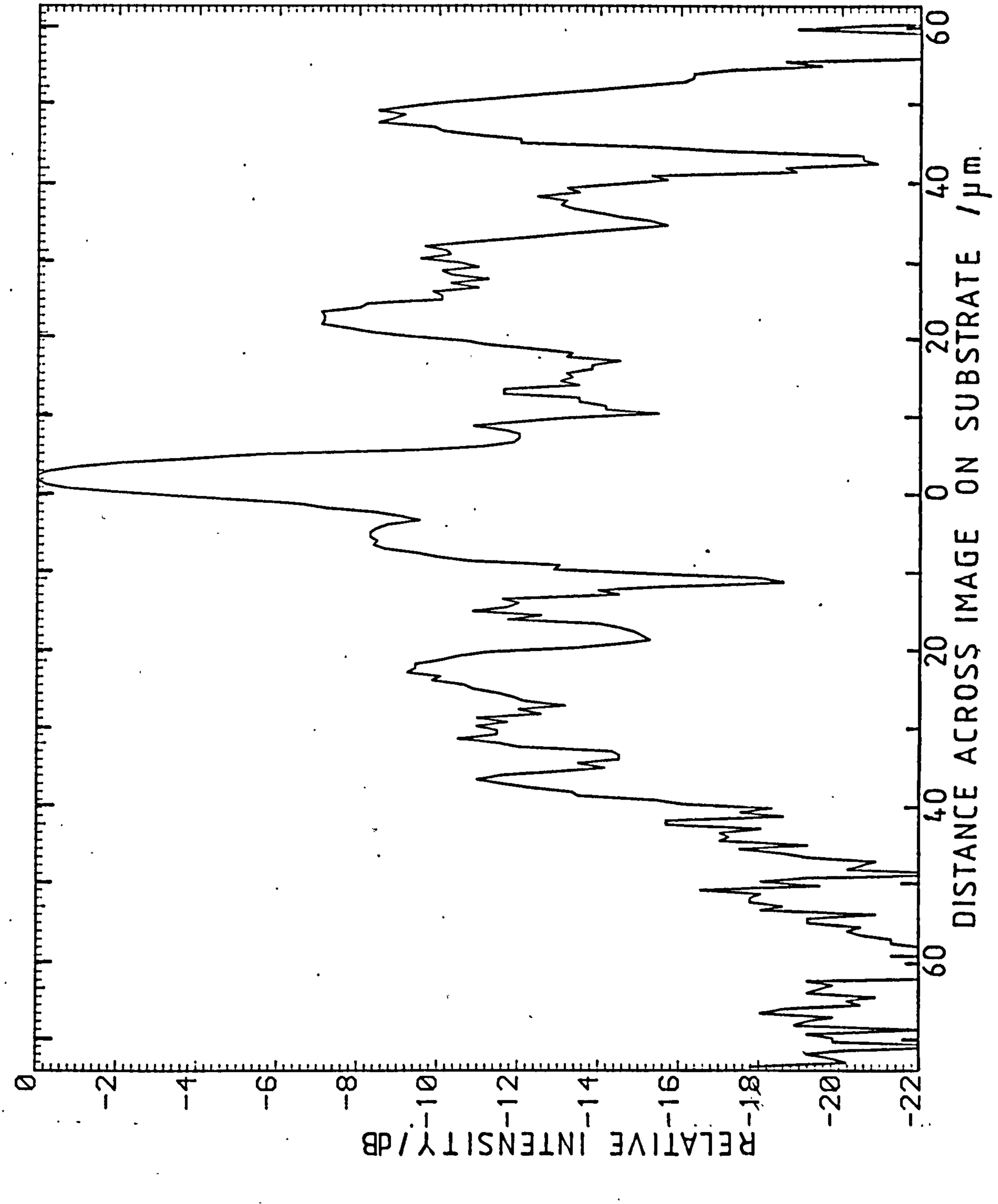

FIG 7.19 Graph of intensity versus distance across a geodesic-lens image.

PAGE NUMBERING AS ORIGINAL

air, measurement of the propagating light beam by out-of-plane scattering near to the prism where it entered the lens depression showed that the beam had been truncated to 2.5mm ±0.5mm wide. The image was magnified by an f/2.8 camera lens of 28mm focal length at a distance of 1.33m and viewed by the same measuring microscope as was used in condition A. The total magnification was 238 times. The image width between nulls was measured to be 8.8μm ±1μm.

Condition D. Because the input beamwidth after prism-coupling seemed to be significantly smaller than the expanded laser beamwidth in air, the input beamwidth was deliberately truncated to about 3mm by an aperture near to the input prism in order to provide more certainty of the beamwidth. The beam as seen via out-of-plane scattering near to the lens aperture was of width 2.75mm ±0.5mm. The image width was measured by the microscope in the same way as in condition C, to be 5.0μm ±0.5μm. This condition was also used to obtain the photograph of Figure 7.17. The central line intensity is very much greater than the surrounding diffracted lines, although the photograph has been printed so as to emphasise the latter.

7.5 COMPARISON OF MEASURED IMAGING-PERFORMANCE WITH THAT CALCULATED FROM PROFILE MEASUREMENTS

The spotwidths measured for conditions A to D are plotted versus input beamwidth in Figure 7.20. For comparison, dashed lines show the width between nulls, D, expected by the simple expression for a truncated Gaussian beam

$$D = \frac{g.\lambda.F}{W}$$

where F is the focal length of the geodesic lens and W is the truncating aperture width. The figure shows curves for three values of the constant g: 2 (the value for a rectangular aperture), 2.5 (the value expected to be

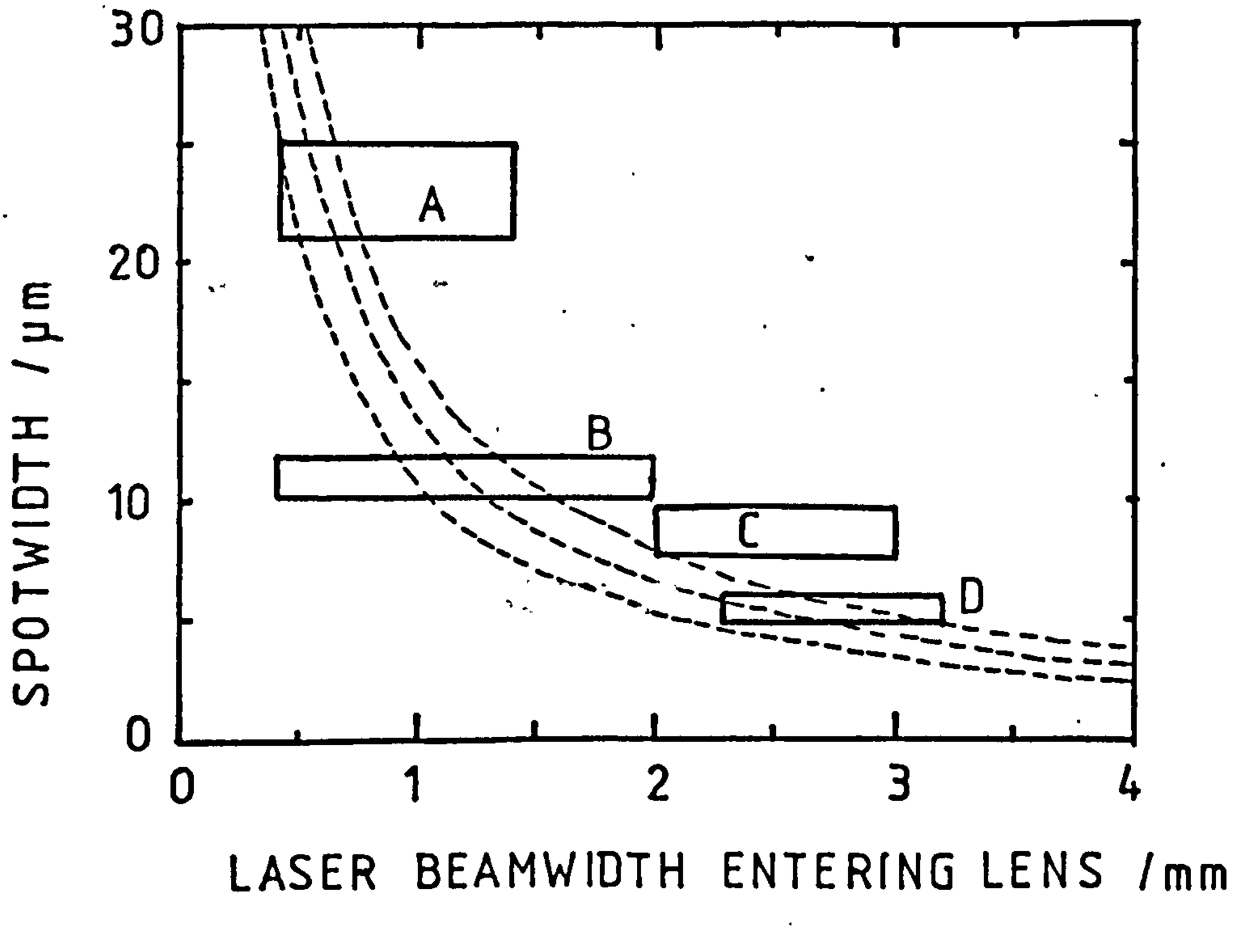

FIG 7.20 MEASUREMENTS OF SPOTWIDTH BETWEEN CLOSEST MINIMA.

DASHED LINES REPRESENT THEORETICAL SPOTWIDTH FOR A GAUSSIAN BEAM FOR TRUNCATION CONSTANT g = 3 (UPPER), 2·5 (MIDDLE) , 2 (LOWER).

A – UNEXPANDED, INTENSE BEAM

B – UNEXPANDED, ATTENUATED BEAM

C – EXPANDED BEAM

D – EXPANDED, TRUNCATED BEAM

appropriate to the dimensions used for the present IOSA design) and 3.0 (a value expected to represent a Gaussian beam with little truncation).

Within the limits of accuracy indicated on the figure, the measurements are consistent with the theoretical curves, and the spot-widths are between the diffraction-limited values and twice the diffraction-limit. According to the results of the ray-tracing calculations which have been shown in Figure 2.14, image broadening by 1.4μm would be expected to be added to the diffracted spot-width by the errors in lens profile introduced by bridging over the regions of very high curvature. If this value is subtracted from each of the measurements shown in Figure 7.20 the practical results fit the theoretical values a little better, but this correction is very small compared with the ovarall uncertainties of measurement. It is not possible to interpret the measurements further because of uncertainty about the intensity distribution of the light beam as it passed through the lens.

Although it is possible to measure the output beam intensity (and therefore spot widths) with considerable accuracy, the intensity profile - or merely the truncated width - of the beam which enters the lens is difficult to assess. Prism-coupling, in particular, is unlikely to transmit uniformly across the entire input beam when more than about 1mm, since the uniformity and cleanliness of the air-gap cannot be well-controlled. It seems most likely that a prism couples less well towards the edges of a wide input beam: the beam entering the lens is therefore likely to be of lower intensity away from the centre than the truncated Gaussian beam which has been assumed in the above comparisons between theory and measurement. Measurements of the beam leaving the beam-expanding lens system indicate that it is not easy to adjust the beam to a clean Gaussian shape. Spikes and overall shape errors are commonly observed.

The problem of relating image intensity profile to the input beam intensity profile can be discussed more fully for the case of condition C. If the propagation of the beam through the system had been Gaussian, the $1/e^2$-width of the input beam of 2.1mm would have produced a diffraction-limited image with $1/e^2$-width of 3.2μm, with no minima in the intensity profile. However the $1/e^2$-width of the image was 8μm and there were clearly defined minima of intensity at a width of 11μm. This measurement of spot-width between nulls would have been expected if the input beam had been Gaussian, but truncated at its $1/e^2$ level at a width of 1.2mm. This value of input beamwidth is between the $1/e^2$-width measured for the beam in air and the value measured for the width of a beam coupled in and out of a plane waveguide (condition A). If the width of the light beam at the lens were also of this value, then this particular lens operated very close to the diffraction limit.

The better than expected image width and focal length performance of the "two-arc" profile lens, as the input beamwidth was increased, could probably be explained by assuming some plausible apodising function such as could be taken from the intensity measurements of table 17. It has been estimated [214] that lenses with waveguides which propagate more than one mode are likely to be effectivly apodised in this manner, the predominant cause of decreased intensity with rays further from the centre of the beam being leaky-mode loss. It can be assumed that the contribution to image degradation from spherical aberration from the outer parts of the lens aperture is far less than if the input beam were of the truncated Gaussian profile which has been assumed.

It is possible that high power density in the focused image caused photorefractive damage [8] during the long period required for careful measurements, particularly for condition A - an unexpanded, intense beam. The consequently worse waveguide scattering and losses

probably degraded the lens performance.

The backgound intensity around the focused spot, as shown in Figure 7.19, is rather high , the highest side-lobe being only 7 dB below the peak intensity. A value of about 13 dB would be expected for a rectangular aperture input beam using the $((\sin x)/x)^2$ function. This value compares with 13 dB [98], 8dB to 12 dB [105] and about 16 dB [5] (if a graph presented in that reference has a linear scale) reported for other aspherical geodesic lenses in titanium-diffused lithium niobate.

7.6 CONCLUSIONS

No commercial measuring instruments are available which can measure the present geodesic lenses to the required precision without modification. Profile Measurement was not found to be straightforward, using either mechanical probe instruments or interferometry, but the measurements which were made implied that the profiles of lenses made by diamond-turning were close to or within the design tolerance of about $\pm 0.5\mu m$ both before and after polishing with the microprocessor-controlled polishing machine.

Interferometry reduces data rapidly by displaying errors in a whole surface profile simultaneously, rather than by scanning over the surface. It would be possible, but expensive, to construct or adapt an interferometer to operate at f/0.3 or better to compare geodesic lens profiles with a master curve (perhaps diamond-turned in aluminium). Holographic correction could be inserted into the comparison wavefront if the master is not sufficiently accurate. An instrument which performs digital image-processing could be used to determine the errors in the lens profile, and the results of the error measurements may be stored, and used in a polisher-correction programme.

Interferometric assessment of the central part of the "two-arc" lens showed that the profile errors (in this case departure from sphericity) were less than ±0.3μm after diamond-turning and less than ±0.8μm after MCPM-polishing.

No accurate mechanical measurements could be made of a complete aspheric geodesic lens profile, apart from on the Moore CNC machines which produced the lenses, and which indicated that errors were probably smaller than 1μm. Measurements of the central part of lenses with roughness measuring instruments showed that these small regions were within 1μm both before and after polishing. The Sira instrument was potentially capable of measuring lens profiles satisfactorily, but modifications to the control and readout systems would be necessary to achieve this and these could not be arranged with Sira without considerable expense. Most of the lens profile measured was within 4μm of the designed profile, but the inaccuracy of the instrument was about ±20μm at the critical part of the lens where the edge-rounding region merges into the inner focusing region. The preliminary work on providing a small instrument dedicated to measuring geodesic lens profiles, using LVDT probes and stepper-motor driven tables, indicated that adequate sensitivity should be available and that sufficient accuracy could be obtained if the measuring probe used appropriate bearings to restrain sideways movement.

Plane single-mode titanium-diffused waveguides can be formed on lithium niobate with surface roughness of about 1.5nm rms. Polishing the waveguide surface could improve this roughness, perhaps to 0.6nm rms - the roughness measured on well-polished substrates before waveguide formation. The roughness in diamond-turned lens depressions is about 15nm Ra. After polishing, the roughness is close to that of plane-polished substrates. The MCPM-polished lens depressions are not, therefore,

expected to contribute significantly more to scattering in surface waveguides due to their roughness than do plane surfaces.

The "two-arc" geodesic lens performed well in terms of image size at large apertures. The spot size and the change in focal length were smaller than would be expected for truncated Gaussian beams. This could be explained qualitatively by the apodisation caused by large losses of light for rays passing close the edges of the lens.

The aspherical geodesic lenses appeared to give spot sizes close to the diffraction limit, and certainly not larger than twice the expected diffraction-widths. It was difficult to assess the imaging performance more accurately because of uncertainty over the intensity profile of the light beam as it passed through the lens depressions. Background light-intensity was higher than reported in the literature for similar lenses. This high level may have been caused by waveguide imperfections, mode-conversion and leakage of light propagated in the curved regions of the waveguide, and/or scattering due to insufficient polishing at the most-curved part of the lens profile.

CHAPTER 8: ECONOMIC ASPECTS OF GEODESIC LENS FABRICATION

8.1 INTRODUCTION

Although the work reported in this thesis only followed one fabrication process to a successful conclusion, the other methods should not be regarded as impractical. The depth to which alternative methods were investigated depended as much on time and machine availability as on a value judgement on the method to be preferred. Indeed the results obtained suggested that several combinations of lens generating and polishing methods appeared to be technically feasible. These methods required such significantly different capital costs and fabrication times that the choice of the most appropriate method of lens fabrication for a potential industrial manufacturer could depend more on economic aspects than on technical superiority.

This chapter presents a calculated economic comparison of the cost of lens fabrication by several apparently feasible methods. For each method an estimate is given for the capital costs of the machines and for the times to fabricate lenses, and from these are derived the cost per lens. This cost per lens, which is the economic basis chosen for comparison of fabrication methods, depends on the number of lenses to be produced, the rate of production required and also on the attitude taken to financial investment. These factors are fully discussed.

No allowances have been made in the cost estimates for any financial incentives which may be available, or for interest or tax payments. The level of incentives and the accounting practices relating to interest and tax allocation vary considerably with time, place and the kind of organisation which is considering making geodesic lenses. When such allowances are made, an organisation's perception of the relative costs of labour and capital investment could either reinforce or even reverse the conclusions drawn in this chapter.

8.2 COST OF MACHINES AND LABOUR

8.2.1 Introduction

The fabrication methods which are considered in this chapter are referred to as follows. The machine called "Aspheriser" is assumed to be the Moore M18 Aspheric Generator or equivalent (e.g. the Moore prototype machine discussed in Chapter 5, or the Pneumo Precision MSG 325). The "Jig Grinder" is a machine such as the Moore G18 CNC discussed in Chapter 5. The "Ultrasonic Grinder" is a more powerful machine than the Mullard drill discussed in Chapter 4, with a rotating-tool facility, central abrasive feed and cross-slides, such as the Dawe Sonimill. The "MCPM" is assumed to be a fully-developed version of the microprocessor-controlled polishing machine discussed in Chapter 6, using one central microcomputer to control up to six MCPM, each with their own integral microprocessors and memory. Various combinations of machines may be used to generate and to polish geodesic lenses. The combinations of machines which are considered in this review are indicated in the following table:

TABLE 18: FIVE COMBINATIONS OF LENS FABRICATION TECHNIQUES

CODE	GENERATING METHOD	POLISHING METHOD
AA	ASPHERISER	ASPHERISER
AM	ASPHERISER	MCPM
JJ	JIG GRINDER	JIG GRINDER
JM	JIG GRINDER	MCPM
UM	ULTRASONIC GRINDER	MCPM

8.2.2 Capital equipment.

Typical capital costs (at 1983 levels) of the machines discussed above are estimated in this section.

a) ASPHERISER: C_a = £360,000. This cost is based on the average price of a Moore M18 AG aspheric generator with three axes and a Pneumo Precision MSG 325 machine with two

axes, plus all necessary auxiliary equipment for lens generation. If the machine is also to be used for polishing, C_a increases slightly to £370,000 - the additional cost being based on that of a grinding head plus modifications to suit polishing parameters such as low speed and rapid tool-wear.

b) JIG GRINDER: C_j = £230,000 for generating only, and C_j = £240,000 for both generating and polishing capabilities. This cost is based on the price of a Moore G18 CNC jig grinder.

c) ULTRASONIC GRINDER: C_u = £100,000. This cost includes an ultrasonic grinder such as the Dawe Sonimill and a CNC lathe such as the Hardinge CHNC machine which would be used to turn and re-turn the large stock of ultrasonic lens-profile tools required.

d) MCPM: C_p = £20,000. This value is the most uncertain of the various capital costs, and may possibly be underestimated for a commercially-manufactured system. It is based on the estimated cost of the MCPM reported in Chapter 6, modified to use components which are a little more precise and reliable, and incorporating local microprocessors and memory which could operate the machine from lens design or profile correction data supplied by infrequent operator intervention via a controlling microcomputer. Typical manufacturing overheads and profit allowance have been included in the estimated price.

e) Central microcomputer for controlling MCPM: C_c = £5000. This cost is similar to that of the Vector MZ system used for the work reported in Chapter 6, with various extra S100-bus interface-cards, enhanced disc-storage and a printer. Many microcomputers with equivalent facilities are available at a similar cost.

8.2.3 Labour requirements.

Estimates of the number of hours required on the machines for generating, T_g, and for polishing, T_p, are given in the table below. These are based on the times taken in the work reported in Chapters 4 to 6, modified with some optimism to what may be expected with little more development in technique than purchasing, and/or reliably constructing, equipment as suggested by the current state of experience. It is realised that there may be a great decrease of the times for any or all processes - a learning curve is commonly followed which results in an almost exponential decrease of fabrication costs to a constant level which is significantly less than the initial costs.

Because it may be possible for one worker to operate more than one CNC machine simultaneously, the labour costs associated with lens fabrication are not strictly related to the times taken on the machines. It has been assumed, perhaps somewhat pessimistically, that one worker would be directly involved full-time with each machine except for the MCPM where a worker could operate two machines simultaneously. These estimates are based on the physical size of the machines as much as on the complexity of their operation. The total labour time per lens, T_l, also includes an allowance for the significant amount of time usually required for changing tools, particularly from generating to polishing when no MCPM is available. This cost element diminishes when the lens fabrication rate requires more than one machine, since each machine may be left set up for a particular grade of generating or polishing tool. In Table 19 below, expressions are given for the total labour time associated with each combination of fabrication method, where the number of generating machines is M_g and the number of polishing machines is M_p.

TABLE 19: LABOUR TIME PER LENS REQUIRED BY EACH COMBINATION OF FABRICATION METHODS.

PROCESS	TIME/ hours		
	GENERATING T_g	POLISHING T_p	LABOUR T_l
AA	2	3	$T_g + T_p + 1/M_g$
JJ	3	4	"
AM	2	2	$T_g + T_p/2 + 2/M_p$
JM	3	3	"
UM	1	8	$2.T_g + T_p/2 + 2/M_p$

The cost per hour of the labour time is assumed to be £20. This is typical of current industrial costs which include marginal overheads such as extra services required (e.g. maintenance staff and fuel). The costs of the lens fabrication machines are not included in labour costs.

8.2.4 Number of machines required

The author carried out a survey (unpublished) which indicates that an average of 1600 hours per year are worked by machine operators in the optical production industry. This assumes working overtime (not continuous-shift working) but losing time for various absences and for machine maintenance. Expressions are given below for the number of machines required to make Q lenses in a period of Y years during which each machine operator works 1600 hours. The number of machines required is given by the next integer above the value of the expressions. It is assumed that one control computer would be required for every six or less polishing spindles.

a) Polish with the generating machine (either the aspheriser or the jig grinder):

The number of machines required M_g, may be calculated by dividing the product of the number of lenses and the time per lens by the total amount of time available, i.e.

$$M_g = Q.(T_g+T_p)/(1600.Y) \quad \text{aspherisers or jig grinders.}$$

b) Polish with the MCPM (having generated with other machines). Similarly to above:

$M_g = Q.T_g/(1600.Y)$ aspherisers, jig grinders or ultrasonic grinders;

and $Mp = Q.T_p/(1600.Y)$ Microprocessor-controlled polishing machines;

The number of control computers required is one-sixth of the number of MCPM, i.e. $M_c = M_p/6$ taken to the next highest integer.

8.3 FABRICATION COST PER LENS

8.3.1 Introduction

The economic criterion which has been chosen by the author to select an appropriate combination of machines is simply the cost per lens of the generating and polishing processes. It is assumed that the costs of purchasing raw materials, preparing plane-parallel substrates, and all other device-fabrication processing are common to every lens-fabrication method and need not be estimated for this comparison.

The cost per lens for each fabrication method depends on the amount of direct labour required and on the cost of using the machines which must be provided. This latter cost depends on whether the capital equipment cost must be paid for by this work alone. This would be necessary if the entire working lives of the machines were devoted to producing geodesic lenses, or if no other work for the machines could be expected. However if only a few geodesic lenses were required (such as was the case for the work reported in this thesis) then the costs of the machines used must be shared with other applications. These two extreme cases and one intermediate case are discussed below.

8.3.2 Small number of lenses

The first case of interest is mostly applicable to a small number of lenses, where the capital equipment could be used for other work. Assuming that the capital cost is to be recovered over five years of operation (a typical requirement for such equipment), then the hourly charge for capital, ignoring interest charges, is calculated by dividing the capital cost by 8000 hours (5x1600). The cost per lens, fabricated by the various combinations of machines, are:

Combination AA - generate and polish on the aspherising machine:

$$C_a.(T_g + T_p)/8000 + 20.T_l = £351$$

Combination JJ - generate and polish on the jig grinder:

$$C_j.(T_g + T_p)/8000 + 20.T_l = £361$$

Combination AM - Generate on aspheriser, polish on MCPM:

$$(C_a.T_g + C_p.T_p + Cc.T_p)/8000 + 20.T_l = £196$$

Combination JM - Generate on jig grinder, polish on MCPM:

$$(C_j.T_g + C_p.T_p + C_c.T_p)/8000 + 20.T_l = £226$$

Combination UM - Generate on ultrasonic grinder, polish on MCPM:

$$(C_u.T_g + C_p.T_p + C_c.T_p)/8000 + 20.T_l = £ 198$$

The last three expressions assume that equal numbers of each type of machine are required for lens fabrication. This is true for small numbers of lenses where only one of each machine is required. Using the data and expressions of sections 8.2.3 and 8.2.4 the number of lenses made per year (Q/Y) below which the above assumption is true is 800 for generating on an aspherising machine, 533 on a jig grinder and 200 on an ultrasonic grinder.

It appears that the methods having the lowest costs are those which include the use of an MCPM, and among these the method using a jig grinder to generate the lenses is about 10% more expensive than the other two.

8.3.3 Number of lenses which justifies MCPM purchase

An intermediate case of interest is that in which the aspheriser or a jig grinder is an existing asset (therefore its capital cost is paid as above) but purchase of an MCPM must be justified on the geodesic-lens work alone. The question is whether to polish lenses on the aspheriser or jig grinder, or whether to buy an MCPM for polishing. The decision depends on the number of lenses to be made. As the number of lenses to be made, Q, increases, the purchase of the MCPM becomes more justified.

The breakeven quantity, above which the cost per lens is less if the MCPM is purchased, may be estimated by equating the capital cost per lens of the MCPM, $(C_p + C_c)/Q$, with the labour cost per lens of polishing on the aspheriser or jig grinder, $C_a.Tp/8000$. The breakeven occurs at about $Q = 8000.(Cc+C_p)/C_a.T_p$. Using this expression, it is found that for more than about 160 lenses the cost per lens becomes progressively less if an MCPM is purchased and used for polishing lenses, rather than continuing to polish on the generating machine.

8.3.4 Large number of lenses

The other major case of interest is when the capital items purchased must be allocated entirely to geodesic lens production. This is mainly applicable to large quantities of lenses, occupying a major proportion or all of the economic lifetimes of the machines.

In this case the number of each machine required is calculated according to the expressions of section 8.2.4; the cost of the machine is divided by the number of lenses according to $Ma.C_a/Q$, $Mj.C_j/Q$, $(Mu.C_u + M_p.C_p + M_c.C_c)/Q$, etc, according to the combination of methods used; and the cost of labour is added.

Figure 8.1 shows the cost per lens for quantities between 100 and 40,000 for an example where all the lenses must be made within three years. The steps in the curves

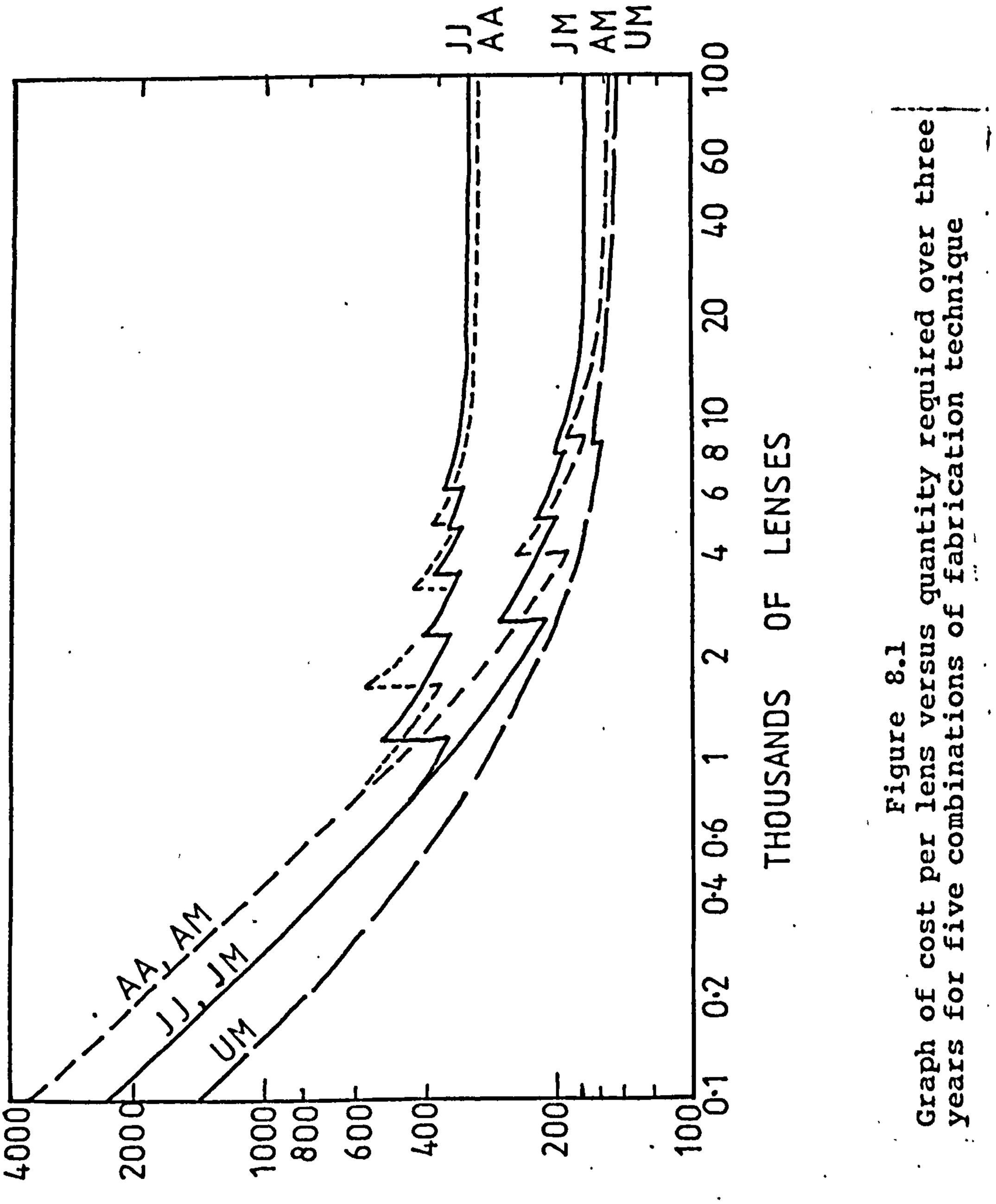

Figure 8.1
Graph of cost per lens versus quantity required over th
years for five combinations of fabrication technique

occur where additional machines must be provided. For the larger quantities these steps are small and have been smoothed out. It is clear that polishing on the aspheriser or jig grinder costs almost the same as using an MCPM up to about 1200 lenses, but using the ultrasonic method costs even less. For more than a few thousand lenses, the methods using the MCPM all cost almost the same, and tend towards half the cost of the other methods for quantities of more than tens of thousands.

As an example, fabrication of 2400 lenses over three years (e.g. 120 complete IOSA systems each of ten individual IOSAs with two lenses) could cost about £260 per lens and require an average of 2.5 workers operating one aspheriser (working at only half capacity), one MCPM and one controlling microcomputer at a total capital cost of £385,000. Alternatively this output could be achieved at a lens cost of £207 with one ultrasonic generator, one tool-profile lathe (both at full capacity), four MCPM and one controlling microcomputer at the lower capital cost of £185,000 but requiring an average of 3.25 operators.

For an even greater numbers of lenses, e.g. 14,400 (720 complete IOSA systems) a manufacturer could employ ten operators with six asphericers, six MCPM and one controlling microcomputer and produce lenses for £225 each, or employ 18 operators with three ultrasonic generators, three tool profile lathes, 24 MCPM and four controlling microcomputers and produce lenses for £177 each.

8.4 CONCLUSIONS

It should be emphasised that it is not easy to draw conclusions on the most economic method of lens production, since this clearly depends on the rate of production, the total number of lenses required and the methods of apportioning capital costs, not to mention the enormous uncertainties in the machining times and associated labour times. The choice of method could also depend on whether a manufacturer could more easily raise capital than recruit and train suitably skilled operators.

The estimates presented in this chapter suggest that the cost of fabricating geodesic lenses could be between £200 and £400 each, depending on the quantity required and the combination of fabrication methods employed (the cost of providing the polished parallel substrates have not been included).

Using the estimates and examples discussed in this Chapter, it appears that for small quantities of lenses the most economical fabrication method would be to use an aspherising machine whose purchase has been justified by being used for work other than geodesic-lens fabrication, particularly if a microprocessor-controlled polishing machine were also available. For more than about 160 lenses it would be economically justified to purchase a commercially-produced MCPM, should such a machine eventually be marketed.

For producing large numbers of lenses it would be most economical to purchase as many MCPM as required to polish the output of the generating machines. The ultrasonic generating method appears to offer the lowest cost.

Because the practical limitations of every lens fabrication method have yet to be adequately established, a manufacturer may prefer to employ the method which has been most fully developed in the present work, or alternatively to employ a method which uses equipment which is already available to him.

CHAPTER 9: CONCLUSIONS

9.1 INTRODUCTION

The work described in this thesis was mainly concerned with the design of geodesic lenses for an IOSA and the evaluation of several alternative methods of fabrication. The following sections summarise the the main results and conclusions arrived at during the work, and make suggestions for further work in this field.

9.2 OVERALL IOSA DESIGN: SUBSTRATE AND LENSES

The general requirements of microwave-spectrum analysers have been discussed in Chapter 1, and the arguments in favour of using an acousto-optic microwave-spectrum analyser in an integrated-optical form have been outlined. An integrated-optical microwave-spectrum analyser (IOSA) is expected to provide rapid, parallel processing of spectra in a relatively light-weight, rugged format. The use of lithium niobate is favoured as the substrate for the IOSA because it is a readily-available material on which a surface may be modified to form waveguides which possesses a particularly good combination of piezo-electric properties and low optical- and acoustic-propagation losses. At present, the IOSA would have to take a hybrid form, using an external light source and an external photodetector array.

In the IOSA, the acousto-optic Bragg deflection takes place in the region between a collimating lens and a Fourier-transform lens. The Fourier-transform lens must therefore focus parallel light-beams which enter the lens at a range of angles, corresponding to the frequency content of the microwave spectrum. The reasons for choosing geodesic lenses have been discussed in Chapter

1. It was hoped that geodesic lenses, compared with other types of element which may be produced by planar fabrication techniques, could provide more efficient operation over a wide range of angles, with little more light loss and in-plane scattering than experienced in the planar region of the waveguide on the IOSA surface.

The work discussed in this thesis involved investigating the design and fabrication of geodesic lenses, concentrating on lenses suitable for an IOSA with the following dimensions and performance criteria:

Material: single-crystal electro-optic quality Y-cut lithium niobate.
Propagating directions: Z-axis acoustic beam, X-axis light beam.
Dimensions: length 65mm, width 14mm, thickness 3mm.
Laser vacuum wavelength: 850nm.
Light detector element spacing: 8μm.
System frequency bandwidth: 1 GHz
System frequency resolution: 4MHz.
Lens diameters: 10mm.
Lens focal lengths: 18.5mm.

Further work could consider the use of a shorter focal length for the collimating lens and a longer focal length for the Fourier-transform lens with the aim of achieving better frequency resolution (although an increase in focal length leads to a larger region on the lens where the power density may be high enough to cause photorefractive damage [8]).

9.3 GEODESIC LENS DESIGN

It has been shown in Chapter 2 that, because of their circular symmetry, geodesic lenses focus light from any point on one circle to a point on another circle, where the circles are concentric with the lens. Because photodetector arrays are usually linear, their use in the IOSA (with its circular focal properties) incurs

defocusing of the image spots which fall onto some of the detector elements. The extent of defocusing encountered depends linearly on the width of lens aperture used by the focused beam. However the size of the image spot due to diffraction depends inversely on the lens aperture used. A compromise on aperture must be made: Chapter 2 has given expressions which may be used to show that an aperture of about 5mm should provide a satisfactory compromise between diffraction and focal-curvature for the above design parameters. For this aperture, the spot-width due to diffraction plus the spot-width due to focal curvature does not exceed the detector element width for an array of up to 280 elements. If the ratio of bandwidth to frequency resolution were required to be increased, it would be necessary to employ a curved photodetector array.

In Chapter 2 the geometrical-optical analysis of geodesic lenses has been introduced and expressions presented which permit ray-tracing to be carried out for any lens profile. Simple expressions have been developed to evaluate the focusing performance of spherical geodesic lenses. It has been shown in Table 1 that the aberrations of a spherical lens working at an aperture of 5mm lead to an image spot-width of thirteen times the 8μm photodetector-element spacing. However, an even more important limitation of spherical lenses is that light does not propagate across the abrupt boundary between the edge of a spherical lens and the surrounding plane waveguide.

In Section 2.3.2 it has been shown that rounding the edge of the lens depression to merge smoothly into the surrounding plane-waveguide region of the IOSA cannot only overcome the problem of propagation loss, but can also reduce the amount of spherical aberration.

The method of Sottini, Russo and Righini for designing geodesic lenses with perfect geometric focusing has been introduced in Chapter 2 and described in detail in

Appendix I. This method has been used to produce the designs of an aspheric lens which was later fabricated. The method was chosen because it is easy to carry out, using simple computer-programming of expressions (described in Appendix I) and a numerical-integration routine which is available in a minicomputer library. Other methods of designing aspherical geodesic lenses which have been published do not provide simple expressions, but rely on complex numerical-optimisation computer programmes.

Problems which were encountered in fabricating a lens of the Sottini, Russo and Righini design led to an investigation of the local radius of curvature over the lens profile. It has been shown in Chapter 2 that the radius of curvature is always zero at two positions on the profile: at the outer edge and at the boundary between the inner (focusing) region and the outer (edge-rounding) region. The lens profile generally only has a very small radius of curvature over short radial distances, but the existence of these features would lead to intolerable loss of light from the surface waveguide, and would also provide insuperable fabrication problems because of the finite sizes of tools and measuring probes.

A method of smoothing over these regions has been devised, and has been discussed in Chapter 2. A series of circular arcs may be fitted theoretically to the lens profile so that the arcs are contiguous in slope, but not in height - steps are allowed, providing that the steps are much smaller than estimated fabrication error tolerances. At the two regions of great curvature, the arcs are allowed to depart from the lens profile by slightly more than the fabrication tolerances.

A lens design has been approximated by 20 arcs, with smoothing over of the highly-curved regions. The maximum departure from the starting design is only 2.5μm, over a very small region near to the edge-rounding boundary. Over most of the lens, the departure is less than 0.1μm. Ray-

tracing of this smoothed lens-profile showed that the geometrical aberration, for an aperture of 6mm, leads to a spot-width of less than 2μm, at a focal length about 3μm shorter than the 18.5mm design-value. This spot-width is just smaller than the expected diffraction broadening, and together with the total spot-width is less than the 8μm detector-element spacing.

In future work it would be useful to carry out more theoretical lens design to increase the local radius of curvature as much as possible, without significantly increasing the focused spot-size. Features described in other published work could be incorporated into the arc-fitting programme: a ray-tracing estimate of the effect of errors as interactive feedback during the manual input of modifications to the lens profile [113], and constraints which ensure continuity of the first two derivatives of the profile [103].

Further theoretical work could be carried out to determine which members of the family of profiles which satisfy a particular focusing requirement possess the least sensitivity to fabrication errors, and do not require very small radii of curvature. This work could simply involve ray-tracing analysis. It is important, but much more difficult, to investigate the parameters of lens design which may be varied to reduce waveguide leakage and the aberrations due to crystal anisotropy. The use of edge-reflecting or geodesic "retroreflectors" to allow longer focusing distances by folding beams on small substrates could also be investigated.

9.4 LENS GENERATION BY ULTRASONIC IMPACT GRINDING

Chapter 4 has included description of attempts to generate geodesic lens profiles by ultrasonic impact grinding. Profile errors have been found to be caused by

wear of the ultrasonic tool and non-uniform abrasion over the lens surface. The profile of a lens made by this method departs by as much as 30μm of the profile of the tool before grinding took place. The wear of the tool was about 11μm after being used to grind one lens completely. It has been found difficult to control the overall penetration-depth of the tool because of uncertainty about the expansion of the tool and transducer assembly due to heat generated during grinding. The lens surface was very rough, and included deep pits.

Improvements could be made to the method. The importance of tool-wear could be diminished by using a series of tools for each lens rather than only one tool. Uniformity of abrasion, less pitting and smoother surfaces, and more uniform tool-temperature could be achieved by using a rotating tool, with abrasive fed into the tool-face through internal holes. The use of diamond-coated tools could be investigated, because such tools may permit greater accuracy due to much slower wear.

Because ultrasonic grinding, of all the methods of generating lenses which were investigated, uses the lowest capital-cost equipment it would seem of economic importance to continue development to improve the method.

9.5 LENS GENERATION BY CNC GRINDING

In Chapter 5 it has been shown that a Moore CNC jig-grinder possesses sufficient accuracy and adequate computer-control to produce geodesic lenses, but that wear of the grinding tools is very great, and severely limits the accuracy of profile generation. One aspect of the tool-wear problem is that the tool could not be maintained with a very small radius of curvature, and therefore the minimum radius of curvature on the lens surface was limited.

Further work could be carried out to diminish the amount of tool-wear. This could be achieved by careful selection of a series of tools of different composition and abrasive-particle size. It is important to establish gauges which would permit much more rapid setting up of the tool and axis aligment. Development of a polishing method for use on the jig grinder would be useful: a slower tool rotation than that use by the grinding tool head would be essential. Polishers such as have been discussed in Chapter 6 could probably be adapted to fit the jig grinder. The GE 1050 computer which was used with the Moore jig grinder would need to be programmed with a very long tape-file to obtain the fine control over the radial-traverse speed which is required for uniform material removal during polishing. Alternatively it may be possible to use a more modern controlling-computer which could provide a more easily-programmed continuously-variable feedrate.

9.6 LENS GENERATION BY CNC DIAMOND-TURNING

It has been shown in Chapter 5 that diamond-turning on a contact-lens lathe can produce lenses with a similar radius of curvature to that required for the geodesic lenses and with a surface finish on lithium niobate which is better than that achieved on the jig grinder. It would be useful to develop the method of using a contact-lens lathe further. A contact-lens lathe could probably be modified by adding microprocessor control to obtain the aspherical profile, and by also exchanging the bearings and slides for ones with greater precision. The main objective would be to obtain sufficient profile accuracy and smoothness that the microprocessor-controlled polishing machine could be used to complete polishing and correct residual profile errors.

However the best method demonstrated by the present work is single-point diamond turning on a CNC aspherising

machine with precision and stability such as that produced by Moore. Better tool-post and setting equipment than was available during the author's work are required, but this is available on more recent production machines from Moore and Pneumoprecision, together with even finer table-movement steps and position control.

Lens depth and profile accuracy with these machines was within 1μm, and would probably be well within 0.5μm if better tool-setting arrangements were provided. Chapter 5 has indicated that there is some anisotropy in turning lithium niobate crystal surfaces. The depth of cutting around an annulus of constant lens-profile radius varies by about 0.1μm, being deepest along an X-axis direction. There is also anisotropy in the roughness. Within diamond-turned lens depressions the roughness has been measured to be generally about 30nm Ra, but for lenses turned on a Y-face there is a sector centred along an X-axis direction of greater roughness - about 40nm Ra. Anisotropy in roughness has also been observed on plane-turned Y-cut lithium niobate surfaces, but here the smoothest sector has been found to be of roughness 6nm Ra, which is the best which could be expected for the tool size and crossfeed rate which have been used.

Further investigation of these anisotropy effects could be carried out with the aim of improving the surface roughness and decreasing the annular variations of depth of cut. The use of different crystal orientations could perhaps lead to less roughness, but the overall IOSA performance must not be sacrificed.

9.7 LENS POLISHING

In Chapter 6 it has been shown that large-area flexible polishers are unsatisfactory when used on the very aspherical geodesic lenses.

The design ,construction and use of a microprocessor-controlled polishing machine (MCPM) has been described in Chapter 6. This machine has been found useful to the author because, once developed, it was available locally, rather than remote and expensive to hire, and because it can be programmed to make fine adjustments to the uniformity of material removed by polishing. The machine has been constructed using inexpensive, simple components which can be aligned to within about 10μm of the ideal positions. The control uses a crude approximation to the polishing-removal law, augmented by empirically-derived corrections. The only feed-back is operator inspection of the lens surface for residual pits and scratches. Despite these apparent inadequacies the MCPM polishes diamond-turned lenses well enough to obtain surface roughness of better than 1nm Ra, and does not alter the profiles which have been diamond turned by more than about 0.5μm. Most of the waviness introduced by the motion of the Moore diamond-turning machine has been removed by polishing.

Further development of the MCPM is desirable to provide more reliability and convenience. Work should continue on developing the hydraulic polishing-head. The provision of positional feedback for the tables would be desirable. The special-purpose measuring-machine development could be completed, and feedback arranged via the microcomputer to permit corrections to the profile by the polishing machine.

9.8 LENS EVALUATION

Mechanical and interferometric measurements which have been discussed in Chapters 5 and 7 indicate that the lens profiles may be produced within about 1μm or better.

Measurement of the imaging performance of these lenses is difficult: it has been found difficult to prism-couple a Gaussian beam, truncated at widths within the range 3mm to 7mm, into a geodesic lens. The prism coupling itself

appears to attenuate the input beam very substantially (more than about 10 dB) beyond widths of about 3mm. Further attentuation may occur due to scattering losses within the waveguide in the lens depression.

The measurements which were made show that the lenses provide images with spot-widths between the diffraction-limited value and twice that value. It is clearly essential to carry out more measurements, particularly on spot-width and focal length as a function of input beamwidth. End-fire coupling of the input beam should permit operation at wider apertures. Better characterisation of the input beam intensity profile is essential, followed by calculations on the expected theoretical image-distribution, perhaps by the Beam Propagation Method (BPM).

Further testing on the application of these geodesic lenses to the IOSA should be carried out, using a SAW-diffracted beam to assess the effect of image width and in-plane scattering on the dynamic range. Because the sensitivity of titanium-diffused lithium niobate waveguides to photorefractive damage at 0.63μm wavelength is much greater than at the IOSA design wavelength of 0.85μm [8], lenses should be assessed at the higher, design wavelength using a GaAlAs diode laser.

9.9 CHOICE OF A GEODESIC LENS FABRICATION METHOD

It is not easy to draw conclusions on the most economic method of lens production (Chapter 8), since this clearly depends on the rate of production, the total number required and the methods of apportioning capital costs, not to mention the enormous uncertainties in the machining times and associated labour times. The use of an MCPM could be economically worthwhile. However, the practical limitations of the competing methods have yet to be established fully enough, and it may well be that a

manufacturer would prefer to use the equipment already available, or to develop the methods which, in this work, have been shown most fully to be suitable. Further assessments of the economic aspects of lens fabrication should be made as better estimates of the operating times and costs arise.

9.10 SUMMARY OF ORIGINAL WORK IN THIS THESIS

The performance requirements and overall design criteria were specified for geodesic lenses which would be suitable for a useful integrated-optical microwave-spectrum analyser, and which could be fabricated on practically-available lithium niobate crystals. This particularly included deriving an expression for the lens aperture which permits a compromise to be made between the opposing effects on image size of diffraction and of field curvature.

Existing theoretical work on geodesic lens design was developed to enable analysis of lenses with any general axisymmetrical lens-generating profile (theoretical or derived from practical measurements) by ray tracing both within and beyond the lens surface.

It was discovered that a method of designing geodesic lenses for perfect geometric imaging, which had been published by Sottini, Russo and Righini, always produces two regions of zero radius of curvature.

A procedure was devised which smooths over the two highly-curved regions of any lens profile which has been designed by the above method. The modified lens profile does not possess regions of great curvature, but is close enough to the original profile that the geometrical image size is not too large for the IOSA application. The smoothing procedure decribes the modified profile in terms

of a series of circular arcs. These circular arcs are useful for describing the lens profiles for computer numerically-controlled machines.

A study was made of the generation and polishing of geodesic lenses using a CNC jig-grinder.

It was shown that the use of single-point diamond-turning for fabricating plane or aspherical surfaces on lithium niobate produced sectors of different surface roughness, radiating (generally in a hexagonal pattern) from the centre of rotation.

The use of a particular diamond-turning aspheric generator was studied, leading to specification of the accuracy to which its axes and tool setting must be made. The machine was used to generate many geodesic lenses.

It was shown that the flexible polishing of a highly curved, very aspheric geodesic lens is not capable of sufficient accuracy. A microcomputer-controlled machine for polishing such lenses was specially designed and constructed.

Lenses were diamond turned and then polished on the above machine. Assessments of surface finish and profile accuracy indicated that the lenses should be suitable for IOSA use. Measurements of imaging performance showed that the lenses performed close to their diffraction limit.

Criteria were established for making an economic choice between the (comparatively expensive) potential combinations of lens-fabrication methods.

9.11 PUBLICATIONS

Publications on this work by the author and colleagues are listed as references 114 to 117.

REFERENCES

1. T.Tamir (Ed), Integrated optics, Springer-Verlag, 2nd Ed (1979).

2. D.B.Anderson, J.T.Boyd, M.C.Hamilton, R.R.August, IEEE Jour. Quant.Elect, 13, 268-275 (1977), An integrated-optical approach to the Fourier transform.

3. M.K.Barnoski, B.U.Chen, T.R.Joseph, IEEE Trans. Crcts. Systs, 26, 1113-1124, (1979), Integrated optic spectrum analyzer.

4. B.Chen, T.R.Ranganath, T.R.Joseph, J.Y.Lee, Tech. Digest, Topical meeting on Integrated & Guided Wave Optics, Nevada (1980), Progress on the development of integrated optic spectrum analyzer.

5. D.Mergerian, E.C.Malarkey, R.P.Pautienus, J.C.Bradley, G.E.Marx, L.D.Hutchinson, A.L.Kellner, Proc. Soc. Photo-Opt. Instr. Eng., 239, 121-127 (1980), An integrated optical radio frequency (rf) spectrum analyzer,

6. D.Mergerian, E.C.Malarkey, R.P.Pautienus, J.C.Bradley, G.E.Marx, L.D.Hutchinson, A.L.Kellner, Appl. Opt., 19, 3033-3034 (1980), Operational integrated optical RF spectrum analyzer.

7. M.Kanazawa, T.Atsumi, M.Takami, T.Ito, IOOC'83 Tokyo, Tech. Digest, paper 30B3-5, 258-259 (1983), High resolution integrated optic spectrum analyzer.

8. D.Mergerian, E.C.Malarkey, R.P.Pautienus, IOOC'83 Tokyo, Tech. Digest, paper 30B3-6, 260-261 (1983), High dynamic range integrated optical RF spectrum analyzer.

9. G.Arvidsson, IOOC'83 Tokyo, Tech. Digest, paper 30B3-8, 264-265 (1983), Lensless integrated optics spectrum analyzer - an experimental feasibility demonstration.

10. S.Valette, J.Lizet, P.Mottier, J.P.Jadot, P.Gidon, S.Renard, A.M.Grouillet, A.Fournier, H.Denis, IEE Conf. Publ. 227, 2nd European Conf. on Integrated Optics, 75-76 (1983), Spectrum analyser on silicon substrate: a key element for many optical integrated devices.

11. E.G.Lean, J.M.White, C.D.W.Wilkinson, Proc. IEEE, 64, 779 (1976).

12. W.S.Oakley, Defense Elect., 1-8 (Oct 1979), Acousto-optical processing opens new vistas in surveillance and warning receivers.
13. M.C.Hamilton, Proc. Soc. Photo-Opt. Instr. Eng., 139, 144-150 (1978), RF frequency sorting in electronic warfare systems with integrated optical circuits.
14. H.J.Whitehouse, K.Bromley, Microwave System News, 91-98 (Apr 1981), Can analog signal processing survive the VHSIC challenge?
15. J.H.Collins, P.M.Grant, Microwave System News, 102-107 (Apr 1981), Signal processing pivotal to next generation ESM receivers.
16. C.Stewart, W.J.Stewart, G.Scrivener, Electron. Lett., 17, 971-973 (1981), 500 MHz bandwidth guided-wave L-band Bragg cell.
17. D.B.Anderson, R.L.Davies, J.T.Boyd, R.R.August, IEEE Jour. Quant. Elect., 13, 275 (1977), Comparison of optical-waveguide lens technologies.
18. R.G.Walker, R.C.Goodfellow,2nd Europ.Conf. Integrated Optics, IEE Conf. Publ. 227, 61-64 (1983), Attenuation measurements on MOCVD grown GaAs/GaAlAs optical waveguides.
19.A.J.N.Houghton, D.A.Andrews, G.J.Davies, S.Ritchie, Optics Comms.,46, 164-166 (1983), Low-loss optical waveguides in MBE-grown GaAs/GaAlAs heterostructures.
20. R.Guglielmi, A.Carenco, 1st Europ.Conf. Integrated Optics, IEE Conf. Publ. 201, 61-62 (1981), Optical bistability in $LiNbO_3$ using a monolithically integrated directional coupler and detector.
21.R.M.DelaRue,G.Stewart,C.D.W.Wilkinson, I.R.Williamson, Electron. Lett.,9, 325 (1973), Frequency-controlled beam steering of surface acoustic waves.
22. T.R.Joseph, B.U.Chen, Proc. 1979 Ultrasonics Symp., 28-33 (1979).
23. R.M.White, Proc IEEE, 58, 1218-1277 (1970), Surface elastic waves.
24. A.J.Slobodnik, Electron. Lett., 10, 233-234 (1974), Surface-quality effects on S.A.W. attenuation on yz

$LiNbO_3$.
25. J.T.Milek, M.Neuberger, Handbook of electronic materials, 8, Electrooptic modular(sic) materials, Plenum (1972).
26. A.M.Glass, Opt. Eng., 17, 470 (1978).
27. J.Van der Donk, J.Vandewege, IEE Conf. Publ. 201, 1st Europ. Conf. Integrated Optics, 29-32 (1981), Second order effects in geodesic lenses.
28. Hitachi literature.
29. G.E.Marx, G.M.Borsuk, Tech. Digest, Topical meeting on integrated and guided-wave optics, Nevada, USA (1980), Evaluation of a photosensor for integrated optics spectrum analysers.
30. E.R.Schumacher, Nval Ocean Systs. Center Tech. Report 480 (1980), Defect-free edge polishing of Lithium Niobate and other optical crystals.
31. C.T.Mueller, C.T.Sullivan W.S.C.Chang, D.G.Hall, J.D.Zino, R.R.Rice, IEEE Jour. Quant. Elect., 16, 363-372 (1980), An analysis of the coupling of an injection laser diode to a planar $LiNbO_3$ waveguide.
32. D.G.Hall, J.D.Spear-Zino, H.G.Koenig, R.R.Rice, J.K.Powers, G.H.Burkhart, P.D.Bear, Appl. Opt., 19, 1847-1852 (1980), Edge coupling of a GaAlAs DH laser diode to a planar Ti:$LiNbO_3$ waveguide.
33. J.R.Carruther et al, J.Appl.Phys., 42, 1846 (1971).
34. J.R.Carruther et al, Appl. Opt., 13, 2333 (1974).
35. R.V.Schmidt et al, Appl. Phys. Letts, 25, 458 (1974).
36. R.J.Esdaile, Ph.D. Thesis, Univ. of Glasgow (1979) Titanium diffused lithium niobate for electrooptic devices.
37. A.D.McLachlan, Ph.D. Thesis, Univ. of Glasgow (1981), Theoretical and experimental investigations of titanium diffused $LiNbO_3$ waveguides.
38. A.D.McLachlan, R.M.DeLaRue, J.A.H.Wilkinson, IEE Conf. Publ. 201, 1st Europ. Conf. Integrated Optics, 4-7 (1981), Titanium diffused $LiNbO_3$ waveguides.
39. M.Micheli, J.Botineau, P.Sibillot, D.B.Ostrowsky, M.Papuchon, Opt. Comms., 42, 101-103 (1982), Fabrication

and characterization of Titanium indiffused proton exchanged (TIPE) waveguides in Lithium Niobate.
40. D.W.Vahey et al, Ferroelectrics, 27, 81-84 (1980).
41. G.B.Brandt, Opt. Eng., 20, 150 (1981), In-plane scattering in glass and niobium oxide waveguides.
42. D.W.Vahey, Proc. SPIE, 176, 62 (1979).
43. J.Singh, Ph.D. Thesis, Univ. of Glasgow (1983), Studies concerning the dynamic range of the integrated optic spectrum analyser.
44. G.G.Roberts, C. Pitt (Eds) Thin Solid Films, 99, (1983), Thin film science and technology, Vol. 3.
45. G.Hatakoshi, H.Inone, K.Naito, S.Umegaki, S.Tanaka, Opt. Acta, 26, 961-968 (1979), Optical waveguide lenses.
46. G.Hatakoshi, S.Tanaka, Optics Lett., 2, 142 (1978).
47. S.K.Yao, D.E.Thompson, Appl. Phys. lett.,33, 635 (1978).
48. R.Schubert, J.H.Harris, IEEE Trans. Microw. Theory Tech., 16, 1048 (1968).
49. P.R.Ashley, S.C.Chang, Appl.Phys. Lett., 33, 490-492 (1978), Fresnel lenses in a thin-film waveguide.
50. R.J.Collier, C.B.Burckhardt, H.L.Lin, Optical Holography, Academic Press, New York (1971).
51. V.Neuman, C.W.Pitt, L.M.Walpita, IEE Conf. Publ. 201, 1st Europ. Conf. Integrated Optics, 89-92 (1981), An integrated acousto-optic spectrum analyser using grating components.
52. P.Mottier, S.Valette, Appl. Opt., 20, 1630-1634 (1981), Integrated Fresnel lens on thermally oxidized silicon substrates.
53. S.Valette, A.Morque, P.Mottier, Electron Lett., 18, 13 (1982).
54. J.Van der Donk, Electron. Lett., 16, 292-294 (1980), Analysis of geodesic lenses by beam propagation method.
55. V.Neuman, C.W.Pitt, L.M.Walpita, Electron. Lett, 17, 165-176 (1981).
56. M.Stockmann, W.Beinvogel, Wave Electron., 4, 221-228 (1983), Planar Bragg-grating lenses in $LiNbO_3$ fabricated by CHF_3 reactive-ion etching.
57. W.S.C.Chang, S.Forouhar, C.Warren, R.X.Lu, IOOC'83

Tech. Digest, Tokyo, paper 29A2-3, 78-79 (1983), Chirped grating lenses in Ti-diffused $LiNbO_3$ waveguides.
58. H.Nishihara, T.Suhara, IOOC'83 Tech. Digest, Tokyo, paper 29A2-1, 74-75 (1983), Applications of electron-beam written gratings to optical IC.
59. G.Hatakoshi, M.Yoshima, K.Goto, IOOC'83 Tech. Digest, Tokyo, paper 29A2-2, 76-77 (1983),Off-axis grating lenses fabricated by EB lithography.
60. T.Suhara, H.Nishihara, J.Koyama, IOOC'83 Tech. Digest, Tokyo, paper 29C5-5, 40-41 (1983), One-gigaherz-bandwidth demonstration in integrated-optic spectrum analyzer.
61. see reference 48.
62. R.Ulrich, R.J.Martin, Appl. Opt., 10, 2077 (1971), Thin film planar lenses.
63. L.P.Boivin, Appl.Opt., 13, 391-395 (1974), Thin film laser-to-fibre coupler.
64. D.W.Vahey, Final report, Optical waveguide geodesic lenses, Air Force Avionics Lab., Ohio, USA, AFAL-TR-78-85 (1978).
65. D.W.Vahey, Proc. IEEE Ultrasonics Symp. CH 1344-1/78, 70-73 (1978), Corrected waveguide geodesic lens for integrated acousto-optics spectrum analyser.
66. S.P.Morgan, J. Appl. Phys., 29, 1358 (1958), General solution of the Luneberg lens problem.
67. T.Van Duzer, Proc. IEEE, 58, 1230-1237 (1970), Lenses and graded films for focusing and guiding acoustic surface waves.
68. C.M.Verber, D.W.Vahey, R.P.Keenan, An investigation for the development of an integrated optical data preprocessor, NASA Contractor report 3151 (1979).
69. D.W.Vahey, C.M.Verber, R.P.Keenan, Proc. Soc. Photo-Opt. Instr. Eng., 139, 151-158 (1978), Development of an integrated optics multichannel data processor.
70. W.H.Southwell, Jour. Opt. Soc. Amer., 67, 1004-1009 (1977), Inhomogeneous optical waveguide lens analysis.
71. W.H.Southwell, Jour. Opt. Soc. Amer., 67, 1010-1014 (1977), Index profiles for generalized Luneberg lenses and their use in planar optical waveguides.

72. J.R.Bush, V.E.Wood, R.P.Keenan, C.M.Verber, Optical information processing for aerospace applications, NAS Conf. Publ. 2207, 251 (1981) Evaporated As_2S_3 Luneberg lens for $LiNbO_3$:Ti optical waveguides.
73. R.F.Rinehart, J. Appl. Phys., 19, 860-862 (1948), A solution of the problem of rapid scanning for radar antennae.
74. K.S.Kunz, J.Appl. Phys., 25, 642-653 (1954), Propagation of microwaves between a parallel pair of doubly curved conducting surfaces.
75. G.Toraldo di Francia, Opt. Acta, 1, 57-163 (1955), A family of perfect configuration lenses of revolution.
76. L.Ronchi, Opt. Acta, 2, 64-80 (1955) Geometrical optics of toroidal junctions in configuration lenses.
77. I.M.Mason, J. Acoust. Soc. Amer., 53, 1123-1128 (1973).
78. G.C.Righini, V.Russo, S.Sottini, G.Toraldo di Francia, Appl. Opt., 11, 1442-1443 (1972), Thin film geodesic lenses.
79. G.C.Righini, V.Russo, S.Sottini, G.Toraldo di Francia, Proc. 1973 Europ. Microwave Conf., 1, Brussels (1973), Paper B.5.5,Geodesic lenses for integrated optics.
80. G.C.Righini, V.Russo, S.Sottini, G.Toraldo di Francia, Appl. Opt. 12, 1477-1481 (1973), Geodesic lenses for guided optical waves.
81. G.C.Righini, V.Russo, S.Sottini, Proc. 9th Int. Conf. of the ICO, Washington, DC (1974), Thin film geodesic lenses.
82. G.Righini, V.Russo, S.Sottini, IEEE Jour. Quant. Elect., 15, 1-4 (1979), A family of perfect aspherical geodesic lenses for integrated optical circuits.
83. S.Sottini, V.Russo, G.C.Righini, Jour. Opt. Soc. Amer., 69, 1248-1254 (1979), General solution to the problem of perfect geodesic lenses for integrated optics.
84. S.Sottini, V.Russo, G.C.Righini, IEE Trans. Crcts & Systs., 26, 1036-1040 (1979), Fabrication tolerances in geodesic lenses: a rule of thumb.
85. S.Sottini, V.Russo, G.C.Righini, Jour. Opt. Soc.

Amer., 70, 1230-1234 (1980), Geodesic optics: new components.
86. S.Sottini, V.Russo, G.C.Righini, IEE Conf. Publ. 201, 1st Europ. Conf. Integrated Optics, 95-98 (1981), FT geodesic system for high-resolution spectrum analyser.
87. S. Sottini, Q.Li, C.C.Lee, C.S.Tsai, IEE Conf. Publ. 227, 2nd European conf. on integrated optics, post-deadlione paper (1983), A hemispherical waveguide acousto-optic correlator.
88. B.Spiller, J.S.Harper, Appl.Opt., 13, 2105-2108 (1974), High resolution lenses for optical waveguides.
89. M.V.Berry, J.Phys. A: Math.Gen., 8, 1952-1971 (1975), Attenuation and focusing of electromagnetic surface waves rounding gentle bends.
90. C.M.Verber, D.W.Vahey, V.E.Wood, Appl. Phys. Letts, 28, 514-516 (1976), Focal properties of geodesic waveguide lenses.
91. V.E.Wood, Appl. Opt., 15, 2817-2820 (1976), Effects of edge rounding on geodesic lenses.
92. D.Vahey, V.E.Wood, IEEE Jour. Quant. Elect., 13, 129-134 (1977), Focal characteristics of spheroidal geodesic lenses for integrated optics.
93. C.M.Verber, D.W.Vahey, V.E.Wood, R.P.Keenan, N.F.Hatman, Final report, Feasibility investigation of integrated optics Fourier transform devices, NASA CR-2869 (1977).
94. W.H.Southwell, Jour. Opt. Soc. Amer., 67, 1293-1299 (1977), Geodesic optical waveguide lens analysis (also see corrections in 69, 792-793 (1979), Geodesic profiles for equivalent Luneberg lenses).
95. B.U.Chen, E.Marom, A.Lee, Appl.Phys.Lett., 31, 263-265 (1977), Geodesic lenses in single mode $LiNbO_3$ waveguides.
96. B.Chen, E.Marom, R.J.Morrison, Appl. Phys. Lett., 33, 511-513 (1978), Diffraction limited geodesic lens for integrated optics circuits.
97. B.Chen, O.Ramer, Final report, Naval Res. Lab. contract NOO173-78-C-0102 (1979), Geodesic lenses for integrated optical circuits.

98. B.Chen, O.Ramer, IEEE Journ. Quant. Elect, 15, 853-860 (1979), Diffraction limited geodesic lens for integrated optic circuit.
99. D.Kassai, E.Marom, Jour. Opt. Soc. Amer., 69, 1242-1248 (1979), Aberration-corrected rounded-edge geodesic lenses.
100. E.T.Aksenov, N.A.Esepkin, A.A.Lipovskii, A.V.Pavlenko, Sov. Tech. Phys. Lett., 5, 531-532 (1979), Geodesic lenses formed in diffusion-fabricated optical waveguides.
101. J.H.Myer, O.G.Ramer, Appl. Opt., 20, 412-416 (1981), Diffraction-limited geodesic lens: a search for substitute contours.
102. G.E.Betts, J.C.Bradley, G.E.Marx, D.C.Schubert, H.A.Trenchard, Appl.Opt., 17, 2346-2351 (1978), Axially symmetric geodesic lenses.
103. G.E.Betts, G.E.Marx, Appl. Opt., 17, 3969-3974 (1978), Spherical aberration correction and fabrication tolerances in geodesic lenses.
104. J.C.Bradley, E.C.Malarkey, D.Mergerian, H.A.Trenchard, Proc. Soc. Photo-Opt. Instr. Eng., 176, 75-84 (1979), Theory of geodesic lenses.
105. D.Mergerian, E.C.Malarkey, R.P.Pautenius, J.C.Bradley, Proc. Soc. Photo-Opt. Instr. Eng., 176, 85-94 (1979), Diamond machined geodesic lenses in $LiNbO_3$.
106. D.Mergerian, J.C.Bradley, R.P.Pautenius, L.D.Hutchinson, A.L.Kellner, E.C.Malarkey, G.E.Marx, Tech. digest, Topical meeting on integrated and guided-wave optics, Nevada, USA (1980), Diamond turned aspheric geodesic waveguide lenses in lithium niobate.
107. J.C.Bradley, L.D.Hutcheson, A.L.Kellner, E.C.Malarkey, D.Mergerian, R.P.Pautienius, Proc. Soc. Photo-Opt. Instr. Eng. 239, 84-89, (1980), Geodesic lens performance characteristics.
108. S.Cornbleet, Microwaves, Opt. & Acoust., 2, 194-200 (1978), Ray paths in a nonuniform axially symmetric medium.
109. S.Cornbleet, P.J.Rinous, IEE Proc. 128 pt.H, 95-101

(1981), Generalised formulas for equiv alent geodesic and non-uniform lenses.
110. J.Van der Donk, P.E.Lagasse, Elect. Lett., 16, 292-294 (1980), Analysis of geodesic lenses by beam propogation method.
111. J.Van der Donk, Ph.D. thesis, Univ. of Gent, Belgium (1982).
113. F.Auracher, Wave Electron., 4, 229-236 (1983), Simple design and error analysis for geodesic lenses.
114. G.F.Doughty, R.B.Wilson, J.Singh, R.M.DeLaRue, S.Wright, Proc.Soc. Photo-Opt. Instr. Eng., 235, 35-41 (1980), Aspheric geodesic lenses in an integrated optics spectrum analyser.
115. G.F.Doughty, R.M.DeLaRue, J.Singh, J.F.Smith, S.Wright, IEE Conf. Publ. 201, 1st Europ. Conf. Integrated Optics ,postdeadline 9-11 (1981), Fabrication techniques for geodesic lenses in Lithium Niobate.
116. G.F.Doughty, R.M.DeLaRue, J.Singh, J.F.Smith, S.Wright, IEEE Trans. CHMT, 5, 205-209 (1982), Fabrication techniques for geodesic lenses in Lithium Niobate.
117. G.F.Doughty, R.M.DeLaRue, N.Finlayson, J.Singh, J.F.Smith, Proc.Soc. Photo-Opt. Instr. Eng., 369, 705-710 (1982), An integrated optical microwave spectrum analyser (IOSA) using geodesic lenses.
118. ed. N.G.Einspruch, VLSI Electronics 1, Academic Press (1981).
119. S.P.Beaumont, P.G.Bower, T.Tamamura, C.D.W.Wilkinson, Appl. Phys. Letts, 38, 436-438 (1981), Sub-20nm-wide metal lines by electron-beam exposure of thin poly (methyl methacrylate) films and liftoff.
120. E.Marom, B.Chen, O.G.Ramer, Opt. Eng., 18, 79-81 (1979), Spot size of focused truncated Gaussian beams.
121. M. Born, E.Wolf, Principles of Optics, 6th ed., Pergamon Press, Oxford (1980).
122. e.g. see reference 104.

123. R.K.Luneberg, Mathematical theory of optics, Brown Univ., Providence, RI, USA (1944) pp189-123.
124. D.F.Horne, Optical production technology, Hilger, Bristol (1972).
125. A.S.DeVany, Master Optical Techniques, Wiley NY (1981).
126. C.Deve, Optical Workshop Principles, 2nd Ed. transl. T.Tippell Hilger, London (1954).
127. D.Malacara, Optical shop testing, Wiley, NY, USA (1978).
128. C.G.Kumanin (Ed.), Generation of optical surfaces, Focal Press, London (1967).
129. G.W.Fynn, W.J.A.Powell, The cutting and polishing of electro-optic materials, Hilger, Bristol (1979).
130. E.Heynacher, Phys. Technol., 10, 124-131 (1979), Aspheric optics: how they are made and why they are needed.
131. J.B.Schroeder, H.D.Dieselman, J.W.Douglas, Appl. Opt., 10, 295-299 (1971), Technical feasibility of figuring optical surfaces by ion polishing.
132. A.M.Karger, Appl. Opt., 12, 451 (1973), Ion beam polishing small aspherics.
133. C.R.Burch, Mon. Not. R.Astron. Soc.,96, 438 (1936), On reflection compensators for testing parabaloids.
134. C.R.Burch, Brit. patent 593 759, Aspherising machine.
135. F.Twyman, Prism and lens making, Hilger, London (1952).
136. J.B.Arnold, P.J.Steger, T.T.Saito, Appl. Opt. 14, 1777-1782 (1975), Tool feed influence on the machinability of CO_2 laser optics.
137. R.Aspen, R.McDonough, F.R.Ritchie, Appl.Opt. 11, 2739-2747, (1979), Computer assisted optical surfacing.
138. D.S.Bajuk, Opt. Eng., 15, 401-406, (1976), Computer controlled generation of rotationally symmetric aspheric surfaces.
139. R.J.Benjamin, Opt. Eng. 17, 574-577 (1978), Diamond turning at a large optical manufacturer.

140. E.L.Church, J.M.Zarada, Appl.Opt., 14, 1788 (1975), Residual surface roughness of diamond-turned optics.
141. D.L.Decker, D.J.Grandjean, Nat. Bur. Standards Spec. Publ. 541, Laser damage in optical materials, 122-131 (1977), Physical and optical properties of surfaces generated by diamond-turning on an advanced machine.
142. T.G.Gijsbers, Proc. Soc. Photo-Opt. Instr. Eng., 235, 44-49 (1980), Colath, the two-axis computer numerically controlled (CNC) / interferometer controlled diamond turning capability of Philips Research.
143. J.Haisma, E.Hugues, C.Babalot, Opt. Lett., 4, 70 (1979), Realization of a bi-aspherical objective lens for the Philips video long play system.
144. S.R.Lange, R.E.Parks, Proc. Soc.Photo-Opt. Instr. Eng. 257, 169-176 (1981), Characterization of scattering from diamond-turned surfaces.
145. D.M.Miller, G.H.Hauser, J.N.Culverhouse, E.N.Greenwell, Proc. Soc. Photo-Opt. Instr. Soc.,? (1978?), Description of a unique machine tool permitting achievement of <15 Å rms diamond turned surfaces.
146. R.E.Parks, Proc. Soc. Photo-Opt. Instr. Eng., 306, 2-12 (1981), Overview of optical manufacturing methods.
147. D.C.Thompson, J.L.Chrislock, L.E.Newton, Proc. Soc. Photo-Opt. Instr. Eng., 306, 144-151 (1981), Development of an inexpensive, high accuracy diamond turning machine.
148. R.Brehm, K.VanDun, J.Teunissen, J.Haisma, Precision Eng.,1, 207-213 (1979), transparent single-point turning of optical glasses: a phenomonological presentation.
149. F.W.Clarke, I.D.A. Tech. Conf., Industrial diamond revolution (1967), Diamond fining of precision optical surfaces.
150. G-H.Chen, Ph.D. Thesis, Univ. of Rochester, NY, USA (1977), High speed fabrication of aspheric surfaces.
151. G-H.Chen, D.T.Moore, Appl.Opt., 18, 559-562 (1979), Ashperical surface polishing with a ring polisher.
152. H.Hashimoto, Appl. Opt., 12, 1717-1720 (1973), Machine for fabricating axially symmetric concave aspherics.

153. F.Cooke, N.Brown, E.Prochnow, Opt. Eng., 15, 407-415 (1976), Annular lapping of precision optical flatware.
154. G.A.Bennett, R.B.Wilson, J.Sci. Instrum., 43, 669-670 (1966), Precision polishing techniques for optics and microwave acoustics.
155. R.B.Wilson, J.Sci.Instrum., 44, 159 (1967).
156. W.Rupp, Opt. Eng.,15, 392-396 (1976), Surface structure of fine ground surface.
157. G.S.Khodakov V.P.Korovkin, V.M.Al'tshu'ler, Sov. J. Opt. Technol. 47, 552-560 (1980), Physical properties of the fine grinding of optical glass.
158. J.Kurdock, T.Saito, J.Buckmelter, R.Austin, Appl.Opt. 14, 1808-1812 (1975), Polishing of supersmooth metal mirrors.
159. J.Noda, I.Ida, Rev. Elec. Comm. Labs, 20, 152-158 (1972), Lapping characteristics of $LiNbO_3$ single crystal.
160. M.F.Ehman, J.Electrochem. Soc.:Solid-state Sci. and Technol., 121,1240-1243 (1974), Surface preparation of ceramic oxide crystals: work damage and microhardness.
161. R.C.Williamson, Proc.IEEE Ultrasonics Symp., 19, 321-328 (1974), Problems encountered in high-frequency surface-wave devices.
162. R.C.Williamson, Proc. IEEE, 64, 702-710 (1976), Properties and applications of reflective-array devices.
163. E.Mendel, SCP and Solid State technol., 27-39 (Aug 1967), Polishing of silicon.
164. A. Strehlow
165. B.Tuck, Jour. Materials Soc., 10, 321-339 (1975), The chemical polishing of semiconductors.
166. R.J.Walsh, A.H.Hertzog, U.S.Patent 3 170 273 (1965), Process for polishing semiconductor materials.
167. Syton Colloidal Silica, Physical Properties and Applications, Monsanto Ltd publ. 53-3(E) M-E-4 (1979).
168. R.B.McIntosh, R.A.Paquin, Appl.Opt., 19, 2329-2331 (1980), Chemical-mechanical polishing of low-scattering optical surfaces.
169. C.M.Verber, D.W.Vahey, V.E.Wood, R.P.Keenan, N.F.Hatman, Final report, Feasibility investigation of

integrated optics Fourier transform devices, NASA CR-2869 (1977).
170. Barr & Stroud Ltd, Private communication.
171. H.E.Bennett, Opt. Eng., 17, 480-488 (1978), Scattering characteristics of optical materials.
172. H.E.Bennett, Opt.Eng. 19, 610-615 (1980), Proposed use of visible optical techniques to evaluate the surface finish of X-ray optics.
173. F.W.Preston, J.Soc. Glass Technol., 11, 214 (1927), The theory and design of plate glass finishing machines.
174. N.J.Brown, P.C.Baker, R.T.Maney, Proc. Soc. Photo-Opt. Instr. Eng., 306, 42-57 (1981), Optical polishing of metals.
175. Mullard Ltd, Ultrasonic drill instruction manual.
176. R.E.Parks, Appl. Opt., 12, 2541-2543 (1973), Aspheric lens elements and spline functions.
177. D.J.Nicholas, J.E.Boon, Proc. Soc. Photo-Opt. Instr. Eng., 235, 92-98 (1980), Production of an aspheric surface for an f/1 focusing lens by a CNC machine.
178. G.M.Sanger, Proc. Soc. Photo-Opt. Instr. Eng., 306, 90-103 (1981), Perspective on precision machining, polishing, and optical requirements.
179. W.R.Moore, Foundations of mechanical accuracy, Moore Special Tool Co., Bridgeport, Conn., USA (1970).
180. G.Boothroyd, Fundamentals of metal machining and machine tools, Scripta Books, Washington, USA (1975).
181. J.Wilks, Prec. Eng., 2, 57-71 (1980), Performance of diamonds as cutting tools for precision machining.
182. K.B.Paxton, G.H.Connors, R.J.Cooley, Appl. Opt., 14, 2274-2279 (1975), Uniform polishing of convex aspheres with an elastic lap.
183. B.C.Willard, Appl. Opt., 19, 488-489 (1980), Aspheric polishing technique with equal polishing rate distribution.
184. R.L.Luckett, Opt. Eng., 11, 114-116 (1972), Fabrication of flexible conforming laps.
185. N.J.Brown, Opt. Eng., 17, 602-620 (1978), Computationally directed axisymmentric aspheric figuring.
186. N.J.Brown, OSA Spring Conf. Appl. Opt., Orlando,

Calif, USA (1980), Design of figuring pads for axisymmetric aspherizing.
187. N.Balasubramanian, M.Sc. Thesis, Univ. Rochester, NY, USA (1980), Development of an aspheric polisher.
188. R.E.Wagner, R.R.Shannon, Appl. Opt., 13, 1683-1689 (1974), Fabrication of aspherics using a mathematical model for material removal.
189. R.A.Jones, Proc. Soc. Photo-Opt. Instr. Eng., 65, 48-51 (1975), Final figuring of a lightweight Beryllium mirror.
190. R.A.Jones, Appl. Opt., 17, 1889-1892 (1978), Fabrication using the computer controlled polisher.
191. R.A.Jones, Appl. Opt., 19, 2072-2076 (1980), Computer controlled polisher demonstration.
192. R.A.Jones, Appl. Opt., 21, 561-564 (1982), Segmented mirror polishing experiment.
193. H.Tsuwa, N.Ikawa, Y.Mori, K.Sugiyama, Annals CIRP, 28, 193-197 (1979).
194. W.H.Augustyn, Proc. Soc. Photo-Opt. Instr. Eng., 171, 22- 31 (1979), Automatic data reduction of both simple and complex interference patterns.
195. K.G.Birch, F.J.Green, NPL Op.Met. 12, (1972), Interferometric testing of aspheric surfaces.
196. K.G.Birch, F.J.Green, J.Phys.D: Appl. Phys. 5, 1982-1994 (1972), The application of computer-generated holograms to testing optical elements.
197. P.M.Emmel, K.M.Leung, Proc. Soc. Photo-Opt. Instr. Eng., 171, 93-99 (1979),A new instrument for routine optical testing of general aspherics.
198. J.S.Loomis, Opt. Eng., 19, 679-685 (1980), Computer-generated holography and optical testing.
199. H.J.Cauldfield, P.Mueller, D.Dvore, A.Epstein, J.S.Loomis, Proc. Soc. Photo-Opt. Instr. Eng., 306, 154-157 (1981), Computer holograms for optical testing.
200. T.L.Williams, Opt. Acta, 25, 1155-1166 (1978), A scanning gauge for measuring the form of spherical and aspherical surfaces.
201. M.Stedman, V.W.Stanley, Proc. Soc. Photo-Opt. Instr. Eng., 163, 99-102 (1979), Machine for the rapid and

accurate measurement of profiles.

202. W.E.Barkman, Proc. Soc. Photo-Opt. Instr. Eng. 192, 153-158 (1979), Noncontact, laser interferometer sweep gauge.
203. I.Powell, Appl. Opt., 20, 3367-3377 (1981), Aspheric surface calibrator.
204. J.D.Garratt, Precision Engineering, 4, 145-151 (1982), A new stylus instrument with a wide dynamicrange for use in surface metrology.
205. J.T.Boyd et al, IEEE J.Quant. Electronics QE-4, 437 (1978).
206. G.B.Brandt, M.Gottleib, Proc. Soc. Photo-Opt. Instr. Eng., 139, 159-166 (1978), Performance limits of integrated optical signal processors.
207. M.C.Hamilton, D.A.Wilk, W.J.Miceli, Opt. Eng., 16, 475-478 (1977), An integrated optical RF spectrum analyzer.
208. L.O.Svaasand et al, J.Crystal Growth, 22, 230 (1974).
209. R.L.Holman et al, Ferroelectrics, 27, 77 (1980).
210. M.N.Armenise et al, IEEE Trans CHMT-5, 212-216 (1982).
211. G.C.Jain et al, Kristall und Technik, 15, K71-K72 (1980).
212. D.G.Hall, Optics Lett., 6, 601 (1981).
213. A.L.Gauler, Opt. Eng., 21, 991-997 (1982), Comparison of two common methods of surface topography.
214. D.W.Vahey, R.P.Keenan, W.K.Burns, Appl. Opt., 19, 270 (1980), Effects of anisotropic and curvature losses on the operation of geodesic lenses in Ti:$LiNbO_3$ waveguides.
215. M.Bocher, An introduction to the study of integral equations, Cambridge Univ. Press (1914).

APPENDIX I: DERIVATION OF EXPRESSIONS FOR THE SLOPE OF EXACT RAY-TRACING LENS (SOTTINI, RUSSO AND RIGHINI) AND FOR THE SECOND DERIVATIVE

Note: numbers in square brackets refer to equation numbers in reference 83.

I.1 EXPRESSION OF PROFILE IN TERMS OF LONGITUDE FUNCTION

The lens surface is restricted to the relatively simple case where its meridional generating curve s(R) is a one-valued function which is continuously decreasing and has a continuous first derivative.

Following the arguments of sections 2.2.3 and 2.2.4 it is clear that the change of longitude (azimuth) for a ray passing through the lens from a point on a circle of radius ρ to the next crossing of the same circle is given by

$$\phi = 2\,K \int_{\rho}^{K} \frac{s'(R)\;\;dR}{R\;(R^2 - K^2)^{\;0.5}} \qquad \text{[A2]....I.1}$$

where K is the impact parameter (the closest approach to the lens centre) and s'(R) is the derivative of the arc length on the geodesic surface with respect to radial position R. Note that s' is related to the slope of the lens profile z' by $s' = (1 + z'^2)^{0.5}$.

Equation I.1 can be manipulated to a form which may be solved for s' after some transformations of variables and satisfying some conditions on the form and values taken by the longitude function $F(\psi)$. Firstly the following changes of variables and their corresponding functions are introduced:

(i) let $x = \rho^2 - K^2$ where $0 \leqslant x \leqslant \rho^2 - b^2$ [A4].....I.2

Since from equation 2.11 the impact parameter is given by $K = \rho \cos\psi$, the new variable $x = \rho^2 \sin^2\psi$ I.3

(ii) A function of the new variable, f(x), is introduced where f(x) is ϕ/K, i.e. $F(\psi)/K$. Using equation I.3 leads to

$$f(x) = \frac{F(\sin^{-1}(x^{0.5}/\rho))}{(\rho^2 - x)^{0.5}} \qquad \text{[A7]}.....\text{I.4}$$

(iii) let $\xi = \rho^2 - R^2$ where $0 \leqslant \xi \leqslant \rho^2 - b^2$ [A5].....I.5

(iv) define a function of this new variable which is equivalent to the function $-s'(R) / R^2$:

$$\text{i.e. } \Phi(\xi) = -\frac{s'((\rho^2 - \xi)^{0.5})}{\rho^2 - \xi} \qquad \text{[A6]}.....\text{I.6}$$

An explicit expression for $\Phi(\xi)$ will lead to the evaluation of the lens profile. The new variables and their functions may be used to transform Equation I.1. into the form

$$f(x) = \int_0^x \frac{\Phi(\xi)\, d\xi}{(x - \xi)^{0.5}} \qquad \text{[A8]}.....\text{I.7}$$

This is an integral of Abel's type [215]. Three conditions are required for a solution to exist:

(i) From the lens geometry defined in Figure 2.9 $0 \leqslant z' \leqslant \infty$, and s decreases as z' increases, therefore $s' = -|(1 + (z')^2)^{0.5}|$ and $-\infty \leqslant s' \leqslant -1$. Sottini, Russo and Righini [83] substituted equation I.6 into equation I.7 and compared the result of the integration with equation I.4 to show that $F(\psi) \geqslant 2\psi$ over the whole interval $b \leqslant R \leqslant \rho$.

(ii) Using Equation I.6, $s'(R) = -R^2 \Phi(\xi)$ [A9]..I.8
Since s'(R) is required to be continuous, $\Phi(\xi)$ must also be continuous. It follows that the solution of Equation I.7 must be continuous.

(iii) It has been shown by Bocher (page 10 of reference 215) that the necessary and sufficient conditions for

Equation I.7 to have a solution which is continuous between 0 and $\rho^2 - b^2$ are:

- f(x) be continuous in the same interval
- f(0) = 0, i.e. a ray incident at a latitude of radius $\rho = K$ (i.e. where that radius is also the closest approach to the centre of the lens) suffers no change of latitude ϕ at or within the radius $\rho = K$ since it does not enter within this radius.
- the integral

$$I(\xi) = \int_0^{\xi} \frac{f(x)\ dx}{(\xi - x)^{0.5}} \quad [A10] \qquad \text{.....I.9}$$

has a continuous derivative in $(0, \rho^2 - b^2)$.

Bocher (page 9, equation 4) [215] shows that if these conditions are satisfied there is a solution (and only one) to Equation I.7:

$$\Phi(\xi) = \frac{1}{\pi} \frac{d}{d\xi} \int_0^{\xi} \frac{f(x)\ dx}{(\xi - x)^{0.5}} \quad [A11] \qquad \text{.....I.10}$$

Substituting the transforms I.2 and I.5 and function I.4 into Equation I.9 gives the following expression for the integral in equation I.9:

$$I(\xi) = \int_0^{\xi} \frac{F(\arcsin(x^{0.5}/\rho))\ dx}{(\rho^2 - x)^{0.5}\ (\xi - x)^{0.5}}$$

$$= 2\rho \int_0^{\arccos(R/\rho)} \frac{F(\psi)\ \sin\psi\ d\psi}{(\rho^2\cos^2\psi - R^2)^{0.5}} \quad [A12] \qquad \text{.....I.11}$$

Using Equation I.8, it can be seen that for a solution to exist it is necessary and sufficient that

- $F(\psi)$ is continuous over the range $0 < F(\psi) < \cos^{-1}(b/\rho)$
- F(0) = 0, i.e. there is no change of latitude for a ray which touches but does not enter a parallel,
- the following function is continuous in (ρ, b) and is not greater than -1:

$$s'(R) = \frac{\rho}{\pi} R \frac{d}{dR} \int_0^{\arccos(R/\rho)} \frac{F(\psi) \sin\psi \, d\psi}{(\rho^2\cos^2\psi - R^2)^{0.5}} \quad [A13] \quad ..I.12$$

(Note that there is an error in the first term on the right-hand side of this equation as printed in reference 83.)

Sottini, Russo and Righini integrated equation I.12 to provide the only solution for the profile of the lens surface:

$$s\ (R) = \frac{\rho}{\pi} \int_\rho^R R \, dR \quad \frac{d}{dR} \int_0^{\arccos(R/\rho)} \frac{F(\psi) \sin\psi \, d\psi}{(\rho^2\cos^2\psi - R^2)^{0.5}} \quad [1]$$

where $\rho \geq R \geq b$ I.13

The lens profile therefore depends on the function $F(\psi)$ and its derivative $F'(\psi)$ with respect to radial position R. $F(\psi)$ and $F'(\psi)$ depend on the focusing requirements of the lens, as determined in the next section.

I.2 LONGITUDE FUNCTION, FOCUSING REQUIREMENTS AND CHOICE OF EDGE-ROUNDING REGION

Consider Figure 2.9 in which rays diverging from any point on a circle of radius b are focused onto a corresponding point on a circle of radius b (or vice versa), these points; by symmetry, being collinear with the centre of the lens. The surface is plane beyond the edge of the lens at radius c. Using Clairaut's theorem as in equation 2.11, the angles between the rays and the tangents to the circles are given by

$$a.\cos\psi_o = b.\cos\psi_1 = c.\cos\psi_2 = K \quad [2] \quad .....I.14$$

The longitudinal distance travelled by a ray between circles a and b is

$$\phi_o = \psi_o - \arccos\left(\frac{a}{b} . \cos\psi_o\right) \quad [3].$$

Similarly the angle traversed between b and c is

$$\phi_1 = \psi_1 - \arccos\left(\frac{b}{c} \cdot \cos\psi_1\right)$$

The lens design function $F_c(\psi_2)$ for the ray travelling between two points on the circle of radius c is given by $\pi - \phi_o - 2.\phi_1$. Using the above two expressions and using I.13 to put angles in terms of ψ_2 leads to

$$F_c(\psi_2) = \pi + 2\psi_2 - \arccos\left(\frac{c}{b} \cdot \cos\psi_2\right) - \arccos\left(\frac{c}{a} \cdot \cos\psi_2\right) \quad [7] \quad \ldots\ldots\text{I.15}$$

This function cannot be used without further modification since the paraxial ray (for which $\psi_2 = 0$) would not be found along the correct longitudinal angle of zero, since $F_c(0) = \pi - \arccos(c/b) - \arccos(c/a)$ cannot generally have the value of zero. To avoid this problem, Toraldo [75] divided the function into two parts, corresponding to the inner (focusing) region and the outer (edge-rounding) region of the lens. $F_c(\psi_2)$ is only required to match equation I.15 inside the latitude of radius d. At the edge of the lens, the function $F_d(\psi_2)$ is required to describe the ray which remains on the plane surface, i.e. the change of azimuthal angle is twice the angle to the latitude circle: $F(\psi) = 2\psi$. The function for the edge-rounding region $F_d(\psi)$ is required to match to the plane at radius c and to the inner region function $F_c(\psi_2)$ at radius d. Both functions must be continuous and without infinite first differentials (i.e. the lens surface must never be at a right angle to the plane surface).

From equation I.14 the angle between a ray and the circle of radius d is $\psi_3 = \arccos(c/d \cos\psi_2)$. This angle (or more simply the radius d) may be arbitrarily selected and either of the two functions $F_c(\psi_2)$ or $F_d(\psi_3)$ may be chosen according to some suitable rules, and then the other function is defined.

Toraldo [75] chose to define the derivative of the arc length s'(R) of the lens profile in the outer region. A

function could be chosen to match the inner function with continuity for radius d, and to be unity (but negative) at radius c to match the plane surface. Toraldo's function was

$$s'(R) = -\left[1 + \frac{c^2 - R^2}{h^2}\right] \text{ for } c \geqslant R \geqslant d \quad [11] \quad \ldots\ldots\ldots I.16$$

where h is a constant. The functions are related by the longitude $2\phi_2$ (see Figure 2.9)

$$\text{where } F_d(\psi_3) = F_c(\psi_2) - 2\phi_2 \quad [9] \quad \ldots\ldots\ldots\ldots I.17$$

Sottini, Russo and Righini calculated this angular difference by integrating equation I.1 and using equation I.15:

$$F_d(\psi_3) = \left(1 - \frac{c^2}{h^2}\right) + 2\left(1 + \frac{c^2}{h^2}\right)\psi_3 - \frac{2\,d^2}{h^2} \cos\psi_3 \sin\psi_3$$

$$+ \frac{2\,d}{h^2}\cos\psi_3 \cdot (c^2 - d^2\cos^2\psi_3)^{0.5} + 2\frac{c^2}{h^2}\arcsin\left(\frac{d}{c}\cos\psi_3\right)$$

$$- \arccos\left(\frac{d}{b}\cos\psi_3\right) - \arccos\left(\frac{d}{a}\cos\psi_3\right) \quad [12] \quad \ldots\ldots I.18$$

As stated above $F_d(0)$ must be zero so that a ray whose closest approach (impact parameter) K is at the edge-rounding region boundary d is not deviated as it touches the circle of radius d. Putting ψ_3 and $F_d(0) = 0$ allows the constant h to be expressed as

$$h = c\left(\frac{\pi - 2\gamma_{12} - \sin 2\gamma_{12}}{\gamma_{13} + \gamma_{14}}\right)^{0.5} \quad 13] \quad \ldots\ldots\ldots I.19$$

where the angles which have been introduced are defined by $d/c = \sin\gamma_{12}$, $d/b = \sin\gamma_{13}$, and $d/a = \sin\gamma_{14}$. The value of h depends on the chosen lens specification: it is real for any set of ratios which provide values of the angles γ between 0 and $\pi/2$. In particular the proportion of the lens taken up by edge-rounding may be freely selected.

I.3 EXACT SOLUTION FOR LENS PROFILE

From equation I.13:

$$s'(R) = -\frac{\rho}{\pi}\int_0^{\arccos(R/\rho)} \frac{F'(\psi)\cos\psi}{(\rho^2\cos^2\psi - R^2)^{0.5}}\, d\psi \qquad [14]$$

.....I.20

Obtaining $F'(\psi)$ by differentiating equation I.18 and integrating equation I.20 with ρ taking the distance of the edge-rounding boundary d, Sottini, Russo and Righini obtained the following expression for s'(R) (with an error in the version printed in reference 83):

$$s'(R) = -\frac{1}{2}\left(1 + \frac{c^2 - R^2}{h^2}\right) + \frac{2}{\pi h^2}\left(d^2 - R^2\right)^{0.5}\left(c^2 - d^2\right)^{0.5}$$

$$- \frac{1}{2\pi}\sin^{-1}\left(\frac{R^2 + b^2 - 2d^2}{b^2 - R^2}\right) - \frac{1}{2\pi}\sin^{-1}\left(\frac{R^2 + a^2 - 2d^2}{a^2 - R^2}\right)$$

$$+ \frac{R^2 - c^2}{\pi h^2}\sin^{-1}\left(\frac{R^2 + c^2 - 2d^2}{c^2 - R^2}\right) \quad \text{for } 0 \leqslant R \leqslant d$$

[15].....I.21

It can be seen that for R = 0 at the centre of the lens s'(0) = -1, and at the edge-rounding boundary where R = d the function s'(d) is the same as in the edge-rounding region, as given by equation I.16.

The lens surface generating profile z(R) may be obtained by integrating the slope z'(R). Since $z'^2 = s'^2 - 1$

$$z(R) = \int_0^R \left(s'(R)^2 - 1\right)^{0.5} dR \qquad [16] \qquad .....I.22$$

The expressions for s'(R) (equations I.16 for the edge-rounding region and I.21 for the inner region) may now be substituted in turn into equation I.22 to obtain the explicit formulae for the meridional generating curve of the geodesic lens.

I.4 DERIVATION OF SECOND DIFFERENTIAL AND RADIUS OF CURVATURE OF THE LENS PROFILE

For the inner region where $0 \leqslant R \leqslant d$,

$$z' = (s'^2 - 1)^{0.5} \qquad \text{and} \qquad s' = U + V + W + X + Y$$

where U,V,W,X,Y are the 5 terms on the right hand side of equation I.19. Differentiating with respect to R:

$$z'' = \frac{s'(U'+V'+W'+X'+Y')}{(s'^2 - 1)^{0.5}} = \frac{(z' + 1)^{0.5}\ (U'+V'+W'+X'+Y')}{z'}$$

where the square root must take a negative value, and

$$U' = R/h^2$$

$$V' = -\frac{2R}{\pi h^2}\left(\frac{c^2 - d^2}{d^2 - R^2}\right)0.5$$

$$W' = -\frac{R}{\pi(b^2 - R^2)}\left(\frac{b^2 - d^2}{d^2 - R^2}\right)0.5$$

$$X' = -\frac{R}{\pi(a^2 - R^2)}\left(\frac{a^2 - d^2}{d^2 - R^2}\right)0.5$$

$$Y' = +\frac{2R}{\pi h^2}\left[\sin^{-1}\left(\frac{R^2 + c^2 - 2d^2}{c^2 - R^2}\right) - \left(\frac{c^2 - d^2}{d^2 - R^2}\right)0.5\right]$$

Therefore the second differential may be expressed as

$$z'' = \frac{(z'^2 + 1)0.5}{z'}\ \frac{R}{\pi h^2}\ P(R,a,b,c,d)$$

where the function $P(R,a,b,c,d) =$

$$\pi + 2\left[\sin^{-1}\left(\frac{R^2 + c^2 - 2d^2}{c^2 - R^2}\right) - 2.Q(c)\right] - h^2\left(\frac{Q(a)}{a^2 - R^2} + \frac{Q(b)}{b^2 - R^2}\right)$$

and the function $Q(x) = \left(\frac{x^2 - d^2}{d^2 - R^2}\right)0.5$

The radius of curvature is given by equation 2.19:

$$C = \frac{(1 + z'^2)^{1.5}}{z''}$$

and, using the above expression for the second differential, z", leads to equation 2.20:

$$C = \frac{\pi h^2}{R} \frac{z' \quad (z'^2 + 1)}{P(R,a,b,c,d)}$$

<u>For the outer region</u> where $d \leqslant R \leqslant c$,

$$z' = (Z^2 + 2Z)^{0.5} \qquad \text{where } Z = \frac{c^2 - R^2}{h^2}$$

$$\text{therefore } z'' = - \frac{2R(Z + 1)}{h^2(Z^2 + 2Z)^{0.5}} = - \frac{2R(z'^2 + 1)^{0.5}}{h^2 . z'}$$

and the local radius of curvature

$$C = - \frac{h^2}{2R} z'(z'^2 + 1)$$

APPENDIX II: DERIVATION OF APPROXIMATIONS USED FOR SMALL ARCS, TOOL-SETTING AND PROFILE-ASSESSMENT ERRORS.

II.1 APPROXIMATION FOR THE DISTANCE FROM A CIRCLE TO A CHORD FOR A VERY SMALL ARC-LENGTH

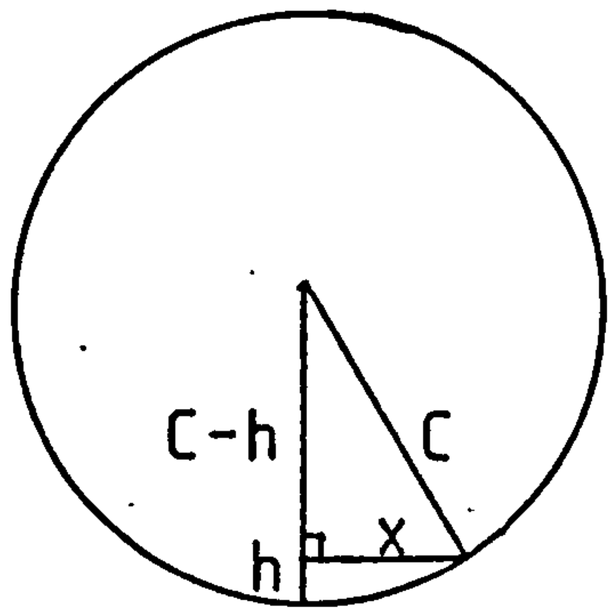

$$x^2 = C^2 - (C - h)^2$$

$$\simeq 2.C.h$$

$$\therefore h \simeq \frac{x^2}{2.C} \qquad \text{.....II.1}$$

II.2 APPROXIMATIONS FOR TOOL-SETTING AND PROFILE-ASSESSMENT ERRORS

For the case when a tool or probe is <u>inside</u> the arc of the lens profile, the profile is referred to as "concave", and when the tool or probe is <u>outside</u> the arc the profile is referred to as "convex".
The tool-tip or measurement-probe radius of curvature is T
The local radius of curvature of lens profile is C
and the cutting or measurement error is ΔE.

(i) Tool or probe tip is displaced from the A-axis in a direction parallel to the lens surface.

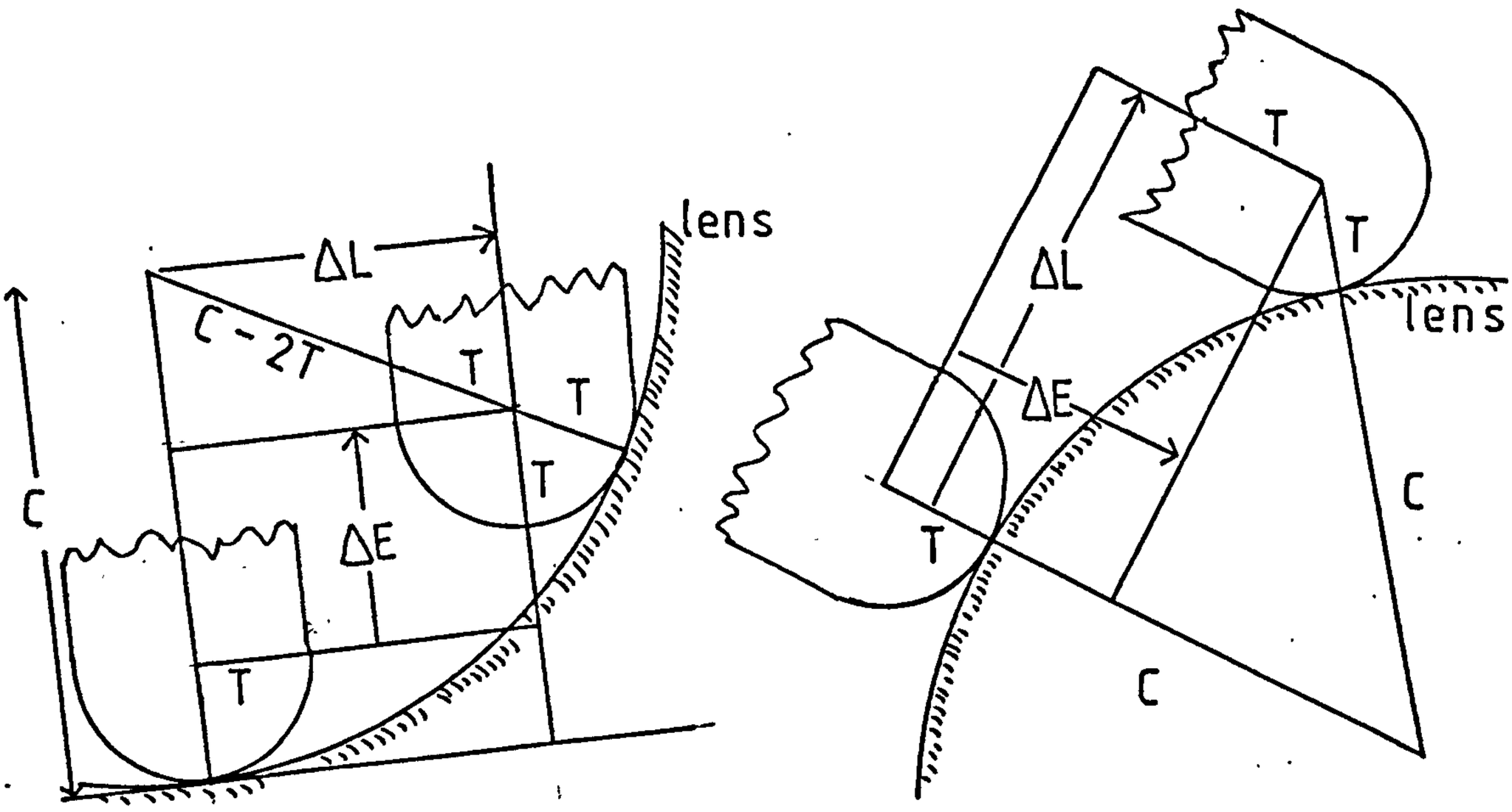

If the lateral error of tool or probe setting is ΔL, then the cutting or measurement error is given by:

$$\Delta E = C \pm T - ((C \pm T)^2 - \Delta L^2)^{0.5}$$

where $-$ for tool inside lens-profile arc (concave),
$+$ for tool outside arc (convex).

Because the magnitude of ΔL is generally a few micrometres, and C and T are generally a few millimetres, then a binomial expansion may be made with all terms but the first negligible. The error may then be expressed as

$$\Delta E \simeq \frac{\Delta L^2}{2\ (C \pm T)} \qquad \text{.....II.2}$$

The direction of the error is such that a tool cuts too deep and a probe measures too shallow when in a concave part of a lens profile, and vice versa when in a convex part. For a concave profile, when the tool or probe tip is of the same, or very similar radius of curvature, the approximation given above is not valid, and the error is potentially very large.

(ii) Tool or probe tip set above or below the centre of rotation of the lens.

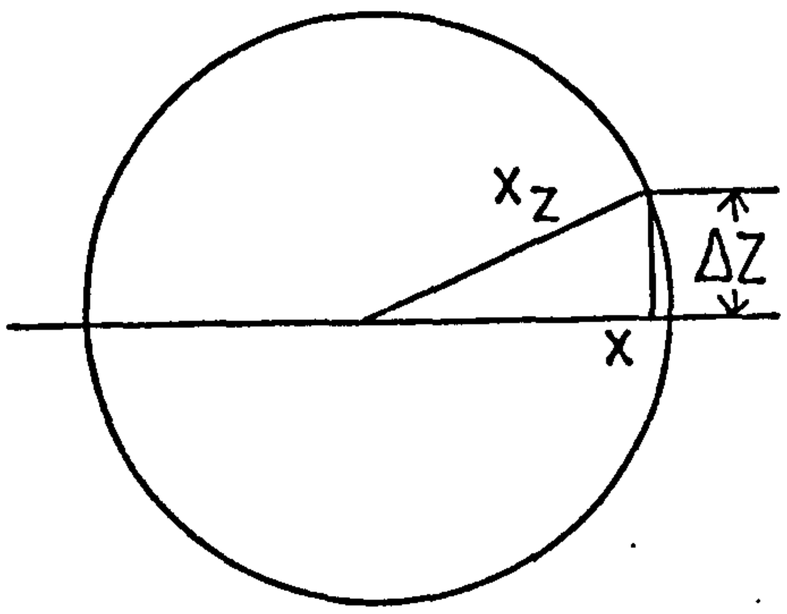

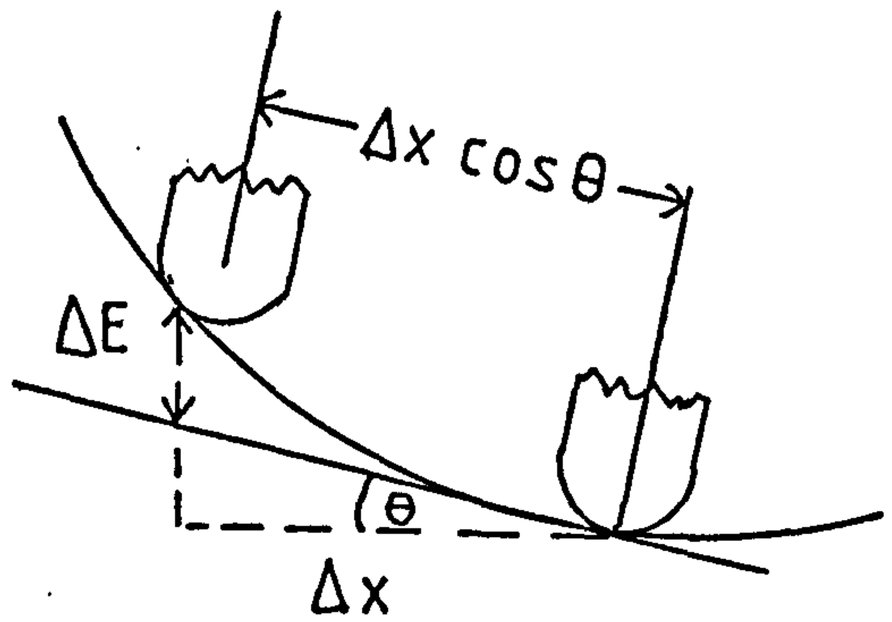

Consider the case when a tool or probe should be at radial position x, but is displaced above or below the axis of rotation of the lens by ΔZ so that it is actually at radial position x_z. Then the error in radial position is given by

$$\Delta x = x_z - x = (x^2 + \Delta Z^2)^{0.5} - x$$

Ths expression may be approximated to

$\Delta x \simeq \Delta Z$ near to the centre of the lens, and

$\Delta x \simeq \Delta Z^2/2x$ over the remainder of the lens.

At a position on the lens where the angle of the slope of the profile is θ, the probe displacement tangential to the lens surface is approximately $\Delta x.\cos\theta$. The error in tool or probe depth normal to the lens surface may be approximated (using equation II.2) by

$$\Delta E \simeq \frac{(\Delta x.\cos\theta)^2}{2\ (C \pm T)}$$

Near to the centre of the lens, where $\theta \simeq 0$,

$$\Delta E \simeq \frac{\Delta Z^2}{2\ (C \pm T)} \qquad \text{.....II.3}$$

and elsewhere on the lens surface

$$\Delta E \simeq \frac{\Delta Z^4.\ \cos^2\theta}{8.x^2\ (C \pm T)} \qquad \text{.....II.4}$$

where $-$ for tool inside lens-profile arc (concave),

$+$ for tool outside arc (convex).

(iii) Tool- or probe-tip is on the A-axis, but the A-axis is displaced laterally along the X-axis away from X = O.

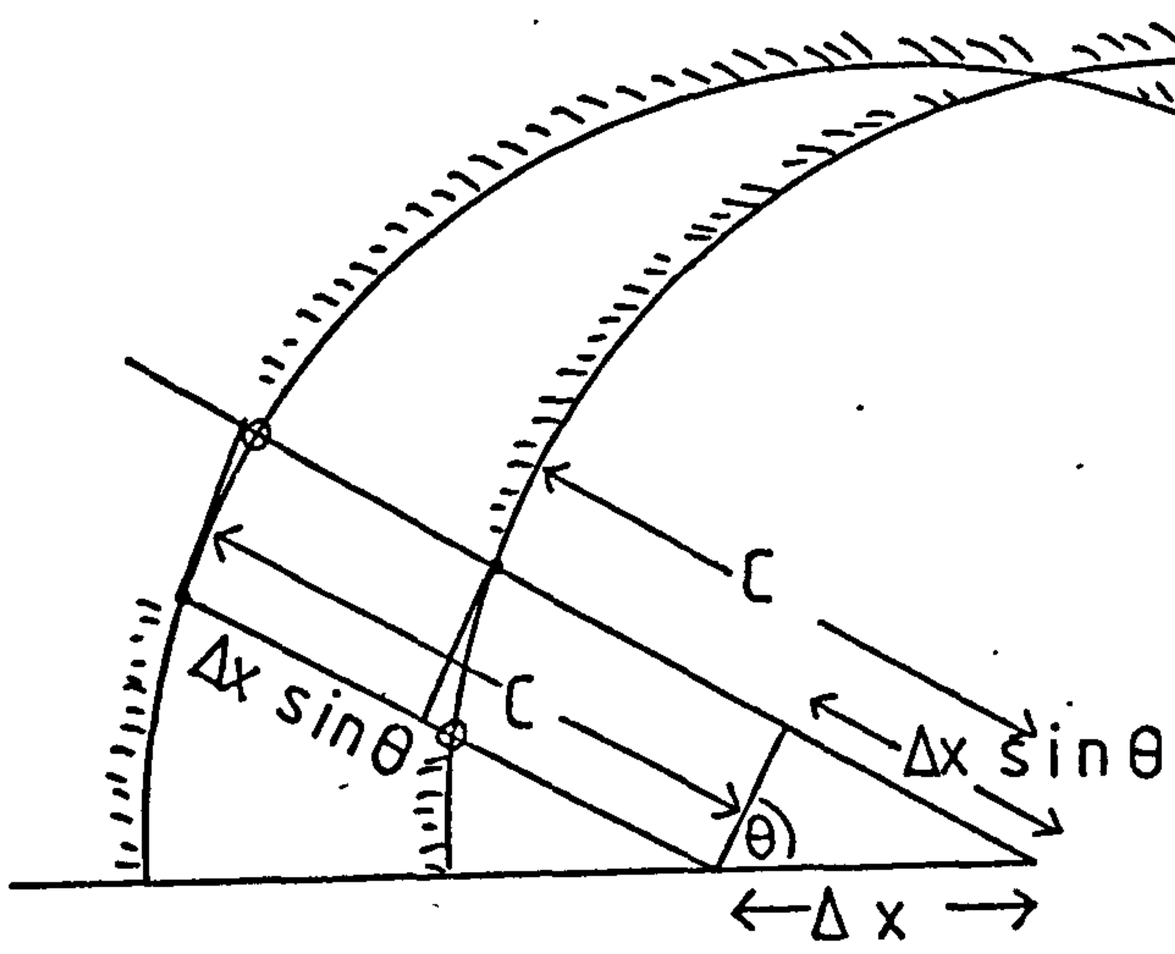

$$\Delta E = \pm \Delta x \left(\sin\theta - \frac{\Delta x . \cos^2\theta}{2.C}\right) \qquad \text{.....II.5}$$

(iv) Tool- or probe-tip is displaced away from the A-axis in a direction normal to the lens surface.

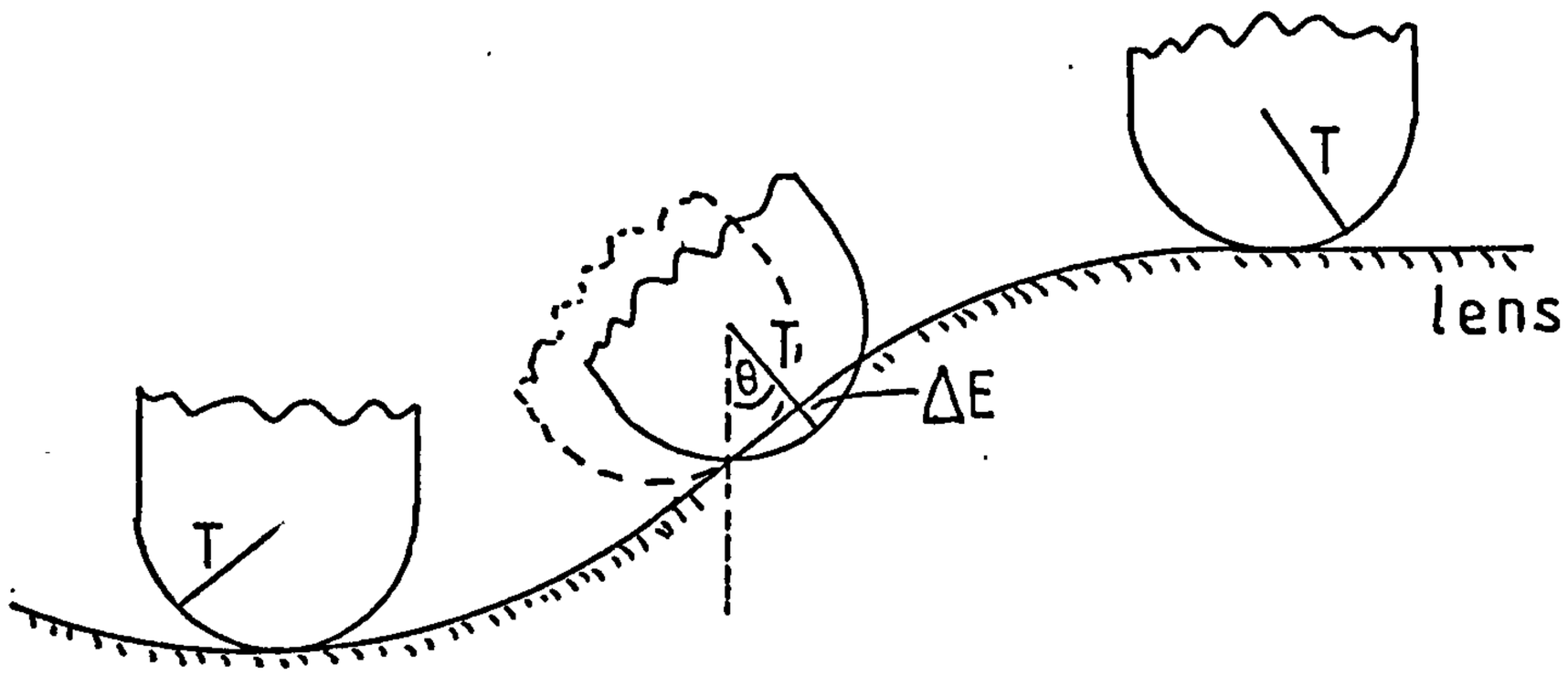

$$\Delta E \fallingdotseq \Delta L \ (1 - \cos\theta)$$

II.3 CONTACT AREA OF FLEXIBLE POLISHING TOOL

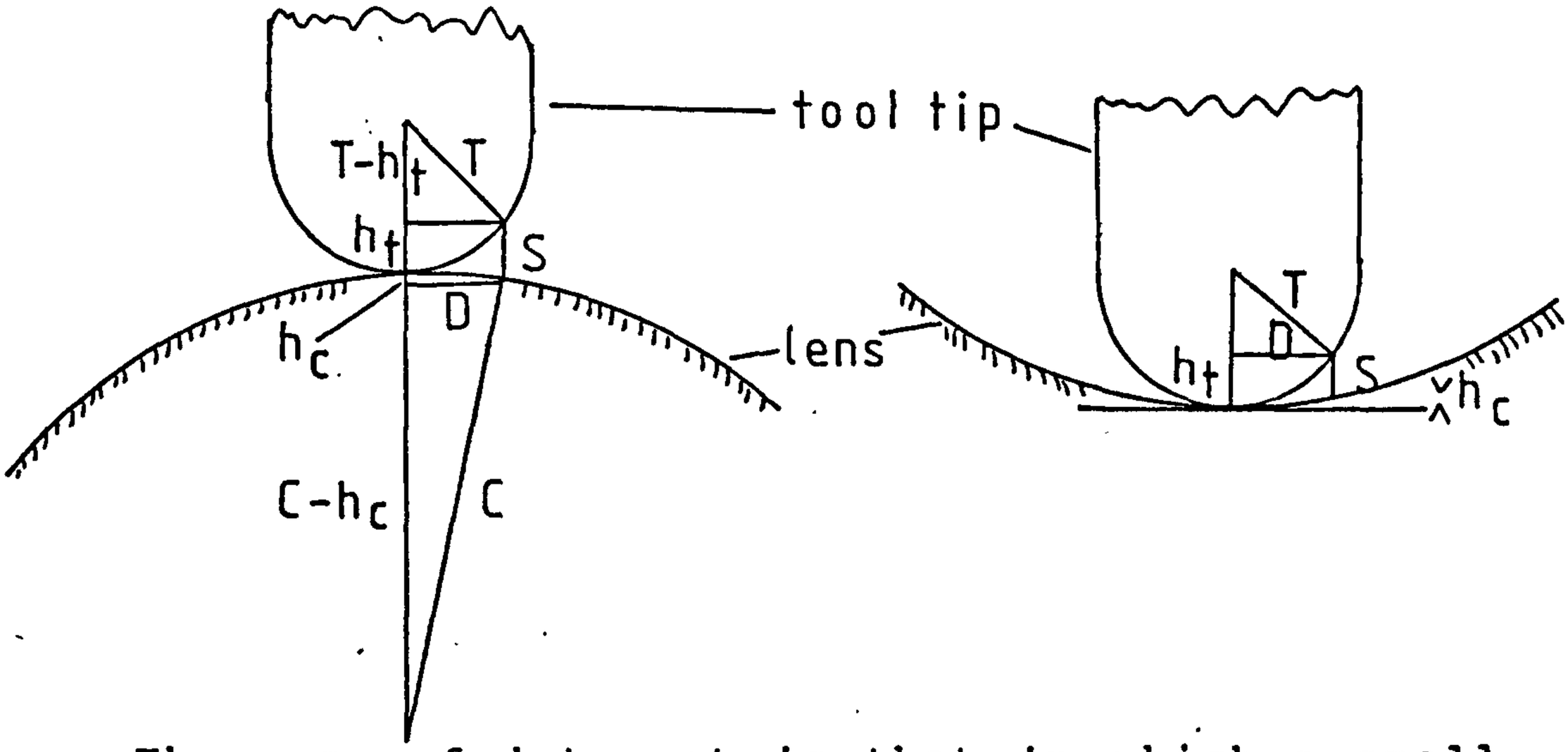

The case of interest is that in which a small, spherical polishing-tool tip of radius T is in contact with the lens surface, of local radius of curvature C, so that the tool is pressed against the lens surface to form a finite area of contact with the abrasive particles between them. The simplifying approximation is made that the pressure is uniform over the area of contact, and decreases to zero pressure at a radius D at which the lens and tool surfaces are separated by a distance corresponding to the size of the abrasive particles S.

From the geometry of the sketches above, using equation II.1,

$$D^2 \simeq 2.h_T.T \simeq 2.h_C.C$$

and $$S = h_T \pm h_C$$

where + for tool outside arc (convex),

and − for tool inside lens-profile arc (concave).

$$S \simeq \frac{D^2}{2.T} \pm \frac{D^2}{2.C}$$

Because the removal rate during polishing is approximately proportional to the area of contact, then the correction to the polishing duration for variable contact area is inversely proportional to the contact area, i.e.

$$\text{time} \propto \frac{1}{T} \pm \frac{1}{C}$$

If the local radius of curvature at the centre of the lens is C_0, then the polishing time correction, relative to the time required at the centre of the lens, is given by

$$\frac{\frac{1}{T} \pm \frac{1}{C}}{\frac{1}{T} - \frac{1}{C_0}}$$

For the example of polishing the aspheric lens profile (page 181) the radius of the polishing tool tip is approximately 3mm and the radius of curvature of the lens surface at the centre is 10.9mm.